

**Commissioning of advanced, dual-recycled
gravitational-wave detectors:
simulations of complex optical systems guided by the
phasor picture**

Dipl.-Phys. Michaela Malec
2006

**Commissioning of advanced, dual-recycled
gravitational-wave detectors:
simulations of complex optical systems guided by the
phasor picture**

Von der Fakultät für Mathematik und Physik der Universität Hannover
und der Faculty of Physical Sciences der Universität Glasgow
zur Erlangung des gemeinsamen Grades

**Doktorin der Naturwissenschaften¹
– Dr. rer. nat. –**

genehmigte Dissertation von

Dipl.-Phys. Michaela Malec

geboren am 18. Oktober 1972 in Hannover

© Michaela Malec März 2006

¹Dieser Grad ist dem Grad **Doctor of Philosophy by Research (Ph.D.)** der Universität Glasgow äquivalent.

**Commissioning of advanced, dual-recycled
gravitational-wave detectors:
simulations of complex optical systems guided by the
phasor picture**

Thesis by Michaela Malec, accepted by
the Fakultät für Mathematik und Physik of the University of Hannover and
the Faculty of Physical Sciences at the University of Glasgow
for the jointly awarded degree

Doktorin der Naturwissenschaften²
– Dr. rer. nat. –

© Michaela Malec March 2006

| | |
|--|-------------------|
| Referent: | Prof. K. Danzmann |
| Korreferent: | Dr. H. Ward |
| External examiner (appointed by the University of Glasgow): | Dr D. McGloin |
| Tag der Promotion: | 6. Februar 2006 |

²This degree is equivalent to the degree **Doctor of Philosophy by Research (Ph.D.)** of the University of Glasgow.

Zusammenfassung

Derzeit beginnt die Datenaufnahme eines internationalen Netzwerkes von großen, laserinterferometrischen Gravitationswellendetektoren. Dies ist der Auftakt zu einer neuen Form der Astronomie, der Gravitationswellenastronomie. Der britisch-deutsche Gravitationswellendetektor GEO 600 ist der einzige des Netzwerkes, der zur Erhöhung seiner Sensitivität mit dem sogenannten Signal-Recycling (SR) ausgestattet ist. Diese Technik erlaubt es, die Sensitivität für Gravitationswellen in einem bestimmten Frequenzband auf Kosten der umliegenden Frequenzen zu erhöhen. Dafür werden mit Hilfe eines Spiegels im Ausgang eines Michelson-Interferometers, dem Signal-Recycling-Spiegel (SR-Spiegel), die Gravitationswellensignale in einem wählbaren Frequenzbereich resonant überhöht. Bei GEO 600 bestimmt die Reflektivität des SR-Spiegels die Breite des Bandes, seine mikroskopische Position die Mittenfrequenz. Die Mittenfrequenz wird im aktuellen Betrieb von GEO 600 bereits über einen weiten Frequenzbereich von derzeit 2 kHz gezielt und flexibel eingestellt. Mit dem Einsatz eines Etalons statt eines herkömmlichen Spiegels möchte man in Zukunft auch die Reflektivität, und damit die Bandbreite des Detektors regeln.

Grundvoraussetzung für einen verlässlichen Langzeitbetrieb dieser Observatorien ist die steile Regelung aller Freiheitsgrade. Dafür werden Regelsignale mit Hilfe von Modulations-Demodulationstechniken von Licht gewonnen. Diese Signale hängen jedoch in einem hochkomplexen optischen System wie GEO 600 von vielen Freiheitsgraden gleichzeitig ab. Verändert man z.B. die Position oder die Reflektivität des SR-Spiegels im Betrieb, werden auch die Regelsignale anderer Freiheitsgrade unmittelbar beeinflusst.

Im Rahmen der vorliegenden Arbeit wurden diese Regelsignale und die dazu gehörenden Lichtfelder mit Hilfe des Programmes FINESSE untersucht. Um mit dem Experiment übereinstimmende Arbeitspunkte zu erzeugen, wurden die Längen der Resonatoren und der Michelson-Armlängenunterschied auf mindestens 1 mm genau bestimmt. Darüberhinaus ist eine Kalibration der SR- und Michelson-Demodulationsphasen mit einer Genauigkeit von $\pm 2^\circ$ gelungen. Mit diesen Eingangsparametern kann der Verlauf der Signalüberhöhung von GEO 600 in einem Bereich von 2 kHz um die jeweilige Mittenfrequenz mit einer Genauigkeit von besser als 5% vorhergesagt werden. Außerdem konnte mit Hilfe von Simulationen eine Matrix erstellt werden, die die einzustellenden Demodulationsphasen und Verstärkungen der SR- und Michelson-Regelungen für verschiedene SR-Verstimmungen enthält. Die Simulation vermag den Verschiebungsprozess des Frequenzbandes maximaler Sensitivität schneller und gezielter zu optimieren, als das im Experiment möglich ist.

Ein weiterer Teil dieser Arbeit ist der Verbesserung der Empfindlichkeit von GEO 600 gewidmet. Zum einen wurde mit Hilfe des Phasorenbildes die Abhängigkeit der Sensitivität von den Resonanzbedingungen der Michelson-Regelseitenbänder untersucht. Allein durch eine Erhöhung der aktuell verwendeten Seitenbandfrequenz um 33 Hz kann die Sensitivität global für niedrige Signalfrequenzen um bis zu 30% verbessert werden.

Zum anderen wurde die Identifizierung technischer Rauschquellen, die die Empfindlichkeit begrenzen, durch die Analyse von Kopplungsmechanismen unterstützt. Für das Laseramplitudenrauschen spielen z.B. die Resonanzen der Rauschseitenbänder eine entscheidende Rolle. Diese Erkenntnis verhalf dazu, eine weitere Rauschquelle mit ähnlichen Kopplungseigenschaften zu finden, das Modulationsindexrauschen.

Tritt ein Etalon an die Stelle des SR-Spiegels, verändern sich die Regelsignale im Vergleich zum herkömmlichen Spiegel. Simulationen zeigen jedoch, dass der Betrieb des Detektors nicht gefährdet ist. Stellt man die Reflektivität des Etalons ein, sollte bei der aktuellen Konfiguration von GEO 600 aus regelungstechnischen Gründen eine Vergrößerung des mikroskopischen Abstands der Etalonoberflächen gewählt werden.

Stichworte: Gravitationswellendetektor, Simulation, Phasorenbild, Sensitivität, gekoppelte Resonatoren, Fehlersignal, Laseramplitudenrauschen, Etalon, FINESSE

Summary

Currently, the data acquisition of an international network of large, laser-interferometric gravitational-wave detectors is about to begin. This preludes a new form of astronomy; gravitational-wave astronomy. The British-German gravitational-wave detector GEO 600 is the only detector of this network featuring signal recycling (SR), an optical technique that allows for increasing the sensitivity in a particular frequency band, at the expense of other, surrounding frequencies. This is achieved by resonantly enhancing the gravitational-wave signals of an arbitrary frequency region inside the so-called signal-recycling cavity, formed by a Michelson interferometer (MI), and a SR mirror at the MI output port. The reflectivity of the SR mirror determines the bandwidth of the enhanced region, the microscopic position, the mid-frequency. The mid-frequency, or detector tuning, of GEO 600 can already systematically be set during the operation within a range of 2 kHz. In future, the detector bandwidth may also be customised, replacing the conventional SR mirror by an etalon whose reflectivity is adjustable.

A basic requirement for a reliable long-term operation of these observatories is a permanent control of all degrees of freedom. The respective control signals are gained by modulation/demodulation techniques applied to light. In an advanced optical system like GEO 600, however, these control signals depend on several degrees of freedom at the same time. Altering, for example, the position or reflectivity of the SR mirror during detector operation instantaneously changes the properties of the control signals of other degrees of freedom.

Within the scope of this thesis, the control signals of GEO 600 and the corresponding light fields were investigated using the program FINESSE. In order to yield operating points that agree with the experiment, the differential MI armlength, and the resonator lengths were determined with an accuracy of at least ± 1 mm. Beyond, we managed to calibrate the SR and MI demodulation phases with $\pm 2^\circ$ precision. Using these input parameters, the shape of the signal enhancement of GEO 600 can be predicted with a deviation of less than 5% from the experiment, within a region of 2 kHz around the respective tuning frequency. Furthermore, a matrix was generated by simulation that contains demodulation phase and gain settings for the SR and MI control loops, enabling a quasi-continuous tuning of the detector. In comparison to an experimental parameter determination, the simulation allows for a more targeted and faster optimisation of the loop parameters.

Another part of this thesis is dedicated to the improvement of the sensitivity of GEO 600. On the one hand, employing the phasor picture allowed for a global examination of the sensitivity dependency on the resonance conditions of the MI control sidebands. Increasing the currently used sideband frequency, by 33 Hz only, can globally enhance the sensitivity for low gravitational-wave frequencies by up to 30%.

On the other hand, analysing the coupling mechanisms of noise sources into the detector output supported the identification of particular sources that limited the detector sensitivity. For the laser-amplitude noise coupling, for example, the noise-sideband resonances play a decisive role. This insight helped to find another source exhibiting similar coupling features, namely modulation-index noise.

With an etalon taking the place of the SR mirror, the control signal features change in comparison with the conventional-mirror configuration. However, simulations indicate that these changes do not compromise the detector operation nor the process of tuning. When adjusting the reflectivity of the etalon in a GEO 600 configuration similar to the current, the distance between the etalon surfaces should, due to control reasons, be increased rather than decreased.

Keywords: gravitational-wave detector, simulation, phasor picture, sensitivity, error-signal, laser-amplitude noise, etalon, FINESSE

Contents

| | |
|--|-------------|
| Zusammenfassung | i |
| Summary | iii |
| Contents | v |
| List of figures | ix |
| Glossary | xiii |
| 1. Optical detection via the modulation/demodulation technique | 1 |
| 1.1. Modulation of light fields | 2 |
| 1.1.1. Phasor diagrams | 3 |
| 1.1.2. Amplitude modulation | 4 |
| 1.1.3. Phase modulation | 4 |
| 1.1.4. Frequency modulation | 6 |
| 1.1.5. Phase modulation of phase modulation | 8 |
| 1.1.6. Amplitude modulation of phase modulation | 9 |
| 1.2. Generation of error-signals | 10 |
| 1.2.1. Conventions | 17 |
| 1.2.2. Cavity control signal in reflection | 19 |
| 1.2.3. Cavity signals in transmission | 24 |
| 1.2.4. Control of a Michelson interferometer | 27 |
| 2. The optical response of GEO 600 | 35 |
| 2.1. Introduction | 35 |
| 2.2. Techniques to enhance the sensitivity | 37 |
| 2.3. GEO 600 response in terms of phasors | 41 |
| 2.3.1. Sideband resonances for different detector tunings | 41 |
| 2.3.2. The Michelson error-signal with signal sidebands | 42 |
| 2.3.3. Tuned detector | 45 |
| 2.3.4. Detuned signal recycling at 5 kHz | 48 |
| 2.3.5. Detuned signal recycling at 1 kHz | 51 |
| 2.4. The importance of the control sidebands for the sensitivity shape | 57 |
| 2.4.1. Comparison of three dual-recycled detector setups | 57 |
| 2.4.2. Consequence: the optimal GEO 600 | 62 |
| 2.5. Projection picture versus FINESSE | 70 |
| 2.6. Conclusion | 74 |

| | |
|---|------------|
| 3. Tuning process of a dual-recycled Michelson interferometer | 77 |
| 3.1. Introduction | 77 |
| 3.2. The longitudinal control of GEO 600 | 78 |
| 3.2.1. Laser frequency stabilisation and power-recycling cavity lock | 78 |
| 3.2.2. Longitudinal control of differential Michelson arms | 81 |
| 3.2.3. Longitudinal control of the signal-recycling cavity | 87 |
| 3.2.4. Lock automation, and the transition to a tunable detector | 90 |
| 3.3. Signal-recycling error-signal | 92 |
| 3.3.1. Sideband properties in the coupled cavities | 96 |
| 3.3.2. Signal-recycling error-signal explanation with phasor diagrams | 100 |
| 3.4. Michelson error-signal | 107 |
| 3.5. Tuning script generation | 111 |
| 3.5.1. Signal-recycling control-loop parameters | 113 |
| 3.5.2. Michelson control-loop parameters | 126 |
| 3.6. Experimental tuning | 131 |
| 3.6.1. Positive, or negative tuning side: this is the question... | 132 |
| 3.6.2. Calibration of simulated parameters | 134 |
| 3.6.3. Necessary accuracy of the FINESSE script and of the calibration with respect to the tuning process | 137 |
| 3.6.4. Towards a tuned detector | 147 |
| 3.7. Tuning process alterations replacing MSR by an etalon | 149 |
| 3.7.1. Etalon characterisation | 150 |
| 3.7.2. Sideband resonance alterations in the signal-recycling cavity | 153 |
| 3.7.3. Tuning parameter alterations | 157 |
| 3.8. Conclusion | 163 |
| | |
| 4. Detector characterisation utilising simulations | 167 |
| 4.1. Introduction | 167 |
| 4.2. 2f signal | 168 |
| 4.3. Optical transfer function | 172 |
| 4.3.1. Determining the signal-recycling cavity length | 172 |
| 4.3.2. Anticipating the optical transfer function of GEO 600 | 174 |
| 4.4. Laser amplitude noise | 176 |
| 4.4.1. Experimental laser-amplitude-noise coupling into $h(t)$ | 177 |
| 4.4.2. Coupling mechanism | 177 |
| 4.4.3. FINESSE results for the amplitude-noise transfer function | 181 |
| 4.5. Conclusion | 186 |
| | |
| A. Signal-recycling demodulation phase calibration | 189 |
| | |
| B. Simulation scripts | 193 |
| B.1. FINESSE scripts | 193 |
| B.1.1. Most adequate FINESSE script for the current optical setup | 193 |
| B.1.2. FINESSE script used before May 2005 | 197 |
| B.2. MATLAB scripts | 200 |

| | |
|---|------------|
| B.2.1. MATLAB script for the estimation of signal-recycling error signal susceptibility to various degrees of freedom | 200 |
| B.2.2. MATLAB script for signal-recycling error signal property optimisation | 209 |
| B.2.3. MATLAB script for differential Michelson error signal evaluation | 217 |
| B.2.4. MATLAB script for the tuning script generation | 220 |
| C. Impact of various parameters on the 2f signal | 227 |
| C.1. Signal-recycling cavity length and tuning | 227 |
| C.2. Schnupp length | 228 |
| C.3. Common losses and MSR reflectivity | 230 |
| C.4. Misalignment | 232 |
| Bibliography | 235 |
| Acknowledgements | 239 |
| Curriculum vitae | 241 |
| Publications | 243 |

List of figures

| | |
|--|----|
| 1.1. The scalar light field in the phasor picture | 3 |
| 1.2. Amplitude modulation | 5 |
| 1.3. Phase modulation | 7 |
| 1.4. Phase modulated phase modulation | 9 |
| 1.5. Amplitude modulation of phase modulation | 11 |
| 1.6. Illustration of the error-signal vector deduction | 16 |
| 1.7. Cavity resonance conditions in reflection for carrier and control sidebands | 20 |
| 1.8. Pound-Drever-Hall signal around carrier resonance in the projection picture | 22 |
| 1.9. Pound-Drever-Hall signal around the lower control sideband resonance in the projection picture | 25 |
| 1.10. Pound-Drever-Hall error-signal amplitude for different demodulation phases | 26 |
| 1.11. Pound-Drever-Hall error-signal amplitude in P and Q comprising all light field resonances | 27 |
| 1.12. Resonance conditions for carrier and control sidebands in cavity transmission | 28 |
| 1.13. Error-signal amplitude in transmission | 29 |
| 1.14. Layout of a simple Michelson interferometer | 30 |
| 1.15. Carrier and sideband phasors at the Michelson ports | 31 |
| | |
| 2.1. Theoretical noise budget of GEO 600 | 37 |
| 2.2. The optical setup of the dual-recycled Michelson interferometer of GEO 600 | 39 |
| 2.3. Theoretical shot noise limited sensitivity for particular detector tunings of GEO 600 | 40 |
| 2.4. Resonance conditions of the Michelson control sidebands inside the signal- recycling cavity | 43 |
| 2.5. Michelson error-signal-vector deduction for a tuned detector | 47 |
| 2.6. Michelson error-signal-vector deduction for a detector detuned to 5 kHz . | 49 |
| 2.7. Shift of the peak sensitivity, explained by the projection picture | 50 |
| 2.8. Michelson error-signal-vector deduction for a detector detuned to 1 kHz . | 52 |
| 2.9. Measured gravitational-wave signal content in P and Q for 1 kHz and 250 Hz detuning | 54 |
| 2.10. Phasor diagram representing the experimental P and Q quadrature | 55 |
| 2.11. Comparison between the theoretical shot noise limited sensitivities of GEO 600 in P, Q, and the best combination of the two quadratures | 56 |
| 2.12. Control sideband properties for varying signal-recycling cavity lengths . . | 59 |
| 2.13. GEO 600 sensitivity for three different signal-recycling cavity lengths . . . | 60 |
| 2.14. Shift of peak sensitivity with detector tuning | 62 |

| | |
|--|-----|
| 2.15. Influence of arbitrary control sideband resonance conditions inside the signal-recycling cavity on the detector sensitivity | 64 |
| 2.16. Michelson control sideband amplitudes depending on the modulation frequency and the detector tuning | 67 |
| 2.17. Deviation of the sensitivity of a detector setup, with optimised control sideband frequency, from that of GEO 600 | 68 |
| 2.18. Ratio of the best and worst possible <i>SNRs</i> at the resonant frequency, versus detuning | 70 |
| 2.19. Comparison of the peak-sensitivity shift prediction of the projection picture with FINESSE | 72 |
| 2.20. Comparison of the predictions of the sensitivity alterations, due to an optimised modulation frequency, by the projection picture with FINESSE . | 73 |
| 2.21. FINESSE result for the sensitivity deviation accounting for waste-light effects | 74 |
| | |
| 3.1. Overview over the longitudinal control loops of the dual-recycled Michelson interferometer of GEO 600 | 79 |
| 3.2. Open loop gain of the power-recycling control | 82 |
| 3.3. Triple pendulum suspension of a Michelson end mirror | 84 |
| 3.4. Open loop gain of the Michelson control | 85 |
| 3.5. Comparison of the Michelson optical gain with the 2f signal | 87 |
| 3.6. Open loop gain of the signal-recycling control | 89 |
| 3.7. Crossover between the lock on the 2f signal and the sideband error-signal | 91 |
| 3.8. Overview of the signal-recycling error-signal amplitude in the plane of modulation frequency and signal-recycling cavity tuning | 94 |
| 3.9. Signal-recycling error-signal amplitude with different demodulation phases | 96 |
| 3.10. Resonance conditions for the signal-recycling control sidebands inside the signal-recycling cavity | 98 |
| 3.11. Signal-recycling sideband amplitudes depending on the modulation frequency and the detector tuning | 99 |
| 3.12. Light field phasors at different points of the power-recycled Michelson interferometer | 101 |
| 3.13. Signal-recycling error-signal vector derivation for a tuned-detector configuration | 102 |
| 3.14. Signal-recycling error-signal vector derivation for a far positively detuned detector configuration | 104 |
| 3.15. Signal-recycling error-signal vector derivation for a far negatively detuned detector configuration | 105 |
| 3.16. Property changes of the Michelson error-signal vector for various detector tunings, explained by the phasor picture | 108 |
| 3.17. Signal-recycling error-signal amplitudes for different tuning steps | 111 |
| 3.18. Measured signal-recycling feedback, calibrated to MSR displacement . . . | 114 |
| 3.19. Justification of the demodulation phase steps for simulation | 118 |
| 3.20. Susceptibility of the signal-recycling error-signal to various degrees of freedom for 4 kHz detuning | 120 |

| | |
|--|-----|
| 3.21. Susceptibility of the signal-recycling error-signal to various degrees of freedom for 0 Hz detuning | 121 |
| 3.22. Comparison of signal-recycling error-signal amplitudes optimised for particular criteria | 122 |
| 3.23. Simulation results for signal-recycling demodulation phases and gains . . . | 123 |
| 3.24. Lower and upper capture ranges of the optimised signal-recycling error-signals | 124 |
| 3.25. Zero crossing locations of the signal-recycling error-signals | 126 |
| 3.26. Michelson error-signal amplitude for a tuned detector | 128 |
| 3.27. Simulation results for the Michelson demodulation phases and gains . . . | 130 |
| 3.28. Zero crossing positions of the differential Michelson error-signals | 131 |
| 3.29. Sideband power measurement indicating the tuning sign of GEO 600 . . . | 133 |
| 3.30. Dependency of the signal-recycling error-signal zero crossing on the demodulation phase, for a detector tuning of 2 kHz | 136 |
| 3.31. Tuning script parameters for the signal-recycling and the Michelson control loops | 138 |
| 3.32. Signal-recycling tuning script parameters for a signal-recycling cavity length deviation | 140 |
| 3.33. Signal-recycling optical-gain dependency on the demodulation phase for various detector tunings | 141 |
| 3.34. MSR position dependency on the signal-recycling demodulation phase for various detector tunings | 142 |
| 3.35. Michelson tuning script parameters for a Schnupp length deviation | 144 |
| 3.36. Optical-gain dependency of the Michelson error-signal on the demodulation phase | 145 |
| 3.37. Michelson optical gain deviations for different Schnupp lengths | 146 |
| 3.38. Variation of the signal-recycling error-signal gain and zero crossing position with the demodulation phase, for $\delta f_m = -80$ Hz | 148 |
| 3.39. Light power and phase shift appearing in etalon reflection | 151 |
| 3.40. Illustration of the phase shift occurring at an etalon for light fields with different frequencies | 152 |
| 3.41. Definition of three tunings associated with an etalon | 153 |
| 3.42. Positions of the signal-recycling and the Michelson control sideband resonances inside the signal-recycling cavity, in the plane of modulation frequency and MSR /etalon position | 156 |
| 3.43. Comparison of the demodulation phases and gains of the most symmetric signal-recycling error-signals, for different etalon/ MSR reflectivities . . . | 159 |
| 3.44. Offsets of the signal-recycling error-signal zero crossings from carrier resonance, for different etalon/ MSR reflectivities | 160 |
| 3.45. Comparison of Michelson demodulation phases and gains, for different etalon/ MSR reflectivities | 162 |
| 4.1. Measurement of the 2f signal | 170 |
| 4.2. Comparison of the measurement with the simulation using default script parameters | 171 |

| | | |
|-------|---|-----|
| 4.3. | Results of the least-square method for the common Michelson losses, the Schnupp length, and the signal-recycling cavity length | 171 |
| 4.4. | Optical transfer-function amplitudes for different signal-recycling cavity lengths | 173 |
| 4.5. | 2f signal comparison of the simulation, using optimised input script parameters, with the measurement | 174 |
| 4.6. | Comparison of measured and simulated optical transfer functions of GEO 600, tuned to 1 kHz | 175 |
| 4.7. | Transfer function of laser amplitude noise to the differential Michelson error-signal | 178 |
| 4.8. | Laser amplitude noise in the phasor picture | 178 |
| 4.9. | Properties of laser amplitude noise sidebands, depending on the frequency | 179 |
| 4.10. | Laser amplitude noise phasors for a Michelson offset from perfect dark fringe | 180 |
| 4.11. | Laser amplitude noise phasors accounting for asymmetric Michelson arm losses | 181 |
| 4.12. | Comparison of the properties of the carrier and control sideband beats . . | 183 |
| 4.13. | FINESSE simulation of the transfer function of laser amplitude noise to h . | 184 |
| 4.14. | Measured transfer function of laser amplitude noise to h , with different demodulation phases | 185 |
| A.1. | Signal-recycling error-signal vectors for a wide range of MSR tunings, for three different detector configurations | 190 |
| C.1. | 2f signal for various signal-recycling cavity lengths and tunings | 228 |
| C.2. | Michelson control sideband amplitudes of the default power-recycled Michelson of GEO 600 in the plane of Schnupp length and power-recycling tuning | 229 |
| C.3. | 2f signal for various Schnupp length offsets | 230 |
| C.4. | 2f signal for various MSR , and MCE / MCn reflectivities | 231 |
| C.5. | 2f signal for various differential Michelson end mirrors' misalignments . . | 232 |
| | Overview of carrier, and signal-recycling and Michelson control sideband frequency relations, and of their resonance conditions inside the dual-recycled Michelson interferometer | 0 |

Glossary

Mathematical and physical constants

| | | | |
|---------------|--------------------|----------------------|---------------------------|
| i | $\sqrt{-1}$ | [1] | imaginary unit |
| c | $\cong 299792458$ | [m s ⁻¹] | speed of light |
| π | $\cong 3.14159265$ | [1] | circular constant |
| $e = \exp(1)$ | $\cong 2.71828183$ | [1] | base of natural logarithm |

Mathematical symbols

| | |
|-----------------|--|
| * | complex conjugate |
| \otimes | particular product of complex numbers equivalent to the scalar product of their vector representatives |
| T | matrix transposition |
| α, β | arbitrary phases |
| α | angle of misalignment |
| Δ | macroscopic deviation |
| δ | microscopic deviation |
| $\delta\chi$ | mirror displacement in units of degrees, $360^\circ \cdot \delta x / \lambda_0$ |
| ϕ | demodulation phase or constant phase of a light field |
| φ | (variable) phase of a light field |
| λ | wavelength |
| ω | angular frequency |
| τ | modulation period $1/f$ |
| a | light field amplitude impinging on an optical system |
| b | light field amplitude at the output of an optical system |
| \mathbf{C} | complex numbers |

| | |
|----------|---|
| E | (space- and) time-dependent electric field |
| E_0 | constant electric field amplitude |
| FSR | free spectral range |
| f | frequency |
| g | transfer-function gain or amplitude ratio |
| H | transfer function |
| h | strain |
| I | photo current |
| \Im | imaginary part |
| $J_j(m)$ | Bessel functions |
| k | wave number ω/c |
| L | length |
| lsq | square deviation between simulation and measurement |
| m | modulation depth |
| N | recordable signal as measure of noise |
| n | noise |
| R | real numbers |
| \Re | real part |
| SNR | signal to noise ratio |
| t | time |
| x | location along the axis of light propagation |
| l, j | numerating indices |

Abbreviations

| | |
|-------------|--|
| AC | amplified current |
| AGC | automatic gain control |
| AM | amplitude modulation |
| AN | amplitude noise |
| ASD | amplitude spectral density |
| BS | beamsplitter |
| BSAR | beamsplitter anti-reflective coating |
| BW | bandwidth |
| C, S | in-phase and in-quadrature component, respectively, of I_{demod} with respect to the signal sidebands |
| CM | compound mirror |

| | |
|------------|---|
| DA | digital to analog |
| DC | direct current |
| EOM | electro-optic modulator |
| ESD | electrostatic drive |
| <i>FSR</i> | free spectral range |
| GEO 600 | British-German gravitational-wave detector |
| HP | high power photodiode |
| HV | high-voltage amplifier |
| IM | intermediate mass |
| LAN | laser amplitude noise |
| LSQ | least-square method |
| Michelson | Michelson interferometer |
| MC2 | second mode-cleaner |
| MCE | central east end mirror |
| MCn | central north end mirror |
| MFe | far east end mirror |
| MFn | far north end mirror |
| M, MI | Michelson |
| MPR | power-recycling mirror |
| MSR | signal-recycling mirror |
| P, Q | in-phase and in-quadrature component, respectively, of I_{demod} with respect to the control sidebands |
| PD | photodiode |
| PDBSs | photodiode in reflection of BSAR |
| PDO | photodiode at south port |
| PDPR | photodiode in reflection of MPR |
| PM | phase modulation |
| PR | power recycling |
| prMI | power-recycled Michelson interferometer |
| R | power reflection |
| S | optical system |
| SB | sideband |
| <i>SNR</i> | signal to noise ratio |
| sqrt | square-root |
| SR | signal recycling |
| srMI | signal-recycled Michelson interferometer |
| T | power transmission |

| | |
|-----|--|
| TEM | transverse electro-magnetic mode |
| TF | transfer function |
| VI | virtual instrument, denotes user programs of LabView |

Indices

| | |
|---------|--|
| → | from ... to ... |
| , ⊥ | parallel and perpendicular vector components, respectively |
| + | upper |
| − | lower |
| × | intersection |
| 0 | carrier |
| am | amplitude modulation |
| car | carrier |
| cav | cavity |
| cross | crossover |
| demod | demodulated |
| et | etalon |
| GW | gravitational-wave signal |
| m | modulation sideband |
| meas | measurement |
| off | offset from carrier or from resonance |
| osc | oscillator |
| p | peak |
| pm | phase modulation |
| ref | reference |
| res | resonance |
| sim | simulation |
| Schnupp | macroscopic Michelson armlength difference |
| waste | waste light |

Chapter 1.

Optical detection via the modulation/demodulation technique

In view of detecting gravitational waves, the first generation of km-scale laser-interferometric gravitational-wave detectors is ready for worldwide network operation and about to reach the design sensitivity. Albert Einstein predicted gravitational waves already in 1916 in his General Relativity as ripples of space-time that occur when masses are accelerated. These space-time deformations are wavelike solutions of the linearised Einstein's field equations and travel at the speed of light changing the distances between free falling test masses [Mizuno95, Hewitson04a, Hild03, Kötter04]. The “stiffness” of space-time, however, causes the interaction with masses to be very faint such that even gravitational waves carrying enormous energies have small amplitudes¹. Therefore only astrophysical events including the acceleration of huge masses lead to appreciable, measurable gravitational-wave amplitudes.

The faintness of gravitational waves is challenging, but at the same time bears a very appealing potentiality for a new astrophysical device. Present astrophysical measurements are mainly based on neutrino detection or electro-magnetic radiation. These methods prohibit the view of all non-radiating members of the universe, and complicate the detection of any promising candidate behind an absorbing object. The weak coupling of gravitational waves, though, facilitates almost unattenuated information about accelerated, huge masses, in particular about distant parts or the birth of our universe.

For the first detection of gravitational waves, and its astrophysical application, a worldwide network of gravitational-wave detectors is needed. GEO 600, a detector of 600 m armlength close to Hannover, is a British-German contribution to the interferometric gravitational wave community which currently comprises six large-scale detectors [GEO, Hewitson05, LIGO, Sigg05, TAMA, Ando05, VIRGO, Acernese05]. Being in its final state of commissioning, GEO 600 takes part in the current science run S5 that has started in winter 2005/2006. At the time of writing this thesis, GEO 600 is only a small factor away from its design sensitivity.

The search for gravitational waves requires a stable operation of the detectors over long time periods of several months or years. This presumes constant states of longitudinal and alignment degrees of freedom of the mirrors. For isolation from seismic events, all

¹The ratio of energy density and space-time curvature amounts to $\sim 10^{43}$ N.

mirrors of GEO 600 are suspended as double or triple pendulums. Still, there is residual motion of the hanging masses that needs to be controlled.

For such a control, adequate *error-signals* have to be found. An error-signal gives a measure for the deviation of a (sub-)system state from the targeted one. After some processing of such an error-signal, the *feedback signal* is passed over to one or several *actuators* to compensate for the effect that causes the deviation. Ideally, each error-signal should depend on only one degree of freedom. However, as the current and future gravitational-wave detectors become more and more complex, an orthogonalisation of the error-signals becomes increasingly difficult.

Microscopic movements of mirrors change the amount of accumulated phase of a reflected beam at a given point. Thus, the light phase carries the relevant information about a mirror's position. This physical quantity, though, is not directly accessible and has to be made detectable by, for example, interference with another light beam as a reference and evaluating the beat signal.

If the two beams have the same frequency, the detection is called *homodyne*, otherwise *heterodyne*. In most cases it is sensible to use the same optical path for both beams. In that case, for a comparison of the two beam phases, it is necessary that the reference depends on the device's states in a way differing from the main beam. The heterodyne detection can be adjusted to obey this criterion.

GEO 600 uses heterodyne detection for all degrees of freedom of the dual-recycled Michelson interferometer. The shape and dependencies of an error-signal amplitude varies with the *configuration* used. Following [Freise03a], a configuration is defined as a certain setup of a control scheme within an optical system, comprising in particular the utilised light fields.

This chapter gives an introduction to the generation of error-signals in optical systems via light field modulation, and demodulation of a photodiode signals. Treating light fields in a so-called *phasor picture* enables an intuitive explanation of crucial error-signal properties, even for advanced configurations.

After a short definition of the light-field convention used throughout this work, the reader will be introduced to the phasor picture. This phasor picture is then applied to illustrate the light field relations for all kinds of modulations. The generation of error signals with the modulation/demodulation technique will be deduced mathematically and then translated into the phasor picture. At the end of this chapter, the phasor picture will be applied to explain the error-signals associated with a simple two-mirror cavity.

1.1. Modulation of light fields

An unmodulated laser light field will in the following be represented by a scalar, electrical field with real amplitude E_0 and positive angular frequency $\omega_0 = 2\pi f_0$. Without loss of generality (w.l.o.g.), the light is assumed to travel from left to right. Defining the axis of propagation to be the x-axis of the usual right-hand coordinate system, the light phase

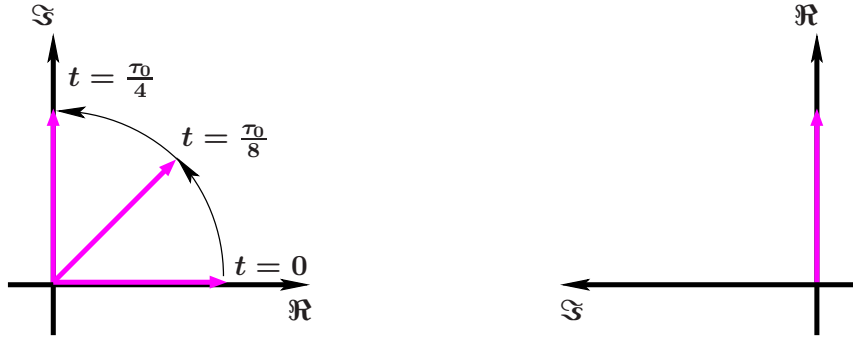


Figure 1.1.: Phasor representing the scalar light field of Equation 1.1. The coordinate system in the left is fixed, such that the phasor rotates anti-clockwise with time with period τ_0 , whereas the coordinate system in the right rotates with the phasor, allowing for a static display of the electric field vector. Without loss of generality (w.l.o.g.), the phase between the two rotations is chosen to be 0° . The coordinate axes are rearranged such that the real axis points upwards.

decreases with increasing x , proportional to the wavevector $k_0 = \omega_0/c$, with c being the speed of light. As the absolute phase offset of the light is anyway only measurable in comparison with another light field, it can be set to zero. This gives

$$E(t, x) = E_0 e^{i(\omega_0 t - k_0 x)}. \quad (1.1)$$

In reality, there is a complex conjugate as second summand that is omitted for simplicity. This does not change any of the following results². In calculations where the longitudinal dependence is not relevant, i.e. accounting only for light effects at one arbitrary location along the axis of propagation without the necessity of comparing different traversed distances, x will, w.l.o.g., be set to 0.

1.1.1. Phasor diagrams

A complex scalar light field, as in Equation 1.1, can be displayed in a complex plane as a vector with length E_0 and phase $\omega_0 t$. If the coordinate system is rigid, this vector, with time, rotates anti-clockwise around the origin with frequency f_0 . To ease the display, the coordinate system can be chosen to rotate with that same frequency such that we get a stationary picture. Furthermore, the real and imaginary axes are displayed such that the real axis points upwards (the benefit of this choice will become clear later). This kind of visualisation of field amplitude properties is called a *phasor diagram*.

Figure 1.1 shows the phasor in a fixed (left) and in a rotating (right) coordinate system.

Phasors can be added by concatenating them together (as usually done with vectors) to get the resulting sum phasor. Multiplication, though, takes place by multiplying their

²The complex number and its conjugate describe parts of one light field that propagate in opposite directions. In sum, they ensure that $E(t)$ is a real number, i.e. a physical quantity.

amplitudes and adding their phases. In the latter case, the individual rotation frequencies add up to the rotation frequency of the resulting phasor. In a coordinate system co-rotating with f_0 , phasors with different frequency $f \neq f_0$ keep a residual rotation with the corresponding frequency offset $f_{\text{off}} = f - f_0$. If $f_{\text{off}} > 0$ Hz, the rotation is anti-clockwise, else clockwise.

1.1.2. Amplitude modulation

A small sinusoidal amplitude modulation, with an initial phase of 90° , of the light field from Equation 1.1 with a so-called *modulation index* m and angular frequency ω_m ,

$$E_{\text{am}}(t) = E_0 e^{i\omega_0 t} (1 + m \cos \omega_m t) = E_0 e^{i\omega_0 t} \left(1 + \frac{m}{2} e^{i\omega_m t} + \frac{m}{2} e^{-i\omega_m t} \right), \quad (1.2)$$

can be interpreted as a sum of three light fields at different frequencies, f_0 and $f_0 \pm f_m$. In the context of modulation, fields with these frequency properties are called *carrier*, and *upper* (+), and *lower* (-) *sideband*, respectively.

With respect to the carrier, the sidebands have a residual frequency of $\pm f_m$, referred to as *modulation frequency*, which is visible particularly on the right hand side of Equation 1.2. This modulation is taken into account in a phasor diagram by “snapshots” of different moments, related to the modulation period $\tau_m = 1/f_m$, as depicted in Figure 1.2. It consists of four pictures with particular phases, 0 , $\frac{\pi}{2}$, π , and $\frac{3\pi}{2}$, of the sidebands (cyan) with respect to the carrier (magenta). The left-hand side shows each field amplitude separately (*individual display*), the right hand side the sum of all fields (red vector at the very right) as required by the superposition principle (*summed display*). The sidebands rotate with f_m in directions set by the sign of their frequency. + and - correspond to anti-clockwise and clockwise, respectively. On the left, the coordinate systems of each subfield are arranged on a third axis of frequency³.

Summing up those three individual light fields obviously results in a periodic amplitude modulation of the carrier light (which is not really surprising considering Equation 1.2). In turn, one can say that such sidebands in general have an influence on the light field power detected by a photodiode, allowing a measurement of the sidebands.

1.1.3. Phase modulation

A periodic modulation of the phase of the light field of Equation 1.1, again with an angular modulation frequency ω_m and modulation index m , can mathematically be described as

³From Section 1.2 on, the frequency axis and the imaginary axis coincide anti-parallelly to ease the view of phasors pointing to the back of the picture and for an easier transfer from the individual display to that of the sum. However, the author finds the kind of visualisation introduced here more suitable to understand the basic concept.

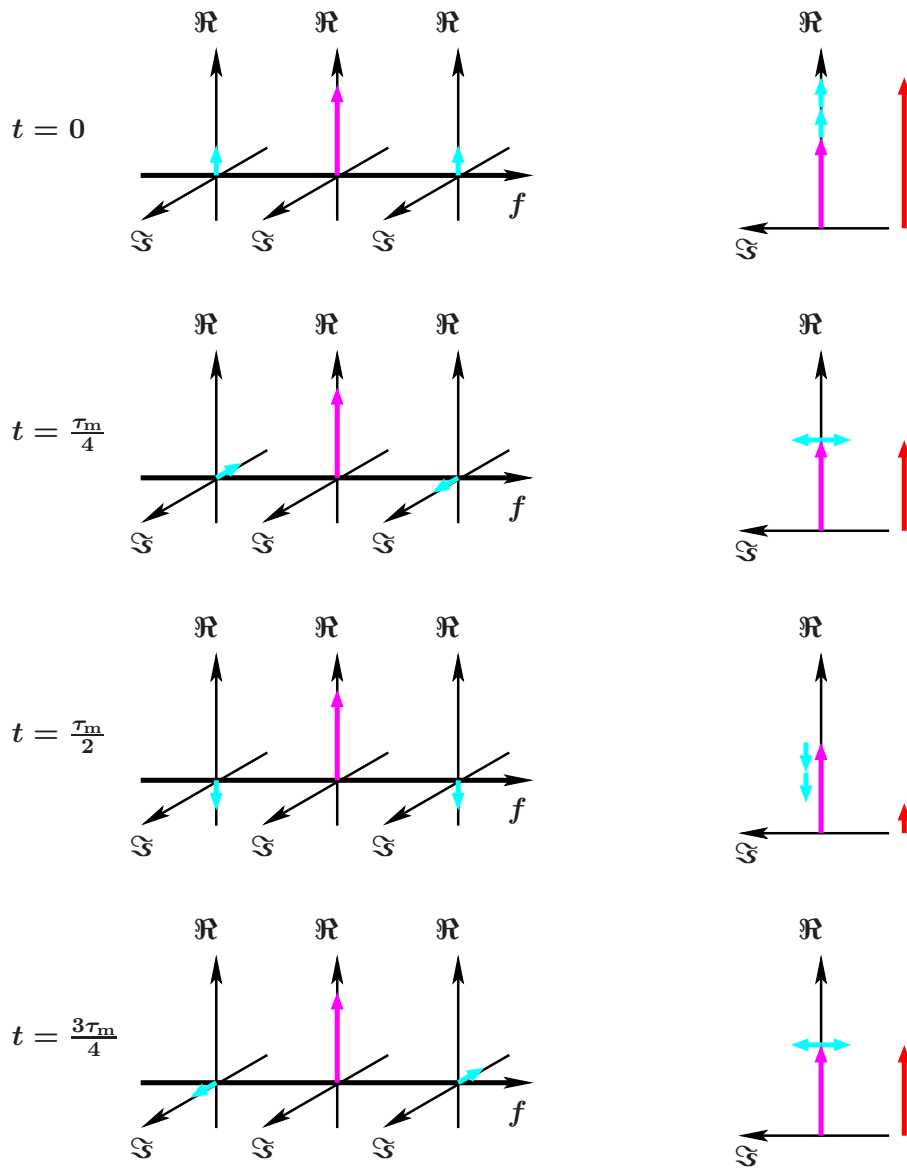


Figure 1.2.: Amplitude modulation for different times within one modulation period τ_m . The left-hand side shows an individual display of each light field of the right-hand side of Equation 1.2 in terms of phasors. The two sidebands (cyan) rotate at frequency f_m with opposite directions around their origin. Their imaginary and real coordinate axes are affixed to a frequency axis. The right-hand side shows a sum display of all light fields corresponding more closely to the mathematical description on the left-hand side of Equation 1.2. In sum (red phasor on the very right), the sidebands cause the amplitude of the light to alter periodically without changing its phase.

$$\begin{aligned}
 E_{\text{pm}}(t) &= E_0 e^{i(\omega_0 t + m \cos \omega_m t)} \\
 &= E_0 e^{i\omega_0 t} e^{im \cos \omega_m t} \\
 &= E_0 e^{i\omega_0 t} \left[J_0(m) + \sum_{j=1}^{\infty} i^j J_j(m) (e^{ij\omega_m t} + e^{-ij\omega_m t}) \right] \\
 &= E_0 e^{i\omega_0 t} [J_0(m) + iJ_1(m)e^{i\omega_m t} + iJ_1(m)e^{-i\omega_m t} + \mathcal{O}(m^2)] \\
 &\approx E_0 e^{i\omega_0 t} (1 + im \cos \omega_m t).
 \end{aligned} \tag{1.3}$$

Here, the $J_j(m)$ represent the Bessel functions of the first kind, of order j ,

$$\begin{aligned}
 J_j(m) &= \sum_{l=1}^{\infty} \frac{(-1)^l}{l!(l+j)!} \left(\frac{m}{2}\right)^{j+2l}, \text{ giving } J_0(m) = 1 - \frac{m^2}{4} + \mathcal{O}(m^4) \\
 J_1(m) &= \frac{m}{2} - \frac{m^3}{16} + \mathcal{O}(m^5) \\
 J_2(m) &= \frac{m^2}{8} + \mathcal{O}(m^4).
 \end{aligned} \tag{1.4}$$

As can be seen in Equation 1.3, a phase modulation is equivalent to a comb of sidebands at frequencies $\pm j f_m$, $j \in \mathbf{N}_+$, around the carrier⁴. For small modulation indices ($m < 1$), only the first-order sidebands ($j = 1$) are relevant. In the following sections, only these sidebands will be considered. Their amplitudes, $im/2$, are phase shifted by $i = \exp(i\pi/2) \hat{=} 90^\circ$. Besides, they are the same as the sidebands of the amplitude modulation. It is, though, important to note that the field described in Equation 1.3 has, in contrast to amplitude modulation, a time-independent absolute value of E_0 . This is, however, no longer true with the approximation made in the last line of Equation 1.3: for certain times, the absolute value reaches $E_0\sqrt{1+m^2}$. This is a consequence of the fact that the higher-order sidebands, compensating effects of elongation due to the first order sidebands, have been neglected.

The phasor diagram in Figure 1.3 might help to understand more easily why a simple phase shift of sidebands (by $\pm 90^\circ$ with respect to the amplitude modulation sidebands) can change the overall amplitude characteristics, making the sidebands “invisible” on a photodetector. The sidebands (cyan) add up constructively in the quadrature perpendicular to the carrier (magenta) and cancel each other when they become parallel. This makes the overall sum vector (red) oscillate periodically around its original vertical position, but leaves the amplitude (almost) constant.

1.1.4. Frequency modulation

A frequency ω_0 modulated with ω_m by an amplitude $\Delta\omega$ can be described as

$$\omega_0 + \Delta\omega \sin(\omega_m t), \tag{1.5}$$

⁴ \mathbf{N}_+ denotes non-negative integer numbers.

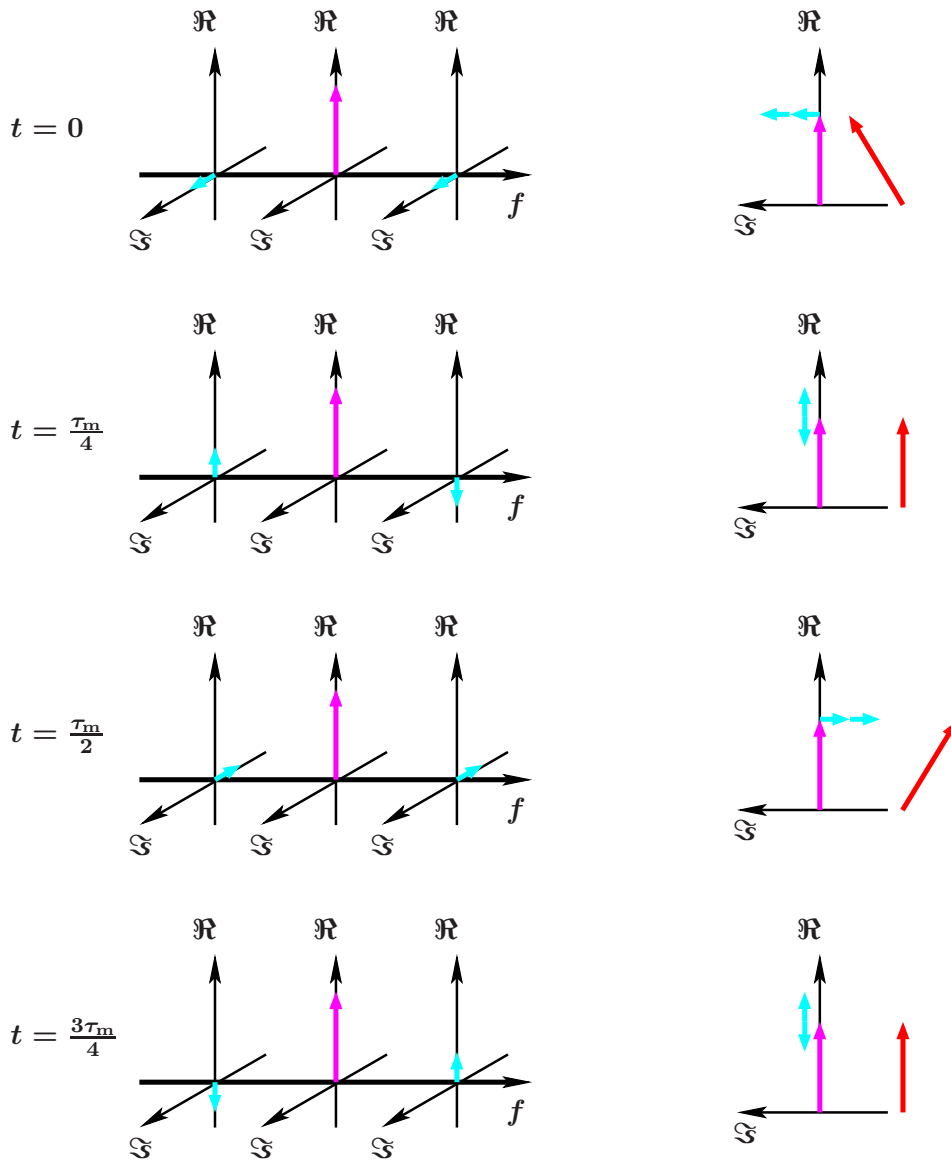


Figure 1.3.: Phase modulation in the phasor picture for different times within one modulation period τ_m . The left-hand side shows the individual display of the carrier and the first-order sidebands' fields of Equation 1.3. The right-hand side shows the sum of these fields. The two sidebands cause the sum vector mainly to oscillate periodically about its original vertical position. In this display, the amplitude of the sum vector changes by a small amount, but only for the sake of a proper view, which requires to a) omit higher-order sidebands and b) give the first-order sidebands a sufficient length.

leading to a total light phase of

$$\varphi(t) = \int [\omega_0 + \Delta\omega \sin(\omega_m t)] dt. \quad (1.6)$$

As the light frequency is the first derivative of the phase, in the case of a time-dependent frequency, an integration is needed to correctly deduce the phase. This yields

$$E_0 e^{i\varphi(t)} = E_0 e^{i \int [\omega_0 + \Delta\omega \sin(\omega_m t)] dt} = E_0 e^{i \left(\omega_0 t - \frac{\Delta\omega}{\omega_m} \cos(\omega_m t) \right)}. \quad (1.7)$$

Thus, a frequency modulation appears as a phase modulation at that same frequency with a scaling modulation index⁵ $\Delta\omega/\omega_m$.

1.1.5. Phase modulation of phase modulation

In an experimental setup, phase modulation is realised (e.g.) with electro-optic modulators (EOMs) that receive a frequency dependent electrical signal generated by oscillators. These oscillators are also subject to noise. More explicitly, the oscillator frequency can vary with time as presumed with the laser frequency in Equation 1.6. In order to investigate this modulation further, one needs to distinguish between the primary phase modulation, with m and ω_m , and the modulation happening to the oscillator, with the angular frequency ω_{osc} and an amplitude of $\pm\Delta\omega$. Furthermore, the expressions upper and lower sidebands will be reserved for the primary phase modulation.

Inserting this into Equation 1.6 and Equation 1.3, we get

$$\begin{aligned} E(t) &= E_0 e^{i(\omega_0 t + m \cos \varphi_m(t))} \\ &= E_0 e^{i \left[\omega_0 t + m \cos \left(\omega_m t - \frac{\Delta\omega}{\omega_{osc}} \cos(\omega_{osc} t) \right) \right]}. \end{aligned} \quad (1.8)$$

The exponential function with the nested cosine can be expanded similarly to Equation 1.3:

$$\begin{aligned} e^{im \cos(\omega_m t + m_{osc} \cos(\omega_{osc} t))} &= J_0(m) + \sum_{j=1}^{\infty} i^j J_j(m) e^{ij(\omega_m t + m_{osc} \cos(\omega_{osc} t))} \\ &= J_0(m) + \dots \\ &\dots + iJ_1(m) e^{i\omega_m t} e^{im_{osc} \cos(\omega_{osc} t)} + \dots \\ &\dots + iJ_1(m) e^{-i\omega_m t} e^{-im_{osc} \cos(\omega_{osc} t)} + \mathcal{O}(m^2) \\ &\approx J_0(m) + \dots \\ &\dots + iJ_1(m) e^{i\omega_m t} \left(1 + i \frac{m_{osc}}{2} e^{i\omega_{osc} t} + i \frac{m_{osc}}{2} e^{-i\omega_{osc} t} \right) + \dots \\ &\dots + iJ_1(m) e^{-i\omega_m t} \left(1 - i \frac{m_{osc}}{2} e^{i\omega_{osc} t} - i \frac{m_{osc}}{2} e^{-i\omega_{osc} t} \right) \end{aligned} \quad (1.9)$$

⁵This modulation index can sometimes be quite high, even exceed 1, such that higher-order sidebands need to be taken into account. This case is known as *wide-band* frequency modulation and discussed further in [Razavi].

assuming $m_{\text{osc}} = -\Delta\omega/\omega_{\text{osc}} < 1$. Thus, new sidebands are created around the primary upper and lower sidebands with a frequency offset of $\pm f_{\text{osc}}$ around $\pm f_m$ and a phase shift of 90° . Around the upper sideband, this phase shift is clockwise (remember, m_{osc} has negative sign), around the lower it is anti-clockwise. This can be understood if one imagines a slight decrease of the frequency of the primary phase modulation: the sidebands' phases will then evolve more slowly, but in opposite directions due to their different signs. In a phasor picture, this can only be achieved with the pairs of additional sidebands having a phase shift of 180° with respect to each other. Figure 1.4 shows the phasor diagram of this state.

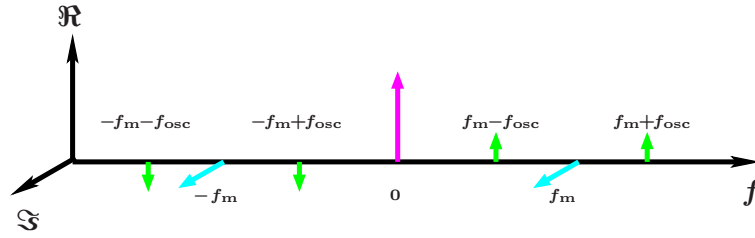


Figure 1.4.: Individual phasor display of phase modulated phase modulation, for $t = 0$. The carrier (magenta) and the first-order sidebands (cyan) of Figure 1.3 are joined by four additional sidebands (red) appearing at $\pm f_{\text{osc}}$ around the primary sidebands. Around the upper sideband, the phase shift of 90° is clockwise, around the lower it is anti-clockwise.

1.1.6. Amplitude modulation of phase modulation

A second possible noise source of oscillators, a time-varying modulation index m , has not yet been accounted for.

Inserting an oscillating modulation index of $m(1 + m_{\text{osc}} \cos \omega_{\text{osc}} t)$ into the first line of Equation 1.3 yields

$$\begin{aligned} E(t) &= E_0 e^{i(\omega_0 t + m(1 + m_{\text{osc}} \cos \omega_{\text{osc}} t) \cos \omega_m t)} \\ &= E_0 e^{i\omega_0 t} e^{i m \cos \omega_m t} e^{i m m_{\text{osc}} \cos \omega_{\text{osc}} t \cos \omega_m t} \end{aligned}$$

Using the identity

$$\cos \alpha \cos \beta = \frac{1}{2} [\cos(\alpha + \beta) + \cos(\alpha - \beta)]$$

and neglecting terms of the order $\mathcal{O}((m m_{\text{osc}})^2)$, one gets

$$\begin{aligned}
 E(t) = & E_0 e^{i\omega_0 t} \dots & (1.10) \\
 \dots & \cdot \left\{ J_0(m) J_0^2\left(\frac{m m_{\text{osc}}}{2}\right) + i J_1(m) J_0^2\left(\frac{m m_{\text{osc}}}{2}\right) \cdot 2 \cos \omega_m t + \dots \right. \\
 \dots & + i J_0(m) J_0\left(\frac{m m_{\text{osc}}}{2}\right) J_1\left(\frac{m m_{\text{osc}}}{2}\right) 2 [\cos(\omega_m - \omega_{\text{osc}})t + \cos(\omega_m + \omega_{\text{osc}})t] + \dots \\
 \dots & \left. - J_1(m) J_0\left(\frac{m m_{\text{osc}}}{2}\right) J_1\left(\frac{m m_{\text{osc}}}{2}\right) \cdot \dots \right. \\
 & \left. \dots \cdot 2 [2 \cos \omega_{\text{osc}} t + \cos(2\omega_m - \omega_{\text{osc}})t + \cos(2\omega_m + \omega_{\text{osc}})t] \right\}.
 \end{aligned}$$

The result becomes clearer when the field phasors get sorted as in Figure 1.5. The second line of Equation 1.10 contains the light fields expected for ideal phase modulation (displayed in magenta for the carrier and cyan for the upper and lower phase modulation sidebands), though slightly attenuated by $J_0^2(m m_{\text{osc}}/2)$. These sidebands will be called *primary sidebands* for convenience. The next line contains additional *first-generation sidebands* generated at $\pm f_m \pm f_{\text{osc}}$ around the carrier⁶ (green phasors around upper and lower sidebands). With the sidebands' phase shift to the carrier of 90° , modulation index variations not surprisingly act like an additional phase modulation of the carrier at these frequencies. Originating from the carrier, these sidebands are relatively strong compared to the *second-generation sidebands* or *sidebands of primary sidebands* (last two lines of Equation 1.10), which are generated by phase modulating the primary sidebands with $\pm f_m \pm f_{\text{osc}}$ (green phasors around carrier and at the edge of the frequency axis). Thus, these second-generation sidebands are anti-parallel to the carrier phasor. Those around the carrier are doubled because both upper and lower primary sidebands contribute with their noise sidebands. Although weak, they can still contribute to the noise performance of the detector and must therefore not be neglected.

1.2. Generation of error-signals

In most interferometric experiments, one is interested in the preparation of particular states of optical systems with respect to a certain light field, in the majority of cases to the carrier. Examples are (anti-)resonances of optical cavities, and the dark (or bright) fringe state of a Michelson interferometer. Measuring light powers in these particular cases yields unipolar signals, only reporting on whether the experiment is in the desired state, called *operating point*, or not. Visualising light phase shifts could in general give information on the direction of the aberration. This information is required to find suitable *error-signals* to be fed back into the system, in order to maintain the desired operating point.

⁶The generation of a sideband in this work relates to the carrier being the field that is modulated. If a sideband originates from a direct modulation of the carrier, it is called *first-generation*, if a first-generation sideband is modulated, the resulting sidebands are second-generation, and so forth, similar to a family tree.

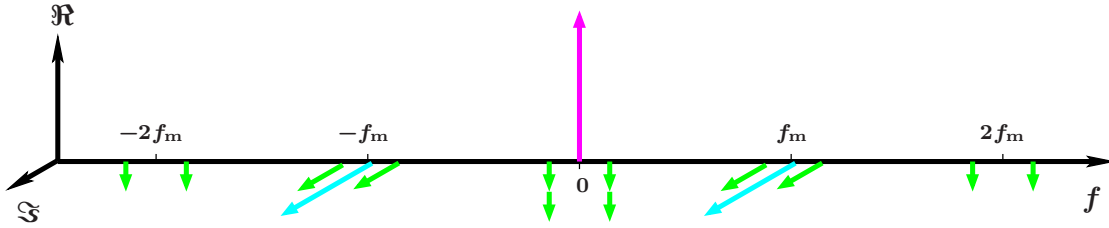


Figure 1.5.: Individual phasor display of an amplitude modulation of phase modulation for $t = 0$. The carrier (magenta) and the first order sidebands (cyan) of Figure 1.3 are joined by twelve additional sidebands (green) appearing at $\pm f_{osc}$ around the carrier, the primary sidebands, and the second-order sidebands (which are not shown). All first-generation sidebands have a phase shift of 90° to the carrier, the second-generation sidebands have a phase shift of 90° to the primary sidebands, in total 180° to the carrier. The second-generation sidebands around the carrier are doubled due to the contribution from each primary sideband.

Thus, what we are looking for is a signal revealing the phase shift of some light field which in turn reveals (the change of) an optical system's state. According to subsections 1.1.2 and 1.1.3, amplitude modulation is visible on a photo diode; pure phase modulation is not. The only reason for this is the particular phase shift of the associated sidebands with respect to the carrier. If we allow for continuous phase offsets of the sidebands from the carrier for times $t = 0$, the amount of amplitude modulation appearing on the photo diode increases, the closer the sidebands' phases⁷ are to 0° (modulo 180°). Thus, the amplitude of the photo diode current is a measure of this phase offset.

However, this method is only applicable as a phase measurement of, for example, the carrier, if the sideband phases change differently from the carrier phase. In general, light fields of different frequencies evolve differently in an optical system. The reflection at a cavity, for example, gives the light components involved a frequency dependent and cavity-state dependent phase and amplitude.

The phase and amplitude relationship between light fields of the same frequency at different points of a general optical system \mathbf{S} is called *transfer function* $H_{\mathbf{S}}$ of \mathbf{S} . Depending on the exact points of interest in \mathbf{S} , one system may yield various transfer functions⁸. As the corresponding field's relationship is about phase and amplitude⁹, it may mathematically be expressed as a phasor (or vector) multiplication, shifting a light field's phase, and at the same time changing its amplitude:

$$b_\omega(t) = H_{\mathbf{S}}(\omega) \cdot a_\omega(t), \quad (1.11)$$

$$H_{\mathbf{S}}(\omega) = g_{\mathbf{S}}(\omega) e^{i\varphi_{\mathbf{S}}(\omega)} \in \mathbf{C}, \quad (1.12)$$

⁷Please note that in the examples from above, for $t = 0$, the pairs of sidebands belonging together have no phase difference from each other.

⁸Again using a cavity as example, there are already three main transfer functions from the entering light field to the reflected, the intra-cavity and the transmitted field.

⁹We are neglecting transversal field dependencies.

where $a_\omega(t)$ and $b_\omega(t)$ are the time-dependent fields of the same frequency ω , at the two measurement points to be compared. The transfer function $H_S(\omega)$ consists of the light frequency dependent amplitude ratio $g_S(\omega) \in \mathbf{R}$ and phase difference¹⁰ $\varphi_S(\omega) \in \mathbf{R}$ between a and b .

The quality of an error-signal depends on the properties of the contributing light fields in combination with the transfer function of the optical system. Investigating the respective photodiode signal with generalised light fields enables us to deduce requirements for the involved fields to obtain a sensible error-signal.

To start with the easiest general case, let us consider modulated laser light a consisting of a carrier a_0 and a pair of sidebands a_\pm as in Equation 1.2 or 1.3. To ease the formulas, common factors, as $E_0 \exp(i\omega_0 t)$, are omitted:

$$a = a_0 + a_+ e^{i\omega_m t} + a_- e^{-i\omega_m t}. \quad (1.13)$$

Let a enter an arbitrary interferometer. The field components will change individually corresponding to their frequencies and the system transfer function. The field b to be detected can mathematically be described by

$$b = b_0 + b_+ e^{i\omega_m t} + b_- e^{-i\omega_m t} \quad (1.14)$$

$$\begin{aligned} &= H_S(\omega_0) a_0 + H_S(\omega_0 + \omega_m) a_+ e^{i\omega_m t} + H_S(\omega_0 - \omega_m) a_- e^{-i\omega_m t} \\ &= g_{S0} a_0 e^{i\varphi_{S0}} + g_{S+} a_+ e^{i(\omega_m t + \varphi_{S+})} + g_{S-} a_- e^{-i(\omega_m t - \varphi_{S-})} \end{aligned} \quad (1.15)$$

with $H_S(\omega_0) = g_{S0} e^{i\varphi_{S0}}$, $H_S(\omega_0 \pm \omega_m) = g_{S\pm} e^{i\varphi_{S\pm}}$, denoting the gain and the accumulated phase of the carrier and the upper and lower sideband, respectively, associated with the optical system.

The corresponding light power that represents the physical quantity detected by a photodiode, will be proportional to the photodiode current. This photo current I can, except for a constant factor, be written as

$$\begin{aligned} I = |b|^2 &= (b_0 + b_+ e^{i\omega_m t} + b_- e^{-i\omega_m t}) (b_0 + b_+ e^{i\omega_m t} + b_- e^{-i\omega_m t})^* \\ &= I_{DC} + 2\Re \{ I_{\omega_m} e^{i\omega_m t} \} + 2\Re \{ I_{2\omega_m} e^{i2\omega_m t} \} \\ &= I_{DC} + 2\Re \{ I_{\omega_m} \} \cos \omega_m t - 2\Im \{ I_{\omega_m} \} \sin \omega_m t + \dots \\ &\quad \dots + 2\Re \{ I_{2\omega_m} \} \cos 2\omega_m t - 2\Im \{ I_{2\omega_m} \} \sin 2\omega_m t, \end{aligned} \quad (1.16)$$

containing components at DC, ω_m and $2\omega_m$, respectively, represented by

$$\begin{aligned} I_{DC} &= |b_0|^2 + |b_+|^2 + |b_-|^2 \\ I_{\omega_m} &= b_+ b_0^* + b_0 b_-^* = g_{S0} a_0 \left(g_{S+} a_+ e^{i(\varphi_{S+} - \varphi_{S0})} + g_{S-} a_-^* e^{i(\varphi_{S0} - \varphi_{S-})} \right) \\ I_{2\omega_m} &= b_+ b_-^* = g_{S+} g_{S-} a_+ a_-^* e^{i(\varphi_{S+} - \varphi_{S-})}, \end{aligned} \quad (1.17)$$

where the asterisk * denotes the complex conjugate. (Please note that $a_\pm \in \mathbf{C}$, as the kind of modulation was not specified in the beginning, whereas $a_0 \in \mathbf{R}$). The real and

¹⁰ \mathbf{R} and \mathbf{C} denote real and complex numbers, respectively.

imaginary parts of I_{ω_m} are called *in-phase* and *in-quadrature* components of the signal, respectively, as they occur in I with the same phase as the original modulation and shifted by 90° , respectively¹¹.

The frequency component of interest is extracted by so-called *demodulation* at a *mixer*. In this chapter, an ideal mixer will be assumed that multiplies I with the original local oscillator signal (or higher harmonics) shifting all components at that frequency to DC. In addition, a low-pass filter after the mixer suppresses all but these DC components. The demodulation, used henceforth, comprises both, a mixer and low-pass filtering.

In general, a local oscillator and the respective frequency component of I will have a phase difference Φ , the *demodulation phase*, that needs to be taken into account in the multiplication:

$$I \cdot \cos(l\omega t + \Phi) = \left(I_{\text{DC}} + \sum_{j=1,2} [I_{j\omega_m} e^{ij\omega_m t} + I_{j\omega_m}^* e^{-ij\omega_m t}] \right) \frac{1}{2} \left(e^{i(l\omega_m t + \Phi)} + e^{-i(l\omega_m t + \Phi)} \right),$$

where $l = 1, 2$ for the harmonics. Neglecting the AC parts of the multiplied signal above yields

$$\begin{aligned} I_{\text{demod}} &= \frac{1}{2} (I_{l\omega_m} \cdot e^{-i\Phi} + I_{l\omega_m}^* \cdot e^{i\Phi}) \\ &= \Re \{ I_{l\omega_m} \cdot e^{-i\Phi} \} \end{aligned} \tag{1.18}$$

$$= \Re \{ I_{l\omega_m} \} \cos \Phi + \Im \{ I_{l\omega_m} \} \sin \Phi \tag{1.19}$$

$$= (\Re \{ I_{l\omega_m} \}, \Im \{ I_{l\omega_m} \}) \begin{pmatrix} \cos \Phi \\ \sin \Phi \end{pmatrix} =: I_{l\omega_m} \otimes e^{i\Phi}, \quad l = 1, 2. \tag{1.20}$$

As before with the phasor representation of light fields, there is a one-to-one equivalence of a complex number to a two dimensional vector, which is applied in the equation above. Thus, the numbers and vectors will henceforth be used synonymously for the respective demodulation-phase or photo-current.

Although $I_{l\omega_m}$ and the demodulation phase are, strictly speaking, not phasors but vectors without oscillating phase, the illustration of them as vectors will nonetheless be included in the term ‘phasor picture’.

Displaying both the demodulation phase and $I_{l\omega_m}$ as vectors in a complex plane, Φ defines a normalised or unit vector $e^{i\Phi}$ on which the signal $I_{l\omega_m}$ is projected during the demodulation process. This projection is equivalent to the scalar product of vectors, yielding the parallel component of one vector with respect to the other, the projection vector, multiplied by the projection vector amplitude (which in this case is 1). Thus, a projection is commutative and associative. The operator symbol for a scalar product between vectors is ‘ \cdot ’. Not to confuse this operator with the simple product of scalar numbers, ‘ \otimes ’ shall define the operation equivalent to a scalar product, applied to complex numbers representing the respective vectors.

Considering the projection of $I_{l\omega_m}$ on $e^{i\Phi}$ makes it clear that for all possible states

¹¹Remember, the modulation was assumed to be a cosine function, see Equation 1.2 and Equation 1.3.

and combinations of light fields, there is always a certain Φ for which I_{demod} will be zero, while rotated by 90° one gets a maximal absolute value (unless $I_{l\omega_m} = 0$). $\Phi = 0^\circ$ yields $\Re\{I_{l\omega_m}\}$, the pure in-phase component of the signal, while $\Phi = 90^\circ$ yields the in-quadrature $\Im\{I_{l\omega_m}\}$ ¹².

Most experimental length controls employ so-called *control sidebands* by phase modulation of light and demodulation of photocurrent at ω_m . The expanded form of Equation 1.19,

$$I_{\omega_m, \text{demod}} = J_0(m)J_1(m)g_{S0}(\cos \Phi [g_{S+} \sin(\varphi_{S0} - \varphi_{S+}) + g_{S-} \sin(\varphi_{S0} - \varphi_{S-})] + \dots \dots + \sin \Phi [g_{S+} \cos(\varphi_{S0} - \varphi_{S+}) - g_{S-} \cos(\varphi_{S0} - \varphi_{S-})]), \quad (1.21)$$

shows the complexity of such a signal, in particular when attempting to intuitively understand relevant features: even with constant Φ , the signal shape depends on a combination of many parameters, the phase differences between the carrier and the sidebands, in combination with the sideband amplitudes, and scales with the carrier amplitude.

Therefore, the author prefers an argumentation with the phasor picture, mathematically close to Equation 1.20. As the demodulation phase only determines which projection of the error-signal will experimentally be seen, the vector expression that needs to be investigated is

$$I_{\omega_m} = b_+ b_0^* + b_0 b_-^* \quad (1.22)$$

$$\cong \begin{pmatrix} \Re\{I_{\omega_m}\} \\ \Im\{I_{\omega_m}\} \end{pmatrix} = \begin{pmatrix} b_0 \otimes b_+ + b_0 \otimes b_- \\ b_0 \otimes (e^{-i\frac{\pi}{2}} b_+) + b_0 \otimes (e^{+i\frac{\pi}{2}} b_-) \end{pmatrix}, \quad (1.23)$$

where \otimes again denotes the operator for complex numbers equivalent to the scalar multiplication of their vector representatives¹³. Using a phasor diagram for Equation 1.22 means that for each phasor product of the carrier and the sidebands, the lengths are multiplied and the phases are added, considering the complex conjugate where indicated; the phasor products' sum represents the total signal. This approach will be referred to as *multiplication method*. The version in Equation 1.23, however, might be slightly more illustrating in practice as every component of the signal I_{ω_m} contains the sum of the projections of the sidebands on the carrier¹⁴ – scaled by the carrier's absolute value (or vice versa). The first and second component (again corresponding to in-phase and in-quadrature) respectively, use sidebands for two different instances of the modulation phase evolution, $t = 0$ and $t = -\tau_m/4$. The sideband phasors representing these times will

¹²The in-phase and in-quadrature angles do not necessarily coincide with the two extremal projections of I_{ω_m} .

¹³Equation 1.23 can be obtained by using the identities

$$\begin{aligned} \Re\{b_+ b_0^*\} &= \Re\{b_+\}\Re\{b_0\} + \Im\{b_+\}\Im\{b_0\} = (\Re\{b_+\}, \Im\{b_+\})(\Re\{b_0\}, \Im\{b_0\})^T = b_0 \otimes b_+ \\ \Im\{b_+ b_0^*\} &= \Re\{b_+ b_0^* e^{-i\pi/2}\} = \Re\{(b_+ e^{-i\pi/2}) \cdot b_0^*\} = b_0 \otimes (e^{-i\frac{\pi}{2}} b_+) \end{aligned}$$

for both addends of each component. The commutativity of the scalar product for the two vectors makes the projection of the sidebands onto the carrier equivalent to the projection of the carrier onto the sidebands.

¹⁴This carrier/sideband projection makes all non-parallel components cancel out. This, again, corresponds to the results of sections 1.1.2 and 1.1.3 as only amplitude modulation (i.e. sideband parts parallel to the carrier) contributes to a photodiode signal.

be called P and Q *phasors*, respectively. Henceforth, this latter approach to determine I_{ω_m} will be called a *projection picture*.

For illustration, the application of the multiplication method and projection picture to obtain the signal vector I_{ω_m} will be explained with the examples of phase and amplitude modulation:

Figure 1.6 is organised in four columns and two rows. The upper and lower rows show the situation for phase and amplitude modulation, respectively. The inner two columns are phasor diagrams of the carrier (cyan) and the modulation sidebands (magenta). The sideband phasors are presented as P and Q sidebands in the left and right diagram, respectively.

The first and last columns illustrate the vector deduction of I_{ω_m} in analogy to Equation 1.22 (multiplication method) and 1.23 (projection picture), respectively. The contributions associated with the lower and upper sidebands are displayed as dashed and dashed-dotted green vectors, respectively, the sum of both, I_{ω_m} , as a solid red vector. In order to distinguish these coordinate axes from the phasor diagrams, they are grey.

The phasor diagrams of phase and amplitude modulation in P and Q are equivalent to the phasor representation Figure 1.3 and 1.2 at the times $t = 0$ and $t = 3\tau_m/4$, respectively. For a better view of angles, however, in Figure 1.6 the phasor plane of each frequency component is rotated clockwise around the real axis (compare with Figure 1.2 for example) such that the imaginary axis overlaps anti-parallelly with the frequency axis. This keeps the rotation direction for upper and lower sidebands anti-clockwise and clockwise, respectively¹⁵.

To start with the multiplication method (first column of Figure 1.6), one has to consider the phasor diagram with the P sidebands only. The two summands of Equation 1.22 are evaluated separately.

First, phase modulation will be investigated. For the summand $b_+b_0^*$, the carrier stays the same as it is purely real. The multiplication of the carrier phasor with b_+ , however, yields a vector with phase 90° and an absolute length corresponding to the product of the absolute length of the carrier and sideband amplitudes. For the second summand in Equation 1.22, $b_0b_-^*$, the lower sideband phasor flips sign at the multiplication, leading to a phase of the phasor of -90° . Thus, the multiplication results in a vector of the same length as the other (the sideband amplitudes are equal), but with opposite direction. In sum, the photodiode signal fraction oscillating with ω_m , I_{ω_m} , is zero.

For amplitude modulation, all phasors in the P phasor diagram are purely real, thus stay unaffected by complex conjugation. Another consequence is that each product vector is real as well. As the two sidebands point in the same direction, their respective product vectors this time constructively add up to the vector of photodiode signal oscillation at ω_m .

For the procedure underlying the projection picture (last column of Figure 1.6), both sideband quadratures need to be considered. The P and Q quadrature sidebands contribute to the real and imaginary component of I_{ω_m} , respectively. Each projection can,

¹⁵Please note that for the sake of visibility, purely imaginary phasors lie above the imaginary axis.

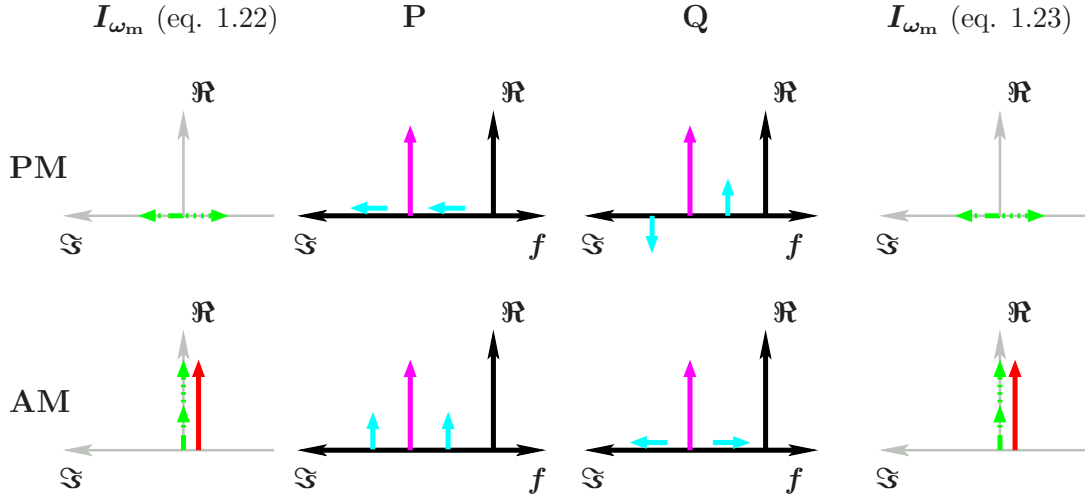


Figure 1.6.: Deduction of I_{ω_m} with the multiplication method (first column) and the projection picture (last column) applied on phase (upper pictures) and amplitude (lower pictures) modulated laser light. The dashed and dashed-dotted green vectors represent the contributions to I_{ω_m} (solid red vector) associated with the lower and upper sideband, respectively. The second and third columns display the phasor diagrams of the carrier (cyan), and the P and Q sidebands (magenta), respectively.

thus, be assigned to one of the axes. For illustration, the projection results are displayed as purely real or imaginary vectors.

Again starting with phase modulation, the P sidebands are perpendicular to the carrier. Therefore, each projection yields zero for the real part of I_{ω_m} . The projection of the Q phasors onto the carrier (or vice-versa), however, is non-zero but has opposite signs for the upper and lower sideband, as indicated by the green vectors on the imaginary axis, pointing to the right and the left, respectively. Thus, the sum gives zero.

With amplitude modulation, the P phasors are parallel to the carrier and to each other. Thus, the projections yield the highest possible absolute values with the same sign for the real part of I_{ω_m} . In Q, the sideband phasors are not only anti-parallelly oriented, but also perpendicular to the carrier. Thus, there is no projection contribution for the imaginary part of I_{ω_m} .

To display I_{ω_m} in a vector plane is not only sensible for illustrating the multiplication method. At the demodulation, where we read out I_{ω_m} from the overall photo-current, and obtain the targeted physical (error) signal (current), a demodulation phase needs to be set. Although Figure 1.6 shows that there is a photodiode signal component at ω_m , it becomes invisible with a demodulation phase of $\pm 90^\circ$. The corresponding unit vector is perfectly perpendicular to I_{ω_m} , pointing like in Figure 1.6.

For complicated optical systems, the dependency of I_{ω_m} on the targeted degree of freedom may be quite complex. Displaying I_{ω_m} in the vector space enables us to intuitively determine an appropriate demodulation phase for a useful control signal. The benefit

of this illustration becomes fully clear in the (sub)sections below, and at the latest in Section 1.2.2.

In the following subsections some examples will be discussed, intuitively deducing error-signal shapes and criteria for the choice of the sideband type and frequency. In the first example both the projection picture and the direct multiplication will be used for comparison. Afterwards only the projection picture will be employed.

1.2.1. Conventions

For the following sections about how to generate a suitable error-signal for some selected optical systems, some more conventions than utilised in the previous sections need to be specified. This subsection contains all conventions used throughout this work to provide the reader with a single place with all necessary information in a condensed form.

A summary of conventions already utilised in the chapters above:

- The phase evolution of the laser light is represented by only one exponential function containing a **positive frequency**. The complex conjugate is omitted.
- In the phasor picture, the **coordinate system rotates with the laser light** frequency. W.l.o.g., the direction of the phasor representing the **light coming directly from the laser coincides with the real axis**.
- Phasors of light fields with **frequencies larger than the laser frequency evolve anti-clockwise with time**.
- All modulations are assumed to be cosine. Thus, **cosine signals are called in-phase**. To yield in-quadrature (equivalent to sine), the signal needs to evolve backwards with time by a quarter period.
- When investigating an **error-signal**, the complete signal, i.e. in **two perpendicular quadratures**, will be deduced. Throughout this work, the **projection picture** will be used¹⁶.

Dealing with transfer functions of optical systems requires the specification of phase changes of light fields at mirror surfaces. There are two conventions that fulfill the condition of power conservation at a beamsplitter. In the first, light keeps its phase at every transmission, and reflection at an optically denser medium, whereas it collects 180° with every reflection at an optically thinner medium.

The second convention provides a phase jump of 90° at every mirror surface transmission and no change at reflection (see [Rüdiger98]). As this convention is symmetric and easier to handle, it will be used throughout this work. Thus:

- **Reflections maintain** a light field's **phase**.

¹⁶There is just one exception in the first error-signal example in the following subsection.

- At every mirror surface **transmission**, light fields experience a **phase jump of 90°** (thus anti-clockwise, regardless of the fields' frequency).

Contrary to other authors,

- in principle **both mirror surfaces** will be **considered**, ensuring a perfect agreement of both mirror conventions.
- phase jumps at surface transitions will only be considered for later interfering light beams if the number of substrate transitions is different. **Phase shifts common to all participating fields are neglected.**

This treatment still conserves the energy as in the considerations made in [Rüdiger98].

Some more comments on optical systems and the projection picture:

- The phasor's coordinate system rotates with ω_0 . However, the carrier can obtain different phases from 0° even in that frame, if
 - some “sudden” phase shifts occur (like in mirror transmission).
 - two carrier phasors from different paths need to be considered.
- **Transfer functions** contain amplitude and phase information **regardless of the initial field's phasor** direction or length. This means that they look the same e.g. for amplitude and phase modulation sidebands (as long as the sidebands have the same frequency).
- Macroscopic lengths are distinguished from microscopic. Microscopic lengths are in the order of the laser wavelength, determining the exact light field phase. In agreement to FINESSE, macroscopic lengths are assumed to fit the laser wavelength, by default 1064nm. The terms **tuning** or **detuning** of a space (or cavity) both refer to the **microscopic length** of that space (or cavity). In most cases, the (de)tuning is equivalent to the offset of spaces (or cavities) from integer multiples of the laser wavelength. Depending on the context, this tuning is given in units of **meters, Hertz or degrees**.

The units of Hertz refer to a light field's necessary offset from laser frequency in order to yield an integer multiple of its wavelength fitting the respective space (or cavity round-trip length). The units of degrees account for the laser light phase evolution along a microscopic length. A shift by one complete wavelength matches 360° .
- A **positive space (or cavity) detuning** is defined as a space (or cavity) **elongated** with respect to an integer multiple of the carrier's wavelength. The light phase decreases with increasing distance traversed (see Equation 1.1). The sign of the phase evolution is also negative when using a constant distance and increasing the light frequency.
- The definition of *parallel* (\parallel) or *perpendicular* (\perp) components of phasors, necessary for the deduction of error-signals in the projection picture, refers to the orientation

of the control sidebands in P. (In case signal sidebands are involved instead of one carrier phasor, please consult Figure 2.5 and the explanation below Equation 2.6.)

- If the optical system and light frequencies allow, spaces will, w.l.o.g., be assumed to be a multiple integer of the wavelengths of all light fields of interest. Alternatively, the light fields' phases will be evolved in time as long as necessary to get a convenient pointing. As the coordinate system common to all phasors anyway rotates with the carrier, this convention affects in particular sidebands, and further simplifies the approach to phasor diagrams.

Please note that a phase evolution in time is equivalent to introducing a certain offset to the absolute demodulation phase, or rotating the orthonormal basis of the photodiode signal vector space. Nonetheless, the newly generated orthogonal quadratures will still be named P and Q, although they do not necessarily relate any more, like 0° and -90° , respectively, to the absolute phase of the local oscillator.

1.2.2. Cavity control signal in reflection

GEO 600 has one slave laser, two mode cleaner and two main interferometer cavities (the power and the signal-recycling cavity) to be controlled. The most important control task is to sense and adjust the length of these cavities with respect to the desired resonant state of a light field. Therefore, error-signals representing cavity lengths are of paramount importance and are all generated by a modulation/demodulation method as described above. Error-signals are usually plotted as a signal amplitude versus the parameter to be controlled, which in most cases is the microscopic length or *tuning* of the cavity, δx . As the signal amplitude should give a measure of how far the optical system is deviating from the intended operating point, it should be zero for the desired tuning and monotonic in a surrounding interval, yielding a bipolar signal.

With the exception of the signal-recycling cavity, all cavity error-signals of GEO 600 are detected in reflection. Figure 1.7 depicts the light field phase shift (lower curves) and gain (upper curves) expected in reflection of an over-coupled cavity¹⁷. Shown are three cavity resonance structures, separated by a fixed multiple of the *free spectral range* $FSR = 2c/L_{cav}$, with c being the speed of light and L_{cav} the macroscopic cavity length. These structures are functions of the microscopic tuning δx of the cavity or of the frequency offset δf of the carrier from (the middle) resonance, indicated by 0 Hz.

Three incoming light phasors, one carrier and two arbitrary modulation sidebands, are positioned such that the carrier is ideally resonant inside the cavity. In this situation, the carrier experiences the largest possible attenuation in reflection (with the given amount of overcoupling), and a phase shift of 180° , whereas the sidebands' amplitude and phase hardly change. If the carrier alters its frequency (indicated by the black arrow pointing to the right-hand side), the sidebands move along the frequency axis by the same amount against the rigid resonance structures. Alternatively, the tuning of the cavity could vary.

¹⁷For the cavity transfer functions please look up the derivations made in [Heinzel95]. Figure 1.7, though, uses the sign of phase evolution given in Equation 1.1.

With respect to the frequency axis, this moves the resonance structures to the left/right for a decreasing/increasing cavity length. If, for example, the cavity gets elongated by δx_m with respect to carrier resonance, the patterns move to the left by the corresponding frequency amount of δf_m , and the lower sideband gets resonant.

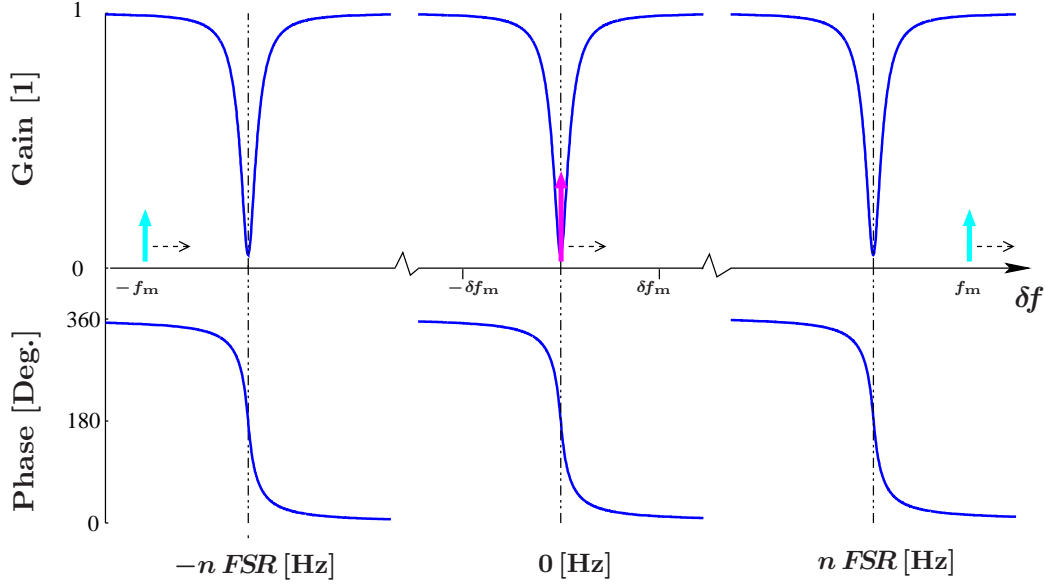


Figure 1.7.: Example of three light phasors, one carrier (magenta) and two arbitrary modulation sidebands (cyan), being back-reflected by an over-coupled cavity. All fields see resonance structures at different multiples of the cavity's FSR , leading to the curves of the gain and phase shift for the reflected light fields. The position of the phasors within the respective pattern indicates the de facto expected amplitude and phase change of the phasor. A frequency shift of the carrier (indicated by the black arrow) at the same time moves the sidebands against the rigid comb of resonance structures. If the carrier coincides with $\pm \delta f_m$, one of the sidebands becomes resonant.

Operating-point carrier resonance

In most cases, the resonance of the carrier inside the cavity is intended, occurring when the carrier frequency matches the dashed vertical line in Figure 1.7 at 0 Hz or 0 m. An example within GEO 600, where this is the desired state of the optical system, is the power-recycling cavity.

At this operating point, the carrier phasor is, in general, purely real, and both sidebands have the same amplitude, but (with only a few exceptions) anti-symmetrically shifted phases.

One requirement for the error-signal, represented by Equation 1.22, is that it should be zero at the operating point. With $b_0 \in \mathbf{R}$ for resonance, Equation 1.22 results in

$$I_{\omega_m} = b_0(b_+ + b_-^*) \equiv 0 \iff b_+ = -b_-^* \iff \Re\{b_+\} = -\Re\{b_-\} \wedge \Im\{b_+\} = \Im\{b_-\}. \quad (1.24)$$

With the cavity transfer function shown in Figure 1.7, this condition can never be fulfilled with simple amplitude modulation. A pair of amplitude sidebands, symmetrically distributed around the carrier, will always have the same real part and opposite signs in the imaginary part.

Symmetric phase modulation sidebands accomplish this requirement regardless of their frequency. However, there are other criteria constraining their offset from the carrier, ideally to half of the FSR ¹⁸, placing them in the anti-resonant condition:

- The amplitude of the sidebands can be maximised at anti-resonance.
- The phase should develop differently from the carrier for small detunings around the operating point. At anti-resonance, for example, the sideband phase is almost the same over a wide range of frequencies or detunings, yielding a definite signal dependence on the carrier phase shift only.

Such a configuration is called Pound-Drever-Hall scheme [Drever83]. (An illustrating approach of the Pound-Drever-Hall error-signal, different from below, can be found in [Bongs95].)

The shape of the error-signal according to Equation 1.22 and 1.23 is qualitatively explained with the phasor diagram shown in Figure 1.8. Again, and in the following, for a better view of angles the phasor plane of each frequency component is rotated clockwise around the real axis.

Figure 1.8 is organised in four columns and three rows. Each row represents a particular (de-)tuning of the cavity with respect to the carrier resonance, δx_0 (corresponding to 0 m in Figure 1.7). From top to bottom: a distinctly shorter, a resonant, and a slightly elongated cavity. All tunings shall belong to the same resonance structure.

In agreement with Figure 1.6, the outer columns display the photo-current part oscillating with ω_m , I_{ω_m} , in the two-dimensional vector plane; the last refers to the projection picture introduced by Equation 1.23, the first is based on the multiplication method as indicated in Equation 1.22. The dashed-dotted and dotted green vectors represent the contributions to I_{ω_m} , associated with the upper and lower sideband, respectively, whereas the solid red vector is the sum of all, the total I_{ω_m} . In the two middle columns of Figure 1.8, the carrier (magenta) and the phase modulation sideband phasors (cyan) are mapped qualitatively for the respective δx , applying the amplitude and phase changes indicated by Figure 1.7. The left of the middle columns displays the cosine phase modulation sidebands for $t = 0$, thus the in-phase situation, the right shows them a quarter period earlier, thus Q. For all cavity tunings, the sidebands' amplitudes and phases are roughly constant. This is the case if the finesse of the cavity is high enough, such that

¹⁸Modulo multiples of the FSR .

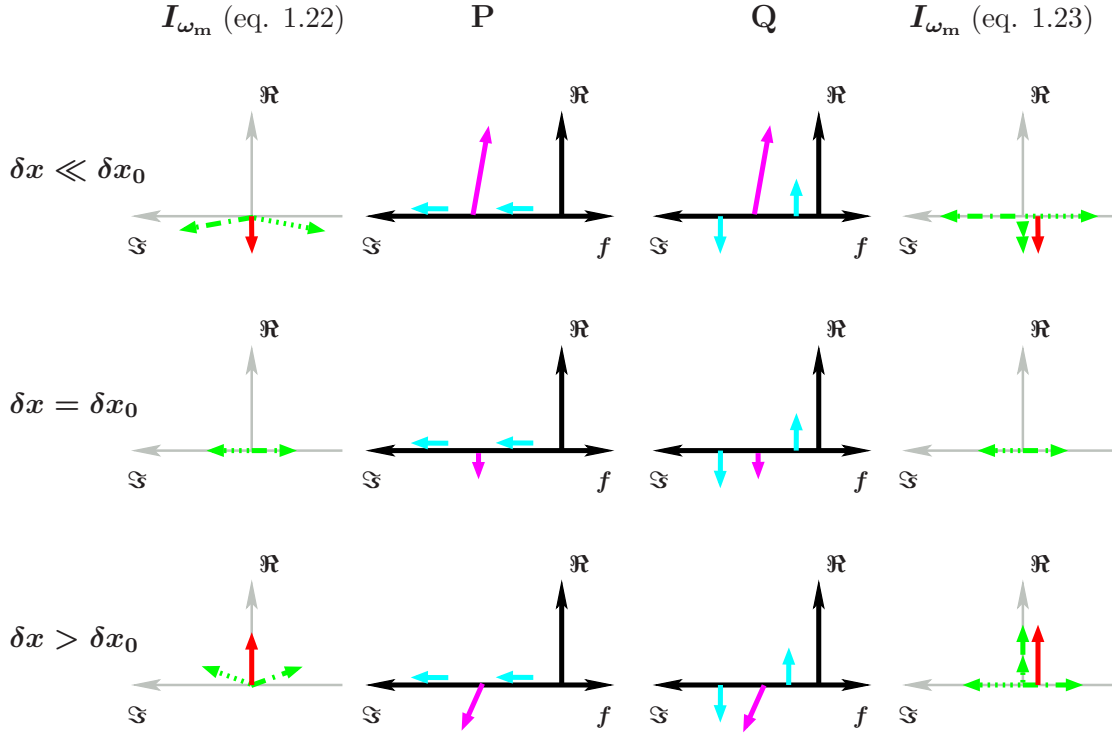


Figure 1.8.: Phasors and I_{ω_m} , belonging to the Pound-Drever-Hall signal around carrier resonance δx_0 . The three rows from top to bottom: the situation of a distinctly shorter, a resonant, and a slightly elongated cavity. The corresponding phasors are displayed in the inner two columns, with the left and right representing the P- and Q-sidebands, respectively. The first and last column depict I_{ω_m} with the different deductions introduced by Equation 1.22 and 1.23, which is complex multiplication and projection picture, respectively.

the sidebands are roughly anti-resonant as long as the carrier frequency moves within the resonance structure.

To compare both approaches to I_{ω_m} , the case of slight off-resonance, $\delta x > \delta x_0$, will be explained in more detail. In that case, the carrier amplitude is still noticeably attenuated and the phase shift is smaller than 180° .

To start with the approach of the first column, illustrating Equation 1.22, the summand $b_+ b_0^*$ is composed by phase shifting the complex conjugate of b_0 by 90° (i.e. anti-clockwise) and scaling it by the sideband's length. The resulting vector is mapped dashed-dotted. $b_-^* b_0$ yields the dotted vector, shifting b_0 by -90° , the phase of the lower sideband's complex conjugate. The sum of both vectors points to the positive real axis (solid red vector).

For the right-hand side, the contribution of each projection to the respective error-signal component is mapped as a separate vector on the corresponding axis. The carrier projection on the P-phasors gives two non-zero contributions for the real component of

I_{ω_m} ; each projection on the Q-phasors is indeed larger, but in opposite directions such that they cancel the imaginary component (the results of the projection on the upper and lower sideband are again dashed-dotted and dotted, respectively). As a consequence, the resulting signal I_{ω_m} is identical to that on the left.

The projection picture makes obvious that no matter what kind of phasor is projected onto the Q-phasors, the result always vanishes due to their anti-parallel nature. Projections on the P-phasors, however, add up maximally. Demodulating with a phase $\Phi = 90^\circ$, which is equivalent to projecting the red error-signal vector onto a unit vector pointing to the left (see Equation 1.18 to 1.20), would therefore yield zero for all detunings around the carrier resonance (which is highly unsuitable as an error-signal). For all δx , a demodulation-phase vector parallel to the real axis yields the largest absolute signal amplitude, in this case highest sensitivity for detunings from the operating point. The slope of such an error-signal as an equivalence to sensitivity is called *optical gain*. Figure 1.11 contains the in-phase and in-quadrature error-signal amplitude for continuously varying microscopic cavity tuning δx . The particular tunings discussed in Figure 1.8 are marked on the graph by the dashed lines around δx_0 .

Control of a detuned cavity

The modulation sidebands being (anti-)parallel for a wide range of cavity tunings like in the subsection above is only a special case due to the assumed high cavity finesse in combination with anti-resonance. In general, the sideband phase changes with changing carrier frequency such that P and Q do not necessarily agree with a maximal or minimal signal, respectively.

This becomes obvious already in the example of light fields in cavity reflection, if the comb of resonance structures in Figure 1.7 moves so far away from the carrier resonance that one of the sidebands resonates inside the cavity. For the lower sideband located within a resonance structure, Figure 1.9 intuitively explains I_{ω_m} with the help of the projection picture that will exclusively be used from now on. The figure is similarly organised as Figure 1.8, but without the first column. The rows represent different cavity tunings - this time around the lower sideband resonance, δx_m -, the first two columns show the respective phasors in P and Q, and the last column displays I_{ω_m} .

For simplicity, the upper sideband in this example remains (nearly) anti-resonant through all considered cavity tunings¹⁹. As the anti-resonant sideband is perpendicular in P to the carrier, it does not contribute to the real part of the error signal. The resulting I_{ω_m} (in red) is not restricted any more to the real or imaginary axis but rotates anti-clockwise with increasing δx . To obtain a maximal projection of I_{ω_m} on the unit vector of the demodulation phase, one needs to adjust Φ for every single tuning. Otherwise, for each tuning there exists exactly one demodulation phase, Φ_0 , modulo 180° , that generates a zero. This fact includes that there is no outstanding point like in the

¹⁹This assumption is realistic for high-finesse cavities in combination with sidebands being a few bandwidths away from exact resonance and anti-resonance. (If the sidebands were too close to anti-resonance, the cavity resonance structure would influence both sidebands.)

carrier resonance case, where I_{ω_m} is zero for all demodulation phases. Nonetheless, one gets a reasonably bipolar error-signal for a whole interval of Φ s, but with different points of zero crossings. The respective zero crossing would play the role of the operating point, putting the cavity in a state with a certain detuning from the carrier resonance. Within GEO 600, this principle is applied for the state of the signal-recycling cavity, which is currently only operated in a detuned state.

The variety of possible demodulation phases for each modulation frequency can be experimentally quite challenging, since it not only fine-tunes the cavity but also determines the complete shape of the error-signal, like for example the region for which the error-signal is close to linear, or the optical gain. In particular the range of the linear region is important for the stability and performance of the respective control loop (see section 2.3.3 of [Grote03b]). Figure 1.10 shows the error-signal amplitude in cavity reflection with respect to the cavity detuning δx around one sideband resonance and shows the effect of different demodulation phases.

Coming back to the carrier resonance as the intended operating point, Φ would be adjusted to give maximal sensitivity, which is non-ambiguous apart from sign²⁰. A maximal optical gain is achieved with $\Phi = 0^\circ$ (see Figure 1.8). Please note that this phase also generates a bipolar structure around the sideband resonance with zero crossing exactly at the resonance (see Figure 1.9 and 1.10). This error-signal structure would in principle compete with the carrier resonance, if there was not the opposite sign. If, for example, a positive error-signal value was interpreted as a negative detuning at the feedback, the detector would still find its real operating point²¹. Figure 1.11 shows the in-phase and in-quadrature error-signal, depending on the detector detuning δx , comprising the resonances of the upper and lower sidebands as well.

1.2.3. Cavity signals in transmission

In some experimental cases, a detection in reflection might be impossible or disadvantageous, enforcing the use of alternative control signals. One possibility is to use an accessible beam being a weak reflection from inside the cavity originating from any existing surface. If this is not an option, a plate-glass, artificially placed inside the cavity, could be used to release some intra-cavity light onto a photodiode. More easily accessible, however, is the light transmitted by the cavity. This, above all, does not degrade the cavity performance like the plate-glass may do. As the light fields coupled-out from inside the cavity and transmitted by the cavity differ only in the amount of attenuation of the intra-cavity light, their Airy-functions should exactly agree in phase and deviate only by a constant factor in gain. Thus, the error-signal should exhibit similar characteristics. The exact amplitudes and optimal demodulation phases, though, depend highly on the particular configuration.

²⁰If Φ was 180° instead of 0° , the sign of the values would simply flip. The sign of the signal is of importance for the sign of the control loop, but does not change the quality of the signal.

²¹The correspondence of error-signal sign and detuning side needs to be determined in the experiment.

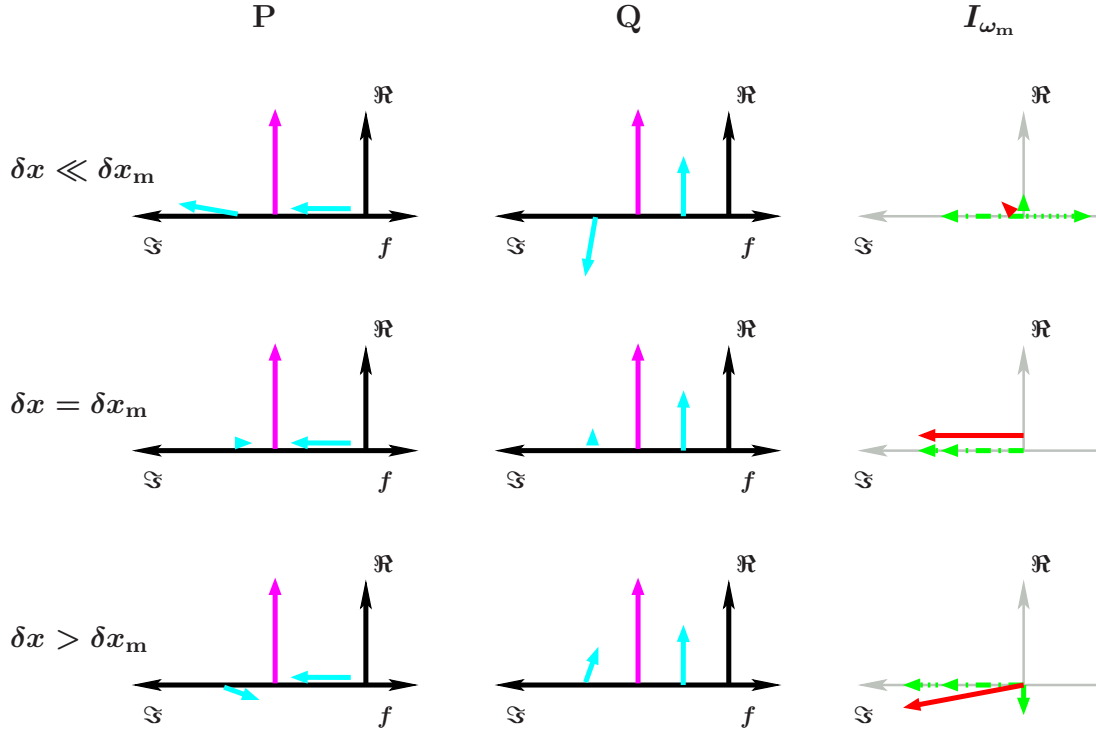


Figure 1.9.: Phasors and I_{ω_m} , belonging to the Pound-Drever-Hall signal for a cavity tuned around the resonance of the lower sideband, δx_m . The three rows from top to bottom: the situation of a distinctly shorter, a resonant, and a slightly elongated cavity. The corresponding phasors are displayed in the first and second column, representing the P- and Q-sidebands, respectively. In agreement with Figure 1.7, only the lower sideband sees different resonance conditions. In the last column, I_{ω_m} is displayed utilising the projection picture of Equation 1.23. The contribution of each phasor projection is represented by a green vector, the resulting vector corresponding to I_{ω_m} is given in red.

To achieve any error-signal in transmission requires that the sidebands pass through the cavity if the carrier is resonant. This is satisfied only close to a sideband resonance as Figure 1.12 suggests. Similar to Figure 1.7, a frequency comb of light fields meets a comb of resonance structures. But here, the highest sideband amplitudes are located around multiples of the FSR . The sideband phases of Figure 1.12 stand for an even integer n . (With an odd multiple²² of the FSR , the phase shifts would have an offset of $\pm 180^\circ$. For the exact phase offset remember that common phase shifts are neglected (see Section 1.2.1).)

²²Free spectral ranges in frequency correspond to half of the laser wavelength. Light with a frequency of an even multiple of the FSR fits into the cavity with an integer number of the complete wavelengths. Assuming this for the carrier, sidebands with a frequency offset of an even multiple of the FSR should do so as well and preserve the former phase difference to the carrier. With odd multiples, $\pm 180^\circ$ are accumulated inside the cavity in half a round-trip.

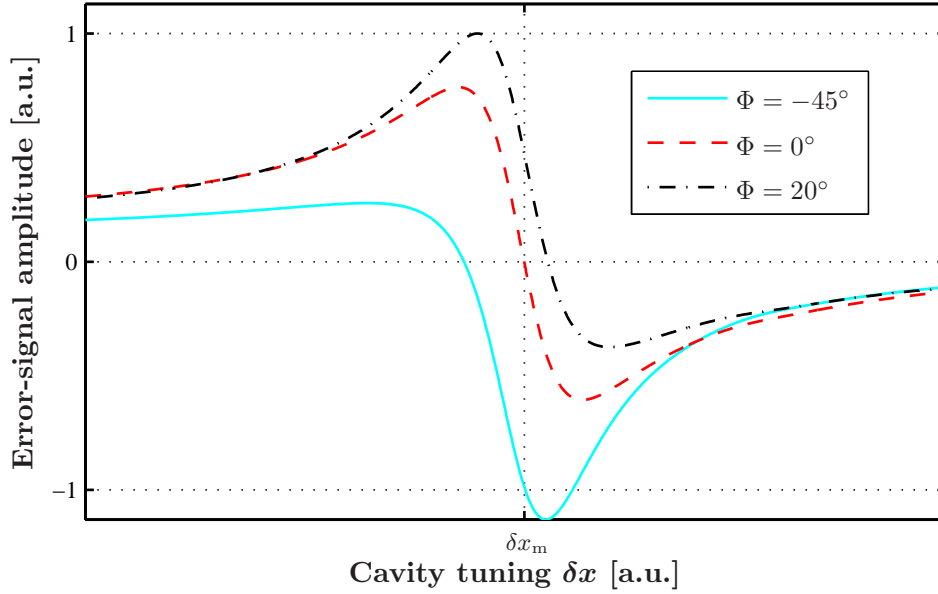


Figure 1.10.: Pound-Drever-Hall error-signal around the resonance of the lower sideband, δx_m , for different demodulation phases Φ . Controlling the complete shape of the error-signal, this phase not only determines the exact position of the zero crossing, but also the optical gain and the region of linearity around the zero crossing.

An exact resonance of the sidebands, however, will make the signal insensitive to small deviations δx from carrier resonance as the phase differences remain constant for all δx . Therefore, the sideband amplitude needs to be balanced against the phase evolution. An offset of the sideband frequencies from a multiple of the *FSR* as for example indicated in Figure 1.12 provides an appreciable amplitude with a still relatively plain phase slope²³.

The error-signal according to this constellation of frequency components is shown in Figure 1.13. The demodulation phase was optimised to give maximal optical gain at carrier resonance. Although Figure 1.13 shows a normalised error-signal, it is important to notice that the signal amplitudes are 80 dB smaller than those of the signal in reflection. Utilising it as a feedback signal requires a very low noise performance of electronics, the local oscillator and the laser beam, and the ultimate shot noise limited performance is poorer. Similar to the Pound-Drever-Hall error-signal, the signal has a bipolar structure not only at the cavity but also at the sideband resonance. The zero crossing around the sideband resonance, though, is no longer exactly at the resonant tuning, as the carrier and the other sideband are no longer perfectly real and imaginary, respectively.

This type of error-signal in transmission was successfully utilised at the Glasgow prototype for a signal-recycled Michelson interferometer with arm cavities [Barr03].

²³The necessary requirement of a zero crossing at the carrier resonance is in any case fulfilled. This follows from the symmetric configuration and cavity transfer function, as explained in Section 1.2.2.

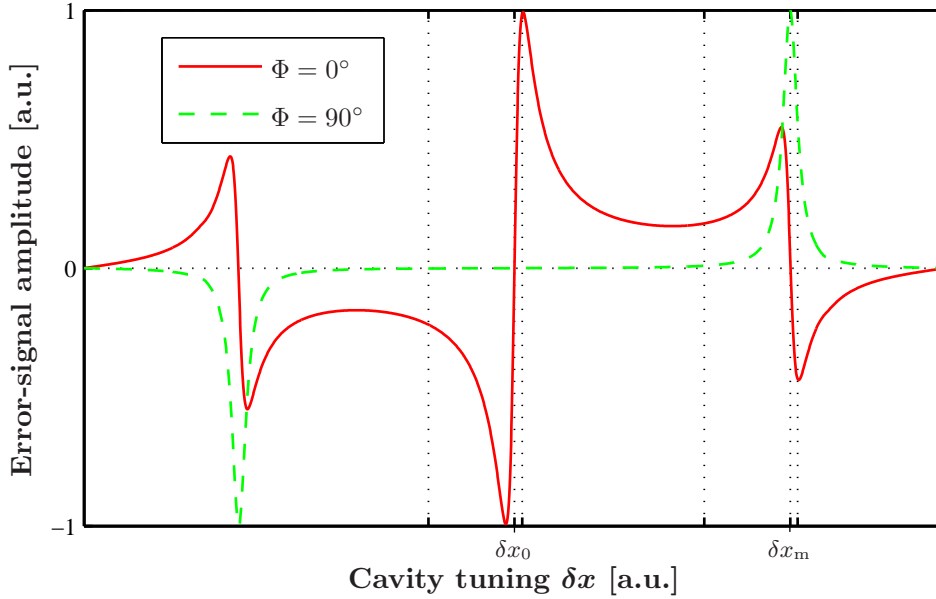


Figure 1.11.: Pound-Drever-Hall error-signal in P ($\Phi = 0^\circ$) and Q ($\Phi = 90^\circ$), comprising the complete tuning region of light field resonances. The dashed lines indicate the three distinct tunings investigated with the phasor picture in figures 1.8 and 1.9. The zero crossings in P occur exactly at the light fields' resonances.

1.2.4. Control of a Michelson interferometer

The heart of the current generation of interferometric gravitational-wave detectors is a Michelson interferometer. Due to the quadrupole nature of gravitational waves, a light field, traveling within a plane perpendicular to the propagation of the gravitational wave, experiences different travel times along nearly all perpendicular directions. This property is exploited by a Michelson interferometer, splitting a beam into two perpendicular beams, which travel along the arms of the Michelson interferometer. The travel time of both beams is compared by back-reflecting and combining them again at the beamsplitter. The interference of the beams appears as brightness or darkness, depending on their phase difference and the port of observation. Figure 1.14 shows a simple Michelson interferometer. The four ports of the beamsplitter **BS** are associated with the cardinal points. Throughout this work, the laser light will always be assumed to enter the interferometer from the west, unifying the terms *west* and *input port*, whereas *south port* is used as a synonym for *output port*. Accordingly, the Michelson arms are called the *east* and *north arm*.

A gravitational-wave will, except for very unfavourable polarisation, differentially change the travel time in both arms and therefore the amount of light appearing at the south and west port of the instrument.

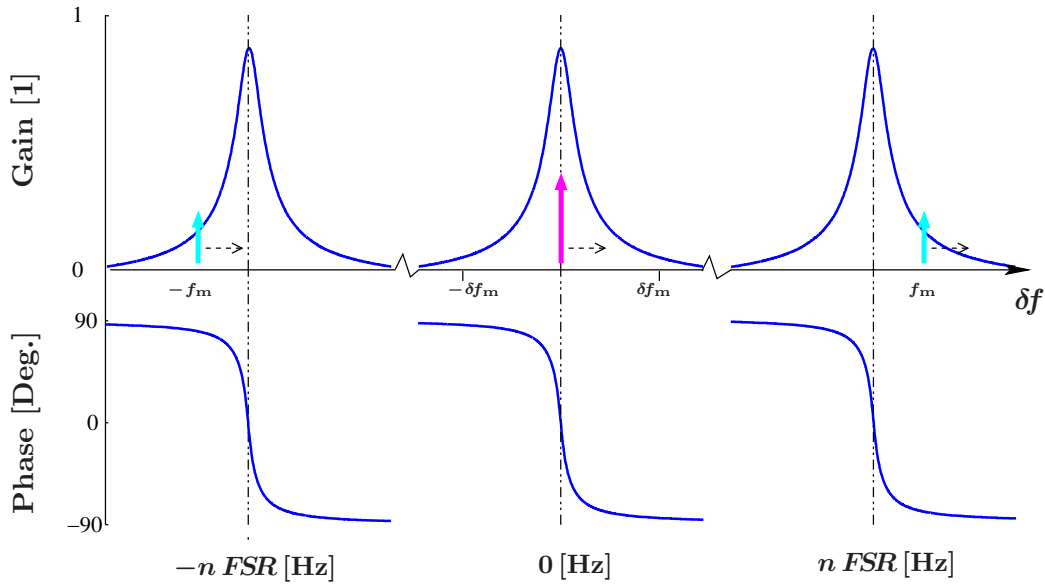


Figure 1.12.: Phasor position within a cavity resonance structure in transmission or inside a cavity. This time, as a trade-off of obtaining a decent sideband amplitude and at the same time a roughly steady phase, for small carrier frequency deviations from cavity resonance, the sideband frequencies need to be placed closer to an integer multiple of the FSR than in the case of cavity reflection, though still well outside the cavity bandwidth. Again, an increasing carrier frequency or increasing cavity tuning in the same way moves the phasor positions against the resonance structures.

The light powers at the west and south ports of a Michelson interferometer are most sensitive to phase differences of the interfering light beams from the arms if the detector is operated at the so-called *mid-fringe*. This refers to the mid amplitude of the sinusoidally shaped intensity signal, where the slope of the sine is highest. Although yielding the best optical gain and a bipolar error-signal, this kind of detector reference-state has a few drawbacks. The main is the dependency of the reference value on power fluctuations caused by a technically limited laser-power stability.

To minimise the sensitivity to power fluctuations, the Michelson arms can, for example, be adjusted such that the light fields interfere destructively at the south, returning all light to the laser. This interferometer state is called *dark fringe* and would entail a detection at the south port only. (The bright port is again sensitive to technical laser power fluctuations.) Besides shot noise, there are some other favourable features of this operating point.

The Michelson interferometer at a dark fringe acts like a perfect mirror for all common attributes of the laser light. Differential effects will, however, show up in the south. An ideal dark fringe therefore completely separates the gravitational-wave signal from the noise sidebands on the laser light. Further, it enables the elaborate interferometric techniques of signal and power recycling (see Section 2.2).

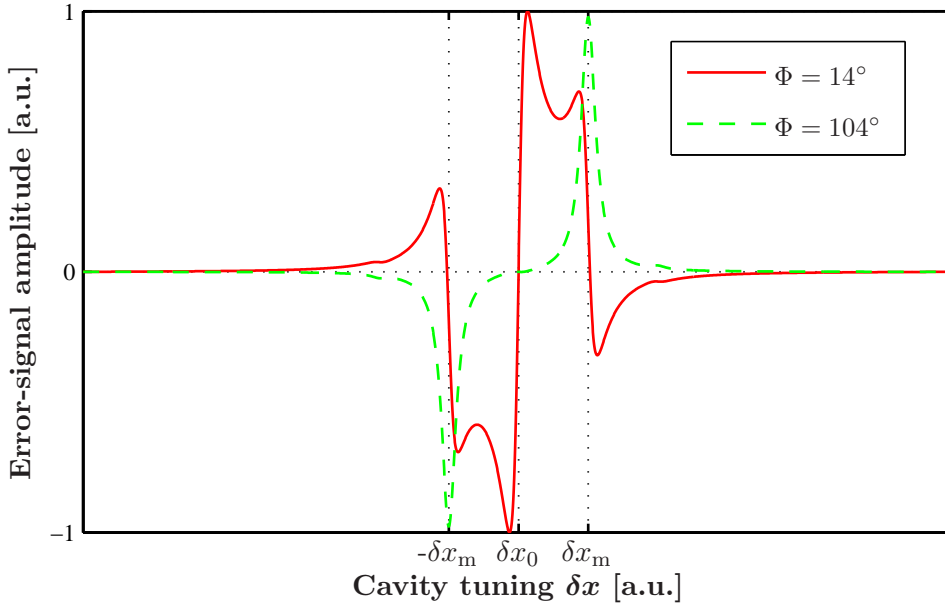


Figure 1.13.: Demodulated error-signal in transmission. The demodulation phases were optimised to give maximal ($\Phi = 14^\circ$) and minimal ($\Phi = 104^\circ$) sensitivity for carrier resonance. The signal has a bipolar structure not only at the cavity but also at the sideband resonance. The normalised amplitude is, however, misleading as the signal is 80 dB smaller than the Pound-Drever-Hall signal generated in reflection (Figure 1.11).

With the operating point at the minimum of the light power, the power itself lacks bipolarity, alike in the cavity examples of the previous section. Again, a modulation/demodulation technique can be applied to solve this problem. To explain the properties of such an error-signal with the phasor projection-picture let us assume a dark fringe, phase modulation of the injected light and an ideally symmetric Michelson interferometer: the beamsplitter has 50% transmission and reflection and no losses at the rear surface, and the losses in both arms are same.

In Figure 1.15, the case of identical armlengths is considered — a so-called *white-light interferometer*. Light fields at the west port are displayed left, those of the south port at the right; the upper two rows of diagrams address the operating point, the dark fringe state, the last two a small microscopic offset. For each state, the first and second row account for P and Q control sidebands, respectively. The interfering partial beams at each port, coming from the north and east arm, are marked as dotted and dashed-dotted lines, respectively. The sum of both is represented by phasors with continuous lines. Sideband and carrier phasors (and the respective sum phasors) are displayed in cyan and magenta, respectively.

The carrier light returning to the west port from the north experiences reflections only. Without any particular arm length tuning (upper part of Figure 1.15), the carrier phasor

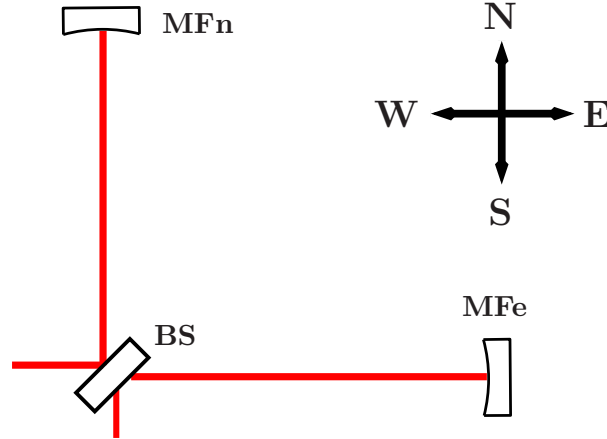


Figure 1.14.: Layout of a simple Michelson interferometer. The laser light enters from the left, called west port associated with the cardinal point. After passing the beamsplitter **BS**, the parts of the beam enter the east and north arm of the Michelson, where they get back-reflected by the far mirrors **MFe** and **MFn**, and interfere at the **BS**.

is (still) purely real in a coordinate system likewise rotating with ω_0 (see the conventions for optical systems specified in Section 1.2.1). The phasor originating from the east arm undergoes a total of four transmissions (two at each beamsplitter surface), adding up to a phase shift of 360° . Thus, both beams interfere constructively.

In the south port, the carrier originating from the north experiences two transmissions, rotating the phasor by 180° , whereas that from the east arm again passes 4 surfaces on the way to the output, yielding 360° . As the beamsplitter is perfectly symmetric, as are the losses in the arms, both phasors cancel exactly and we get a perfect dark fringe, the intended operating point.

The phasors of the sidebands rotate along the Michelson arms with $\pm\omega_m$ offset from the carrier, such that their phases, the pointing directions of their phasors, depend on their overall pathlengths. We can, however, w.l.o.g., for simplicity assume that the overall optical path in the Michelson arms is an integer multiple of the sidebands' wavelength²⁴ (see again Section 1.2.1). This is done with the dark-fringe sideband phasors in Figure 1.15. The first and the third rows display the sidebands of a cosine phase modulation, for a dark fringe state and a small offset, respectively. The second and last rows deal with the same detector situation but a quarter modulation period earlier, thus with sinusoidal modulation sidebands.

²⁴ Alternatively, we could wait at any spot and picture the next moment of integer multiple of the modulation period τ_m . “Waiting” is, by the way, equivalent to the choice of the demodulation phase Φ . Rewriting Equation 1.18 assures mathematically:

$$I_{\omega_m} e^{-i\Phi} = (b_+ b_0^* + b_0 b_-^*) e^{-i\Phi} = (b_+ e^{-i\Phi}) b_0^* + b_0 (b_- e^{i\Phi})^* \quad (1.25)$$

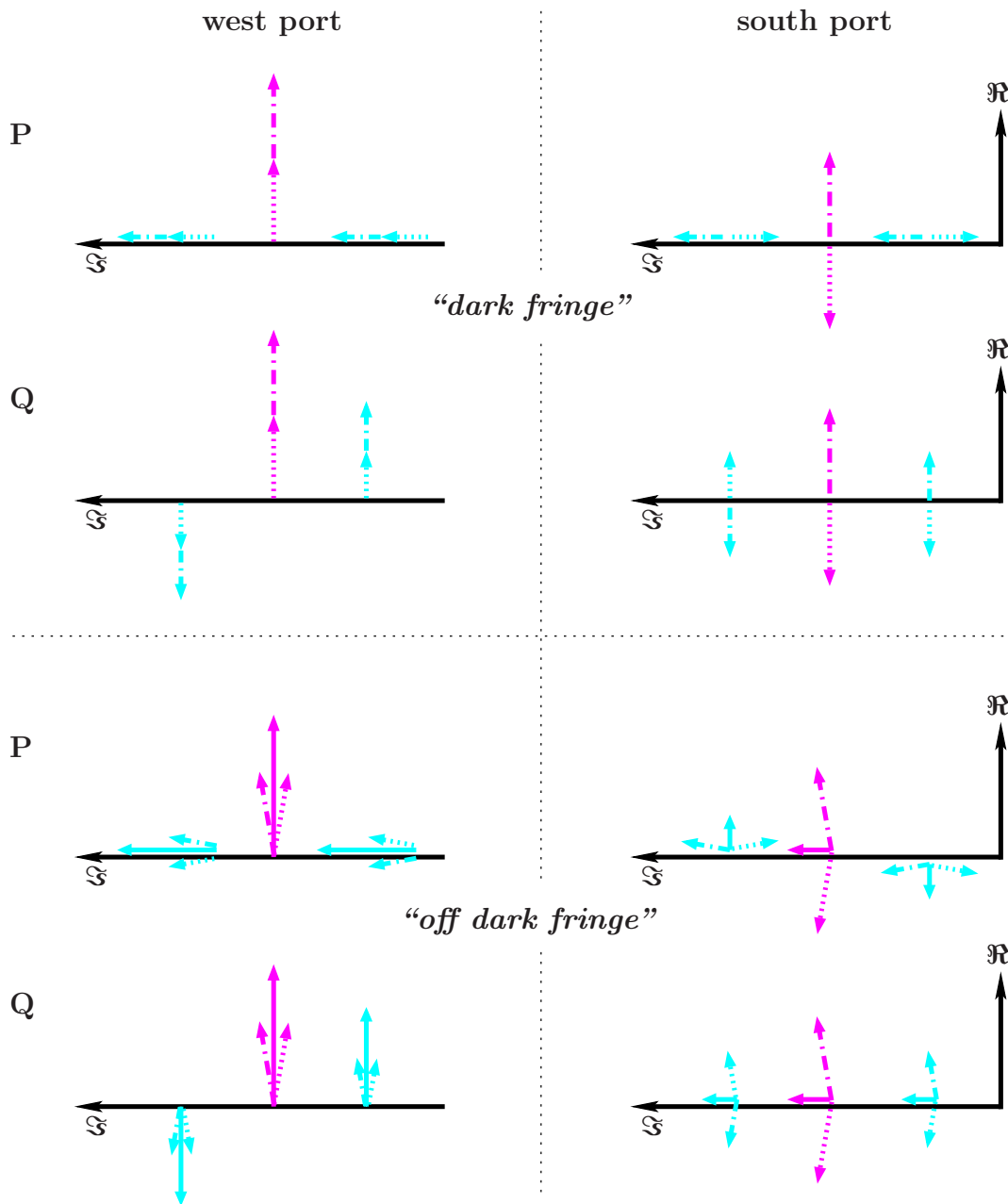


Figure 1.15.: Carrier and sideband phasors at in- and output port of a Michelson interferometer for two states: a perfect dark fringe and a slight offset from the dark fringe. The figure is split into four quadrants. The quadrants on the left display the light field phasors at the input or west port, the right side those from the output or south port. The dark fringe state is depicted in the upper half of the figure, the lower part shows a state with a small offset from the dark fringe. Each quadrant contains two diagrams, accounting for P (upper) and Q (lower) control sidebands. The carrier and sideband phasors are displayed in magenta and cyan, respectively. Light fields originating from the north arm are dotted, those from the east arm dashed-dotted. The respective sum phasor, where necessary, is a solid line and correspondingly coloured.

With the Michelson interferometer at the dark fringe, all modulation sidebands at the west port are, with respect to the incoming phase, unchanged, since they undergo zero or four transmissions. They add up to phasors keeping the condition of pure phase modulation. In the south, however, the sidebands interfere destructively as with the carrier.

Therefore, the error-signals at both ports yield a zero for the dark fringe, for every demodulation phase.

If the Michelson interferometer is detuned from the dark fringe by a small amount $\pm\delta L$ (see the lower pictures of Figure 1.15), say the north arm is stretched and the east squeezed by δL , such that the optical pathlength difference between both arms amounts to $4\delta L$, the phasors of the different arms will rotate to opposite sides for each frequency component, diminishing some of the light at the west port and instead rerouting it to the south.

In these off-dark-fringe pictures, two carrier phasors from different optical paths need to be compared. Thus, the real axis of the coordinate system agrees with a carrier traveling along the average pathlength of both arms. This reference is equivalent to the carrier phasor in the dark-fringe situation. With this reference, the phase fronts of the carrier coming from the north arm ($+\delta L$) fall behind in comparison with the dark-fringe carrier phasor. Thus, the phasor diagram sees the phase of the carrier, coming from the north-arm, shifted by $-2\delta L/\lambda \cdot 2\pi$. The same consideration holds for the sidebands.

Still, at the west port, the phasor sums of all frequency components point in the same direction keeping a perfect phase modulation, therefore zero for the demodulated error-signal. In the south, however, with the initial dark fringe condition of the P sidebands equally appearing on the imaginary axis, the resulting phasor-sums at the upper and lower frequency will always point to the opposite direction and perfectly cancel²⁵ (as they have same lengths). A quarter period later, however, they not only add up but are also completely parallel to the residual carrier, giving an error-signal bigger than zero:

$$I_{\text{demod}} = 2E_0^2 J_0(m) J_1(m) \sin\left(\frac{2\delta L(\omega_0 + \omega_m)}{c}\right) \sin\left(\frac{2\delta L\omega_0}{c}\right). \quad (1.26)$$

Although at first glance this appears as the desired error-signal, there are two drawbacks putting this impression into perspective. Close to a dark fringe, the absolute light field amplitudes increase linearly. For deviations smaller than $10^{-9} \times \lambda_0$, like those originating from gravitational waves²⁶, the error-signal amplitude will be too faint as it scales with the product of carrier and sideband amplitude at the south, thus $10^{-16} \cdot E_0^2 J_0(m) J_1(m)$, almost quadratically with one of their phases²⁷. The phasor rotations in Figure 1.15 are

²⁵With the same argumentation, the error-signal gained with amplitude modulation of the light field, entering the Michelson, would yield a constant zero at the south port. The signal at the west port would not be suitable with amplitude modulation because it has a non-vanishing value for the operating point.

²⁶A supernova in our galaxy would cause a strain $h = 2\delta L/L \sim 10^{-18}$, introducing a mirror displacement of $\delta L \sim 10^{-15} \text{ m} \approx 10^{-9} \times \lambda_0$.

²⁷Close to a dark fringe, the carrier and sideband phase shifts are almost identical. With $\omega_m = 2\pi 15 \text{ MHz}$, for example, the difference of phase shift between the carrier and the sidebands for $\delta L = 10^{-9} \cdot \lambda_0$ will, at the beamsplitter, amount to

$$\delta\varphi = \frac{2\delta L \omega_m}{c} \approx 6 \cdot 10^{-16} \text{ rad} \approx 4^\circ \cdot 10^{-14}.$$

exaggerated for the sake of clarity.

The second aspect is the error-signal not being bipolar. If the armlengths deviate from the dark fringe to the other direction (north arm is squeezed and east stretched), all phasors flip at the same time, leading to the same sign in projection.

All things considered, with this technique it is impossible to generate a suitable error-signal for a Michelson interferometer with equal armlengths, neither at the west nor at the south port.

However, the fallacy introduced by too big phasor rotations in Figure 1.15 leads immediately to the key for an error-signal improvement. Some macroscopic armlength difference, $\Delta L_{\text{Schnupp}}$, generating an optical pathlength difference between both arms of $2\Delta L_{\text{Schnupp}}$, could provide the sidebands with a sufficiently high phase offset for a decent, bipolar error-signal. For an overall pathlength difference of $2\Delta L_{\text{Schnupp}} = 10$ cm and $\omega_m = 2\pi \times 15$ MHz, both values in the order of GEO 600 parameters, the absolute sideband phase shift in each arm amounts to

$$\Delta\varphi = \frac{\Delta L_{\text{Schnupp}} \omega_m}{c} \approx 2 \cdot 10^{-2} \text{ rad} \approx 1^\circ,$$

improving the signal strength by 6 orders of magnitude²⁸. The second benefit of the macroscopic armlength difference is that any microscopic armlength difference will hardly influence the sideband phasors. Thus, if δL changes sign, only the carrier phasor will flip, ensuring the necessary bipolarity.

Among various other possible configurations, applying phase modulation for the phase read-out of the carrier at a Michelson interferometer (for an overview, please view section 1.3 in [Heinzel99]), this scheme explained above, called the *Schnupp modulation* after Lise Schnupp [Schnupp88], was selected for the operation of all actual gravitational-wave detectors. The armlength difference $\Delta L_{\text{Schnupp}}$ is accordingly called the *Schnupp length*.

Accounting for $\Delta L_{\text{Schnupp}}$, the error-signal in Q (and thus the overall signal) changes to

$$I_{\text{demod}} = 2E_0^2 J_0(m) J_1(m) \sin\left(\frac{\Delta L_{\text{Schnupp}} \omega_m}{c}\right) \sin\left(\frac{2\delta L \omega_0}{c}\right), \quad (1.27)$$

which agrees with the derivation made by [Heinzel99] (equation 1.44). (Note that the sign matches as well if the tuning directions conform.)

The overall phase shift is $4\pi \cdot 10^{-9} \text{ rad} \approx 8^\circ \cdot 10^{-7}$.

²⁸This armlength difference will of course increase the light power and shot-noise level on the photodiode. However, the shot noise and the signal both scale with the sideband amplitude and therefore cancel in the shot noise limited signal-to-noise ratio (see Section 2.2). The benefit of increasing both is that the shot noise can be dominated by the sidebands.

Chapter 2.

The optical response of GEO 600

2.1. Introduction

The derivation of the differential Michelson error-signal yielded by the Schnupp modulation technique (Section 1.2.4) makes it clear that the signal amplitude generated by a gravitational wave in a simple Michelson interferometer will be very faint. To enhance this amplitude with the given detection technique, various optical detector designs were developed and compared (see for example [Mizuno95]) and there are continuously new ideas developing [Mizuno97, Harms03, Freise03a]. But even with a certain given optical configuration, it is important to know the crucial criteria to globally optimise the sensitivity of the final setup.

In general, there are mainly two contributions to the sensitivity: the optical gain of the output signal and the noise sources contaminating the detection. The optical gain is equivalent to the slope of the targeted error-signal that determines how visible some gravitational wave signal may become in principle.

The ability, though, to see nothing but a real gravitational wave, depends on whether the overall noise shows up in the output at a comparable level. Possible sources are:

- **Seismic noise:** The ground vibrates, always. Causes can be human-made, like traffic, machines, experimentalists or animals running around, but there is also natural ground motion due to earth tides, earthquakes or the surf of the sea. This motion causes an uncorrelated displacement of the test masses which produces a spurious signal at the detector output.
- **Thermal noise:** All optical components and their suspensions (or mounts) are subject to thermal fluctuations. The Brownian motion, associated with the temperature of the mirrors or suspensions (or mounts), excites motions of mirror surfaces or the mirrors themselves. The dissipation channels are internal friction, and thermal expansion in combination with thermal conduction. These motions affect the light phases similarly to gravitational waves.
- **Thermo-refractive noise:** The refractive index of optical components is temperature dependent. Temperature fluctuations will thus cause a varying optical pathlength of the light, impinging on mirror surfaces, or passing substrates, like that of the beamsplitter.

- **Shot noise:** The detection process of light power is equivalent to counting photons. Their arrival time is Poisson distributed. These power fluctuations, apparent at every photodiode, are indistinguishable from gravitational-wave signals.
- **Photon pressure noise:** Every photon reflected by a mirror at the same time exchanges momenta with the mirror mass. The laser power inside the Michelson arms generates on average a constant radiation pressure force on the mirrors that slightly changes their equilibrium position. However, photons that appear at the dark port due to vacuum fluctuations, enter the Michelson, and differentially beat with the carrier originating from the bright port. These beats cause differential power fluctuations in the two arms, thus a differential motion of the respective mirrors. This, like seismic mirror motion, competes with gravitational waves.

All non-optical noise sources change the effective pathlength of the light inside the Michelson interferometer¹. Their characteristic frequency regime depends rather on mirror and suspension properties, and only partially on the optical setup itself. Figure 2.1 relates the respective pathlength change of some particular noise sources². to the corresponding differential test mass displacement in GEO 600. The linear spectral density of the displacement is already related to the length of the Michelson arms, and thus given in $[1/\sqrt{\text{Hz}}]$, corresponding to the dimensionless space-time strain, $h = 2\delta L/L$, caused by a gravitational wave.

The specific optical setup of the detector sets not only the optical noise level (omitted in Figure 2.1), but also determines the transfer of gravitational-wave signals to the output photodiode. This transfer may well be frequency dependent such that gravitational waves of same amplitude but different frequencies yield different photo-current amplitudes. In relating the white shot noise appearing at the photodiode, back to the equivalent gravitational wave amplitude or strain, one needs to account and compensate for the frequency dependent signal enhancement of the optical system. The ratio of the expected shot noise to the optical signal transfer sets the *shot-noise-limited sensitivity*. In order not to waste any of the possible sensitivity, the optical setup should ideally enhance the signal as much as necessary for the shot-noise-limited sensitivity to follow the total noise curve given by the other sources. For GEO 600, this corresponds to the dashed line in Figure 2.1.

With the currently available laser power and the technically limited size of a plain Michelson interferometer, the shot-noise-limited sensitivity is orders of magnitude away from the target. However, there exist various optical techniques to improve the shot-noise-limited sensitivity.

At the beginning of this chapter, the optical techniques, incorporated in GEO 600, will be motivated and explained. The expected characteristics of the differential output signal of GEO 600 will then be discussed applying the phasor picture. This will stress the role of the demodulation phase on the sensitivity and the connection between detector tuning and the real peak sensitivity of the optical instrument. Special attention will

¹So does the radiation pressure noise, but it shall not be accounted for in the following.

²For the estimation of the substrate thermal noise shown in Figure 2.1, a mechanical quality factor of 5×10^6 is assumed for the fused silica mirrors and the beamsplitter. Recent research, however, indicates that this value may be more than an order of magnitude higher [Ageev04, Penn].

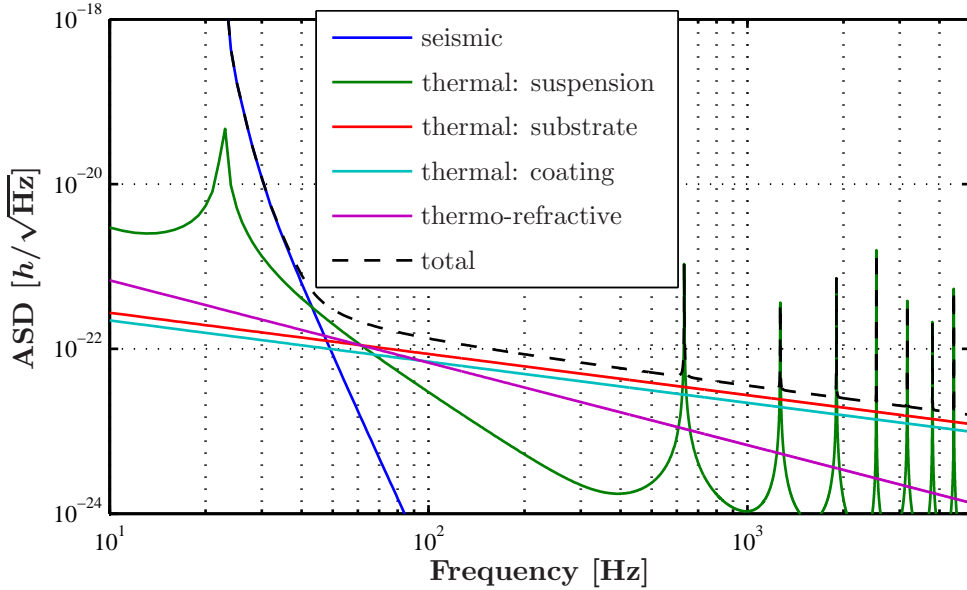


Figure 2.1.: Theoretical noise budget of GEO 600, accounting for non-optical noise sources. The anticipated pathlength change is given as amplitude spectral density of the equivalent strain.

be given to possibilities of globally optimising the signal yield in the shot noise limited SNR , dependent on the control sidebands' resonance condition inside the interferometer. Radiation-pressure effects are not accounted for.

2.2. Techniques to enhance the sensitivity

The error-signal received at the south port gives a measure for the Michelson deviation from the perfect dark fringe state, thus a measure for the strength of the gravitational wave (see Section 1.2.4). The question to discuss is how this signal amplitude can be enhanced to yield a higher sensitivity for the weak ripples of space-time.

A passing gravitational wave will alter the phases of the carrier as shown in Figure 1.15, with a given frequency $\omega_{GW} = 2\pi f_{GW}$. This phase modulation can therefore be pictured in the form of sidebands around the carrier with a frequency offset ω_{GW} . These sidebands associated with the gravitational wave will henceforth be called *signal sidebands*. As obvious from the derivation made with Figure 1.15, the error-signal amplitude scales with the gravitational wave strength, i.e., the signal sideband amplitude $\sqrt{P_{GW}}$, and with the control sideband amplitude, $\sqrt{P_m}$,

$$I_{\omega_m} \propto \sqrt{P_{GW}P_m}. \quad (2.1)$$

For the sensitivity to gravitational waves, however, the SNR is crucial, as the real gravitational wave signal is contaminated by the different noise sources present at the detector output. For the following estimations of SNR , only shot noise will be considered as this is the relevant noise source when optimising the signal yield with respect to the control sideband properties. It is proportional to the square-root of the whole amount of light at the photodiode. This light covers not only all sidebands³ but also some waste light P_{waste} , coming from imperfections of the optical system like asymmetries at the beamsplitter or from losses of the different Michelson arms. Altogether this gives

$$SNR \propto \frac{\sqrt{P_{\text{GW}} P_{\text{m}}}}{\sqrt{P_{\text{m}} + P_{\text{waste}}}} \approx \sqrt{P_{\text{GW}}} \quad \text{for } P_{\text{m}} \gg P_{\text{waste}}. \quad (2.2)$$

If a certain amplitude of control sidebands is at disposal, only the signal sidebands' amplitude matters. There are two possibilities to enhance these signal sidebands:

- Directly increase the signal sidebands by placing a mirror at the south port which reflects the light back into the Michelson interferometer. This technique is called *signal recycling*. The signal sideband amplitudes can, when on resonance, constructively accumulate inside this so-called *signal-recycling cavity*, built by the Michelson interferometer and the *signal-recycling mirror* (**MSR**).
- The larger the carrier the stronger the sidebands. There are two ways to enhance the carrier power:
 - As with a dark fringe, the carrier is completely reflected back to the west port, a mirror at the input port, building the *power-recycling cavity* together with the Michelson interferometer, can resonantly enhance the carrier power. Consistently, this technique is called *power recycling* and the mirror is called *power-recycling mirror* (**MPR**).
 - The generation of control sidebands attenuates the carrier power. Minimising the modulation index helps to conserve as much of the carrier as possible. Nonetheless, a method to have a decent sideband amplitude for the error-signal is to choose an appropriate frequency to resonate in one of the cavities. As the signal-recycling cavity properties, like detuning and finesse, are geared to special gravitational wave sources and might change during operation, the frequency offset of the Michelson control sidebands from the carrier is chosen to be about a multiple of the FSR of the power-recycling cavity.

Up to now, GEO 600 is the only large-scale gravitational-wave detector worldwide employing both interferometric techniques. In combination, they are called *dual-recycling*. The dual-recycled Michelson interferometer setup of GEO 600 is shown in Figure 2.2.

³The signal sidebands can, however, be neglected due to their anticipated small amplitude.

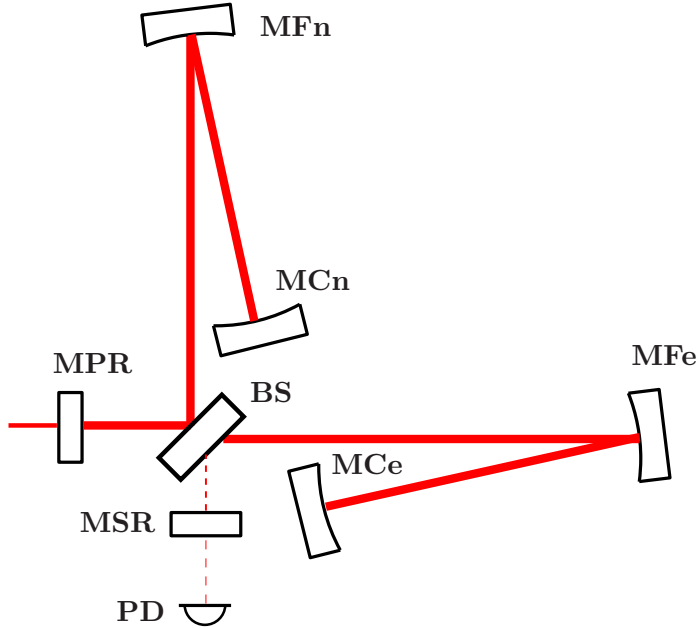


Figure 2.2.: The setup of the dual-recycled Michelson interferometer of GEO 600. The Michelson arms are folded once to double the optical path lengths. A control system (not shown) ensures a dark-fringe condition of the Michelson. At the west port, the power-recycling mirror (**MPR**) forms a cavity with the Michelson to enhance the carrier power. At the south port, the signal-recycling mirror (**MSR**) reflects the signal sidebands back into the interferometer, resonantly enhancing them inside this signal-recycling cavity.

Signal recycling with different tunings

Different types of sources of gravitational waves radiate with various frequencies and waveforms. A supernova explosion generates broadband waves whereas pulsars, for example, excite the space-time with one very particular frequency. With the current gravitational-wave detectors it is impossible to consider all sources equally at one time with the best sensitivity.

The signal-recycling cavity will, for example, only enhance gravitational wave frequencies in a certain band around the respective resonance. Targeting different gravitational wave sources requires, therefore, different resonant frequencies (wide bandwidths will again attenuate the maximally possible sensitivity [Mizuno95]). This is achieved by tuning the microscopic signal-recycling cavity length, for example with the microscopic position of **MSR**. If the signal-recycling cavity is resonant with the carrier frequency, the detector is called *tuned*, otherwise it is called *detuned*⁴.

⁴Nonetheless, if, for example, the signal-recycling cavity is detuned to resonate with signals of particular frequency f_{res} , the idiomatic expression of the detector being “tuned to f_{res} ” will be used.

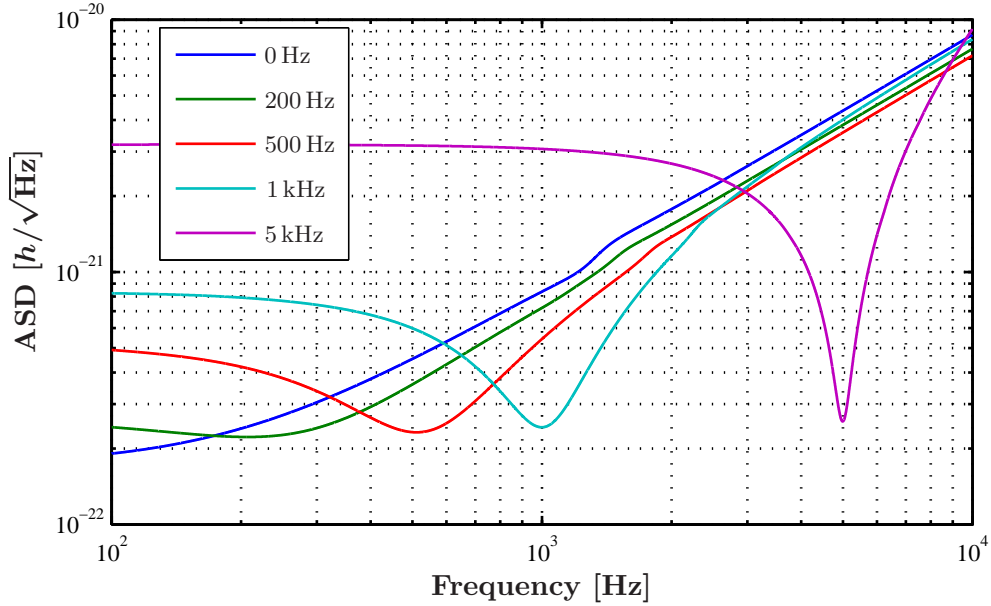


Figure 2.3.: Amplitude spectral density of the shot noise limited sensitivity for particular detunings of the signal-recycling cavity. Whereas the shot noise is constant for all frequencies, the signal sidebands get enhanced inside the cavity. Thus, relating the noise to detectable strain h , one obtains inverted Airy-function curves. All graphs were calculated for ≈ 1.3 kW at **BS**, and **MSR** reflectivity of 98.14%. However, the best sensitivity value of the tuned and 200 Hz detuned cases are superior to the other tunings.

Figure 2.3 shows the theoretical shot noise limited sensitivity of the actual dual-recycled GEO 600 setup, with the signal-recycling cavity being resonant with the carrier frequency, and with four tuning offsets from carrier resonance, maximising the signal sidebands at audio frequencies of 200 Hz, 500 Hz, 1 kHz and 5 kHz. As the shot noise is constant for all frequencies but gets related to the equivalent strain of a possible gravitational-wave signal, the sensitivity curves progress like inverse Airy-functions⁵. Although the mirror setup does not change, the best sensitivity value improves the smaller the detuning. At detunings higher than the signal-recycling cavity bandwidth, effectively only one signal sideband gets enhanced; the amplification of the other sideband increases with decreasing detector tuning.

⁵The humps above 1 kHz appear because of carrier beats with the signal sidebands around the control sidebands (see also the explanations on Page 72 about Figure 2.21, and Section 4.4).

2.3. GEO 600 response in terms of phasors

2.3.1. Sideband resonances for different detector tunings

The examples of error-signal generation in Section 1.2 ff. mainly dealt with symmetric constellations concerning the phase and amplitude evolutions of light components. With a detuned detector, however, this symmetry is broken, giving rise to special parameters of light fields that need to be considered for all error-signals and especially the detector sensitivity.

To investigate the properties of all frequency components contributing to the Michelson error-signal, the expected phases and amplitudes will be derived starting from the phasor relations of a simple Michelson interferometer around a dark fringe, as shown in Figure 1.15. There is only one difference that needs to be kept in mind:

Figure 1.15 represents a white light interferometer. GEO 600, however, has a macroscopic armlength difference of $\Delta L_{\text{Schnupp}} = 50.5 \text{ mm}$, yielding an overall optical path-length difference between both arms of $2\Delta L_{\text{Schnupp}} = 101 \text{ mm}$. Therefore, the control sideband phasors will qualitatively always look the same as in the off-dark-fringe state, even if the Michelson has a dark fringe for the carrier.

Applying power-recycling at the west port will, in the ideal case of carrier resonance, not change any qualitative phase feature of neither the carrier nor the control sidebands at any Michelson port.

As the light fields enter the cavity through **MPR**, their phases will commonly be shifted by 180° . Thus, this phase shift can be neglected (see Section 1.2.1). Because of the cavity resonance, the fields interfere constructively. This enforces the phases of the sum phasors to be the same as of all partial beams, w.l.o.g. to that of Figure 1.15. The amplitudes are enhanced by the maximal gain factor of the cavity⁶. These phase and amplitude considerations hold for all Michelson ports.

The detuning of the signal-recycling cavity can be adjusted to match a targeted signal frequency. Therefore, the particular resonance condition of each field inside this cavity needs to be considered when evaluating the fields at the south port behind **MSR**. To obtain the power build-up and transmission phase shift for each contributing field component, the position of the respective frequency on the frequency axis, with respect to the signal-recycling cavity resonance structure, needs to be known. Figure 2.4 shows the qualitative, frequency-dependent amplitude and phase change of a light field that passes the signal-recycling cavity. The figure covers three different cavity tunings. In all cases, the carrier and the control sidebands are assumed to be resonant inside the power-recycling cavity.

⁶With the current FINESSE script representing GEO 600, given in Appendix B.1.1, the power-recycling gain is roughly one order of magnitude higher for the carrier than for the sidebands, ~ 800 versus ~ 110 , respectively, as for the sidebands the dark fringe condition of the Michelson is not ideal. The Schnupp length and losses inside the Michelson lead to a Michelson reflectivity of 99.855% and a transmission of 280 ppm for the Michelson control sidebands, whereas it is 99.884% and 8×10^{-3} ppm, respectively, for the carrier.

The first row represents a tuned signal-recycling cavity. The second and third demonstrate a positively detuned signal-recycling cavity (see Section 1.2.1). The 1 kHz and 5 kHz detunings are distinct examples for one or no control sideband being resonant inside the signal-recycling cavity, respectively. In the case of GEO 600, the FSR of the signal-recycling cavity is chosen to be smaller than that of the power-recycling cavity by roughly 10 Hz, and the frequency offset of the control sideband from the carrier is $\pm 119 FSR_{PR}$, indicated by the magenta, dashed-dotted vertical lines at $\pm 119 FSR_{PR}$ on the frequency axis. 0 Hz (black, dashed vertical line) stands for the carrier frequency.

The phases and amplitudes evolve, depending on the **MSR** tuning, qualitatively like in Figure 1.12. Due to the particular phase conventions summarised in Section 1.2.1, the phase transfer from the cavity input to the transmitted output is, except for bandwidth, exactly the same as from the light at the south of the beamsplitter, *without MSR*, to the light behind **MSR**, with an existing signal-recycling cavity.

In the case of the carrier and the control sidebands being on resonance, the partial phasors of each will again add up most ideally, sustaining the phasors' phases inside the signal-recycling cavity (i.e. 0° phase shift). The additional 180° by passing through **MSR** to the photodiode, is common and may again be neglected.

Please note that the signal-recycling cavity bandwidth is wider for the control sidebands than for the signal sidebands.

Due to the macroscopic armlength difference ΔL_{Schupp} , the Michelson is partially transmitting for the control sidebands when it is at the dark fringe condition for the carrier. With the resonance condition inside the power-recycling cavity, the amount of control sidebands in the south will be enhanced as well. Because of energy conservation, the effective reflectivity of the resonant power-recycled Michelson interferometer — being the compound input mirror to the signal-recycling cavity — is less than that of the pure Michelson.

This is different for the signal sidebands. The (almost) perfect reflection of the pure Michelson interferometer for the signal sidebands rules out any effect of the power-recycling cavity.

2.3.2. The Michelson error-signal with signal sidebands

As already mentioned in Section 2.2, the carrier appearing in the south due to the gravitational wave of frequency f_{GW} can be expressed by two sidebands with an offset of $\pm f_{GW}$ from the carrier frequency. To get I_{ω_m} as in Equation 1.23, b_0 will be split into the sum of b_+^{GW} and b_-^{GW} , necessitating four summands per component which are the scalar product of each control sideband with each signal sideband.

In order not to lose any information about I_{ω_m} , regarding the control sidebands, two linearly independent sidebands, P and Q, needed to be considered. It is the same for the signal sidebands: the sensitivity estimate is only complete if two perpendicular components are considered, i.e., a sinusoidal carrier phase modulation with an initial phase of 90° as well as 0° . To distinguish these orthogonal signal sideband situations from the

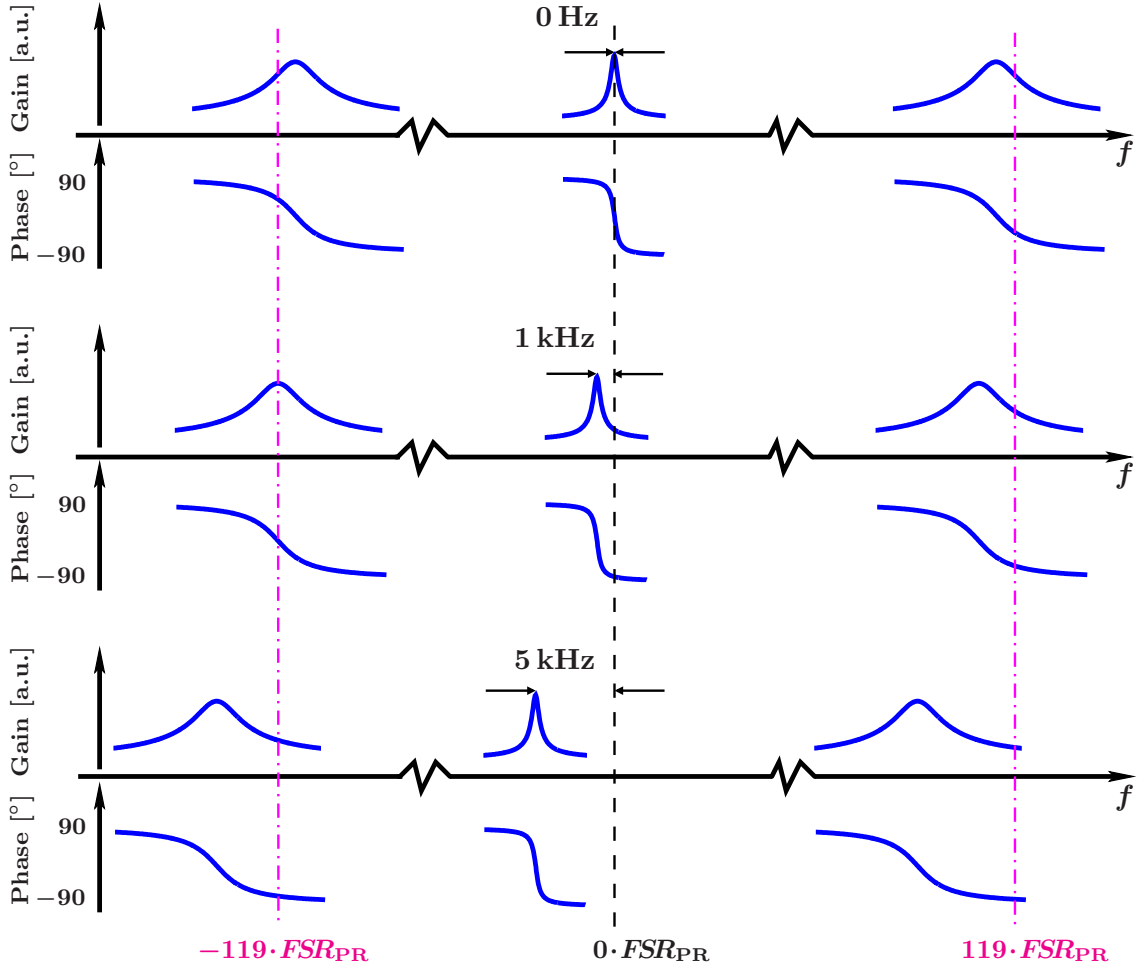


Figure 2.4.: The resonance conditions of the Michelson control sidebands inside the signal-recycling cavity for three different tunings, 0 Hz, 1 kHz and 5 kHz. The control sidebands are assumed to be located around the carrier at the ± 119 th multiple of FSR_{PR} ; the carrier and sideband frequencies are indicated by the dash-dotted vertical lines. For each tuning, the upper blue graphs represent the qualitative amplitude enhancement due to the signal-recycling resonance condition, the lower curves the dispersive phase shift. FSR_{SR} is smaller than FSR_{PR} by approximately 10 Hz. Thus, the resonance structure in the tuned detector is for both sidebands symmetrically shifted towards the carrier frequency. Detuning the detector moves the rigid comb of resonance structures (blue solid curves) against the fixed comb of light frequencies (black dashed, and magenta dashed-dotted lines). For a detuning of roughly 1 kHz, the lower control sideband resonates inside the signal-recycling cavity. The bandwidth of the signal-recycling cavity differs for the carrier (and signal sidebands closely around) and the control sidebands due to the different reflectivities of the compound (input) mirror formed by the power-recycled Michelson.

control sidebands, the cosine and sine signal sidebands will henceforth be called *C* and *S sidebands*, respectively. This yields a vector for each component of I_{ω_m} , $(I_{PC}, I_{PS})^T$ for the in-phase component regarding the control sidebands, and $(I_{QC}, I_{QS})^T$ for the corresponding in-quadrature component:

$$I_{\omega_m} \hat{=} \begin{pmatrix} I_P \\ Q \end{pmatrix} = \begin{pmatrix} I_{PC} + i I_{PS} \\ I_{QC} + i I_{QS} \end{pmatrix} \hat{=} \begin{pmatrix} \begin{pmatrix} I_{PC} \\ I_{PS} \end{pmatrix} \\ \begin{pmatrix} I_{QC} \\ I_{QS} \end{pmatrix} \end{pmatrix} = \dots \quad (2.3)$$

$$\dots = \begin{pmatrix} \begin{pmatrix} b_+^{\text{GW}} \otimes (b_+ + b_-) + b_-^{\text{GW}} \otimes (b_+ + b_-) \\ (e^{-i\frac{\pi}{2}} b_+^{\text{GW}}) \otimes (b_+ + b_-) + (e^{i\frac{\pi}{2}} b_-^{\text{GW}}) \otimes (b_+ + b_-) \end{pmatrix} \\ \begin{pmatrix} b_+^{\text{GW}} \otimes (e^{-i\frac{\pi}{2}} b_+ + e^{i\frac{\pi}{2}} b_-) + b_-^{\text{GW}} \otimes (e^{-i\frac{\pi}{2}} b_+ + e^{i\frac{\pi}{2}} b_-) \\ (e^{-i\frac{\pi}{2}} b_+^{\text{GW}}) \otimes (e^{-i\frac{\pi}{2}} b_+ + e^{i\frac{\pi}{2}} b_-) + (e^{i\frac{\pi}{2}} b_-^{\text{GW}}) \otimes (e^{-i\frac{\pi}{2}} b_+ + e^{i\frac{\pi}{2}} b_-) \end{pmatrix} \end{pmatrix} \quad (2.4)$$

P and Q in Equation 2.3 refer to in-phase and in-quadrature control sidebands, respectively, C and S to in-phase and in-quadrature signal sidebands, respectively. In the term 2.4, \otimes is again the operation between complex numbers equivalent to the scalar product of their phasor representatives. I_P and I_Q will equivalently be used for the complex numbers as well as for their respective vectorial counterpart.

Focussing on the transfer function from signal sidebands to I_{ω_m} , demodulated with a particular demodulation phase Φ , the operation

$$I_{\omega_m} e^{-i\Phi} = I_P \cos \Phi + I_Q \sin \Phi$$

(equivalent to Equation 1.18) maintains amplitude and phase information for the signal throughput. In judging the sensitivity, the absolute value of this transfer function will be crucial. Therefore, each component I_P and I_Q can be represented by its absolute value or vector length $\sqrt{I_{PC}^2 + I_{PS}^2}$ and $\sqrt{I_{QC}^2 + I_{QS}^2}$, respectively⁷.

The way to go is to combine and project all four sideband components separately, each in-phase and in-quadrature for both, control and signal sidebands. Determining I_P and I_Q sets the two components of I_{ω_m} . With this vector, principal characteristics and dependencies of the sensitivity can be investigated.

The procedure will be layed out in the following chapters, discussing the particular examples of detector tunings from Figure 2.4 in more detail.

⁷As in FINESSE the shot noise is equal in all quadratures, a quadratic summation of two quadratures is in principle equivalent to a frequency-dependent choice of a demodulation phase achieving a maximum error-signal. Instead of yielding the complete I_{ω_m} vector length as in the two-dimensional projection pictures applied before, however, the procedure is here applied separately to each P and Q component of I_{ω_m} .

A quadratical summation of the (remaining) P and Q quadratures (or, in the end, of all four quadrature components of I_{ω_m}), though, might not achieve the best *SNR* in the experiment: some noise sources appear differently in the P and Q quadratures, particularly in phase. With an appropriate choice of demodulation phase, the noise may ideally cancel at particular frequencies (see Section 4.4). Currently, the shot noise is accounted for in the experimental weighting of P and Q for $h(t)$ (see [Hewitson04b]).

2.3.3. Tuned detector

Figure 2.5 qualitatively shows the phasors of all light fields contributing to the differential Michelson error-signal. The phasor diagrams comprise three different gravitational wave signal frequency regions, indicated on the left. The particular quadrants of the figure, separated by the dashed black lines, account for the different quadratures of the signal and control sidebands. The pictures are arranged as follows: on the left, the signal sidebands for a cosine gravitational wave are shown (C), on the right for a sinusoidal gravitational wave (S). The upper three rows stand for resonant, slightly off-resonant and largely off-resonant signal sidebands beating with the in-phase control sidebands (P). In the lower three the same signal sidebands beat with the in-quadrature control sidebands (Q).

To comprehend the phasors, the upper left figures will be explained in detail while for the others only relevant new features, necessary for the understanding, will be accounted for.

Starting points are the resulting P phasors at the south port of the Michelson interferometer, as shown in the lower right corner of Figure 1.15. Figure 2.4 instructs how to alter these initial phasors: the control sidebands are symmetrically off-resonant from the signal-recycling cavity, therefore the lower sideband phase rotates clockwise by a certain amount, the upper, anti-clockwise by that same value.

To obtain more convenient control sideband phasor angles, the “snapshot” may be made even earlier in time to conceive an overall lower and upper P sideband rotation of -90° and $+90^\circ$, respectively, of the phasors shown in Figure 1.15 in Section 1.2.4 (see the conventions summarised in Section 1.2.1): as a sideband phasor evolution in time is equivalent to a rotation of the coordinate axes of the photo-current vector space, this will only introduce an offset in the pointing of I_{ω_m} within this ortho-normal basis, or an offset in the demodulation phase (see in particular Equation 1.25). The (equal) amplitudes of the two control sidebands, and of I_{ω_m} , remain untouched by this time evolution.

The signal sidebands may have arbitrary frequencies. Depending on the particular frequency value, their amplitudes and phases get changed by the signal-recycling cavity as indicated by the blue graphs centered around or close to $0 \cdot FSR_{PR}$ in Figure 2.4. For the tuned detector case, the upper most graphs need to be considered.

To deal with the resonant case of the signal sidebands, let us assume a very low frequency, but not exactly 0 Hz. (Their position on the frequency axis of Figure 2.5 is only of symbolic substance.) The resonant sidebands are equally enhanced and remain unrotated in the C quadrature such that they become anti-parallel to the control sidebands. Beating each control with each signal sideband produces a “double-in-phase” contribution to the overall signal

$$I_{PC, \text{res}} = -4 |b_+^{\text{GW}}| \cdot |b_+|,$$

as $|b_+| = |b_-|$, and $|b_+^{\text{GW}}| = |b_-^{\text{GW}}|$.

Off-resonant signal phasors are, in the tuned signal-recycling cavity case, symmetrically arranged around the resonant carrier frequency.

Slightly off-resonant ($f_{\text{GW}} > 0 \text{ Hz}$), the signal sidebands are less amplified compared to the resonant case above. The upper signal sideband phase decreases while the lower increases by the same amount. This rotation, together with the weaker amplitude enhancement, reduces the amount of signal detected in the south port to

$$I_{\text{PC,off}} = 4 \cdot (b_+^{\text{GW}} \otimes b_+) = -4 b_{+,||}^{\text{GW}} \cdot |b_+|, \quad (2.5)$$

with the index \parallel indicating the absolute value of b_+^{GW} component parallel to b_+ .

In the largely off-resonant case ($f_{\text{GW}} \gg 0 \text{ Hz}$), the signal sidebands are very much attenuated. In addition, they are anti-parallel to each other and perpendicular to the control sidebands giving no signal at all after demodulation.

In the figure quadrant below, the signal sidebands are the same, but the control sidebands are evolved by a quarter period making them anti-parallel to each other such that they constantly cancel any beat.

On the upper right, the signal sidebands represent a situation a quarter of the gravitational wave period earlier. In case of resonance, the S sidebands are maximally increased, but point to opposite directions on the imaginary axis such that they cancel each other. The control sidebands are in-phase, so parallel to each other, but perpendicular to the signal sidebands. (So even if the signal sidebands did not cancel, there would be no error-signal contribution.)

Slightly off-resonant, the sideband amplitudes are less enhanced, but inversely rotated. This enables us to sense the other component of each sideband, with respect to the situation on the left (as the sidebands are rotated by $\pm 90^\circ$) giving

$$I_{\text{PS,off}} = 4 \cdot \left[\left(e^{-i\frac{\pi}{2}} b_+^{\text{GW}} \right) \otimes b_+ \right] = 4 b_{+,\perp}^{\text{GW}} \cdot |b_+|. \quad (2.6)$$

\perp indicates, alike the index \parallel , the absolute value of the C phasor component with respect to the P phasors, as represented on the upper left of Figure 2.5 (see also Section 1.2.1). This means, $b_{+,\perp}^{\text{GW}}$ and $b_{+,||}^{\text{GW}}$ are fixed, orthogonal components of the particular sideband b_+^{GW} (perpendicular and parallel, respectively). The scalar numbers stay the same even if the sideband quadrature changes (i.e., they rotate with the signal phasor). Thus, in the PC quadrant of Figure 2.5, the signal-sideband component referring to the control sidebands amounts to $b_{+,||}^{\text{GW}}$, whereas in the PS quadrant it is $b_{+,\perp}^{\text{GW}}$ which is the part of that signal sideband currently parallel to the control sidebands. In particular, $\sqrt{b_{+,||}^2 + b_{+,\perp}^2} = |b_+|$.

Largely off-resonant, the control and the signal sidebands become parallel, perfectly detecting the complete signal amplitude. This is, however, very much attenuated such that the resulting error-signal is small.

The figures below show the same signal sidebands with the Q control sidebands who again permanently cancel every possibly occurring beat.

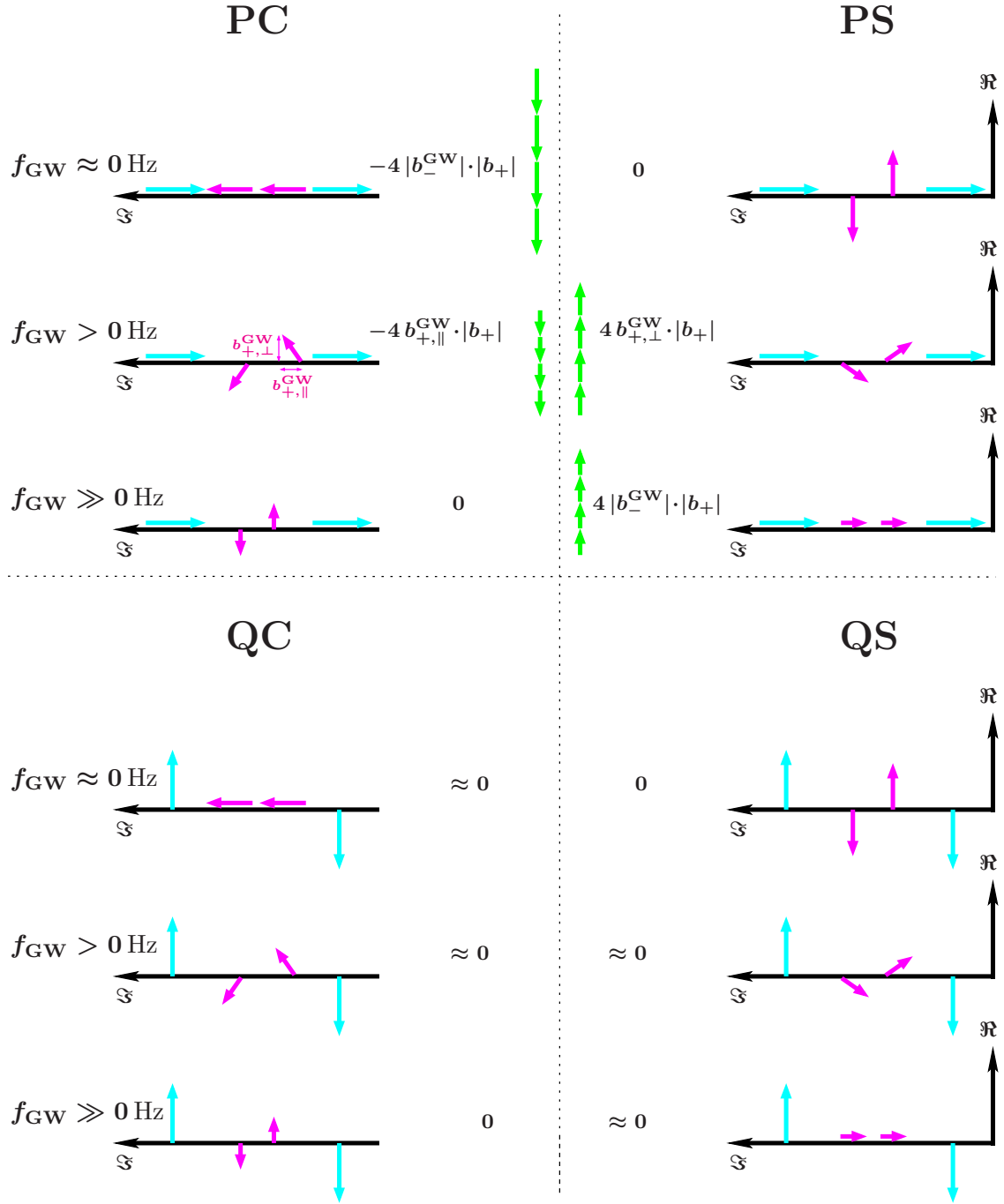


Figure 2.5.: Phasors at the south port of a tuned dual-recycled Michelson interferometer: the figure is split into four parts, combining the contributing phasors in all possible quadratures with each other. The figure quadrants are captioned with the corresponding quadrature combination. Each quadrant is again subdivided into three rows, accounting for different frequency regions of the signal sidebands. The result of all projections is displayed as the green vectors and the corresponding terms in the middle of the figure.

Putting everything together, the best obtainable SNR can be determined separately for every frequency region by evaluating $|I_{\omega_m}|$ as given in Equation 2.4, and normalising with the occurring shot noise, $\sqrt{|b_+|^2 + |b_-|^2}$. It will for all frequency regions amount to

$$SNR \propto \frac{4 |b_+^{GW}| \cdot |b_+|}{\sqrt{2} |b_+|} = 2\sqrt{2} |b_+^{GW}|, \quad \forall f_{GW} \quad (2.7)$$

yielding the complete signal amplitude. Thus, the sensitivity decreases by the same amount as the Airy-function for the signal sideband amplitude. Due to the phase symmetry of the control sidebands, the signal for all frequencies fully appears in one control sideband quadrature only, but the signal content moves from the C quadrature to the S quadrature for increasing f_{GW} . This highlights once again the necessity of considering both signal quadratures for the detector sensitivity.

2.3.4. Detuned signal recycling at 5 kHz

For the phasor picture explaining the detector response with 5 kHz detuning, again the amplitudes and phases of the phasors of Figure 1.15 should be combined with the gain and dispersion curves given in Figure 2.4. For the situation of 5 kHz detuning, both control sidebands are on the positive frequency side of the resonance. Therefore, their relative amplitudes and phases will roughly remain the same, causing the P sidebands to be the one who cancel and the Q sidebands to remain parallel with same amplitude. This is displayed in Figure 2.6, which is arranged in the same way as Figure 2.5: the upper half is dedicated to P, the lower to Q control sidebands, the left figures deal with cosine gravitational waves, the right with sine waves. Unlike Figure 2.5, the three gravitational-wave signal frequency regions cover low frequencies, resonance and high frequencies.

As the upper projections all obtain roughly zero because of the canceling control sidebands, only the lower ones will be commented on. The cosine signal sidebands on the left-hand side are, at low frequencies, both parallel to each other and the Q control sidebands, as all of them are positively detuned from cavity resonance. Passing the resonance corresponds for the lower and upper signal sideband to a decrease and increase of frequency, respectively. The properties of the upper signal sideband thus don't change significantly as it moves on the "wing" of the resonance curve. The lower sideband changes lengths and phase with respect to the cavity transfer function. What becomes obvious is that for low frequencies, all signal is gathered from the cosine signal form, while for resonance the sinusoidal signal is crucial. First neglecting the contribution of the upper sideband because of its faint amplitude, the initial cavity bandwidth and resonance frequency are conserved in the SNR ,

$$SNR_{b_-^{GW}} \propto \frac{2 |b_-^{GW}| \cdot |b_+|}{\sqrt{2} |b_+|} = \sqrt{2} |b_-^{GW}|, \quad \forall f_{GW}. \quad (2.8)$$

However, accounting for the upper sideband, the response shape gets distorted towards lower frequencies. This distortion also changes the frequency position of maximum sensitivity to lower frequencies.

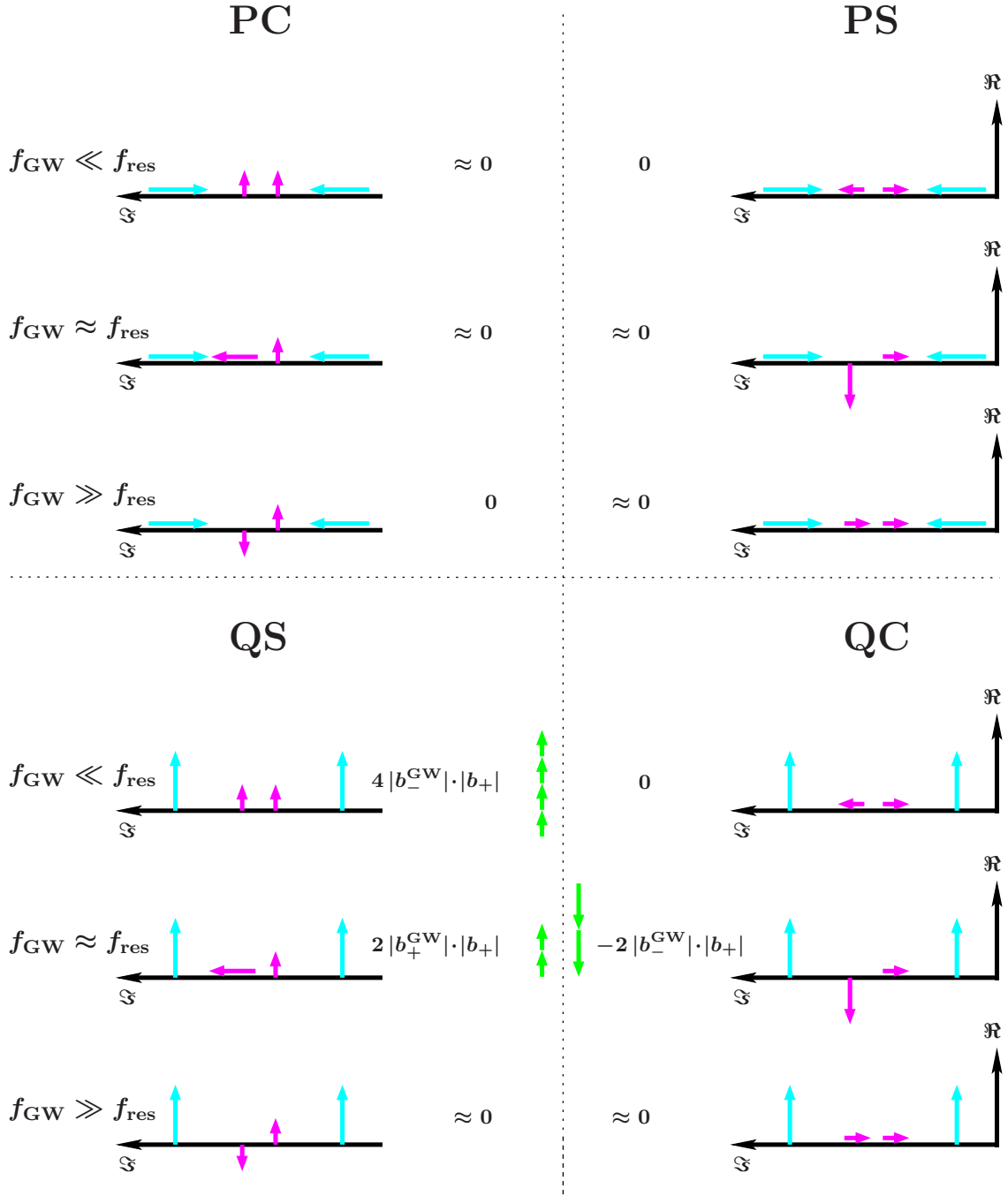


Figure 2.6.: Phasors at the south port of a dual-recycled Michelson interferometer, detuned by 5 kHz: the four sub-figures again combine the contributing phasors in all possible quadratures with each other. This time, the three rows of each quadrant display the frequency regions of the signal sidebands of low, resonant, and high frequency. Obviously, the signal is completely contained in Q. The yield of the signal is optimal at low frequencies. At high frequencies, though, the detector’s sensitivity is very poor.

For the sake of view, all projection results are vertically oriented, although in a two-dimensional coordinate system, the projections in Q yield imaginary, thus, “horizontal” components of I_{ω_m} .

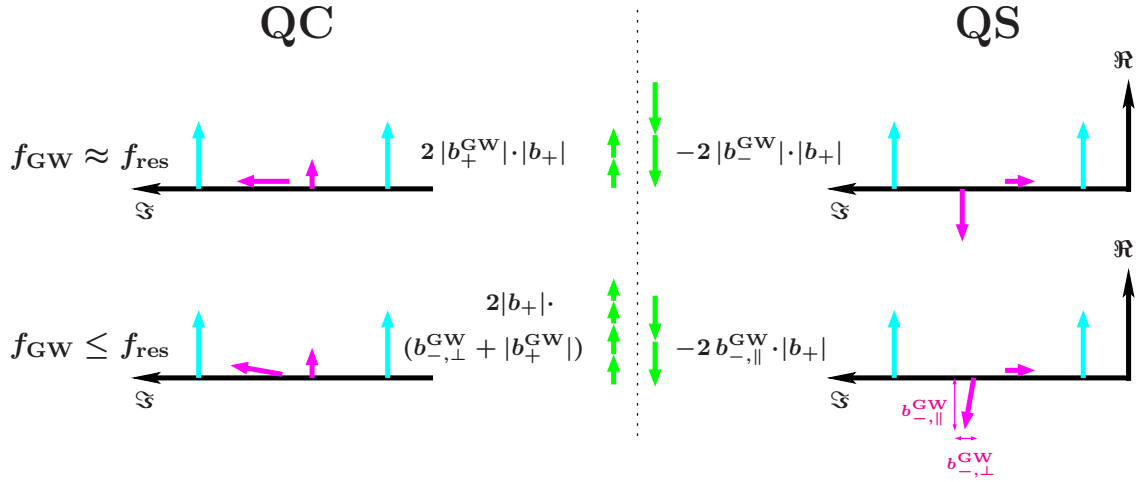


Figure 2.7.: Phasors belonging to I_Q around the signal sideband resonance inside the signal-recycling cavity. The upper row shows the exact resonance, whereas in the lower row the signal sideband frequency is slightly below resonance. $b_{-, \perp}^{\text{GW}}$ and $b_{-, \parallel}^{\text{GW}}$ again denote the components of the C signal phasor and refer to the control sidebands in P. (This is equivalent to referring S signal phasors to control sidebands in Q.)

This gets plain with the following comparison of exact signal sideband resonance inside the signal-recycling cavity, with slight off-resonance towards lower frequencies. These two situations are depicted in Figure 2.7. The SNR occurring on the photodiode will be made up of the components I_{QC} and I_{QS} , at resonance amounting to

$$SNR_{\text{res}} \propto \frac{\sqrt{(2|b_+^{\text{GW}}| \cdot |b_+|)^2 + (2|b_-^{\text{GW}}| \cdot |b_+|)^2}}{\sqrt{2|b_+|^2}} = \sqrt{2} \sqrt{|b_+^{\text{GW}}|^2 + |b_-^{\text{GW}}|^2}. \quad (2.9)$$

Slightly off-resonant, the amplitude of the lower signal sideband, $|b_-^{\text{GW}}|$, is roughly constant, while the phase changes rapidly. Therefore, b_-^{GW} will be made up of two components, $b_{-, \parallel}^{\text{GW}}$ and $b_{-, \perp}^{\text{GW}}$. Like in Section 2.3.3, \parallel and \perp define the absolute value of the C signal sideband component parallel and perpendicular to the P control sidebands, respectively, as displayed in the first quadrant of Figure 2.6. The SNR will be

$$SNR_{\text{off}} \propto \sqrt{2} \sqrt{(b_{-, \perp}^{\text{GW}} + |b_+^{\text{GW}}|)^2 + b_{-, \parallel}^{\text{GW} 2} = \sqrt{2} \sqrt{|b_-^{\text{GW}}|^2 + |b_+^{\text{GW}}|^2 + 2b_{-, \perp}^{\text{GW}} \cdot |b_+^{\text{GW}}|}. \quad (2.10)$$

This is bigger than SNR_{res} if $|b_+^{\text{GW}}| \neq 0$ and the lower sideband amplitude, $|b_-^{\text{GW}}|$, is not too much attenuated compared to resonance.

As a consequence, when determining the exact tuning of the signal-recycling cavity (e.g. to compare simulation with experiment), the maximal SNR only indicates the rough **MSR** position. The necessary deviation for an exact match of sensitivity depends on the detector tuning and the particular control sideband frequency. In this example, though, the peak is only shifted by ~ 1 Hz.

2.3.5. Detuned signal recycling at 1 kHz

With this last example of tuning, a new peculiarity appears: one of the control sidebands becomes resonant inside the signal-recycling cavity (see the middle row of Figure 2.4), whereas the other is off resonance, but still close to the bandwidth of ~ 1 kHz. Due to this, neither of the P and Q sidebands are negligible nor do they cancel being ideally anti-parallel. Figure 2.8 shows the in-phase and in-quadrature phasors of the control and signal sidebands similarly to Figure 2.6, i.e., for three signal frequency regions. They are again deduced by applying the resonance condition indicated in the middle row of Figure 2.4 to the phasors of Figure 1.15.

All sidebands except for the upper control sideband are purely real or imaginary. This time, the signal sidebands will, for convenience, serve as the reference projection phasors for the control sidebands in the sense that the components of the upper control sideband, $b_{+,\parallel}$ and $b_{+,\perp}$ are defined based on the low frequency (DC) phasors of the gravitational wave signal in C. Thus, these components coincide with the real and imaginary parts of the P phasor:

$$\begin{aligned}
 b_{+,\parallel} &:= -\left[b_+ \otimes b_{\pm,\text{DC}}^{\text{GW}}\right] / \left|b_{\pm,\text{DC}}^{\text{GW}}\right| = -\Re\{b_+\} \\
 \text{and} & \\
 b_{+,\perp} &:= \left[\left(e^{-i\frac{\pi}{2}} b_+\right) \otimes b_{\pm,\text{DC}}^{\text{GW}}\right] / \left|b_{\pm,\text{DC}}^{\text{GW}}\right| = \Im\{b_+\}.
 \end{aligned} \tag{2.11}$$

The SNR , again determined as $|I_{\omega_m}|$ divided by shot noise, yields after simple algebraic transformations (assuming $|b_+^{\text{GW}}| \approx |b_-^{\text{GW}}|$ for low and high f_{GW}),

$$\begin{aligned}
 SNR(f_{\text{GW}} \ll f_{\text{res}}) &\propto \frac{\sqrt{4|b_+^{\text{GW}}|^2(|b_+|^2 + |b_-|^2 - 2|b_-| \cdot b_{+,\parallel})}}{\sqrt{|b_+|^2 + |b_-|^2}} \\
 &= 2|b_+^{\text{GW}}| \sqrt{1 - 2\frac{|b_-| \cdot b_{+,\parallel}}{|b_+|^2 + |b_-|^2}}
 \end{aligned} \tag{2.12}$$

for low frequencies,

$$SNR(f_{\text{GW}} \gg f_{\text{res}}) \propto 2|b_+^{\text{GW}}| \sqrt{1 + 2\frac{|b_-| \cdot b_{+,\parallel}}{|b_+|^2 + |b_-|^2}} \tag{2.13}$$

for high frequencies, and

$$\begin{aligned}
 SNR(f_{\text{GW}} \sim f_{\text{res}}) &\propto \sqrt{2\frac{(|b_+^{\text{GW}}|^2 + |b_-^{\text{GW}}|^2)(|b_+|^2 + |b_-|^2) + 4|b_+^{\text{GW}}| \cdot |b_-^{\text{GW}}| \cdot |b_-| \cdot b_{+,\perp}}{|b_+|^2 + |b_-|^2}} \\
 &= \sqrt{2\left[|b_+^{\text{GW}}|^2 + |b_-^{\text{GW}}|^2 + 4|b_+^{\text{GW}}| \cdot |b_-^{\text{GW}}| \frac{|b_-| \cdot b_{+,\perp}}{|b_+|^2 + |b_-|^2}\right]}
 \end{aligned} \tag{2.14}$$

for resonance.

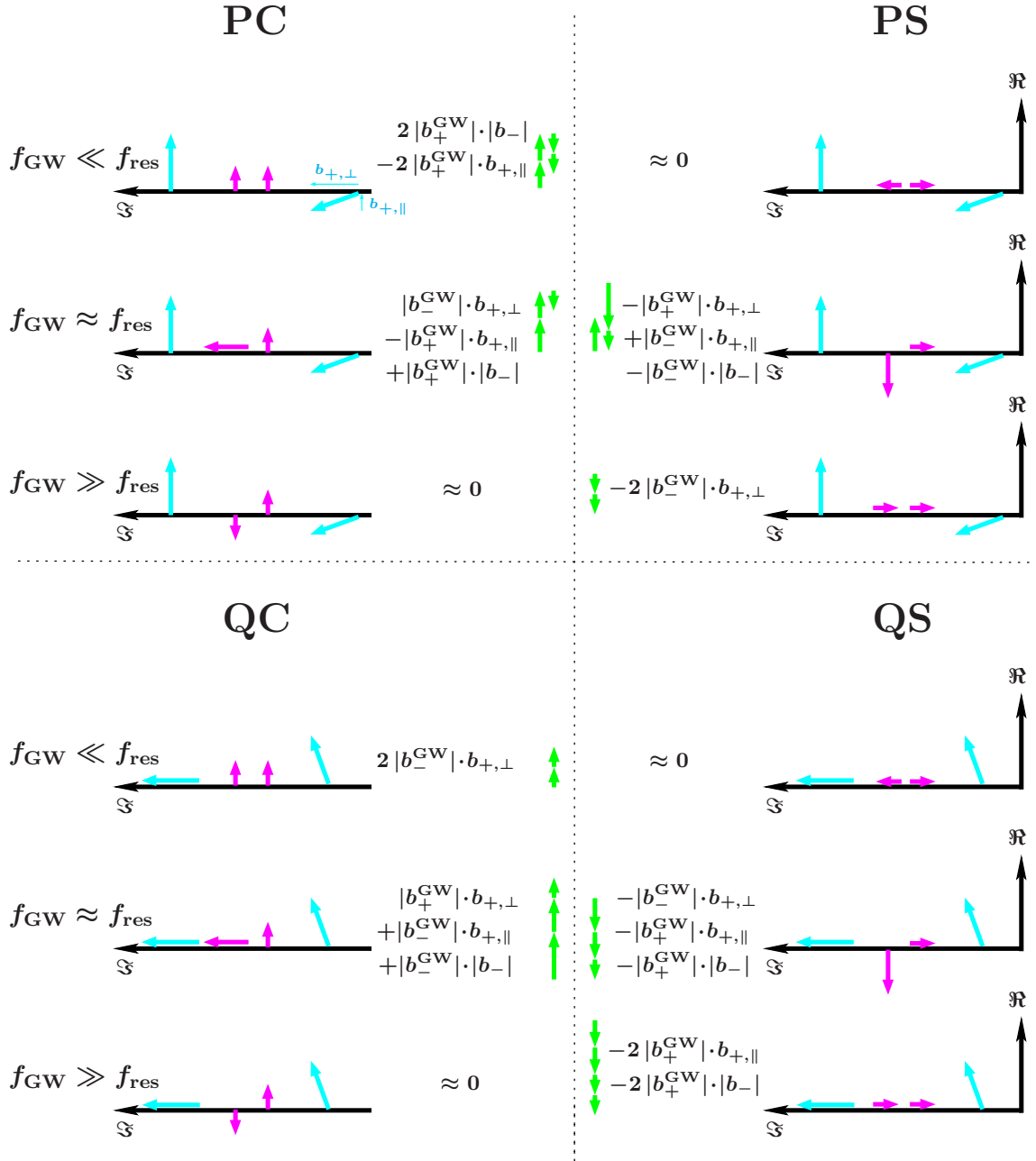


Figure 2.8.: Phasors at the south port of a dual-recycled Michelson interferometer, detuned by 1 kHz. The figure is composed equivalently to Figure 2.6. Apparently, the signal is almost equally distributed between P and Q, and there exist no frequency regions where the detector is blind for signals.

The cavity resonance shape is again conserved if accounting for only the lower signal sideband and the SNR is the same as in Equation 2.8. Here, the second signal sideband, however, enhances high and resonant frequency values and beats destructively at low frequencies. This will also slightly shift the frequency of peak sensitivity to higher frequencies⁸.

The experimental demodulation phase

Up to the detuning example of 1 kHz, the signal I_{ω_m} was contained in only one control sideband quadrature. This was due to the fact that the control sideband amplitudes were assumed to be equal. Thus, there existed always one demodulation phase where the control sidebands could cancel regardless of the signal frequency. Applying an arbitrary pair of perpendicular demodulation phases on the resulting I_{ω_m} still yields a constant ratio, for all f_{GW} , of the signal components regarding these two quadratures. The absolute value of the projection of I_{ω_m} on a particular demodulation phase vector can be regarded as the *signal content* in that respective quadrature.

As in this example the sideband amplitudes differ, the condition for a complete cancellation can never be fulfilled: with a constant demodulation phase one can only ensure a minimal or maximal signal for a certain frequency (regime). Thus, the ratio of the signal contents referring to any orthonormal basis of demodulation phases must change dependent on the gravitational-wave frequency.

This dependency of the signal content in perpendicular quadratures on detuning was seen in the GEO 600 experiment. Up to June 2005 the detector was operated mainly at 1 kHz detuning, in autumn 2005 at a detuning of roughly 300 Hz.

Figure 2.9 displays fits to optical transfer function measurements of GEO 600, from the differential Michelson end mirror displacement (thus referring to twice the displacement of one end mirror) to the error-signal output, where the photodiode signal is demodulated with two perpendicular demodulation phases. For the detector tuned to roughly 1 kHz and 250 Hz, the solid blue and cyan lines show the signal transfer into P, whereas the dashed red and dashed-dotted magenta lines show the signal content in Q, respectively.

For a tuning of 1 kHz, the signal content in the two quadratures obviously exhibits a strong dependency on the signal frequency. At the detuning of 250 Hz, the ratio of signal content of the quadratures is roughly constant over the complete frequency range.

⁸This can be proved considering two extremal cases of the b_+ pointing.

If $b_{+,\perp} = |b_+|$, the yield of SNR for low and high frequencies is the same, namely

$$\sqrt{2(|b_+^{GW}|^2 + |b_-^{GW}|^2)} = 2|b_+^{GW}|,$$

whereas it is maximal at resonance. Thus, the resonance frequency embodies also the maximal sensitivity.

If, however, $b_{+,\parallel} = |b_+|$, we have the same situation as in the case of 5 kHz detuning, just with the control sidebands being rotated by 90° . Evaluating the projection terms ensures the peak sensitivity to be at higher frequencies than the cavity resonance.

As the SNR is continuous, the peak sensitivity should be located somewhere in between if $|b_+| > b_{+,\perp}, b_{+,\parallel}$.

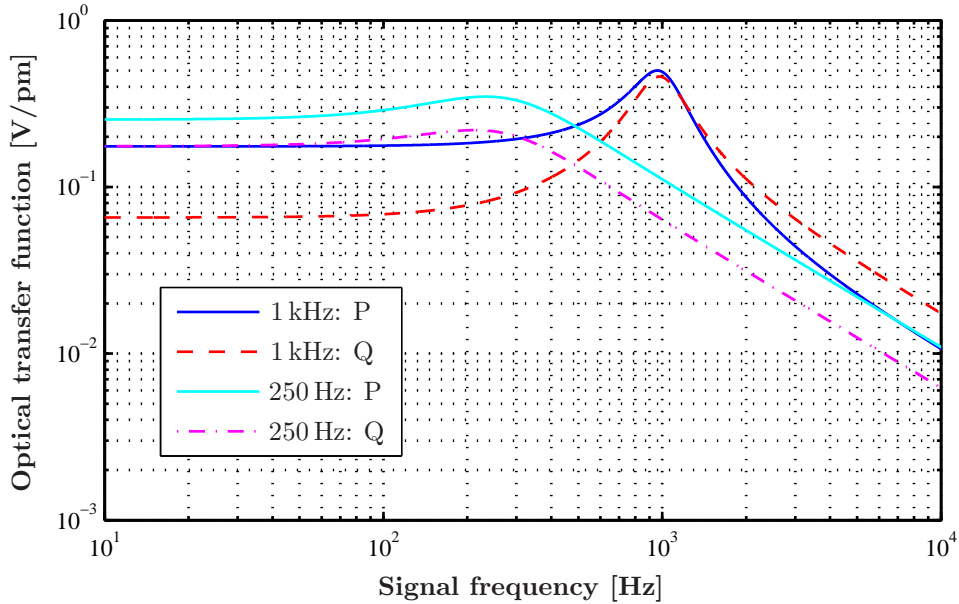


Figure 2.9.: Fits to optical transfer function measurements of GEO 600, from the differential Michelson end mirrors' displacement to the error-signal output, where the photodiode signal is demodulated with two perpendicular demodulation phases, marked in the legend with P and Q. The detector is tuned to roughly 1 kHz and 250 Hz. The absolute scaling of the graphs belonging to different detector tunings cannot be compared as the error-signal is repeatedly rescaled to fit the dynamic range of the loop electronics.

Please note that the absolute scaling of the graphs for different detector tunings cannot be compared as the error-signal output is repeatedly rescaled for considerations of the dynamic range of the loop electronics.

For the error-signals utilised in the experiment, the demodulation phase is usually optimised to yield largest signal content at low frequencies. This is crucial for the feedback to the actuator(s), since it improves the *SNR*.

Thus, in the GEO 600 experiment, the term *in-phase* or *P* (*in-quadrature* or *Q*) signal in the majority of cases refers to an error-signal, with the demodulation phase adjusted for maximum (minimum) sensitivity for low frequency deviations from the operating point⁹.

In the phasor picture, the demodulation phase situation according to a corresponding Q can easily be derived by evolving the control sideband phasors of Figure 2.8 as long as the components parallel to the low frequency cosine signal sidebands cancel each other. This is displayed on the lower part of Figure 2.10. Equivalently, a quarter modulation

⁹However, the on-line calibration process of the $h(t)$ channel which agrees with the error-signal for the differential Michelson, requires a further alteration of P and Q. In order to being able to reliably fit the detector transfer function to a model of a complex pole and a real zero, the demodulation phase for Q needs to be $\sim 20^\circ$ off from the ideal value. This, at the same time, determines P.

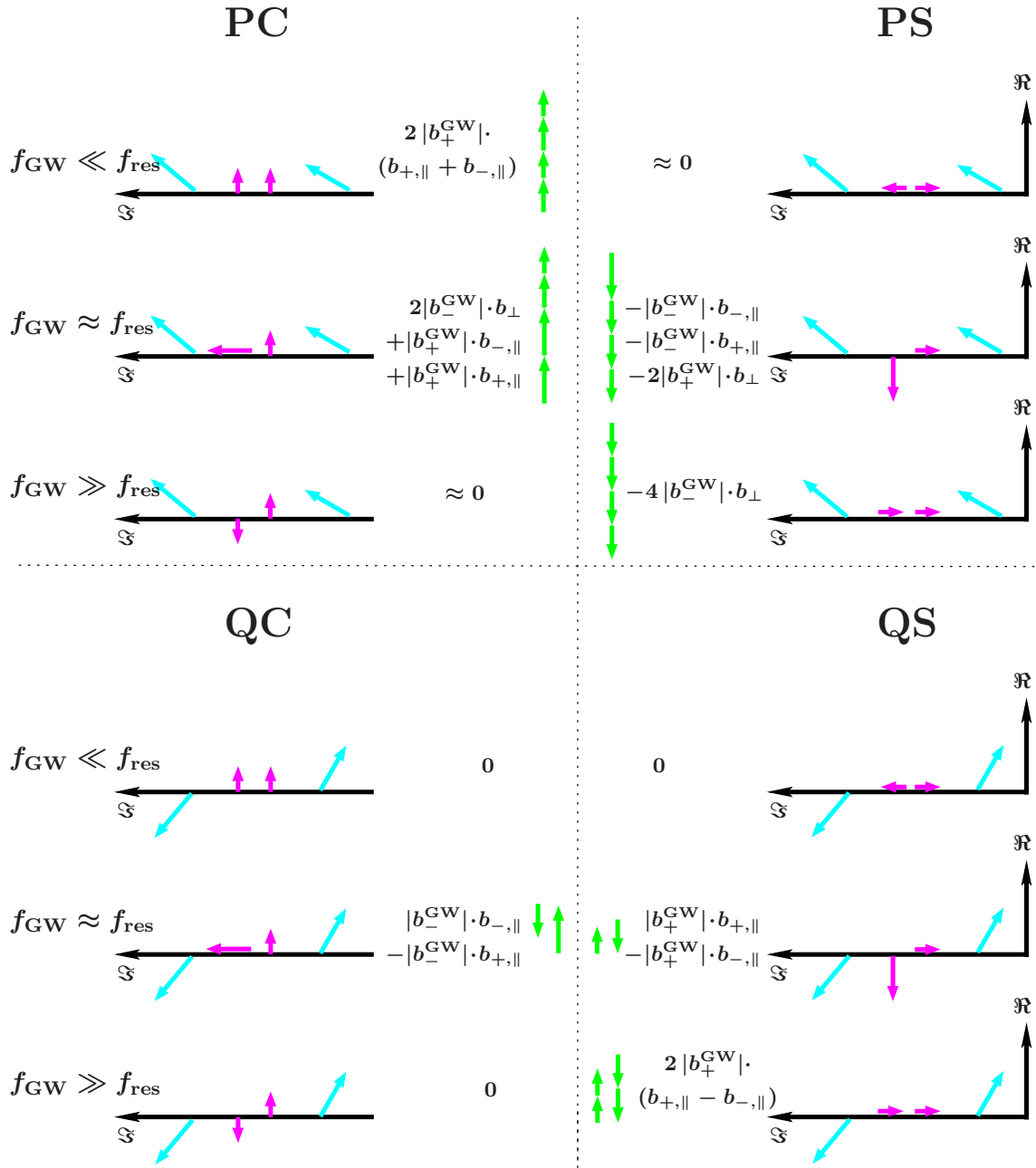


Figure 2.10.: Phasor diagram of the light fields at the south port of GEO 600, with a detuning of 1 kHz. The difference to Figure 2.8 are the control phasor pointings: alike in the real experiment, they are chosen such that for low signal frequencies the output vanishes in Q. Although, with this choice, the signal is for all frequencies mainly contained in P, the content in Q increases the higher the signal frequency becomes.

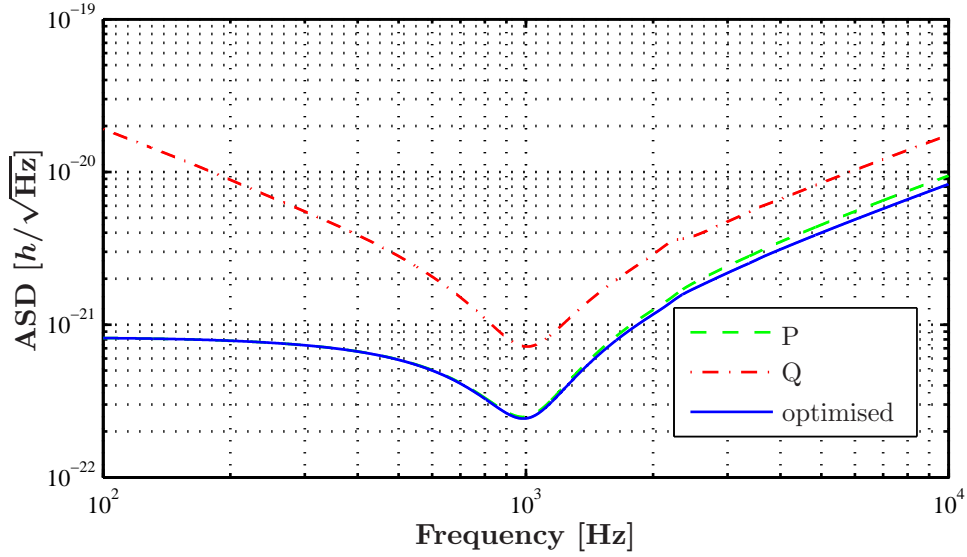


Figure 2.11.: Theoretical sensitivity of GEO 600 with the demodulation phase optimised to yield P and Q (dashed green and dashed-dotted red line, respectively) as displayed in Figure 2.10. Combining the signal content of both quadratures to generate the complete I_{ω_m} , one can choose new demodulation phases, optimised for each signal frequency. The solid blue curve shows such an optimised sensitivity: up to almost 1 kHz, the optimum agrees very well with P. Only at higher frequencies, the importance of Q becomes evident.

period later, at the in-phase signal, these same components of equal lengths appear on the perpendicular axis and add up (see upper part).

Although P and Q both contain some signal at resonant and high frequencies, P dominates the complete frequency range¹⁰. Determining the maximally possible shot-noise limited sensitivity, by dividing the shot noise by $|I_{\omega_m}|$ for all f_{GW} , yields of course exactly the same result as before. For comparison, all three sensitivity graphs are displayed in Figure 2.11. They were directly generated by FINESSE using the current script describing GEO 600 (see Appendix B.1.1 for the optical parameters). Obviously, the content of sensitivity in Q becomes relevant only at frequencies higher than 2 kHz which confirms the qualitative result of the projection picture.

¹⁰This might, however, be different for arbitrary Michelson control sideband frequencies (that are not constrained to the current power-recycling resonance).

2.4. The importance of the control sidebands for the sensitivity shape

Comparing the results for the SNR for all three tunings, it becomes obvious that the signal-recycling cavity resonance condition for the control sidebands matters for the sensitivity to gravitational waves, and that it is impossible to optimise the signal read-out or sensitivity in all frequency regions at once.

The crop of signal is best for the tuned case as for all frequency regions the amplitude of both signal sidebands gets projected completely onto both control sidebands (even though various signal quadratures are needed).

Comparing the signal yield for detuned states, for $f = f_{\text{res}}$ and high frequencies, the yield of the signal is better for a 1 kHz detuning than for the 5 kHz case. However, the low frequency region falls behind in comparison with 5 kHz detuning. This gives raise to the general question: which frequency regions are worth optimising for SNR , and what kind of detector setup could fulfill these requirements.

In this subsection, the derivations made with the simple projection picture will be employed to find a best, GEO 600-like, detector setup concerning the control sideband properties.

To get a feeling for the relevant dependencies, first, three dual-recycled setups for one detuning will be compared. They are chosen to yield exposed conditions for the control sidebands, based on the knowledge above.

Then, the dependency of the sensitivity shape on the control sideband properties will be investigated for a wide range of detunings. This enables, on the one hand, a targeted optimisation of the detector setup. On the other hand, only this deep understanding qualifies to compare a dual-recycled detector, featuring a simple signal-recycling mirror, with one exhibiting an etalon instead (see Section 3.7).

For most of the following results, the field properties used to calculate the sensitivities based on the projection picture method, will numerically be given by FINESSE. Unless otherwise stated, the parameters of the most accurate detector setup of GEO 600 will be used. A FINESSE file of this setup can be found in Appendix B.1.1.

2.4.1. Comparison of three dual-recycled detector setups

To assure the comparability of different detector setups, the same signal sidebands need to be provided:

- The carrier power inside the Michelson arms needs to be the same to ensure the same signal sideband amplitude.
- The signal-recycling cavity bandwidth and tuning for the signal sidebands need to be preserved: This is necessary to obtain the same signal sideband amplitude and phase progression in the frequency interval of interest.

This is easily achievable by keeping all mirrors and tunings for the carrier in all the setups. The detuning of 5 kHz may well serve as an example tuning. The phasor situation of Figure 2.8 can be generalised to any pair of control sidebands regardless of the resonance condition of the lower sideband:

- According to the choice of demodulation phase, any pair of control sidebands can be evolved in phase until the lower sideband is purely real. To compare the sensitivities, anyway $|I_{\omega_m}|$ will be evaluated such that the absolute demodulation phase is arbitrary.
- In equations 2.11 to 2.14, $|b_-|$, $b_{+,||}$ and $b_{+,\perp}$ remained general. The only constraint for the validity of these equations is that the “frame of reference”, i.e., the signal sideband phasors, are qualitatively the same as in Figure 2.8. Thus, the crucial requirement is that the detuning is larger than the signal-recycling cavity bandwidth for the signal sidebands. For lower detunings, the two signal sidebands will exhibit significantly different pointings for the specified frequency regimes of gravitational-wave signals such that the projection terms differ from those utilised in equations 2.11 to 2.14.

However, the closer the tuning to 0 Hz, the less extraordinary the particular control sideband properties, as one draws near the tuned case. There, for all control sideband frequencies, the amplitudes are equal, and the phases are shifted by the same amount, but to opposite directions which is equivalent to a time evolution not altering the amplitude or phase modulation content of the carrier.

- In the current GEO 600 setup, the Michelson sideband frequencies are off-set from the power-recycling cavity resonance. This deviation anti-/symmetrically changes the phases/amplitudes of the sidebands entering the south arm. Assuming, for simplicity, the ideal case of no waste light appearing in the output, the amplitude change does not matter for the shot-noise limited sensitivity. The phase shift, however, changes the signal-recycling resonance condition of the control sidebands: the upper sideband resonates inside the signal-recycling cavity for a tuning of ~ 650 Hz (see Figure 2.16 and the explanations on page 129). For a signal-recycling tuning of 5 kHz, though, the phase and amplitude relations are roughly the same for both control sidebands, and Figure 2.4 may be consulted.

Equations 2.12 to 2.14 suggest constructing setups that generate control sidebands with roughly parallel, perpendicular, and anti-parallel P phasors. The parallel and anti-parallel situations support the detection of low and high signal frequencies, respectively, the perpendicular should level both extreme regions, enhancing the sensitivity at resonance.

However, the perfectly parallel and anti-parallel control sidebands produce similar projection terms in their respective sensitive frequency region. In order to get three very different situations, the perfectly perpendicular and anti-parallel setups will be joined by one situation where the sideband phasor pointings are “in-between” being perpendicular and parallel. This last example agrees with GEO 600.

Such a (relative) phasor rotation is accessible by a change in the resonance conditions of the control sidebands inside the signal-recycling cavity. A “simple” variation of modu-

lation frequency, however, changes the resonance condition of the control sidebands not only inside the signal-recycling cavity, but also inside the power-recycling cavity, and in addition alters the coupling of the two cavities through the Michelson interferometer. In general, the resulting phases are intuitively hard to comprehend.

Instead, the signal-recycling cavity length will be changed. Elongating (or shortening) the signal-recycling cavity decreases (or increases) the FSR_{SR} , reducing (or increasing) the distances of the signal-recycling resonance structures of Figure 2.4.

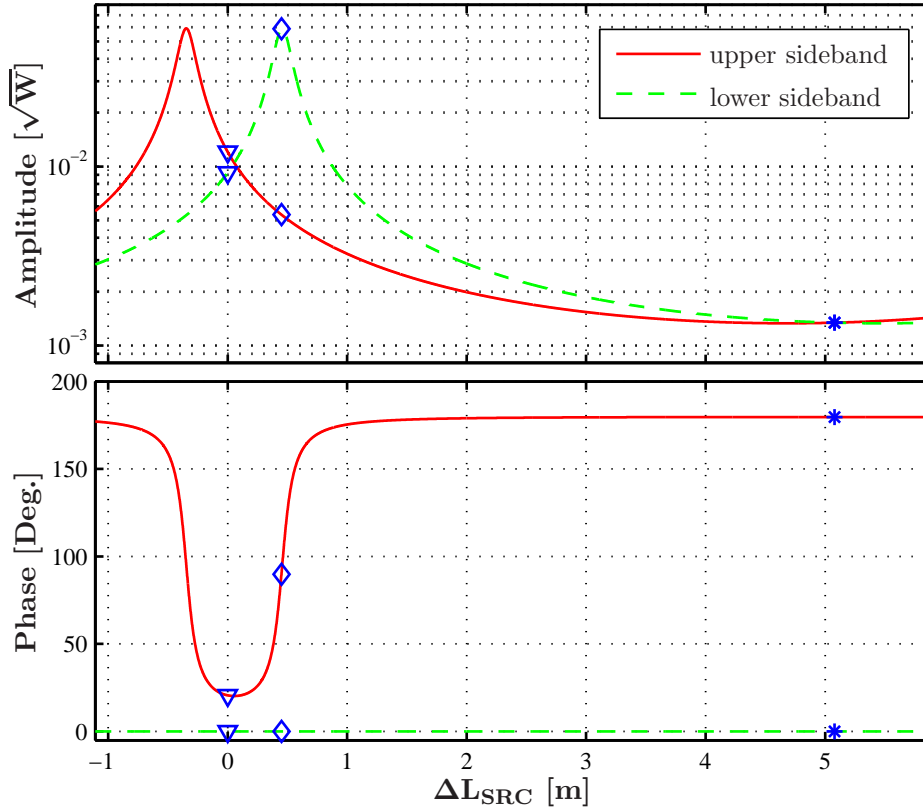


Figure 2.12.: Amplitudes and phases of the control sidebands behind the MSR of a GEO 600-like detector, but with various signal-recycling cavity lengths. 0 m corresponds to the default length of GEO 600. For all lengths, the detector is detuned to 5 kHz, and the sideband phases are evolved to yield a real lower sideband. The stars, diamonds and triangles indicate cavity lengths suitable for a comparison of sensitivities. The lengths generate anti-parallel, perpendicular, and GEO 600-like phasors.

Figure 2.12 shows the control sidebands' amplitudes and phases at the output photodiode of a GEO 600-like detector detuned to 5 kHz, but with varying signal-recycling cavity length. 0 m corresponds to the GEO 600 setup. Both fields' phases are for all lengths evolved to yield a real lower sideband.

The amplitudes' maxima indicate signal-recycling cavity lengths where the respective sideband is resonant inside the cavity, detuned by 5 kHz. The upper sideband's phase has two dispersive structures, around the upper and lower sidebands' resonances. Before it could reach 0° , though, the next resonance forces it back to 180° . With a higher detuning, the resonances were further away from each other allowing for parallelism of the phasors.

The stars, diamonds and triangles indicate the field properties for signal-recycling cavity lengths providing anti-parallel, perpendicular and GEO 600 phasor pointings, respectively.

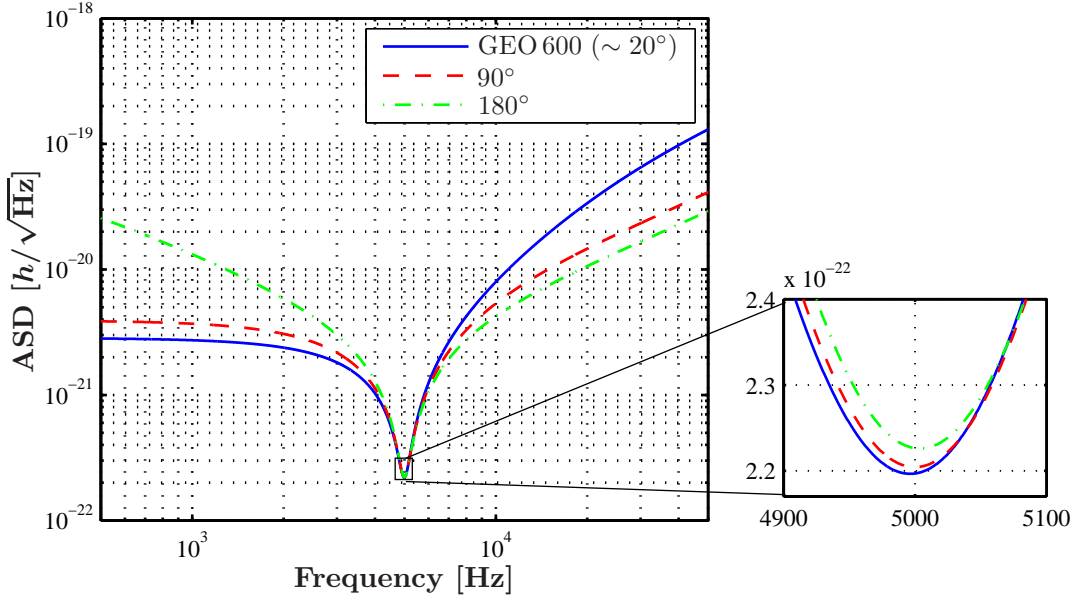


Figure 2.13.: Strain sensitivity for three detectors with different signal-recycling cavity lengths, tuned to 5 kHz. As expected, the sensitivity at low frequencies is best for the GEO 600-like setup, whereas at high frequencies anti-parallel sideband phases yield the best signal read-out. The picture on the right shows the zoomed-in sensitivity at the resonance. The peak sensitivities slightly differ, and the peak position matches the signal-recycling resonance frequency only for perpendicular control sideband phasors.

Figure 2.13 shows the detector sensitivities for these three different control sideband phasor situations of Figure 2.12. The anticipated sensitivity differences in the particular frequency regions are all well displayed:

- At high frequencies, the sensitivity is best for anti-parallel and worst for GEO 600-like control sidebands. In the low frequency region it is the opposite. The ratio of the “best-sensitivity” curve in the respective region to the perpendicular case of sideband phasor pointing is roughly $\sqrt{2}$. The differences of the “worst-sensitivity” curves for the respective frequency regions to the dashed one are much higher. The phasor picture explains it (together with the equations 2.12 and 2.13): the perpendicular control sidebands always enable some signal read-out with at least one sideband, creating non-zero components I_{PC} and I_{QC} , or I_{PS} and I_{QS} , for low or

high frequencies, respectively. The other control sideband constellations are either anti-parallel to each other or perpendicular to the signal phasors at the respective low sensitivity frequency region, obtaining no signal. In the opposite frequency region, one of the components yields the best possible read-out. Thus, compared to the perpendicular sideband situation, the possible sensitivity improvement is $\sqrt{2}$, whereas the ratio at the other frequency end is continuously increasing.

- At resonance, the perpendicular control sidebands are better than the anti-parallel ones, because there are no destructive projection terms. At first glance, it might seem astonishing that the GEO 600 sideband constellation yields the best sensitivity. Careful interpretation of Equation 2.14, though, makes it clear that the term containing the sidebands' projection, $|b_-| \cdot b_{+,\perp} / (|b_+|^2 + |b_-|^2)$, does not only depend on the control sideband phasors' relative pointing but also on their relative amplitudes. As both have to obey the signal-recycling cavity transfer function at the same time, they cannot be optimised independently of each other. Thus, the projection-term depends on the phasors' position inside the resonance structure.

As visible in Figure 2.12, the sideband amplitudes differ most in the perpendicular case and are of similar size at the signal-recycling cavity length of GEO 600. Thus, if the cancellation of control sidebands in one quadrature is not guaranteed (like in the parallel and anti-parallel case), chances are good that the sensitivity at resonance is better than in the perpendicular case, although not the complete $|b_+|$ contributes to the projection.

- The peak positions of the three curves are shifted against each other. In the perpendicular case, it agrees with the resonance frequency of the lower signal sideband. In case of GEO 600, the peak frequency is slightly shifted towards DC, whereas for 180° the peak sits at higher frequencies. This is exactly what was derived in the subsections before (see 2.3.4 and 2.3.5).

With Figure 2.7 and the derived Equation 2.10, it could be shown for the example of 0° that the real maximum SNR is shifted from signal-recycling cavity resonance depending on the exact signal sideband properties. The same formula is valid for anti-parallel sideband phasors, with $b_{-,\perp}^{\text{GW}} = -\Re\{b_-^{\text{GW}}\}$. Comparing the phasor pictures of Figure 2.7 with Figure 2.8, both extremal control sideband situations should yield a maximal peak shift.

To get an upper limit for the peak deviation from signal-recycling cavity resonance, Equation 2.10 is worth closer investigation. It shows in particular that the possible shift of the peak SNR is larger, the larger $|b_+^{\text{GW}}|$, and this depends on the detuning.

Figure 2.14 displays the peak shift, based on an evaluation of Equation 2.10 around the resonance, as a function of detuning. The signal sidebands, used for the calculation, obey the Airy-function of the signal-recycling cavity that was availed for the detector examples above, with a bandwidth of roughly 400 Hz. Thus, as Equation 2.10 requires the detuning to be above the bandwidth, the display of the graph is limited to lower frequencies by 400 Hz.

Clearly, the peak shift decreases for increasing detuning. It amounts to maximally ~ 40 Hz. This has consequences especially for the parameter estimations for the simulation

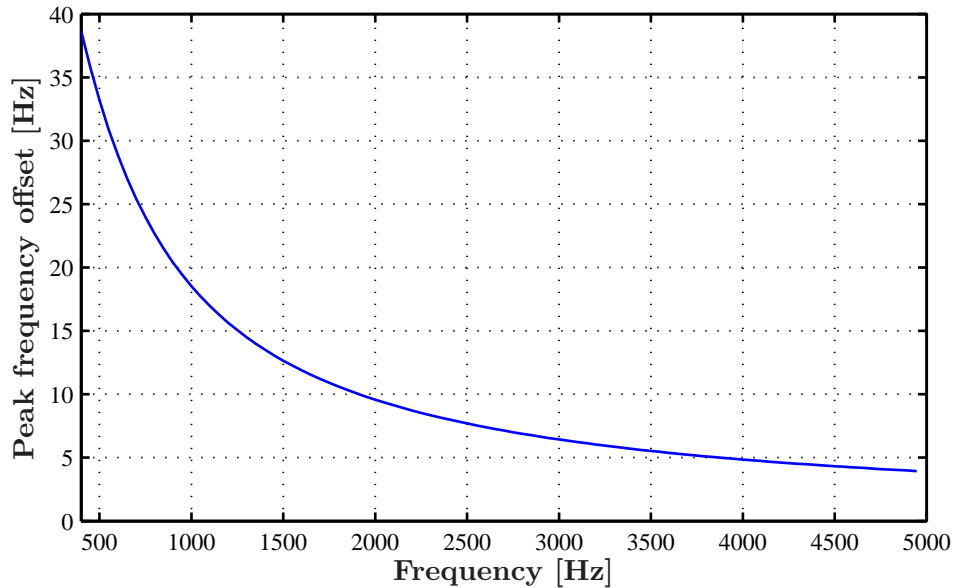


Figure 2.14.: Frequency shift of peak sensitivity dependent on the detector tuning, in case of anti-parallel control sideband phasors. To determine the offset, Equation 2.10 was evaluated assuming a signal-recycling cavity bandwidth of 400 Hz, as it appears at the GEO 600 detector.

script representation of GEO 600. It means that the position of the peak sensitivity only contains rough information on the real tuning of the detector, i.e. the microscopic **MSR** position. Any parameter adjustment utilising experimental results, needs a careful estimation of the required accuracy of the tuning.

2.4.2. Consequence: the optimal GEO 600

The sections above led to the result that the sensitivity shape not only depends on the specific signal-recycling cavity properties, like tuning, macroscopic length and mirrors, but also on the resonance condition of the Michelson control sidebands inside this cavity. The (resonant) power-recycling cavity only matters in terms of forming the compound input mirror to the signal-recycling cavity, together with the Michelson interferometer. Thus, the signal-recycling cavity bandwidth, and amount of sideband light occurring at the output photodiode, are influenced¹¹.

Another finding was that the *SNR* cannot be optimised for the complete frequency band of the detector at once. This immediately leads to two questions:

- Which frequency regions are of greatest interest?

¹¹The last two properties should not be underestimated for neither the simulation nor the experiment.

- As the control sidebands are supposed to be fixed for all detector tunings and have to obey the resonance condition in this varying signal-recycling cavity: Is there any possibility or tool to optimise the signal yield globally for all tunings?

The aim of any dual-recycled detector is to specialize for a specific frequency. Thus, this frequency, and a certain band around it, remain the target to optimise for. Secondly, low frequencies are preferable to high frequencies, especially for the first generation of earth-bound gravitational-wave detectors. In the low frequency region, the strongest gravitational-wave signals inside the detectable band are expected to occur, and the source numbers are much more promising.

In particular, GEO 600 was, with its elaborate pendulum suspensions for the interferometer mirrors, especially designed to give good sensitivities at low frequencies.

To answer the second question, it is advisable to first shelve the targeted frequency regions and find a global answer. An evaluation of the terms $b_{+,\perp} \cdot |b_-|/(|b_+|^2 + |b_-|^2)$ and $b_{+,\parallel} \cdot |b_-|/(|b_+|^2 + |b_-|^2)$, from Equation 2.12 to 2.14, for all imaginable combinations of resonance conditions for both sidebands independently from each other, should cover the answer for any kind of dual-recycled detector setup¹². In this plane of possible resonance conditions, the embedded, realistic combinations of resonance conditions can then be shown.

The left and right pictures of Figure 2.15 display the targeted terms, associated with Equation 2.14, and Equation 2.12 and 2.13, respectively. The parameter plane assigns the resonance condition of each control sideband within the frequency-dependent transfer function of the signal-recycling cavity. In order to be as general as possible, the sideband's resonance condition is expressed as a deviation from resonance in units of signal-recycling cavity bandwidths for the control sidebands¹³. A positive sign of deviation means a sideband frequency or detector tuning higher than the resonant. (A comparison with Figure 2.4 might help to illustrate the resonance conditions.) The equipotential lines are colour coded but also accompanied by their respective numerical values. They indicate the range for both terms to be within $[-0.5, 0.5]$. The meaning of the grey bars is explained further below, in the second item of Page 65.

The symmetry of these pictures is eye-catching. There are two axes of symmetry which are both crossing the origin of the resonance-condition plane, one with slope 1, the other with slope -1 . They will be called *positive* and *negative diagonal*, respectively. The positive diagonal mirrors the values belonging to the lower right half of the plane to the upper left in both pictures. The negative diagonal is likewise a symmetry axis for the upper right and the lower left half of the planes. However, in the left picture, the term values are anti-symmetric. Both diagonals hold some kind of sensible combination of resonance conditions for both control sidebands:

¹²For the control sidebands, the only assumption required is that the sidebands still represent a perfect phase modulation when they exit the power-recycled Michelson to the south. This is always the case inside a GEO 600-like detector.

¹³Please keep in mind that this bandwidth might differ depending not only on the reflectivity of **MSR**, but also on the sideband's resonance condition inside the power-recycling cavity, and the power-recycling cavity properties.

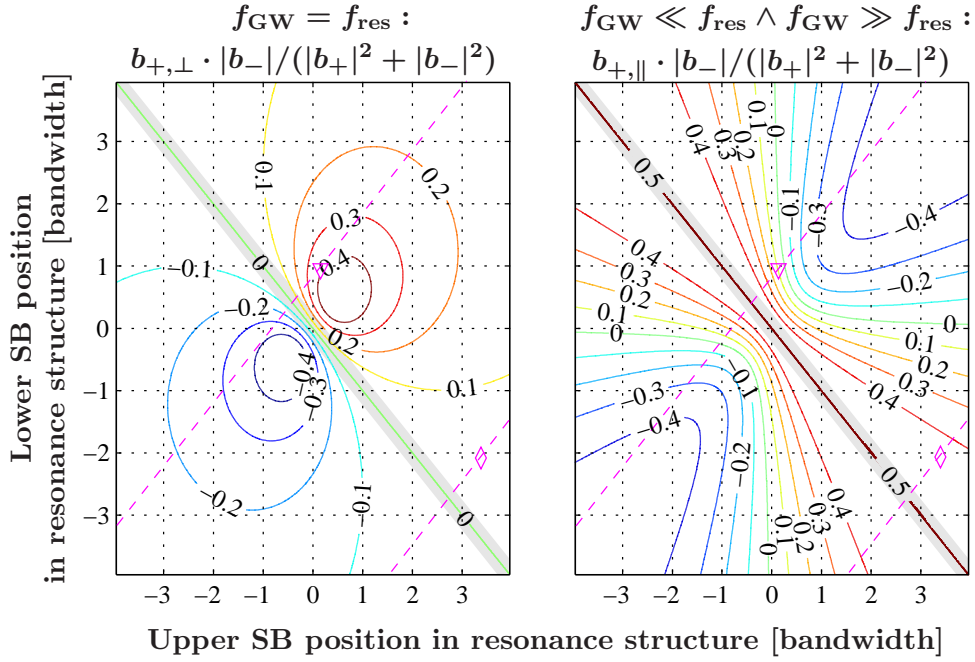


Figure 2.15.: The two pictures display the terms $b_{+,\perp} \cdot |b_-| / (|b_+|^2 + |b_-|^2)$ and $b_{+,\parallel} \cdot |b_-| / (|b_+|^2 + |b_-|^2)$ of equations 2.14, and 2.12 and 2.13. The terms are evaluated for varying resonance conditions of the upper and lower control sideband inside the signal-recycling cavity. The dashed magenta lines with slope 1 represent the conditions for the sidebands of the previously used detector setups, for different detector tunings. The triangle and diamond again mark GEO 600 and the optical setup with perpendicular sideband phasors at 1 kHz detuning, respectively (compare with Figure 2.12). Please note that the plane units are given in bandwidth of the signal-recycling cavity for the control sidebands. This does not only depend on the mirror properties, as for the signal sidebands, but also on the complete particular configuration.

- The **negative diagonal** joins all sidebands that are anti-symmetrically arranged inside a resonance structure. This is always the case, if a detector is tuned to 0 Hz (please compare with Figure 2.4).

Thus, this diagonal in general represents **tuned detectors** with different *FSRs* or signal-recycling cavity lengths.

- The **positive diagonal** comprises sidebands symmetrically disposed inside a resonance structure.

In particular, the origin can be associated with a tuned detector whose signal-recycling cavity also resonates with the control sidebands. For the upper most picture of Figure 2.4 this would mean that the dashed-dotted lines, marking the ± 119 th *FSR*_{PR}, sit exactly at the maximal enhancement of the signal-recycling cavity. Starting from there and tuning the detector upwards, both sidebands have exactly the same deviation from resonance. The same is true for any negative de-

tuning, only with negative sign of the deviation.

Thus, the positive diagonal stands for **all possible tunings** of the particular detector that resonates with the Michelson control sidebands if it is tuned to carrier resonance.

Expanding this insight to the rest of the plane, as a logical consequence, all lines parallel to the positive diagonal stand for various tunings of one explicit detector.

In the same way, all lines parallel to the negative diagonal represent particular tunings of detectors with different *FSRs*.

The magenta coloured, dashed lines with slope 1 stand for two of the previously used detector examples. As in Figure 2.12, the GEO 600 detector is marked by a triangle, the perpendicular phasor case by a diamond. Both marks are on the lines at a position corresponding to 1 kHz tuning¹⁴.

Before discussing optimal detector configurations, two properties of the terms need to be commented:

- The lower left half of the left picture shows negative values for the respective term. This is correct for the numerical evaluation of the term, but in reality all values should be positive. This is because for negative tunings, the signal C phasors for low frequencies in Figure 2.8 would point just to the opposite side. Thus, in this case the correct definition of the phasor projection component would be $b_{+,||} = \Re\{b_+\}$ instead of $-\Re\{b_+\}$.
- Studying the phasor diagrams for the tuned detector case assured that the signal yield is optimal for all frequencies. The values along the negative diagonals of the pictures of Figure 2.15, however, indicate worst sensitivity for all gravitational-wave frequencies for tuned detectors. Please keep in mind, that the terms are only valid for detunings larger than the signal-recycling cavity bandwidth for signal sidebands (see page 58). For the example detectors, this is 400 Hz, corresponding to position offsets of ± 0.2 around the negative diagonals. The invalid region for this case is marked in both graphs by the grey bar. However, as the size of the invalid region varies depending on the signal-recycling cavity bandwidth ratio for the signal and the control sidebands, these bars, in opposition to the values of the mathematical expressions, cannot be generalised.

Looking for the best possible resonance conditions to enhance the signal crop of low and resonant frequencies, Figure 2.15 suggests exactly the detector represented by the positive diagonal: investigating each tuning separately, one needs to compare the values on each line parallel to the negative diagonal. Doing this, the left arrangement shows for all tunings a maximum value at the positive diagonal, and the right a minimum, indicating maximal possible signal read-out at resonant and low frequencies, respectively.

¹⁴The signal-recycling cavity bandwidth for the control sidebands was ≈ 1.9 kHz. The upper sideband's resonance in the GEO 600 case is at around $\sim +650$ Hz tuning, in the perpendicular case it is at ~ -5 kHz. Thus, the corresponding detector lines should cross the negative diagonal at ~ -0.34 and ~ 2.8 with respect to the upper sideband axis.

Creating such a setup means that the control sidebands should be resonant inside the tuned signal-recycling cavity.

The signal yield for low gravitational-wave frequencies is enhanced more, the smaller the signal-recycling cavity bandwidth for the control sidebands: this makes the negative term values in the right graph already available at lower tuning frequencies. According to Equation 2.12, the smaller this term, the better the *SNR* for low gravitational-wave frequencies.

With a small signal-recycling cavity bandwidth, the best signal read-out for resonant signal frequencies occurs at low detector detunings. Then, the highest values of the respective mathematical expression appear already at small frequency deviations from a resonant position inside the resonance structure of the signal-recycling cavity.

To construct a setup that fulfills this requirement, either the mirror properties of the detector, like location and reflectivities, need to be altered, or the control sideband frequency has to be adjusted.

Varying the mirror properties and positions enables the most exact shaping of the resonance structure of the signal-recycling cavity for the control sidebands. Developing a new detector, this knowledge should be incorporated. However, a too close assimilation of the *FSRs* of the power-recycling and signal-recycling cavity should be avoided. This could complicate the control of the signal-recycling cavity close to tuned detector states (see Section 3).

The control sideband frequency is very easily accessible. However, in a given setup, a “simple” change of frequency not only changes the conditions inside the signal-recycling cavity, but also inside the power-recycling cavity¹⁵. Changing the control sideband frequency around the power-recycling resonance, for example, not only alters the effective reflectivity of the power-recycled Michelson, but also changes the phase of the reflected light, in particular of the light approaching from the south, being back-reflected from **MSR**. Thus, the frequency position of the control sideband resonance inside a signal-recycling cavity with fixed mirrors will counter-intuitively shift while tuning the sideband frequency. Due to this feature, there might be several frequency solutions (within one *FSR*) fulfilling the requirement of being resonant inside a tuned signal-recycling cavity.

As mentioned above, a small bandwidth of the signal-recycling cavity supports the sensitivity for low gravitational-wave frequencies already for low detector detunings. The bandwidth automatically decreases when the sideband frequency leaves power-recycling resonance. Considering a power-recycled Michelson only, the intra-cavity power is highest at the power-recycling resonance, yielding the highest possible power in transmission for injected light from the south as well as from the west. Away from the resonance, the transmitted power is less. In this case, the input compound mirror gets a higher effective reflectivity.

The good signal read-out at low frequencies has, however, to be traded against the overall control sideband power at the output port which determines not only the *SNR*

¹⁵For small frequency changes, we can safely assume constant properties of the compound mirror built by the Michelson.

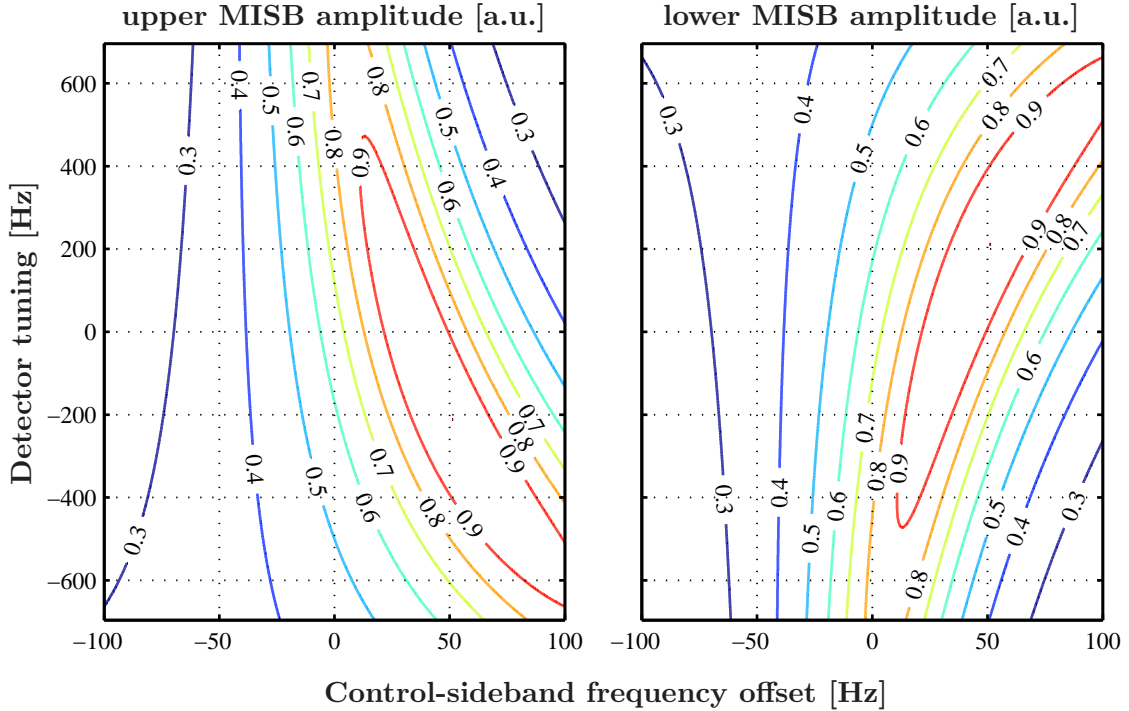


Figure 2.16.: Amplitude of the control sidebands, for the differential Michelson error-signal, (MISBs) appearing behind **MSR**. The amplitude is normalised to yield 1 for the maximum. It is displayed above the plane of detector tuning and sideband frequency. 0 Hz on the x -axis denotes the experimentally used value that is also adopted in the simulations as a default value, unless otherwise stated.

but also the ability to lock the Michelson. A small signal-recycling cavity bandwidth and, for example, a control sideband resonance at 0 Hz **MSR** tuning leads to a very much attenuated sideband power at high detunings. In the control loop, this needs to be compensated by a higher electronic gain and might impose a limit on the experiment. Regarding sensitivity, if the sideband power becomes comparable to the waste light, the SNR decreases for all frequencies.

Simulations of the current setup of GEO 600, show a bandwidth of the signal-recycling cavity, for the control sidebands being resonant inside the power-recycling cavity, of ~ 10 kHz. The power-recycling cavity end mirror reflectivities differ for the Michelson sidebands by 500 ppm only such that the reflectivity of the resonant power-recycled Michelson is around 80%. With such a low reflectivity of the input mirror to the signal-recycling cavity, both, the sideband power occurring behind **MSR** as well as the signal-recycling cavity bandwidth, can be improved by detuning the sideband frequency by a certain amount from power-recycling resonance¹⁶.

¹⁶For this reason, the experimentally used sideband frequency differs from the 119th FSR_{PR} by 52 Hz.

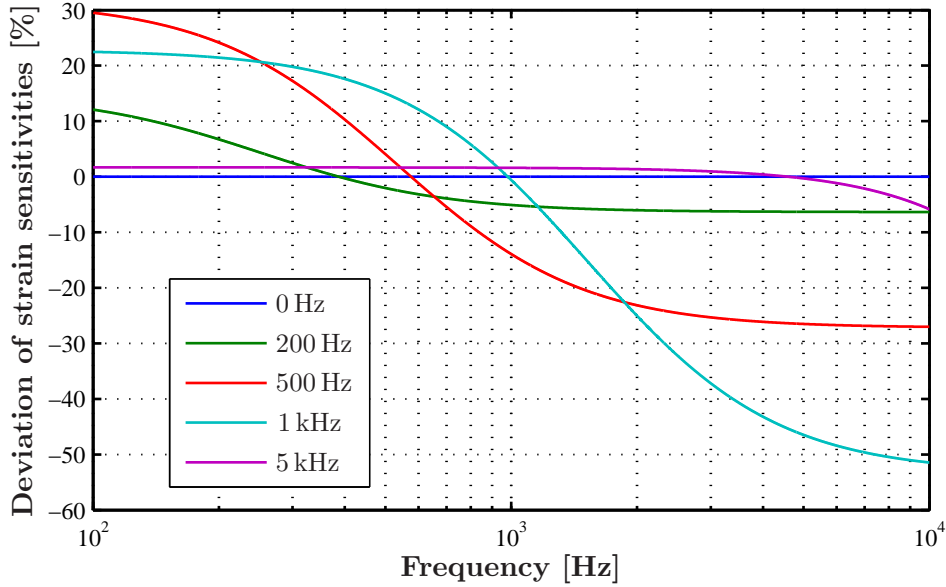


Figure 2.17.: Deviation of the sensitivity of the detector setup with optimised control sideband frequency from that of GEO 600, for special detector tunings. The sensitivity curves were obtained utilising the projection picture with the sideband properties provided by FINESSE. As expected, the sensitivity for low and resonant frequencies is better than in the GEO 600 case, where at high frequencies the GEO 600 setup is preferable.

The left and right pictures of Figure 2.16 display the amplitudes of the upper and lower control sidebands, respectively, at the output photodiode for a varying sideband frequency and detector tuning. The sideband frequency is shown as a deviation from the actual, experimentally used value. (Unless explicitly stated otherwise, this frequency is also utilised in simulations.)

The horizontal line in Figure 2.16, crossing the origin, represents detector configurations with a signal-recycling cavity resonant for the carrier and different Michelson sideband frequencies. Tracing the amplitude values on each vertical line yields the Airy-function for the particular Michelson sideband frequency depending on the signal-recycling cavity tuning. As a consequence of Figure 2.15, we are aiming for sideband frequencies that resonate in a tuned signal-recycling cavity. Translated to Figure 2.16, this is equivalent to searching for a vertical line for which the maximal amplitude sits somewhere on this horizontal line crossing the origin. This is clearly the case around +33 Hz detuning and should also be true close to -50 Hz. Accounting for the preferred small bandwidth and high sideband amplitude, the higher frequency is chosen to, in the following, compare the theoretical shot-noise limited sensitivity with the actual experimental setup.

Figure 2.17 displays the sensitivity deviation of the detector setup with optimised sideband frequency from current GEO 600, for different tunings. For the sensitivity compari-

son, the absolute values of the respective error-signal vectors were used which is identical to applying the optimal demodulation phase for each gravitational-wave frequency. The computation, based on the projection picture, utilised sideband properties provided by FINESSE. That includes the consideration of shot noise that is only caused by the control sidebands.

A negative deviation value indicates a sensitivity worse compared to the actual GEO 600. Thus, with the exception of tuned detectors, the optimised detector setup supports, as anticipated, frequencies below the resonance at the expense of higher frequencies. The gain and losses in the respective frequency regions are roughly the same, for example $\pm 30\%$, for a detuning of 500 Hz. In the tuning examples above 500 Hz, the higher the detuning, the less the sensitivity gain at low signal frequencies and the more the loss at high signal frequencies, and vice versa for lower tunings. Thus, the optimised setup is preferable, in particular for low detunings. Nonetheless, an improvement of low frequencies by more than 10% should justify a possibly high sensitivity loss on the other side of the resonance.

The signal yield improvement at the resonance depends on the tuning. Assuming, one could in Equation 2.14 achieve the highest value for $b_{+,\perp} \cdot |b_-| / (|b_+|^2 + |b_-|^2)$ for all tunings, the maximum possible improvement of the *SNR* would have to account for the transfer function of the signal-recycling cavity. The ratio of the best and worst *SNRs*,

$$\frac{SNR_{\text{best}}}{SNR_{\text{worst}}} = \frac{|b_+^{\text{GW}}| + |b_-^{\text{GW}}|}{\sqrt{|b_+^{\text{GW}}|^2 + |b_-^{\text{GW}}|^2}},$$

is displayed in Figure 2.18 as a function of signal-recycling cavity detuning, in units of signal-recycling cavity bandwidth for the signal sidebands. As Equation 2.14 is valid only for detector tuning frequencies larger than the signal-recycling cavity bandwidth (see Page 58), Figure 2.18 can only be trusted for tuning values above 1. The invalid tuning interval is denoted by the grey shading. This validation limit yields a maximum possible improvement of ~ 1.2 . In addition, the worst case assumption is far too pessimistic about the signal yield of a real, fixed detector setup. In a comparison of realistic detector setups, the improvement at resonance will, thus, appear much weaker. Consequently, any kind of detector optimisation should rather act in accordance with the demands for high or low signal frequencies¹⁷.

¹⁷Theoretically, for a detuning larger than the signal-recycling cavity bandwidth for the signal sidebands, the best possible signal read-out at f_{res} could be achieved by adjusting the signal-recycling cavity bandwidth for the control sidebands to be twice the particular detuning f_{res} . Then, the maximum of the left picture in Figure 2.15, at $\sim (0.5, 0.5)$, would occur at the respective tuning frequency. In a real experiment, though, this is hard to achieve for two reasons: the condition that the control sidebands are resonant in the tuned detector should always be fulfilled, and the sideband power has permanently to exceed the waste light power at the output.

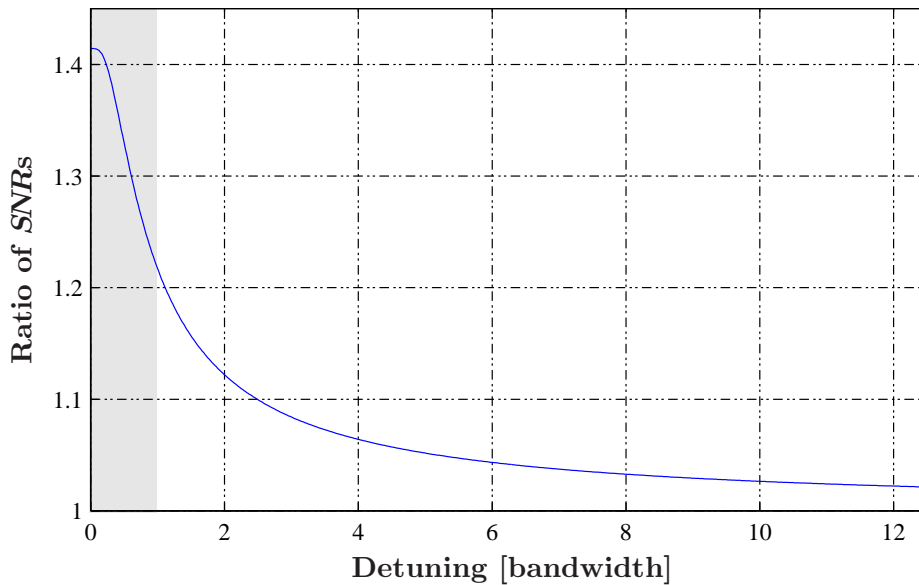


Figure 2.18.: Ratio of the best and worst possible $SNRs$ at the resonant frequency, versus detuning. The detector tuning is displayed as signal-recycling cavity bandwidth for the signal sidebands. In the GEO 600 case of 400 Hz, the tuning axis comprises the frequency interval of [0 Hz, 5 kHz].

2.5. Projection picture versus FINESSE

In order to comprehend and use the projection picture, the field phases were deduced applying as many simplifications as possible. In the evaluation of the results following from the simple picture, however, the “real” field properties, provided by FINESSE, were utilised. These properties still gave the expected answer, verifying the simplifications about the fields.

The results following from Equation 2.12 to 2.14, however, are still to be verified as for them only the “real” field properties of the control sidebands were considered. The sidebands’ pointing was very much simplified and fixed.

The simulation tool FINESSE lends itself to testing the projection picture results. However, it is much more powerful and realistic in computing sensitivities, transfer functions and error-signals, than the simple projection picture. It accounts, for example, also for signal sidebands occurring around the control sidebands, for higher-order sidebands or higher-order modes in case of mode-mismatch.

This offers two kinds of testing. One would be an equal comparison of results, considering only first-order sidebands and neglecting mode-mismatch. With this, the validity of predictions, regarding field simplifications only, can be determined. Using FINESSE with all integrated tools rather allows the investigation of the importance of mode-mismatch or higher-order sidebands.

In general, forming an opinion about the projection picture is much more sophisticated if the results hold out against FINESSE, neglecting extra effects or not.

Before considering the weight of effects that are not accounted for with the projection picture, let us first check with FINESSE how the quantitative predictions following from the formulas 2.12 to 2.14 look if the signal sidebands' pointing is realistic. In that case, the extra effects FINESSE is able to account for need to be switched off to ensure comparability. Whereas there exist commands to disable higher-order modes and sidebands, the effect of signal sidebands around control sidebands can only be attenuated by disposing of the carrier at the output and reducing the control sidebands' modulation index as much as possible. However, this contribution will not vanish completely.

Thus, for the following direct comparisons between the projection picture and FINESSE, the most actual detector setup of GEO 600 is utilised, with the exception that the loss in both Michelson arms is symmetrised, and the modulation index for the control sidebands is $\sim 10^{-2}$. To obtain the same carrier power inside the Michelson as before, the laser power is accordingly reduced. Higher-order modes and sidebands were disabled.

Figure 2.19 compares the results of FINESSE for the shift of the peak sensitivity from the signal-recycling cavity resonance for the lower signal sideband, (solid line) with the analytical result in Equation 2.10 following from the projection picture, as displayed in in Figure 2.14 (dashed-dotted line). To yield comparable detector setup conditions, i.e., anti-parallel control sideband phasors for all detector tunings, the signal-recycling cavity length of GEO 600 needed to be elongated by roughly 5 m for the respective FINESSE simulation.

The FINESSE and projection picture results agree very well for high detunings. The lower the detector tuning, the larger the difference, at most 8 Hz for 400 Hz detuning. As Equation 2.10 is only valid for high tunings, this feature was expected. The lower limit to the detector tuning for the validity of all deduced equations between Equation 2.9 and 2.14 was led by qualitatively assessing the signal phasors' phases in the phasor diagrams of Figure 2.6 to 2.8. With this approach, the limit was estimated to be approximately the signal-recycling cavity bandwidth (please follow the detailed argumentation on Page 58).

Whereas Equation 2.10 was analytically deduced by phasor diagrams assuming particular signal sideband field properties, all sensitivity curves in this thesis derived with the projection picture, utilise the full information on field amplitudes and phases provided by FINESSE. Thus, the agreement of the projection-picture sensitivity curves with FINESSE should not depend explicitly on the tuning, but rather on the importance of effects that FINESSE is able to account for¹⁸.

Consequently, the sensitivity deviation of a detector setup with optimised control sideband frequency from the configuration of GEO 600 should agree well for the projection picture and FINESSE. Figure 2.20 compares this sensitivity deviation for the two approaches, for different detector tunings, supposing the best demodulation phase for each gravitational-wave frequency of the particular sensitivity curve. The solid lines display the results of FINESSE. The corresponding projection picture outcome from Figure 2.17

¹⁸The impact of these effects can, of course, differ for various detector tunings.

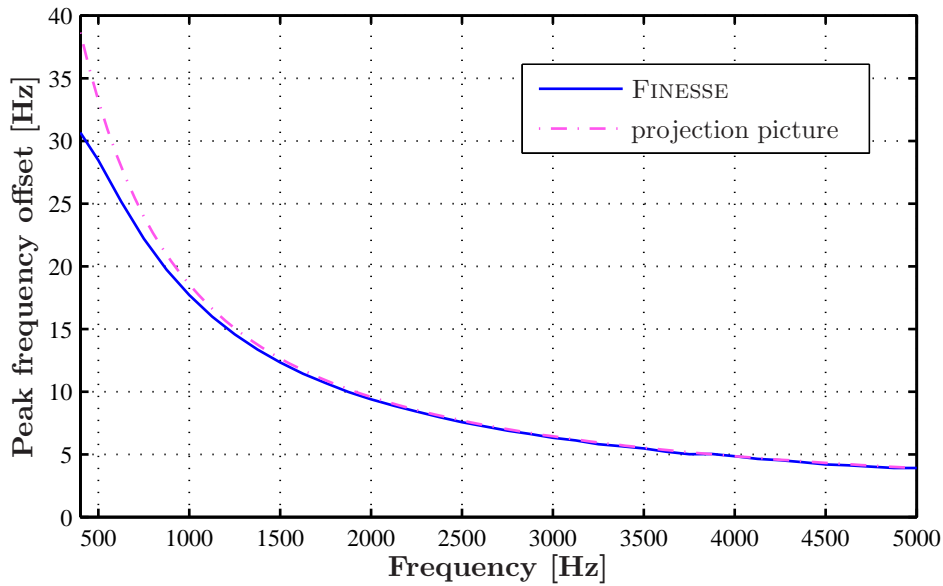


Figure 2.19.: Frequency shift of the peak sensitivity dependent on the detector tuning. The solid and dashed-dotted lines represent FINESSE and projection picture results, respectively. The dashed-dotted line is the same as in 2.14. The agreement for high detunings is very good and gets worse, the closer the detuning to the signal-recycling cavity bandwidth, as anticipated with the validity regime of the phasor diagram of Figure 2.8.

is, for each tuning, represented by a dashed-dotted line of the respective colour. The agreement for low detunings is very good and deviates more for higher tunings, mainly around the resonance. As all extra effects of FINESSE were disabled, the only source for disagreement are the signal sidebands around the control sidebands in combination with the carrier appearing at the south port due to asymmetries of the Michelson arms (see also Figure 4.6 and Section 4.4).

In the real experiment, all occurring sideband beats, and higher order modes and sidebands contribute to the shot-noise limited sensitivity, and need to be accounted for. Thus, to predict an improvement of an optical setup in sensitivity, a powerful simulation tool like FINESSE should be used. However, the FINESSE input file, representing GEO 600, is not perfect. Depending on the targeted function to be simulated, the inaccuracies more or less contaminate the results. Figure 2.21 shows the same comparison as Figure 2.20, but includes higher order modes and sidebands, differential losses and modulation indices corresponding to measurements.

Although at first glance the figures 2.20 and 2.21 differ a lot, in fact the shape of the curves are roughly the same, except for a hump occurring at different frequencies above 1 kHz. These humps are the consequence of the DC carrier beating with the signal sidebands around the control sidebands (see Section 4.4 for these sidebands' transfer function to the detector output).

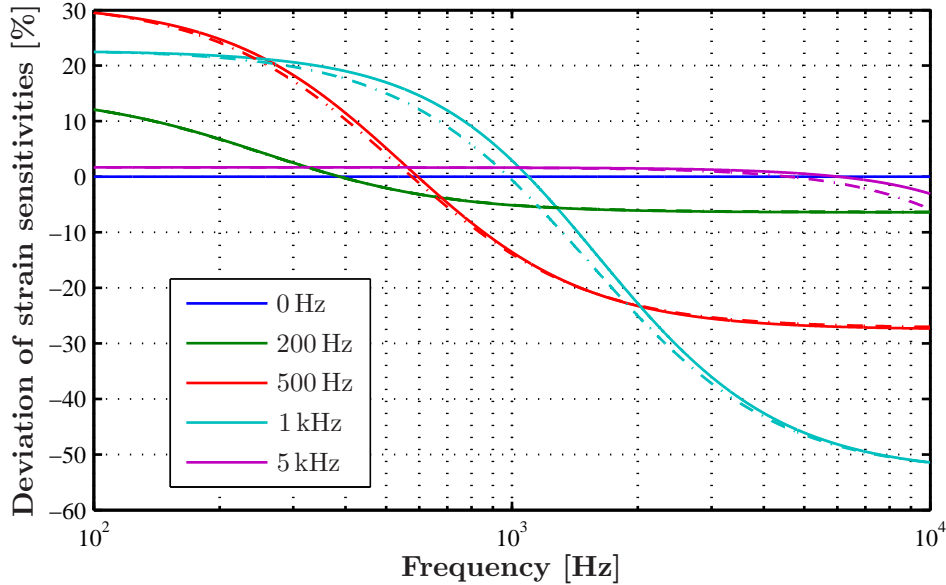


Figure 2.20.: Comparison of the results of the projection picture (dashed-dotted) and FINESSE (solid) for the deviation of the sensitivity of the optimised sideband frequency setup, with that of GEO 600. The lower the tuning, the better the agreement. For detector tunings higher than 1 kHz, FINESSE predicts a larger sensitivity improvement than the projection picture.

The different absolute values of the deviation curves show that the sensitivity depends on the control sidebands' effective amplification. This is already visible with the blue curve comparing the tuned detector-setups. As Figure 2.16 indicates, the sideband amplitude for tuned detectors is in the optimised case roughly 20 % higher than the default amplitude. The improvement in sensitivity is of the same order. At 500 Hz, the amplitudes are nearly the same. For all higher detunings, the sideband amplitude of the default setup is higher than for the optimised sideband frequency.

The sensitivity gain being roughly proportional to the sideband amplitude indicates very high carrier waste at the south. Indeed, shortly before this work was written, a new **MPR** was installed with a low transmission of ~ 900 ppm. This highlighted losses inside the power-recycling cavity due to the Michelson interferometer that are not yet understood. In the simulation, one part of these losses was guessed to be differential Michelson arm losses, another part to be caused by mode-mismatch due to the far end mirrors. Some power measurements, made at the south port, indicate less waste light than the simulation finds. However, as the observations made so far do not consistently explain the losses seen, the nature of the loss channel remains unknown. As many features of the experiment, like transfer functions, are well described by the actual script, it is currently the best available representation of the experiment.

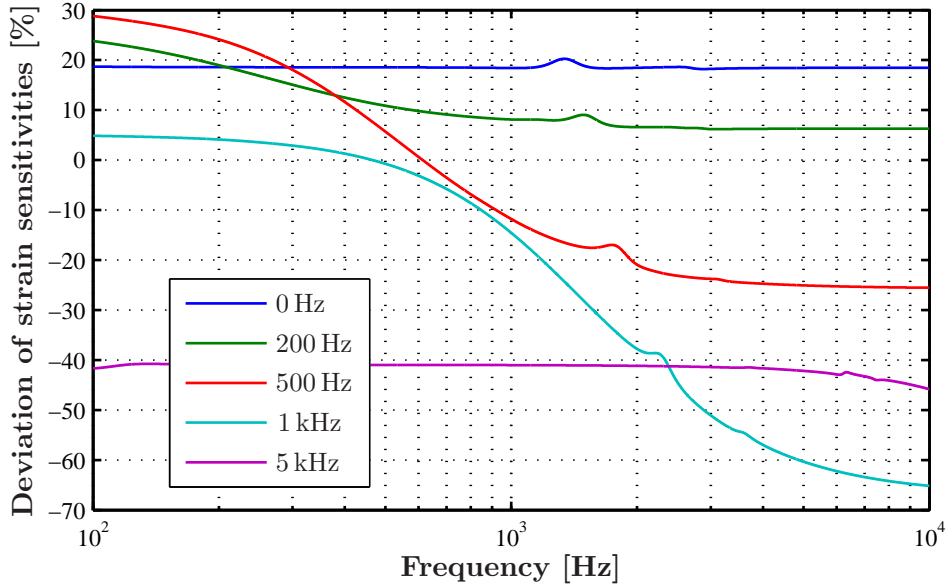


Figure 2.21.: FINESSE result for the sensitivity deviation of the optimised and original GEO 600 setup, for particular detunings. This simulation accounts for asymmetries in the Michelson arms and higher order modes and sidebands. The curve shapes are very similar to Figure 2.20, except for a detuning dependent offset and a hump above 1 kHz.

Assuming that the simulated output powers of GEO 600 were like in the experiment, the modulation index would need to be increased until the sideband power exceeds the waste light. A frequency optimisation of the control sidebands in such a setup will exhibit the same sensitivity deviation levels as predicted in Figure 2.21, though including a hump above ~ 1 kHz.

2.6. Conclusion

In this chapter, phasor diagrams were applied to determine the differential detector output, containing the strain, $h(t)$, of gravitational waves. Via the simple and illustrative projection picture, that only considers first order signal and control sidebands, the main characteristics of sensitivity curves can be predicted and explained.

Considering not only two signal sidebands for the Michelson error-signal, but also the two possible quadratures of gravitational waves, leads to a four-dimensional error-signal vector that is able to reproduce the optical gain of the dual-recycled Michelson interferometer, in magnitude and phase. The presented mathematical frame-work also enables us to relate this vector to optical transfer functions employing particular demodulation phases (see Section 2.3.2).

The projection picture shows that the sensitivity shape only roughly follows the Airy-function for the resonant signal sideband. Depending on the control sidebands' properties, the non-resonant signal sideband more or less distorts the resonance structure and moves the frequency of maximum sensitivity (see Section 2.3.3 to 2.3.4, and in particular Figure 2.13 and 2.14 in Section 2.4.1).

The control sideband properties at the output photodiode are influenced by all mirrors and macroscopic and microscopic lengths occurring in the dual-recycled Michelson interferometer. One practical consequence of the control sidebands' influence on the shape of the sensitivity curve is that, without detailed knowledge about the detector, the frequency of peak sensitivity only gives a rough approximation to the real signal-recycling cavity tuning. This becomes important, for example, when trying to compare experimental sensitivity curves with simulations, or for (further) predictions about (other) error-signals related to the experiment.

With the projection picture it could generally be shown that the amount of signal contained in a demodulated error-signal depends not only on the demodulation phase, but also on the control sideband amplitude (see Figure 2.9 and comments on Page 53).

With equal sideband amplitudes, there exists one demodulation phase such that the respective error-signal contains the entire gravitational-wave signal for the complete detection bandwidth. Moreover, for arbitrary pairs of perpendicular demodulation phases, the ratio of signal content is constant for all frequencies (see figures 2.5 and 2.6).

If, however, one control sideband amplitude significantly exceeds the other (which is the case if the resonance conditions for both sidebands differ inside the dual-recycled Michelson) the signal content is exchanged between error signals of arbitrary perpendicular demodulation phases over the detection bandwidth (see Figure 2.8).

The parameter space responsible for the shape of sensitivity curves of a dual-recycled Michelson interferometer is huge. Without an illustrating picture of the error-signal, tremendous simulational effort is necessary to make any global qualitative statement about coupling mechanisms from features of the optical setup or signal transfer to particular sensitivity characteristics.

The projection picture enables, with only a few simplifications, to circumvent blind searches by analytical calculations for a global, dual-recycled-detector-setup comparison regarding the differential-signal yield, for a wide range of detunings (see equations 2.12 to 2.14). Numerically evaluating the analytical expressions indicates that for all signal-recycling cavity tunings the best sensitivity for low and resonant gravitational-wave frequencies can be achieved if both control sidebands resonate in a tuned signal-recycling cavity. Particularly for low frequencies, the smaller the signal-recycling cavity bandwidth for the control sidebands the better. Resonant frequencies are hardly worth an optimisation, as the best possible improvement, comparing to a very pessimistic worst case, is limited to 1.2. The larger the difference between the control sideband frequency and the next integer multiple of the signal-recycling free spectral range, the better the sensitivity for high gravitational-wave frequencies at the expense of low and resonant frequencies. These predictions are, due to the initial simplifications, limited to detunings larger than

the signal-recycling cavity bandwidth for the signal sidebands (see Section 2.4.2 and Page 58).

In order to meet the requirements for the control sidebands for any kind of optimisation, the optical configuration needs to be altered systematically. As the installation of GEO 600 is already finished, the only parameter accessible for a change is the modulation frequency of the control sideband. Consulting FINESSE simulations with the current optical setup of GEO 600 for an optimisation of the sensitivity for low signal frequencies, there exist two control sideband frequencies close to the 119th signal-recycling free spectral range that resonate in a tuned signal-recycling cavity, but only one has a decent amplitude and an acceptable signal-recycling cavity bandwidth (see Figure 2.16). Comparing the current GEO 600 setup with this best possible optimisation in situ, an improvement of up to 30 % at 100 Hz should be obtainable (see figures 2.17, 2.20, and 2.21).

The predictions still hold qualitatively, if signal sidebands around control sidebands, or higher order modes and sidebands are accounted for¹⁹, as done by FINESSE (see Section 2.5).

¹⁹Please note that throughout this chapter the transfer of technical noise sources, associated with optics, was not considered. To compare sensitivity curves, the best possible signal read-out was assumed, and the shot noise appearing at the output photodiode was simply divided by the optical transfer function. A noise transfer that possibly differs for various configurations, could, in principle, lead to a different optimal setup.

Chapter 3.

Tuning process of a dual-recycled Michelson interferometer

3.1. Introduction

GEO 600 is presently the only large-scale gravitational-wave detector of the worldwide network that incorporates dual recycling (please consult Section 2.2 for an explanation of this interferometric technique). A respective upgrade of the other gravitational-wave detectors is planned for the second generation. The commissioning of such a dual-recycled detector requires an adequate control of all degrees of freedom, including not only longitudinal but also alignment of the involved mirrors. Particularly with regard to operating as an observatory, an automation of the startup (or *lock acquisition*), and of successive changes of the detector peak sensitivity or bandwidth, to match a special gravitational-wave source, are indispensable. (The peak sensitivity and bandwidth depend on the microscopic position and the reflectivity of the signal-recycling mirror, respectively.) For this an extended knowledge of the signals needed for control, especially their dependencies on various degrees of freedom, is necessary. This huge parameter space is accessible only via simulations, which in the past have contributed heavily to the understanding of the detector.

To date, trading off the bandwidth and frequency of maximum sensitivity at GEO 600, and considering the sensitivity of the other first-generation gravitational-wave detectors, we aim for a final detuning in the order of ~ 100 Hz. However, simulations show that locking the detector directly in that state is very difficult. The lock probability is much higher in a largely detuned state [Grote03a, Grote03b]. Moreover, an auxiliary error-signal (*2f signal*) for the signal-recycling cavity length degree of freedom is necessary for the acquisition of lock. The current strategy is to first catch and lock the mirrors of the detector to a position corresponding to a detuning of roughly 2.4 kHz. Then, after switching to a less noisy signal-recycling error-signal (*sideband signal*), the detuning is shifted down to the desired value, without interrupting the lock. The technique to shift the frequency of peak sensitivity in situ was first investigated at the Garching 30 m prototype [Heinzel99].

To implement such a transition without loss of lock, error-signal characteristics for each signal-recycling state need to be tracked within a very large parameter space. Once the

detector is locked, it can be regarded as being in a quasi-static state. Predictions for a slow continuous movement of the signal-recycling mirror **MSR** without the loss of lock can therefore be made with a frequency domain simulation program like FINESSE (see [FINESSE] for download and further information).

This chapter deals with the process of continuous tuning of the frequency of peak sensitivity for a dual-recycled detector with an optical setup similar to GEO 600. Before analysing the error-signals for the relevant degrees of freedom, first the generation of these error-signals and the respective control loops will be described. However, the explanations here will focus on features relevant for the tuning process. Subsequently, the phasor picture is used to illustrate the properties of the signal-recycling and Michelson error-signals to be expected, and to relate these properties to detector attributes. This knowledge is then used to qualitatively predict the evolution of parameters relevant for the signal-recycling and Michelson control loops. In order to quantitatively determine the control-loop parameters, various optimisation criteria for the error-signals will be discussed and the respective simulation results presented and evaluated. In the end, the same parameters are presented for a detector utilising an etalon instead of a conventional signal-recycling mirror.

3.2. The longitudinal control of GEO 600

For the operation of the dual-recycled Michelson of GEO 600, three degrees of freedom need to be controlled: the differential armlength of the Michelson interferometer, the signal-recycling cavity length, and the lengths of the power-recycling cavity or, alternatively, the laser frequency. Although at GEO 600, in the frequency bandwidth of the detector, the laser frequency is stabilised against the power-recycling cavity length, the associated control is called power-recycling control. Figure 3.1 shows an overview of the dual-recycled Michelson of GEO 600 surrounded by the respective control loops, and includes one of the two mode-cleaners. The paths for the Michelson, and the power- and signal-recycling cavity are marked solid blue, dotted magenta and dashed green, respectively. The dashed-dotted cyan path represents the so-called $2f$ signal path that contributes to the Michelson and signal-recycling lock acquisition. The following subsections describe each of the controls, focussing mainly on the facts necessary to allow for the development of a successful strategy for a continuous tuning.

The power-recycling control is not critical for the tuning process. It is nonetheless briefly explained. For the sake of completeness the lock acquisition is outlined as well.

3.2.1. Laser frequency stabilisation and power-recycling cavity lock

The light source of GEO 600 is an injection locked master-slave laser system with an output power of 14 W. This laser light successively passes two mode-cleaner systems that filter out beam geometry fluctuations and reduce the amplitude and frequency noise. The amplitude and frequency noise of a light beam passing a cavity is filtered out for Fourier

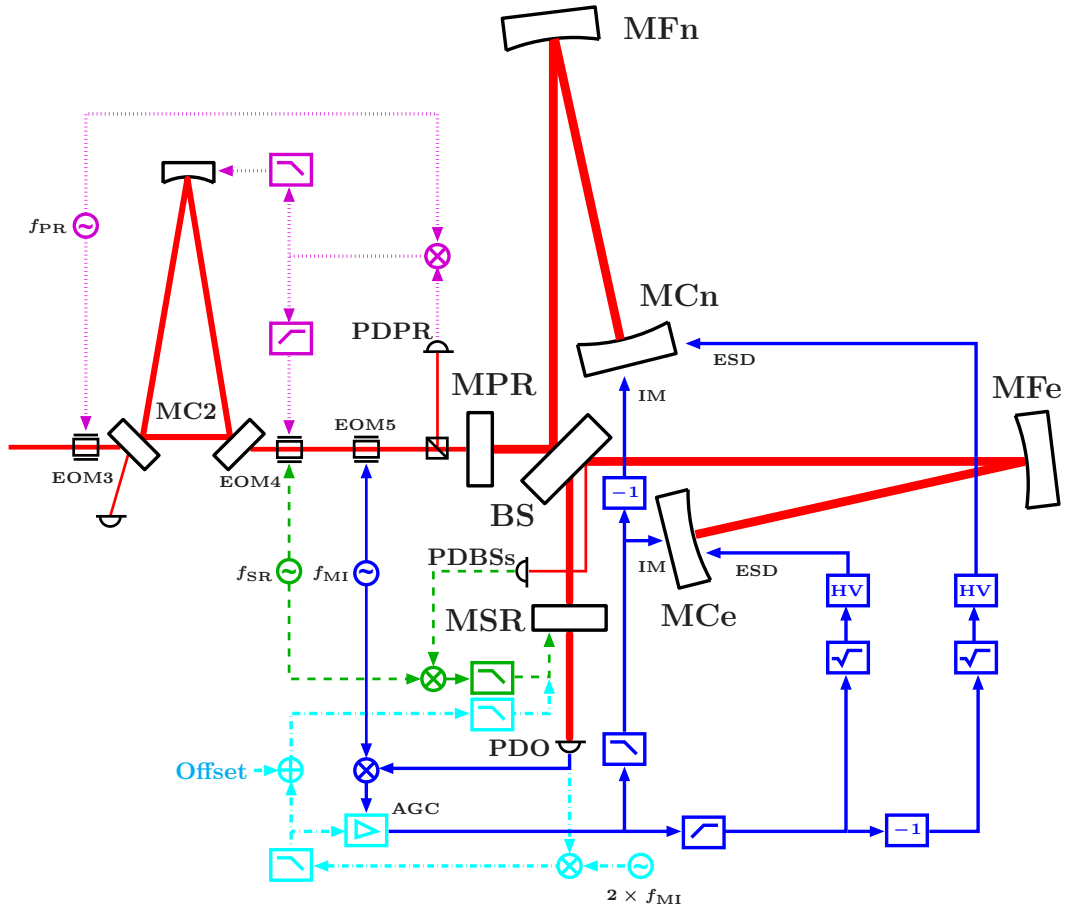


Figure 3.1.: Overview over the longitudinal control loops relevant for the lock of the dual-recycled Michelson interferometer of GEO 600: the control paths for power and signal recycling, and the differential Michelson are marked with dotted magenta, dashed green, and solid blue lines, respectively. The path for the so-called $2f$ signal, contributing to both the differential Michelson and the signal-recycling error-signals, is displayed by dashed-dotted cyan lines.

frequencies above the cavity pole which is equivalent to half of its bandwidth. Thus, the longer the cavity and the larger the finesse, the smaller the bandwidth, and the better the filtering effect. In addition, the relative length noise of the cavity, $\delta L/L$, improves with increasing length, as the absolute mirror motions are independent of the cavity length. The first and second mode-cleaners are triangular ring cavities of ~ 8 m round-trip length and a with finesesses of 2700 and 1900, respectively. The bandwidths are of the order of 10 kHz.

To acquire a stabilisation or *lock* of the mode-cleaners and the laser, the master-laser crystal is locked to the length of the first mode-cleaner. The length of the first mode-cleaner is then stabilised to the length of the second mode-cleaner (MC2). At frequencies lower than 10 Hz MC2 is locked to the pathlength inside the master laser. This lock is also called *DC-lock*¹. More details on the laser and mode-cleaner systems can be found in [Brozek00a, Brozek00b, Zawischa02, Willke00, Willke00, Freise03a] and [Freise03a, Gößler02, Gößler03, Grote04], respectively.

With this chain of control, the rms length change of MC2, together with the open loop gain of the control, determines the residual frequency noise in front of **MPR**.

The frequency stabilisation has, in general, two main purposes: one is to facilitate the acquisition of resonance of the laser light inside the power-recycling cavity, i.e., the *lock acquisition*. The main purpose is, however, the reduction of laser frequency noise that couples into the output of the Michelson: as explained in Section 1.2.4 and 2.2, the error-signal generation for the differential Michelson necessitates a macroscopic armlength difference: the so-called Schnupp length. Due to this asymmetry, the Michelson is sensitive to frequency fluctuations of the incoming light. The light leaking out of MC2 has a residual rms frequency deviation of $30 \text{ mHz}/\sqrt{\text{Hz}}$ at 100 Hz. Early and more recent calculations [Brozek99, Freise03b], however, indicate a requirement of ~ 5 to $100 \mu\text{Hz}/\sqrt{\text{Hz}}$ at 100 Hz (depending on the exact optical configuration of GEO 600, as for example the deviation from the dark fringe or the amount of detuning), in order to not contaminate the output signal.

To nonetheless meet the requirements, above 50 Hz the length of MC2, and thus the laser frequency, is locked to the power-recycling cavity length. With an effective length of ~ 1.2 km and a Finesse of roughly 6600 and 460 for the new and old **MPR**², respectively, the bandwidth is 2 or even 3 orders of magnitude lower than for the mode-cleaners, and the relative length stability is improved by factor 300, assuming the same rms mirror motion. The mirrors of the signal-recycled Michelson interferometer, and **MPR** are suspended as triple, and double pendulums, respectively. Having one pendulum stage less than the interferometer mirrors, **MPR** dominates the frequency stability of the power-recycling cavity in the detection band of 50 Hz to 5 kHz. The double-pendulum attenuation of the

¹The DC-lock is particularly necessary for the power-recycling lock acquisition (see the *Locking sequence* in Section 3.2.4). The mode-cleaner mirrors are suspended as double-pendulums with resonance frequencies around 1 Hz. Depending on the seismic conditions, the rms movement of the mode-cleaner mirrors below 10 Hz may amount to $1 \mu\text{m}$. The associated frequency change of the carrier leads to fringe rates at the unlocked power-recycling cavity of $\sim 100/\text{s}$.

²Before May 2005, when the new, high-reflective **MPR** (with $T_{\text{MPR}} = 900$ ppm) was installed, GEO 600 was operated with a lower-reflective mirror, with $T_{\text{MPR}} = 1.35\%$.

seismic noise yields a frequency stability of $\sim 0.2 \mu\text{Hz}/\sqrt{\text{Hz}}$ at 50 Hz (neglecting coupling effects from vertical to longitudinal mirror movements, see page 3 in [Grote03b]). Thus, at 100 Hz the power-recycling cavity is better than the requirements by a factor of 100 to 2000, depending on the optical configuration (see paragraph above).

The power-recycling error-signal is generated by the Pound-Drever-Hall technique (see Section 1.2.2), phase modulating the laser light impinging on MC2 with $f_{\text{PR}} \approx 37.16 \text{ MHz}$ at EOM3³, and detecting with **PDPR** in reflection of **MPR** (see dotted magenta paths in Figure 3.1). Up to 1 kHz, the error-signal is fed back to the length of MC2. For higher frequencies, the actuation takes place at EOM4, just in front of **MPR**. The particular open loop gains and phases for the two actuator paths, and for the combined loop are displayed in Figure 3.2. The unconditional stability⁴, i.e., the phase of the sum exceeding -180° plus a certain phase margin, makes the loop very robust during the time of lock acquisition of the Michelson⁵.

Once the Michelson interferometer is locked to the dark fringe, the power-recycling cavity should be very insensitive to the tuning of the signal-recycling cavity. As with a dark fringe, ideally no carrier light is exchanged between the power and the signal-recycling cavity (of course, except for gravitational-wave sidebands), the carrier amplitude and phase is completely determined by the tuning of the power-recycling cavity only. Thus, the power-recycling loop does not require any further considerations when tuning the signal-recycling cavity.

3.2.2. Longitudinal control of differential Michelson arms

The Michelson interferometer is the basic optical system for the detection of differential length changes, and thus, of gravitational waves. Its intended operating point, the dark fringe, makes sure that all light incident on the Michelson is reflected back, enabling power-recycling and signal recycling. As deviations from the dark fringe increase, the coupling of amplitude and frequency noise into the Michelson output signal, the respective control loop and, in particular, the actuator performances, are of vital importance to achieve design sensitivity.

Actuators

The Michelson error-signal, being the targeted output containing the gravitational-wave signal, requires a low-noise actuator in order not to introduce additional noise when feeding back to the Michelson end mirrors. The coil-magnet system used for actuation

³The modulation frequency is set to resonate inside MC2. With 37.16 MHz, the frequency lies approximately in the middle of the 296th and the 297th multiple of FSR_{PR} . Thus, it very well satisfies the requirement deduced in Section 1.2.2 for the generation of the Pound-Drever-Hall error-signal.

⁴The difference of the cavity transfer function with two differing **MPRs** is irrelevant as it only moves the pole frequency (by roughly one order of magnitude).

⁵After lock acquisition of the Michelson, the unconditional stability is relinquished for the sake of increased loop gain below 2 kHz, adding two integrator stages.

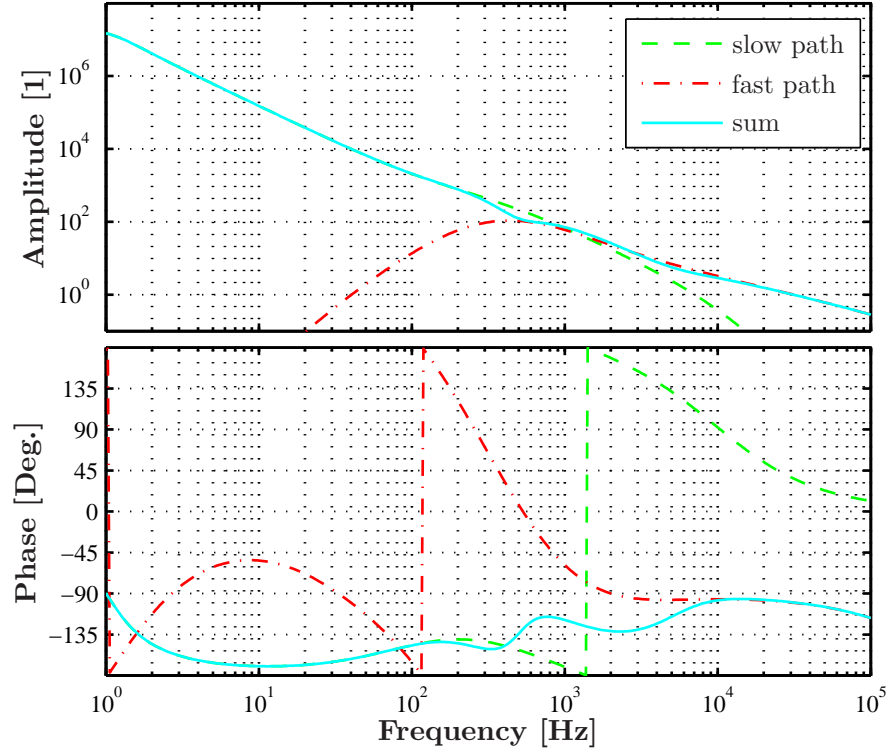


Figure 3.2.: Overall open loop gain (upper graph) and phase (lower graph) of the power-recycling control loop. The slow path (dashed green line), controlling the position of one mirror of MC2, and the fast path (dashed-dotted red line), feeding back to EOM4, have a cross-over frequency of ~ 1 kHz. The phase of the combination of the two (solid cyan line) ensures unconditional stability of the loop which is useful in the lock acquisition process.

of the other mirrors of the detector requires magnets to be fixed on the mirror to be controlled. This has two disadvantages: on the one hand magnets are sensitive to time-dependent magnetic field gradients that may exert unwanted forces on the mirror; on the other hand, having the magnets stuck directly on the mirror could degrade the very high quality factors⁶ of the mirrors and increase the associated thermal noise.

GEO 600 is the first large-scale gravitational-wave detector actuating on the Michelson end mirror displacement with an *electrostatic drive (ESD)*. An ESD moves the mirror by a strong electric field that acts on the dielectric mirror substrate. For this, four pairs of thin gold electrodes are coated in comb-like, interlocked structures onto a fused silica substrate, the so-called *reaction mass*, that has same size as the end mirrors. Each

⁶The quality factor is important for the thermal noise level of the mirror (see [Goßler04] for a detailed explanation). GEO 600 is the first large-scale gravitational-wave detector utilising a monolithic silica pendulum as the lowest stage of the triple pendulum suspension to increase the quality factor Q . Depending on the pendulum mode, the measured Q varies between 10^5 and 10^7 [Smith04a].

electrode pair is arranged in one of four quadrants allowing for alignment forces as well. The comb fingers are separated by 5.5 mm. The range of the resulting electric field is sufficient for a mirror distance between 1 to 3 mm from the ESD.

As mentioned above, the main interferometer mirrors are suspended as triple pendulums to more effectively filter seismic noise. In order to bring the mirror and reaction mass close together without degrading the seismic noise isolation, the reaction mass is suspended next to the mirrors with an identical pendulum system. Figure 3.3 shows the arrangement of the two triple pendulums. The suspension in the front holds the mirror, the one in the back holds the reaction mass. There are three different mass stages, the upper, the intermediate, and the lower level where either **MCe** or **MCn** are located.

The electric field of the ESDs is only able to apply pulling forces on the dielectric mirror. Hence, in order to obtain a bipolar actuation, a bias of the field is required. This is accomplished by applying a constant, high voltage to one electrode, while the feedback signal is applied to the other. Another difference from the commonly used coil-magnet actuators is that the electric force is proportional to the square of the field amplitude, hence, to the square of the voltage applied: on the one hand, the electric field induces a dipole to the dielectric proportional to the field, on the other hand, the force applied to the polarised dielectric is proportional to the field from the ESD. Using an analog control, this is accounted for by a square-root (sqrt) circuit in the path of the drive voltage. (For digital controls it can be done digitally.) The resulting maximum applicable force of $500 \mu\text{N}$ is, in combination with the Michelson error-signal, sufficient for lock acquisition.

However, the sqrt-circuit introduces additional noise. Once the Michelson is locked, the mirrors have a comparably small rms motion. If the symmetric signal is significantly smaller than the bias voltage, the force gets approximately linear to the signal voltage, and the sqrt-circuit can simply be bypassed. (More details on the ESD actuator can be found in section 1.3 of [Grote03b].)

With this operation method, though, the maximal possible displacement shrinks to $< 100 \text{ nm}$. This necessitates another actuator in lock for the expected large mirror movements at frequencies close to the pendulum resonances. The low-frequency actuation is achieved with three coil-magnet actuators situated at the intermediate level, between the reaction and intermediate masses (IM). Due to the transfer function of the lowest pendulum, the applicable force from the intermediate level on the end mirror decreases with $1/f^2$, but at low frequencies the force enables a displacement of up to 0.1 mm.

The far Michelson mirrors, suspended 600 m from the beamsplitter, are controlled only in the very low frequency region ($< 0.1 \text{ Hz}$) to compensate motions below pendulum resonances.

Control loop

The Michelson control loop is represented in Figure 3.1 by the solid blue path. As already mentioned in Section 1.2.4, the error-signal is generated with the Schnupp (or *frontal*) modulation technique. The respective modulation (or *Schnupp*) frequency is applied on

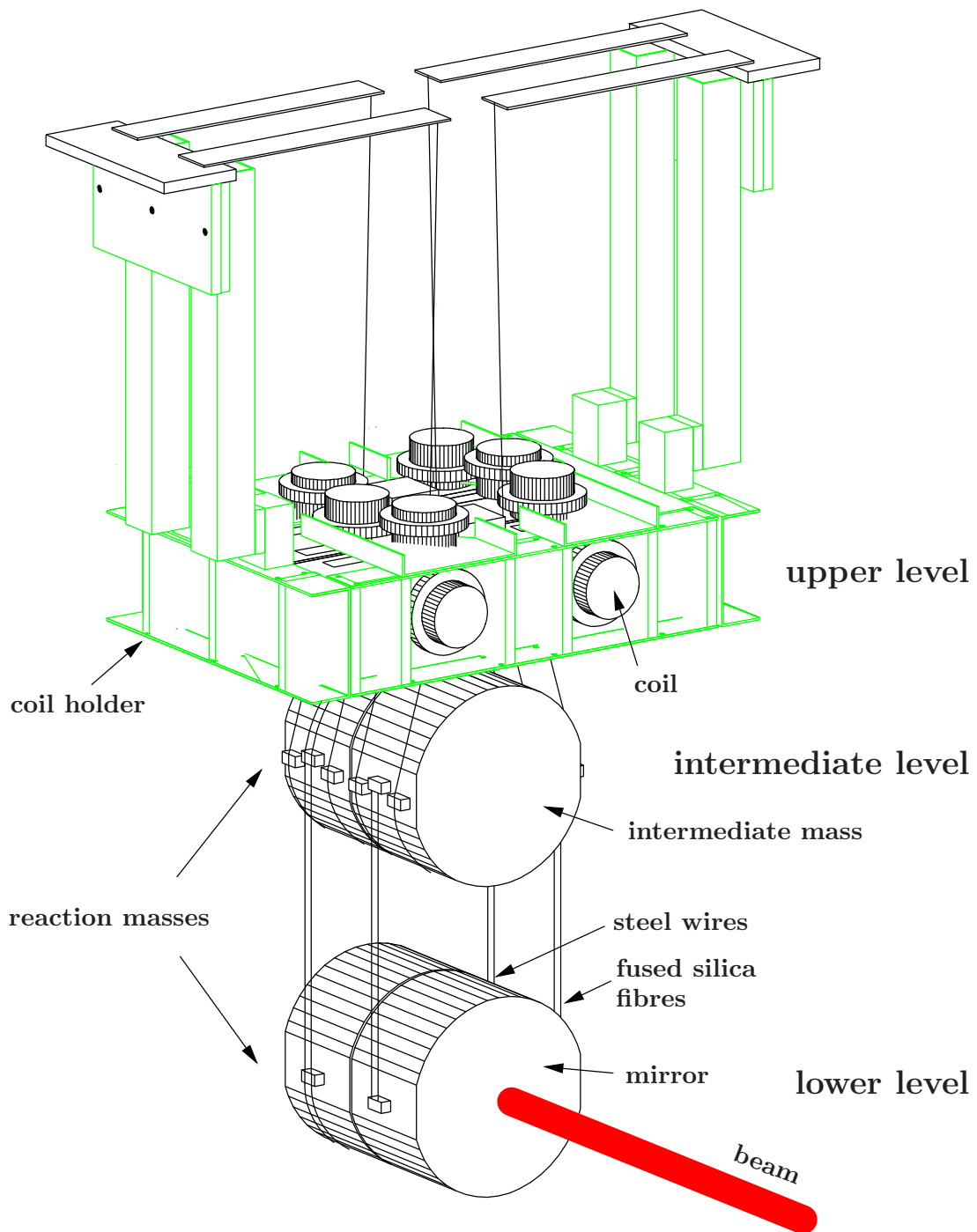


Figure 3.3.: Triple pendulum suspension of one Michelson end mirror (front suspension) and its corresponding reaction mass (back suspension). Whereas the coils of the *local control* of the upper mass are visible, the coil-magnet actuators of the intermediate-mass stage are hidden between the reaction and the intermediate masses (IM).

EOM5 in front of **MPR**. Accounting for Equation 1.27, the Schnupp frequency is currently chosen to be 14.904927 MHz, yielding maximum amplitude at the output photodiode PDO, the place of the error-signal detection, for a detector detuning of ~ 1 kHz. The frequency is close to the 119th multiple of the *FSR* of the power-recycling cavity⁷, being 125.251 kHz. After demodulation of the PDO signal at the mixer, the error-signal gets split and processed. One path differentially applies the low-frequency part of the error-signal to the IMs, the other forwards the high-frequency content to the ESDs by passing the high-voltage amplifier (HV). The sqrt-circuit is only applied for lock acquisition, as explained above.

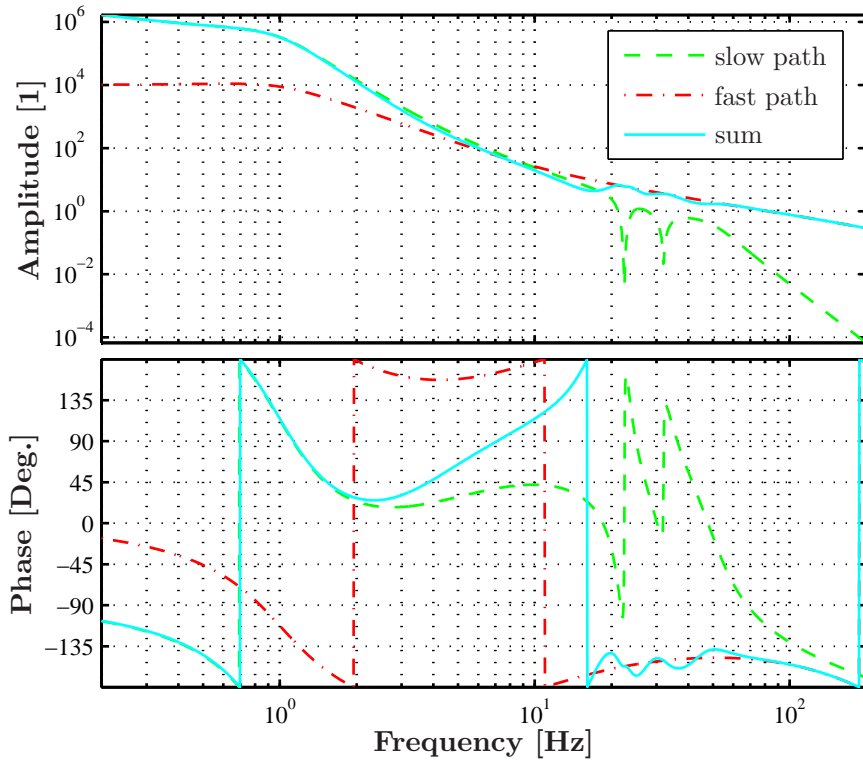


Figure 3.4.: Overall open loop gain (upper graph) and phase (lower graph) of the Michelson control loop. The slow path (dashed green line), applying to the IMs, and the fast path (dashed-dotted red line), feeding back to the ESDs, have a cross-over frequency at ~ 7 Hz. The phase of the combination of the two (solid cyan line) indicates a conditional loop stability for unity-gain frequencies between 30 Hz and 120 Hz. With the nominal unity gain frequency of ~ 80 Hz, the gain may only vary by a factor of 0.275 to 1.64.

⁷Due to the coupling of the two recycling cavities, the exact power-recycling resonance does not necessarily yield the largest sideband power at the output. An exact resonance rather degrades the reflectivity of the power-recycled Michelson being the compound input mirror to the signal-recycling cavity. Figure 2.16 shows the Michelson sideband amplitude behind **MSR** depending on the frequency and signal-recycling cavity tuning.

Figure 3.4 displays the open loop gain (upper) and phase (lower) of the slow (dashed green lines) and fast path (dash-dotted red lines), and of the combination of the two (solid cyan lines). For lock acquisition, the fast path alone is valid (acquisition mode), in lock the sum of the two paths is applied (run mode). The cross-over between the fast and slow paths happens to be at ~ 7 Hz. The phase dependency of both the acquisition and run mode yields a conditionally stable loop. A phase margin of 30° is for both modes guaranteed for unity gain frequencies between 30 Hz and 120 Hz. With the nominal unity gain frequency of ~ 80 Hz, the correspondingly tolerable gain deviation lies between 0.275 and 1.64.

After the power-recycling cavity is locked, the signal-recycling and differential Michelson tuning are still uncontrolled. Influencing the modulation sideband amplitudes appearing at PDO, the signal-recycling cavity tuning can make a difference of more than an order of magnitude to the optical gain of the Michelson. In order to stay within the tolerable gain interval during the lock acquisition process, the error-signal needs to get normalised with respect to the modulation sideband amplitudes. Referring to Equation 1.17, the photodiode signal demodulated with twice the modulation frequency (hence the name 2f signal) is proportional to the product of the sideband amplitudes, giving a measure of their height. Thus, this signal is suitable and used for real-time normalisation⁸ during the lock acquisition process, also called *automatic gain control (AGC)*. The respective path leading to the AGC box inside the Michelson loop is marked dashed-dotted cyan in Figure 3.1.

As the Michelson error-signal slope depends not only on the sidebands but also on the resonance of the carrier inside the signal-recycling cavity (in case of deviations from the perfect dark fringe, the carrier enters the signal-recycling cavity), the modulation sidebands' product only roughly matches the optical gain. Figure 3.5 enables a direct comparison of the Michelson error-signal slope (solid blue line) with the 2f signal evolution (dashed-dotted magenta line) depending on the signal-recycling cavity tuning. The two graphs agree very well in a wide range of detunings. For tunings below ~ 1 kHz, however, they split up⁹. At 350 Hz they already differ by a factor of 2. Thus, for an operation of the detector over a large frequency range, in particular for low detunings, a different, deliberate compensation of the optical gain deviations is necessary. As soon as the lock is fully acquired, the detector is in a well-defined state allowing for a determined gain control instead of the normalisation by the 2f signal.

⁸In the experiment, the 2f signal is generated by demodulating the PDO signal not exactly at twice f_{MI} , but 30 kHz away. The resulting, oscillating signal is then rectified and low-pass filtered. This is done to yield a signal independent of the demodulation phase. Mathematically, the additional frequency of 30 kHz can be attributed to the “constant” demodulation phase, alternating it with time. By rectifying and low-pass filtering, the signal at $2f_{\text{MI}}$ is averaged over all demodulation phases. Thus, for all signal-recycling cavity tunings, the same kind of weighing of the demodulation phases is done, and the signal has consequently a constant proportional factor to the sideband amplitudes' product.

⁹The range of agreement of the two graphs is even wider than shown, namely up to $\sim \pm 20$ kHz, neglecting absolute detunings below ~ 1 kHz. The larger range is not shown in order to focus on the maximum intended lock acquisition and tuning range of the detector.

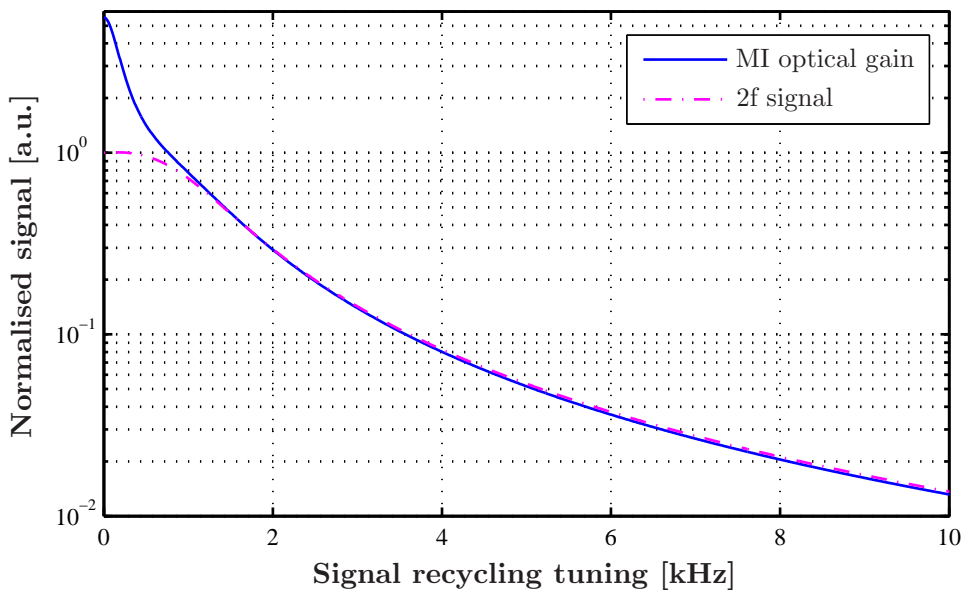


Figure 3.5.: Comparison of the Michelson error-signal slope evolution, depending on the signal-recycling cavity tuning, with the corresponding 2f signal. The two signals are normalised to match in the largest possible frequency interval. Still, below ~ 1 kHz they differ significantly. A difference of factor 2 is reached at 350 Hz detuning.

3.2.3. Longitudinal control of the signal-recycling cavity

The tuning of the signal-recycling cavity determines the resonance frequency for the gravitational-wave signal-sidebands, and thus the frequency of peak sensitivity. In targeting particular gravitational-wave sources of well-defined frequency, it may be advantageous to tune the signal-recycling cavity to resonate with this frequency. These cases require holding the signal-recycling cavity at a particular tuning with a decent offset from the carrier resonance. Beyond, it is desirable to switch between different frequencies of peak sensitivity during detector operation.

Section 1.2.2 explains how to obtain a Pound-Drever-Hall error-signal in cavity reflection that is suitable to hold that cavity at a constant tuning away from carrier resonance. The basic idea is to address a zero crossing appearing around one of the control sidebands' resonances which is adopted for the GEO 600 detector. The flexibility to obtain different signal-recycling cavity tunings can be achieved by correspondingly changing the modulation frequency.

This technique can, however, not be copied exactly one-to-one for GEO 600, as the targeted signal-recycling cavity is combined with the power-recycling cavity and the Michelson interferometer. The power-recycled Michelson, being the compound input mirror to the signal-recycling cavity, has for example different reflectivities and transmissions for

different light frequencies. Considering arbitrary modulation sideband frequencies for signal recycling and the very high finesse of the power-recycling cavity, the sidebands will for most frequencies be anti-resonant inside the power-recycling cavity. With the current setup, the transmission of the power-recycled Michelson (prMI) for a (close to) anti-resonant modulation frequency around 9 MHz is ~ 1 ppm, and $R_{\text{prMI}} = 99.993\%$. Thus, with $R_{\text{MSR}} = 98.15\%$, the signal-recycling cavity is a highly undercoupled cavity for most of the applicable modulation frequencies, and the sideband amplitude leaking out of the optical system through **MPR** is too weak to yield a decent error-signal amplitude in comparison with the large shot noise.

Targeting beats with the carrier, it is no alternative to switch to the output port in the south in order to avoid shot noise, and to gain modulation sideband amplitude: there is almost no carrier if, under perfect mode-matching and alignment, the Michelson is successfully operated at dark fringe. The Michelson arms are the only places where the carrier and the modulation sidebands both are present. This suggests three points for detection: either in transmission of one of the end or far end mirrors, or in reflection of the anti-reflective coating of the beamsplitter (**BSAR**). For historical reasons¹⁰, the light reflected from **BSAR** is used¹¹.

The respective control loop path is displayed dashed green in Figure 3.1. A modulation frequency around the 72nd *FSR* of the signal-recycling cavity ($FSR_{\text{SR}} = 125.2416$ kHz) is applied on EOM4. The error-signal is detected with PDBSs in reflection of **BSAR**, and is fed back, after demodulation and some electronic processing, to coil/magnet actuators at the lowest triple pendulum level of the **MSR**/reaction-mass suspension system¹².

For the lock acquisition it is important to decelerate **MSR** within the monotonic region of the error-signal around the targeted zero crossing. Guided by the error-signal deduction in Section 1.2.2 (or to anticipate, in Section 3.3.2), the width of the complete error-signal structure is expected to be in the order of the signal-recycling bandwidth. This corresponds to a limit of the one-sided monotonic region of ~ 200 Hz, or equivalently of ~ 1 nm only. Beyond, with the strong error-signal shape dependency on small dark fringe offsets and Michelson mirror misalignments (see Figures 2.9 and 2.11 in [Grote03b]), this *sideband signal* experimentally turned out to be infeasible for lock acquisition. Instead, the monotonic $2f$ signal of Figure 3.5 is used to capture **MSR**. In Figure 3.1, the dashed-dotted cyan path, leading to **MSR**, displays the corresponding control path: the same signal used for the AGC of the Michelson control is commuted to a suitable, bipolar

¹⁰Originally, the transmission of all Michelson mirrors and the reflection of **BSAR** were specified to 50 ppm such that none of them promised an improved *SNR*. The far end mirrors were unattractive due to their distance from the point of actuation. A detection at the end mirrors, located close beside **MSR**, is for space reasons inconvenient.

¹¹The enhanced modulation sideband amplitude at the south port can, however, be exploited with a read-out of the beat of the two control sidebands, demodulating the PDO signal with ~ 6 MHz. This is planned to be implemented in the near future. Recent simulations indicate that the signal-to-noise ratio of the corresponding error-signal is larger by a factor of roughly 6 with respect to the currently used signal-recycling error-signal.

¹²The suspension looks similar to Figure 3.3 but without the intermediate level. The coils are embedded in the reaction mass, and the magnets are glued onto the rear mirror surface opposite to the coils.

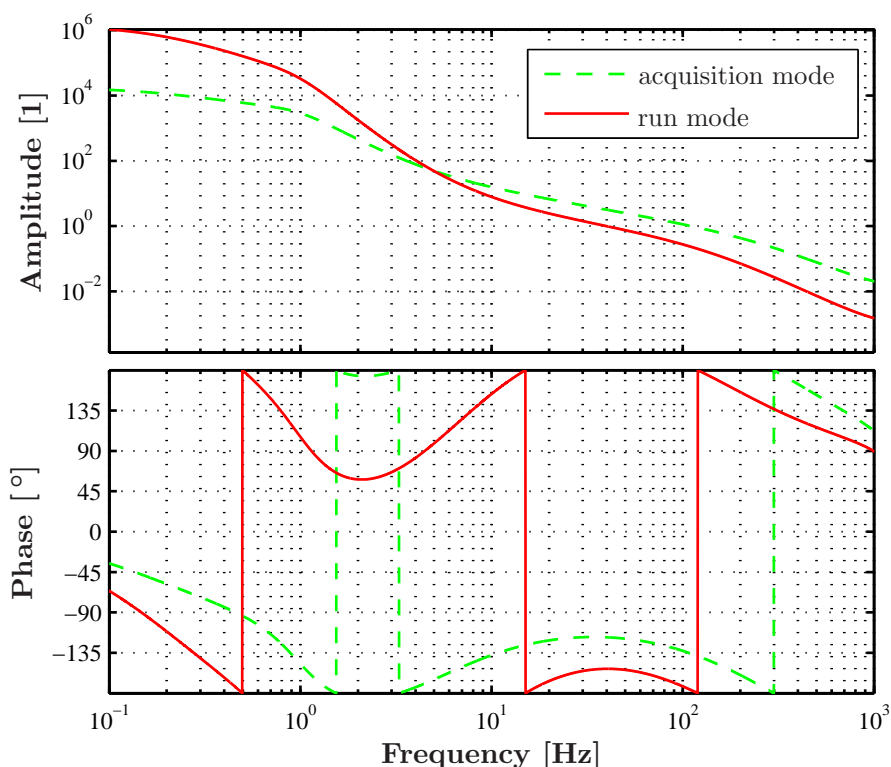


Figure 3.6.: Overall open loop gain (upper graph) and phase (lower graph) of the signal-recycling control loop. The acquisition mode (dashed green lines) uses the $2f$ signal, whereas the run mode applies the error-signal generated with the signal-recycling control sidebands.

error-signal by applying an offset. The amount of offset adjusts the exact signal-recycling operating point. Currently, it is set to yield a detector tuning of ~ 2.4 kHz.

Figure 3.6 shows the overall open loop gains (upper graph) and phases (lower graph) of the control loops using the $2f$ signal (dashed green lines, labelled “acquisition mode”), and the sideband signal (solid red lines, labelled “run mode”). As for the lock acquisition a large peak force is necessary, the acquisition bandwidth is roughly twice the run-mode bandwidth. In return, the run mode has a higher DC gain together with a steeper gain shape allowing for an improved loop performance and lower noise at high frequencies, once **MSR** is locked.

Each of the two loops yield a conditionally stable control servo. In the run mode, even if only a 20° phase margin is required, a stable loop is only probable for unity gain frequencies between 24 Hz and 69 Hz. Assuming a targeted unity gain frequency of roughly 40 Hz, the gain margin is limited to $[0.5, 2]$. Hence, when investigating the sideband error-signal for tuning purposes, the gain limits need to be accounted for.

The gain margin of the acquisition mode, comprising almost 2 orders of magnitude, is no problem in combination with the $2f$ signal. The $2f$ signal slope varies by $[0.4, 1]$ within the frequency range of $[1 \text{ kHz}, 5 \text{ kHz}]$.

3.2.4. Lock automation, and the transition to a tunable detector

Control management

The acquisition of dual-recycling lock is a complex process with three degrees of freedom, and all error-signals (more or less) depending on all of them. The requirements on the control loops are different for free oscillating mirrors of the dual-recycled detector, as is the case before lock acquisition, and successfully caught mirrors. Hence, (at least) two different control modes exist, that need to be supervised separately, and the transition between them requires some coordination.

All main longitudinal controls, for lock acquisition and the tuning process, have analog circuits¹³. However, each electronic rack features a digital bus system that allows the possibility of supervising and setting particular circuit parameters with a *LabView* based computer controlled system.

Several LabView user programs (so-called *VIs*), monitor parameters of particular control subsystems and rule actions that are necessary for an automated lock acquisition or operation. For the global management of these parameters, an interface called *data socket server* connects the computers running the VIs with the computers connected to the digital bus system.

The response time of LabView for writing parameters to the digital bus amounts, however, to $\sim 100 \text{ ms}$, and the data sampling rates vary. Furthermore, the writing of more than one parameter at the same time is unreliable. Thus, for the process of lock acquisition a micro-controller stage is implemented providing reaction times of 1 ms and a sampling of several analog inputs with a rate of 1 kHz .

Locking sequence

The locking sequence described here assumes the mode-cleaners are already locked. Before the controlled operation of the dual-recycled detector, all respective mirrors move freely, excited from seismic noise.

The locking sequence starts with power-recycling. With the DC-lock applied to the second mode-cleaner (see Section 3.2.1) which sets the laser frequency, the fringe rate of the power-recycling error-signal is still larger than, but of the same order as that of the Michelson error-signal¹⁴. The chances to traverse a carrier resonance while the Michelson mirrors are close to a dark fringe are high. A dark fringe maximises the carrier

¹³Exceptions are the longitudinal drift control, and the active seismic isolation.

¹⁴Without DC-lock, the fringe rates are $\sim 100/\text{s}$, and 2 to $3/\text{s}$, respectively.

contribution to the error-signal, thus, the respective optical gain which enhances the probability of success when a lock seems possible. As the loop is unconditionally stable, though, the lock is very robust under various Michelson tunings.

The power-recycling loop can hold the lock until the Michelson traverses its operating point. Then, the micro-controller activates the fast path of the Michelson loop (see Figures 3.1 and 3.4), applying the sqrt-circuit for the feedback to the ESDs. 200 ms after the lock succeeds, the slow path to the intermediate mass is turned on to extend the low frequency suppression.

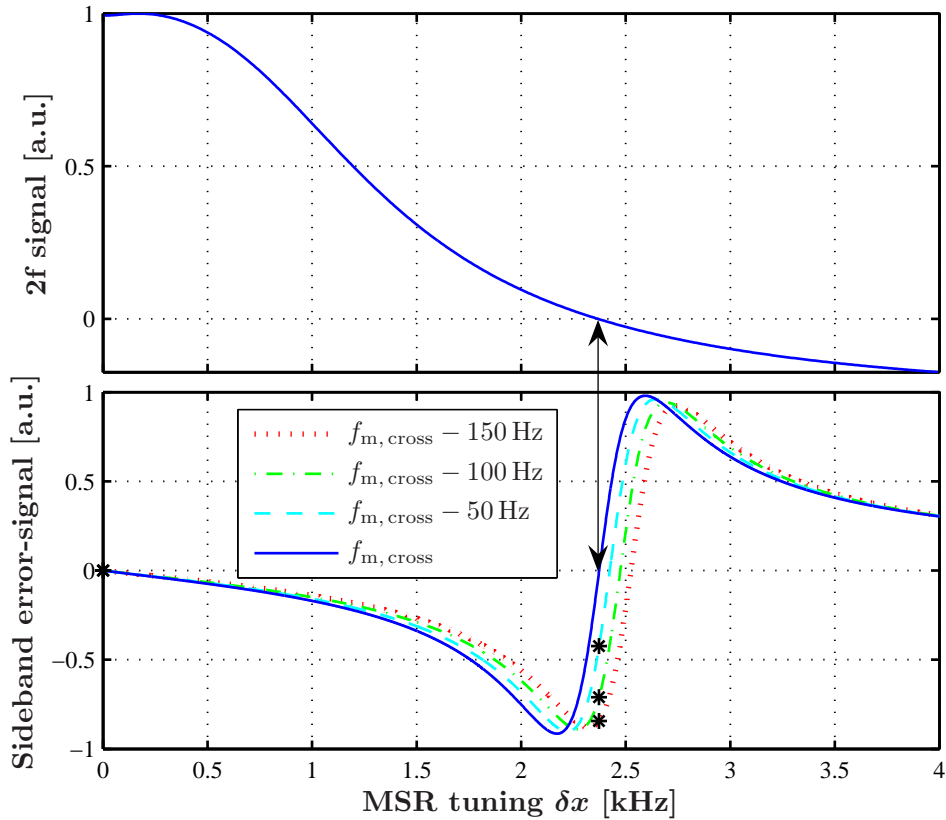


Figure 3.7.: Illustration of the crossover between the $2f$ signal (upper graph) and the sideband error-signal (lower graph). After lock acquisition, **MSR** is for ~ 200 ms locked to the position of the zero crossing of the $2f$ signal (upper end of the double arrow). During that time, LabView successively increases the signal-recycling modulation frequency, changing the sideband error-signal amplitude appearing for that current **MSR** tuning (see black stars on the particular curves). For $f_{m,cross}$, the zero crossings of the two error-signals agree, and the **MSR** control is taken over by the sideband error-signal.

If the Michelson interferometer is locked to the dark fringe, the signal-recycling loop attempts locking as soon as the $2f$ signal traverses a zero crossing, set by the offset

introduced in the loop. Currently, the operating point is set to a detuning of ~ 2.4 kHz. Please consult [Grote03a, Grote03b] for further details about the lock acquisition process.

The tunable detector

For the quasi-continuous tuning process, the signal-recycling control needs to switch from the 2f to the sideband signal. This process is illustrated in Figure 3.7 showing the 2f signal in the upper graph, and various sideband error-signals in the lower. The 2f signal is negatively shifted to yield a zero crossing at the desired **MSR** tuning for lock acquisition, ~ 2.4 kHz. While **MSR** is locked to the position of the zero crossing of the 2f signal (upper end of the double arrow), LabView successively increases the signal-recycling modulation frequency¹⁵, changing the sideband error-signal amplitude appearing for that current **MSR** tuning (see black stars on the particular curves). If the operating point of the sideband error-signal, defined by the zero crossing of the error-signal, crosses the current **MSR** position, the micro-controller switches between the two error-signals, as indicated by the double arrow.

With the help of a look-up table¹⁶, and using the sideband error-signal, the LabView-based tuning process continuously transfers the detector to the desired tuning¹⁷ which is currently 330 Hz.

3.3. Signal-recycling error-signal

If all of the interferometer control systems are operating, apart from that for the signal recycling mirror **MSR**, the remaining uncontrolled degree of freedom is essentially equivalent to the position of **MSR**. The operating point is then defined by a zero crossing of the signal-recycling error-signal with respect to the mirror position. For the Pound-Drever-Hall error-signal (see Figure 1.11 in Section 1.2.2) it could be shown with the phasor picture that there potentially exist two more zero crossings on top of that at the carrier resonance, each around one control sideband resonance. Led by this picture, it is plausible that the signal-recycling cavity error-signal should exhibit similar features: the modulation frequency determines the crude position of the respective zero crossings of the error-signal and therefore some of the possible locations to which the mirror can be locked [Freise00]. This will be investigated in the following section.

¹⁵For that large signal-recycling cavity tunings the control loop properties hardly change, such that varying other parameters is, in principle, unnecessary.

¹⁶This look-up table is the tuning script to be generated by simulation (see Section 3.5).

¹⁷Currently, at the final detuning the signal-recycling analog filters are replaced by digital filters with steeper decay in frequency. In order to further increase the *SNR*, the sideband error-signal is then gained at the south port, evaluating the beat between the two modulation sidebands at ~ 6 MHz instead of the carrier and the signal-recycling sideband. To improve the noise performance of the Michelson error-signal at this targeted detuning, the error-signal is detected with a high-power photodiode instead of a quadrant photodiode.

Figure 3.8 shows the magnitude of the error-signal for the signal-recycling feedback loop as a function of **MSR** position and modulation frequency: every horizontal cut corresponds to the more common, two dimensional error signal magnitude with respect to the **MSR** position for a fixed modulation frequency, alike Figure 1.11. The displacement δx of **MSR** from the tuned point, is expressed as the angle

$$\delta\chi = 360^\circ \cdot \delta x / \lambda_0, \quad (3.1)$$

with 1064 nm being the laser wavelength λ_0 . The modulation frequency axis is expressed as detuning δf_m from the modulation frequency $72 \times FSR_{SR}$ which is close to that yielding a tuned detector¹⁸. The demodulation phase is adjusted to give a symmetric error-signal shape of highest possible slope at the origin of Figure 3.8¹⁹; this demodulation phase is kept constant throughout the complete figure. The error-signal has been mapped linearly to an almost grey-scale-like density to give the clearest qualitative representation of the data: At the bright parts the error-signal is positive, at the dark regions negative. Each region has an additional shading to distinguish high from low absolute values. Therefore, transitions between bright and dark regions with high contrast in general mark zero crossings. These withdraw for example in the diagonal, horizontal and vertical lines. Shifting δf_m slowly from -10 kHz to 0 Hz while locking on a zero crossing of one of the diagonal lines, allows for a continuous sweep of the **MSR** position from a large detuning ($\delta\chi_m = \pm 15^\circ \approx \pm 10$ kHz) to the tuned state. The diagonals indicate an almost linear relation between δf_m and $\delta\chi_m$ with

$$\delta\chi_m = \pm 180^\circ / FSR_{SR} \cdot \delta f_m, \quad (3.2)$$

with $FSR_{SR} = 125.2416$ kHz being the free spectral range of the signal-recycling cavity. Equation 3.2 will in the following be used to determine the detector tuning associated with the **MSR** position²⁰ $\delta\chi_m$. In this case, the detector tuning is represented by the value of δf_m . Using Equation 3.1 and Equation 3.2, the **MSR** position will, throughout this work, be given in meters, Hertz or degrees, depending on the context.

With respect to the $\delta\chi = 0^\circ$ axis, the diagonals are symmetric. Moreover, the optical gain for one constant δf_m is exactly the same on both sides, leaving the sign of **MSR** detuning ambiguous²¹.

The direction of the modulation frequency detuning is important. Along the diagonal

¹⁸Without power-recycling, a tuned detector would be achieved with any modulation frequency being exactly any multiple of FSR_{SR} . The power-recycling cavity resonance, however, shifts this resonance (see below).

¹⁹The slope refers to $\delta\chi$ as argument, hence, to the horizontal direction in the displayed parameter plane.

²⁰As shown in Section 2, in particular Equation 2.10, the frequency of detector peak sensitivity does not necessarily agree with the resonance frequency of the signal-recycling cavity.

²¹In the classical approach, the sign of the signal-recycling cavity detuning does not change the shape of the detector's sensitivity: In a detuned state, the detector enhances only the one signal sideband with the fitting sign as it does for the control sidebands (Figure 3.11). As both signal sidebands are originally generated with equal amplitude, it is indistinguishable which one is resonant. Considering quantum-noise effects, however, the sign of detector detuning becomes apparent in the sensitivity. Positive signal-recycling cavity tunings only, i.e. $\delta\chi > 0^\circ$, introduce a second, opto-mechanical resonance in the sensitivity at low frequencies.

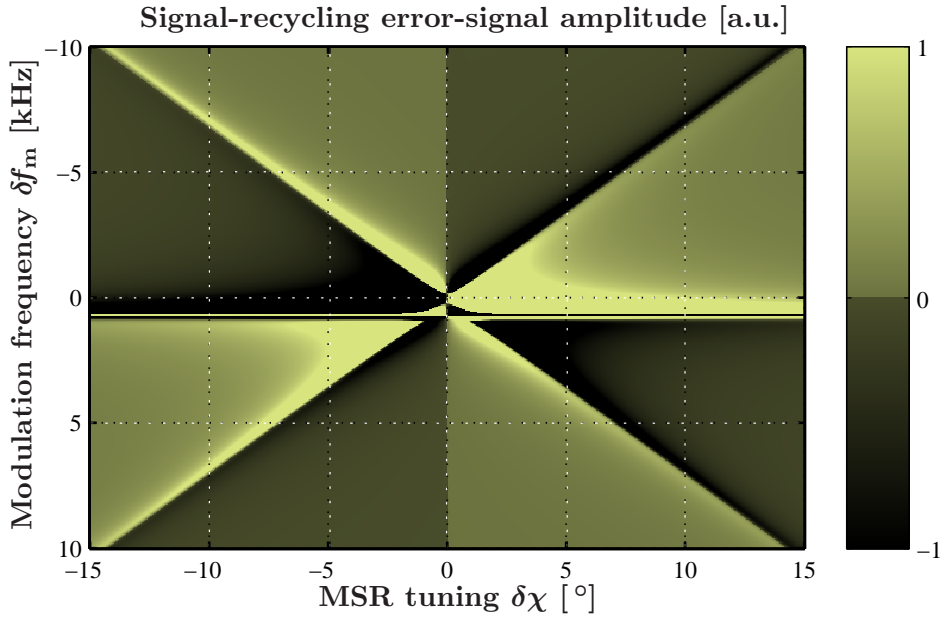


Figure 3.8.: Error-signal magnitude for the signal-recycling feedback loop in the plane of the **MSR** position and the modulation frequency, given in detuning δf_m from the 72nd multiple of FSR_{SR} . (The demodulation phase is kept constant for all δf_m .) The displacement $\delta\chi$ of **MSR** is given in degrees from the tuned case. The locations of the zero crossings of the error-signal are at the borders between bright and dark regions. Continuously transferring the detector from a detuned to tuned state without losing lock means to trace one of the diagonal lines towards the origin by slowly sweeping the modulation frequency.

lines, one has to face a change of error-signal slope sign around $\delta f_m \approx +700$ Hz, abruptly pushing the mirror away in an experimental tuning process. This does not necessarily have to be critical, but complicates the down-tuning process further and should thus be avoided.

If the sign of the feedback signal is well defined, the ability of the servo-system to hold the mirror at the operating point is determined by two features of the error-signal: the absolute value of the slope of the error-signal at the operating point, together with the given electronic feedback loop gain, sets the unity gain frequency of the control loop, and thus decides on stability. The range of mirror displacement for which there is a restoring force on the mirror yields the maximally tolerable rms movement. These properties are called *optical gain* and *capture range*, respectively (see a more detailed definition of the capture range below).

For each fixed modulation frequency, the only variable left to optimize the error-signal is the demodulation phase. This phase influences all attributes of the demodulated signal:

the exact position of the zero crossing and the capture range of the subsequent feedback loop, but particularly the slope at the zero crossing.

Figure 3.9 shows the characteristics of some signal-recycling error-signals for the detuned detector with various demodulation phases. With feedback operating, the error-signal amplitude corresponds to the force acting on the mirror at the specific mirror position. The slope of the line that directly connects the respective, local error-signal point with the zero crossing, determines the overall feedback loop gain in sign and (roughly²² in) amplitude (for a given electronic gain). The allowable gain variation, restricted by the varying phase margin crucial for loop stability (see Section 3.2.3), determines the valid interval of capture range. However, to ease the following investigations and keep consistency with earlier Ph.D.thesis [Grote03b], the capture range will additionally be restricted to the monotonic region around the respective zero crossing. (For most error-signals, with this definition, the capture range is equivalent to the monotonic region.)

Even if locked, a certain symmetric rms movement of **MSR** around the detuned operating point will still remain. To hold the mirror at one particular operating point, it is enough if the rms movement is slightly smaller than the capture range of the error-signal. In a tuning process, however, the mirror could easily exceed the capture range of the subsequent error-signal pattern when the shift of this pattern along the **MSR** position axis was too large or too fast. This will finally limit the maximum allowed speed of the signal-recycling cavity tuning. In respect of gain and capture range optimisation, the error-signal in Figure 3.9, achieved with a demodulation phase of 144° , exhibits the most promising shape: it is not only the most symmetric signal around the zero crossing, balancing the capture ranges to both sides of the operating point, but also yields the steepest slope at the zero crossing.

In the following subsection, the error-signal characteristics will be explained with the help of phasor diagrams. This will not only allow for a profound understanding of the signal but also enable the prediction of the progression of signal parameters, crucial for a successful feedback when tuning the signal-recycling cavity of an operating, dual-recycled detector.

²²The exact gain definition, especially with respect to loop stability, is connected to the definition of transfer functions, and in principle only holds for the strictly linear region of the error-signal around a zero crossing. (For the consideration of loop (in-)stabilities, an operating point is in any case necessary, as the option of being on the wrong side of the error-signal is crucial.) However, in order to sensibly expand the validity of a transfer function to non-linear regions, one could consider, for example, a mirror movement with certain excitation frequency f_{exc} and an amplitude exceeding the linear region of the error signal. This will yield a time-dependent feedback signal with main periodicity of f_{exc} , but containing higher frequency components as well. With Fourier-transformation, one would still be able to determine the amplitude and phase shift contained in the output signal for this particular frequency. This amplitude, divided by the excitation amplitude of the mirror movement, would represent the gain. The slope of a line, as characterised above, should give a good approximation for that gain.

This approach is supported by experimental observations: Some large seismic excitations do not terminate a mirror lock immediately, but first introduce an up-ringing oscillation lasting for some seconds. This could be explained by a mirror position so far away from the zero crossing that it still sees the restoring force of the error-signal, but the gain, associated with the oscillation frequency as explained above, is too low to provide stability.

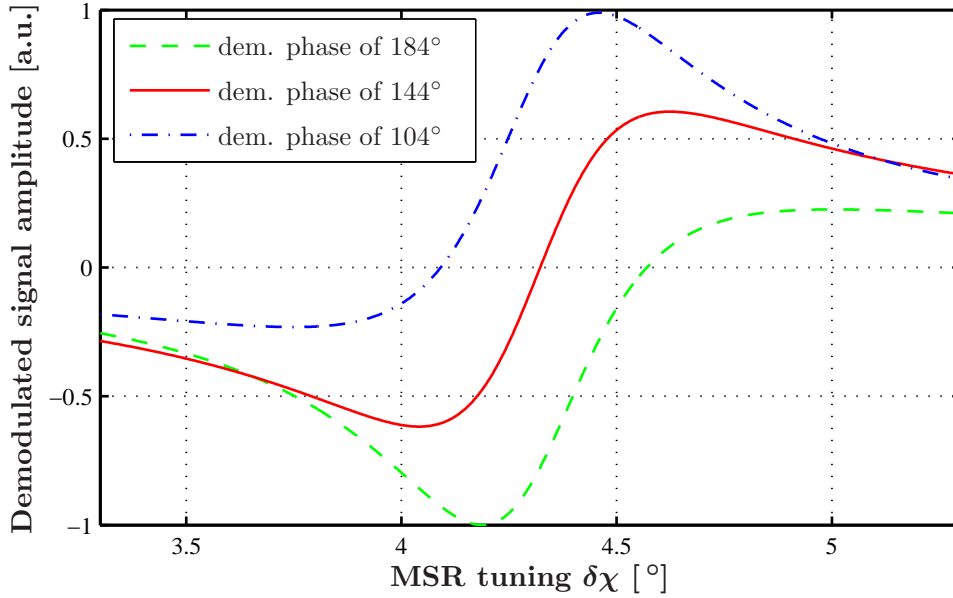


Figure 3.9.: Characteristics of the error-signal magnitude for a signal-recycling control sideband frequency δf_m around 3 kHz. The only parameter that differs is the demodulation phase changing the main characteristics as for example the position of the zero crossing and the corresponding slope.

3.3.1. Sideband properties in the coupled cavities

Looking at the signal-recycling error-signal vector, the carrier's, and sidebands' phasors need to be deduced for various **MSR** tunings. To do so, the position of the fields' frequencies within both cavities' resonance structures needs to be known. Moreover, we would like to relate the resonances to the signal sidebands. Figure 3.10 displays the frequency relations of carrier (vertical dashed black line), signal-recycling control sidebands (vertical solid green lines) and signal-recycling cavity resonance structures (gain and phase curves in blue) for three signal-recycling cavity tunings. From top to bottom, **MSR** is positively detuned, tuned and negatively detuned. In these examples, the modulation frequencies, being $\leq 72 \times FSR_{SR}$ due to the considerations from above on Figure 3.8, are set such that at least one of the sidebands is resonant inside the signal-recycling cavity.

With the restriction of δf_m being negative, the power-recycling cavity resonance will, for a start, be neglected. (To provide a complete figure, though, the power-recycling resonance frequency is marked by the vertical, dash-triple-dotted lines.) Ignoring the power-recycling cavity, the bandwidths of all signal-recycling resonance structures are the same.

The targeted detunings are in these examples presupposed to have the same absolute value. In combination with $\delta f_m < 0$ Hz for the sideband frequencies, this requires δf_m to

be the same for both detuned cases. The only difference is that for positive detuning, the upper sideband is resonant inside the signal-recycling cavity, and vice versa.

The resonance frequencies of the tuned signal-recycling and power-recycling cavities are easily determined by multiples of their free spectral ranges, $n FSR_{SR}$ and $m FSR_{PR}$ ($m, n \in \mathbf{Z}$), respectively. These values, however, do not automatically yield the frequencies of maximal sideband enhancement inside one of these cavities. Due to the cavities' coupling through the Michelson, the sideband amplitudes depend very much on both cavity states.

For the process of down-tuning, the power-recycling cavity is constantly resonant for the carrier light, while the operating point of the signal-recycling loop moves successively. Figure 3.11 shows the amplitudes of the upper and lower signal-recycling control sidebands, $SB_{+,SR}$ and $SB_{-,SR}$, respectively, inside the signal-recycling cavity. In agreement with Figure 3.8, the modulation frequency varies within an interval of ± 10 kHz around the aimed 72nd FSR_{SR} multiple, and the **MSR** is tuned between $\pm 15^\circ$. Dark regions indicate a high sideband amplitude.

According to the horizontal line at $\delta f_m \approx 700$ Hz of Figure 3.8, there emerges one constant frequency of resonance of that same value. As this enhancement is hardly influenced by the **MSR** tuning, it must be connected to the power-recycling cavity resonance.

The second frequency of (locally) maximal enhancement varies (almost) linearly with changing signal-recycling tuning. The maxima roughly obey the expression

$$f_{\pm,SR} = f_0 \pm (72 - \delta\chi/180^\circ) \cdot FSR_{SR}, \quad (3.3)$$

agreeing with the positions of the zero crossings on the diagonals in Figure 3.8. This again confirms the correlation of sideband resonances and zero crossings.

Please note that for almost all $\delta\chi$, $SB_{\pm,SR}$ have two enhanced frequency regions. For the tuned case, $\delta\chi = 0^\circ$, the frequencies are separated by ~ 700 Hz. The amplitudes originating from the power-recycling resonance are increased compared to the signal-recycling resonance. Due to the logarithmic colour scaling of Figure 3.11, this gets only visible for large absolute values of $\delta\chi$. The amount of enhancement depends on the finesse of the cavities, and is, with the current setup of GEO 600, higher for power-recycling²³.

The influence of the cavity resonances on each other becomes noticeable only if f_{SR} is close to both cavities' resonances. The purely power-recycled and signal-recycled Michelson represent the compound input and output mirror, respectively, to the signal-recycling and power-recycling cavity, respectively. Thus, if f_{SR} is far from one compound mirror's (CM) resonance, the light coming from the opposing recycling mirror and impinging on the CM will get no phase shift in reflection, and see a high power reflectivity.

As soon as f_{SR} approaches, for example, the power-recycling resonance, the reflection of the power-recycled Michelson decreases, and the light gets phase shifted at reflection.

²³In the commissioning phase of the dual-recycling experiment, the frequency resonant inside the power-recycling cavity was first disregarded as the sideband frequency generating an error-signal for tuned signal recycling. The real detuning of the detector, however, was different from the expected, applying Equation 3.2, by several hundred Hz. This inconsistency was solved and explained by simulations.

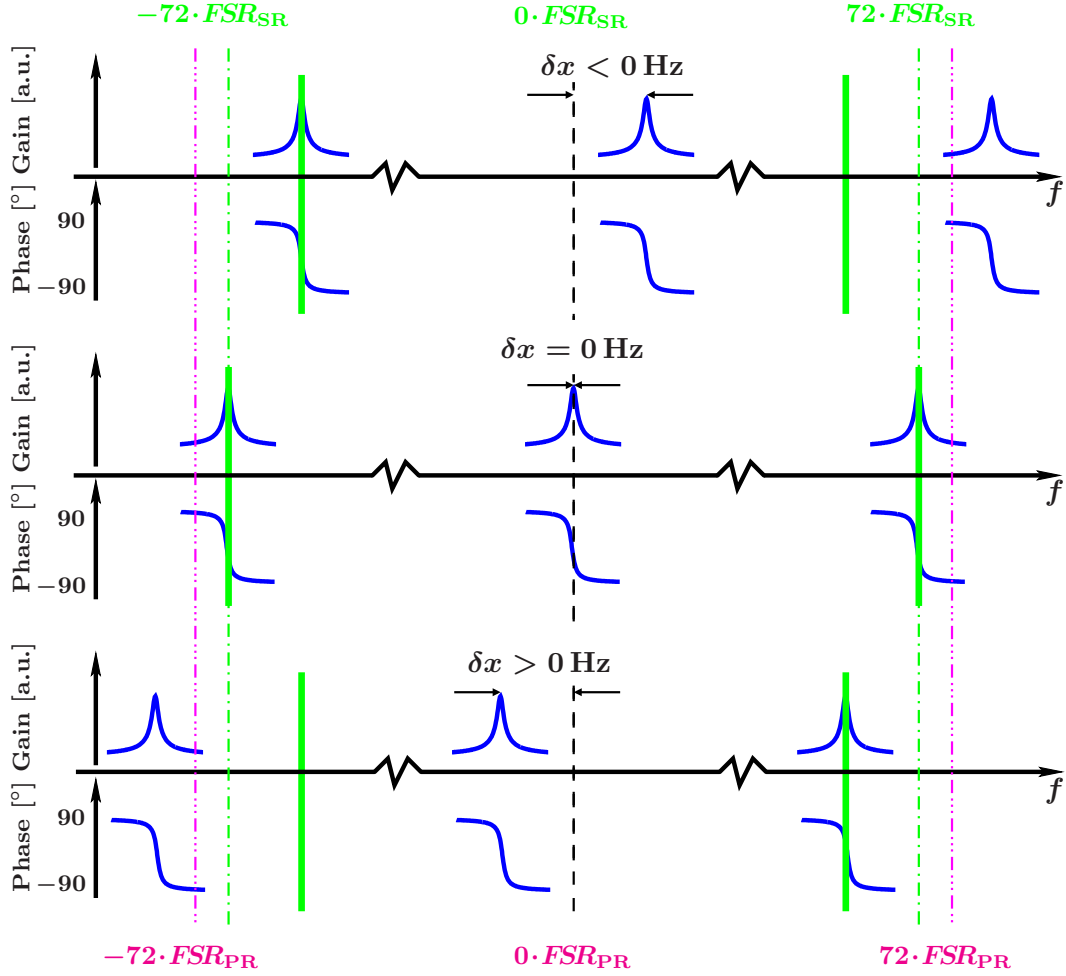


Figure 3.10.: The resonance conditions of the signal-recycling control sidebands inside the signal-recycling cavity for negative, 0 Hz and positive detector tunings, from top to bottom. The control sidebands, marked by the green solid lines, are located around the carrier at roughly the ± 72 nd multiple of FSR_{SR} ; the exact frequency depends on the tuning. The carrier resonance and $FSRs$ of the signal-recycling and power-recycling cavity are indicated by the dashed, dashed-dotted, and dashed-double-dotted vertical lines, respectively. FSR_{SR} is smaller than FSR_{PR} by approximately 10 Hz. Thus, $\pm 72FSR_{SR}$ are symmetrically shifted from $\pm 72FSR_{PR}$ towards the carrier frequency. For each tuning, the upper blue graphs represent the qualitative amplitude enhancement due to the signal-recycling resonance condition, the lower curves the dispersive phase shift. Fine-tuning the signal-recycling cavity moves the rigid comb of resonances against the fixed comb of light frequencies: to the right for negative tunings, to the left for positive.

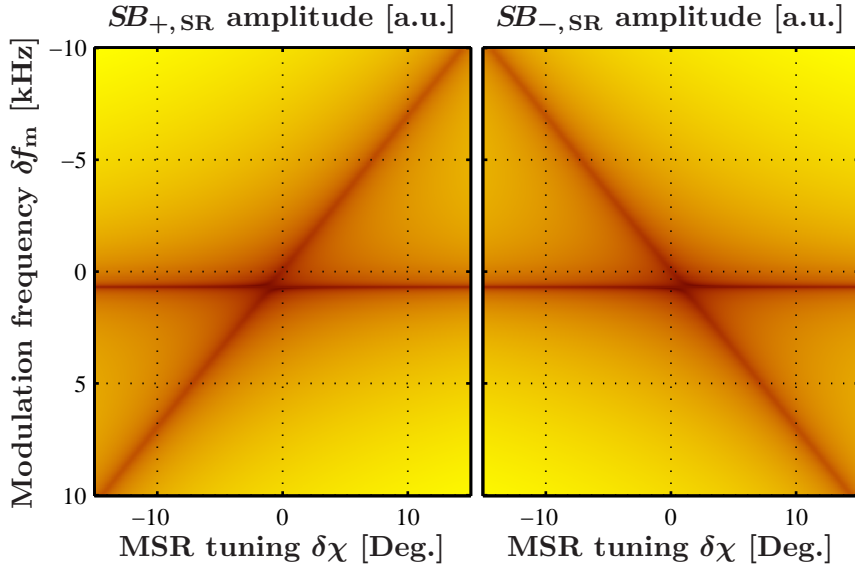


Figure 3.11.: Upper and lower signal-recycling sideband amplitudes inside the signal-recycling cavity, in the plane of **MSR** tuning and modulation frequency. As in Figure 3.8, the modulation frequency is given as an offset δf_m from the frequency being resonant in the tuned signal-recycling cavity, the displacement $\delta\chi$ of **MSR** is given in degrees from the tuned case, with 180° corresponding to a detuning of half a wavelength ($\lambda_0/2 = 532 \text{ nm}$) or 125 kHz in terms of frequency of peak detector sensitivity. For the sake of visibility, the fields' amplitude is logarithmically color scaled. Red (or dark) regions (in contrast to the bright yellow) stand for a high amplitude. The strong enhancement at constant frequency ($\delta f_m \approx 700 \text{ Hz}$) corresponds to the power-recycling resonance, the other to signal-recycling. For each detuning away from the tuned case, only one sideband with particular frequency is resonant in the signal-recycling cavity.

The decrease of reflectivity is the reason for the increase of the sidebands' enhancement inside the signal-recycling cavity (compare horizontal cuts of the plots). The phase shift distorts the ideal linearity of the diagonal close to $\sim (\pm 1^\circ, 700 \text{ Hz})$. The same is valid vice versa if the signal-recycling cavity gets resonant with f_{SR} (compare vertical slices of the plots). More on the topic of coupled cavities can be found in Section 3.7.

In summary, two main results are obtained with Figure 3.8 and 3.11: (i) Generally, there is at least a rough coincidence between the **MSR** tuning yielding a control sideband resonance inside the signal-recycling cavity, and the zero crossing of the signal-recycling error-signal generated with that same sideband²⁴. Thus, the relevant error-signal shape will be located around that resonance. (ii) There exists a sideband frequency region around $\delta f_m \approx 700 \text{ Hz}$, where the error-signal exhibits extraordinary features, including a change of gain sign. Thus, targeting a continuous **MSR** tuning over a wide range, GEO 600 only uses negative δf_m .

²⁴The correlation is even exact, the further away from the power-recycling resonance.

3.3.2. Signal-recycling error-signal explanation with phasor diagrams

In order to explain the properties of the signal-recycling error-signal with phasor diagrams, the contributing field phasors appearing at the antireflective coating of the **BS** need to be known. Again, the conventions summarised in Section 1.2.1 are to be applied.

Figure 3.12 displays the power-recycled Michelson of GEO 600, with phasors qualitatively representing the expected carrier (magenta) and control sideband (cyan) field properties. The signal-recycling control sidebands enter the optical setup as phase modulation sidebands. In transmission of a simple **MPR** or beamsplitter, all fields remain unchanged. In contrast to the carrier and Michelson control sidebands, though, these sideband frequencies are in general, with avoidable exceptions, well outside the resonance structure of the power-recycling cavity. Thus, they will, inside the power-recycling cavity, experience an anti-symmetric phase shift of almost $-$ and $+90^\circ$ for the lower and upper sideband, respectively. In the south, the carrier cancels whereas the sidebands get transmitted with equal amplitude and a common resulting phase²⁵ of -90° . The reason is the Schnupp asymmetry of the Michelson arms (please compare with Figure 1.15 in Section 1.2.4).

To yield the phasors at the antireflective beamsplitter coating (**BSAR**), where the signal-recycling error-signal for a dual-recycled detector is generated (see Figure 3.1), the resonance conditions of the sidebands inside the signal-recycling cavity need to be applied to all phasors of Figure 3.12. Particularly, the phasors inside the Michelson arms are the result of the superposition of the phasors coming from west and south. However, the sideband phasors originating from the west can, for the signal-recycling error-signal, be neglected:

- They always represent a perfect phase modulation. Any signal-recycling cavity tuning introduces only an anti-symmetric phase shift and identical reflectivities of the signal-recycled Michelson. In addition, due to the ideal dark fringe condition, the carrier at the **BSAR** is not influenced by the signal-recycling cavity tuning.
- The mathematical operation of vector projection is associative. Thus, the addends of the superposition can be evaluated separately.

As a consequence, the control sideband phasors from the west give no contribution to the error-signal phasor, and only those from the south need to be considered.

In case of a tuned detector, displayed in the middle row of Figure 3.10, both sidebands exactly resonate inside the signal-recycling cavity. Thus, the cavity being at the operating point, maintains the two phasors' phases and enhances them equally in amplitude. If the cavity is slightly shorter, thus negatively detuned, the curves in the middle row of Figure 3.10 move to the right, to higher frequencies, providing the sidebands with positive phase shifts, and vice versa.

²⁵As before (in Section 1.2.4), inside the Michelson all transitions at the beamsplitter, even the common, are taken into account (different from the introduced convention to neglect common transitions).

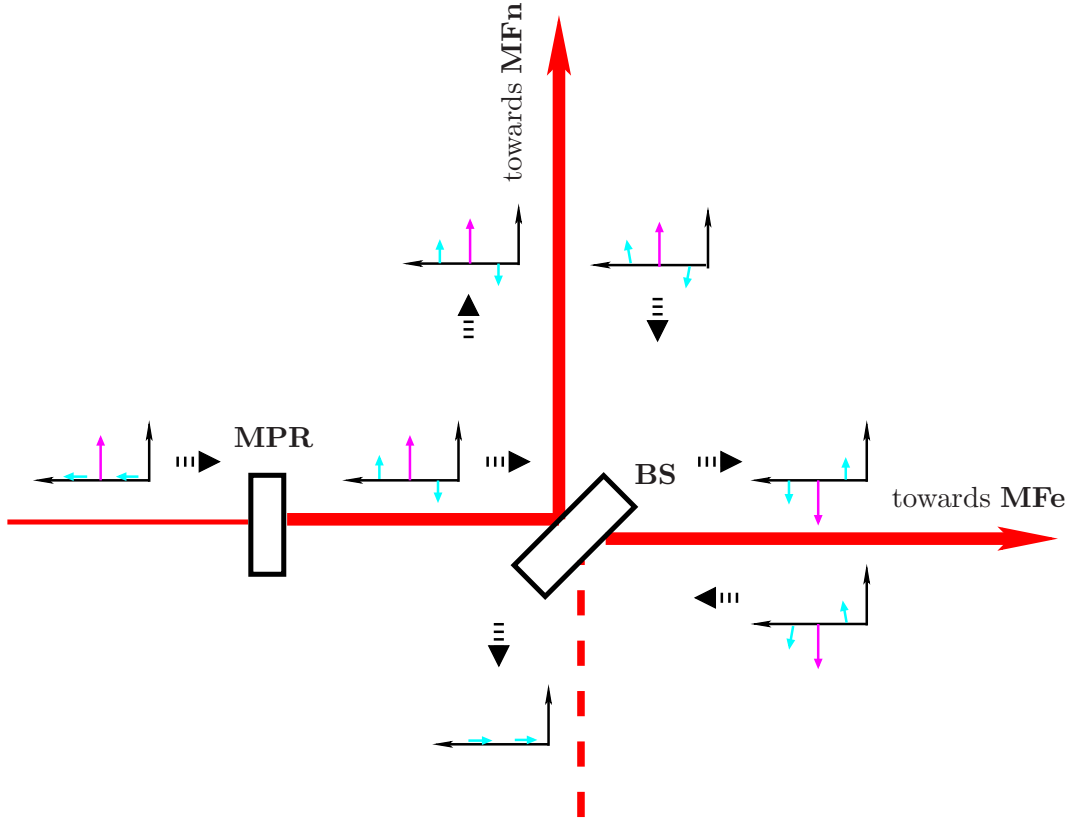


Figure 3.12.: Phasors representing the carrier (magenta) and signal-recycling control sidebands (cyan) at different points of the power-recycled Michelson interferometer of GEO 600. The far and end mirrors of the Michelson are omitted for clarity. The thick, dashed black arrows indicate the propagation direction of the phasors.

Figure 3.13 derives the error-signal vector in case of a tuned-detector configuration, for five different signal-recycling cavity tunings δx , separately accounted for in five rows. The three columns from left to right display the P and Q control sideband phasors²⁶ and the error-signal vector with its real and imaginary component contribution from the single beats.

Similarly to the Pound-Drever-Hall error signal around carrier resonance, the signal is completely contained in one quadrature, here P, and absolutely symmetric. The optimal demodulation phase for best sensitivity is obviously 0° , modulo 180° . For all demodulation phases, the highest error-signal amplitude can be expected around the cavity linewidth, where the trade-off of sideband amplitude and projection angle to the carrier phasor ($\pm 45^\circ$) is best. The error-signal extrema limit the monotonic area around the zero crossing, and thus each mark an upper limit for the upper and lower capture range.

²⁶Please note that the carrier from west and the sidebands from south, all experience two surface transitions at the **BS** which in this case are again, consequently, commonly neglected.

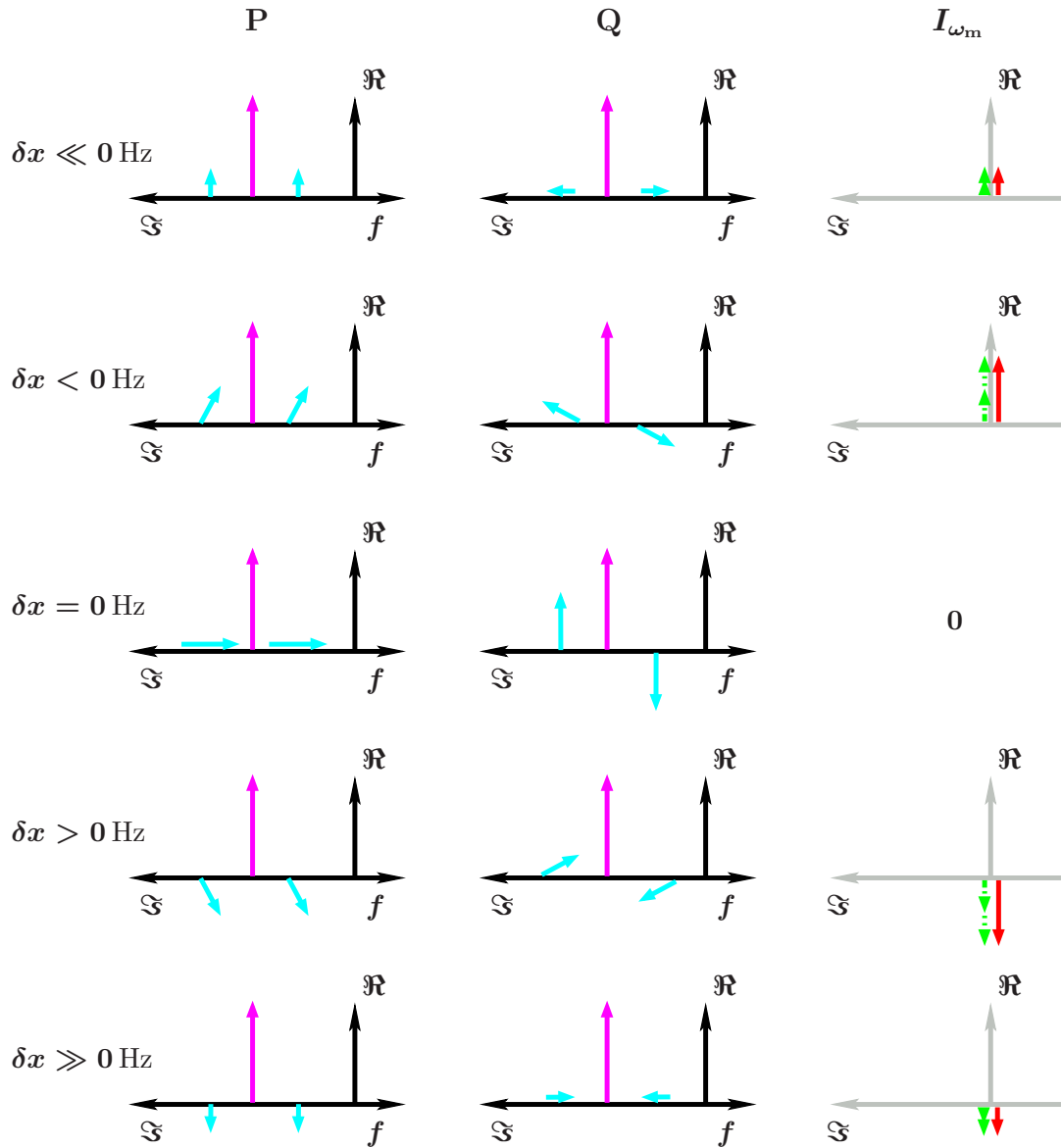


Figure 3.13.: Signal-recycling error-signal vector derivation for a tuned-detector configuration. The five rows contain phasor constellations for different cavity tunings δx , each indicated at the left. As marked at the top, the three columns from left to right display the P and Q control sideband phasors (cyan), together with the carrier (magenta), and the error-signal vector (red), respectively. For a better comprehension, the single beat contributions to the error-signal's real and imaginary components originating from P and Q are represented by dotted and dashed-dotted green vectors, respectively. Tuning **MSR**, both control sidebands obey the same resonance condition. The carrier remains the same as the Michelson is set to the dark fringe condition, keeping out any effect from the signal-recycling cavity.

For a positively, far detuned configuration, the phasors for different cavity tunings around the operating point are comprised in Figure 3.14. The field phasors can be derived by applying the resonance conditions of the sidebands, covered by the lowest row of Figure 3.10, to the phasors in the south of Figure 3.12: whereas the lower sideband is constantly phase shifted by -90° , the upper sideband's phase goes through a shift from $+90^\circ$ to -90° as the signal-recycling cavity resonance, while elongating the cavity, passes the sideband frequency.

The composition of Figure 3.14 is the same as of Figure 3.13. In contrast to before, the error-signal vector rotates in the complex plane for varying cavity tunings and does not vanish automatically at sideband resonance, but only for large negative tuning offsets (i.e. when the cavity gets closer to carrier resonance).

As in the case of Pound-Drever-Hall lock on the sideband (see Section 1.2.2), all error signal properties, like the gain, the position of the zero crossing (deciding on the exact detector tuning), and signal shape, completely depend on the choice of the demodulation phase (as the sideband frequency is fixed). Aiming for an error-signal with high gain and a zero crossing near the sideband resonance tuning, a demodulation phase of $\Phi \approx 0^\circ$ is a good choice.

For very far detunings, the lower sideband's amplitude is so small that it may be neglected. Then, $\Phi = 0^\circ$ yields a zero crossing exactly at the tuning of sideband resonance and a most symmetric error-signal with highest gain. The maximum demodulated error-signal amplitude will again, like in the tuned case, occur close to the cavity linewidth, where the upper sideband's amplitude is attenuated by $\sqrt{2}$, and the projection angle is $\pm 45^\circ$, reducing the parallel projection by factor $\sqrt{2}$. With different Φ , the range before reaching maximum (or minimum) error-signal improves on one side, but simultaneously gets worse on the other. As the rms motion of a mirror is symmetric around its mean position, the capture ranges to both directions are equally important. A symmetric error-signal accounts for both at the same time. More on criteria for error-signal optimisation can be found in Section 3.5.1.

The closer the intended signal-recycling cavity's operating point, δx_m , to the tuned state, 0° , i.e., the carrier resonance, the bigger the influence of the lower sideband. In particular, the error-signal vector is longer for $\delta x > \delta x_m$ and shorter for $\delta x < \delta x_m$ (compared to configurations with larger δx_m). To keep the zero crossing close to the sideband resonance and ensure a decent gain within the given possibilities, the demodulation phase would need to follow and rotate clockwise. Another effect of the increasing power of the lower sideband is that the error-signal loses symmetry, reducing the capture range towards lower **MSR** tunings for the benefit of the upper capture range. If aiming for highest symmetry, at least close around the zero crossing, the position of the zero crossing will be shifted with respect to the sideband resonance to the opposite side from tuned. Thus, the sideband frequency offset δf_m from carrier resonance does not necessarily agree with the detector tuning, even if the demodulation phase was optimised for best error-signal symmetry or highest gain (which are both well accessible in the experiment; a technique to determine the signal-recycling error-signal shape in a closed loop, together with simulations, is discussed in Section 3.6.2).

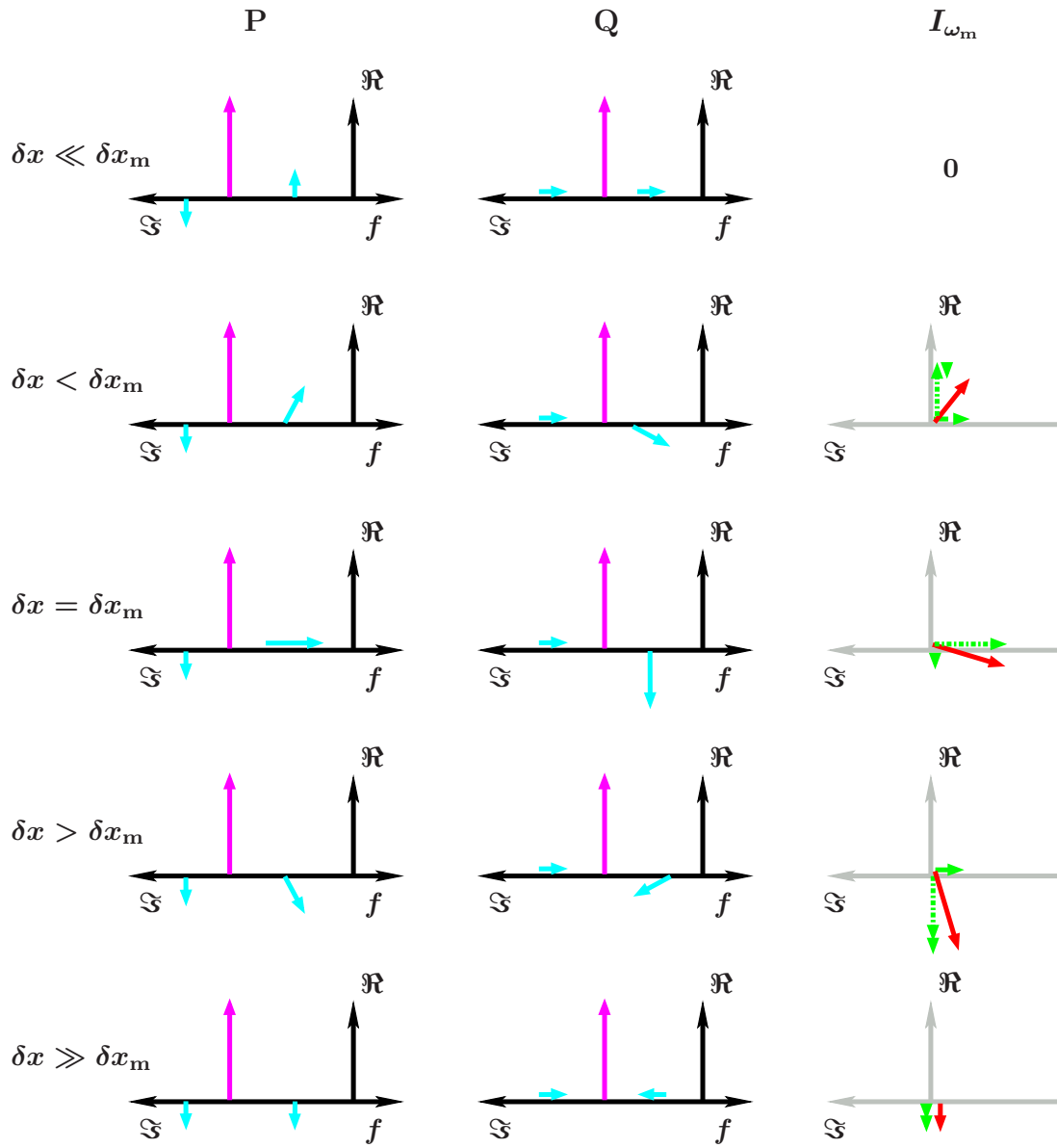


Figure 3.14.: Signal-recycling error-signal vector deduction for a far positively detuned detector configuration. The figure structure is the same as in Figure 3.13. While the **MSR** position increases, however, only the upper control sideband passes the signal-recycling resonance; the lower remains constant. Consequently, the error-signal vector rotates clockwise in the complex plane.

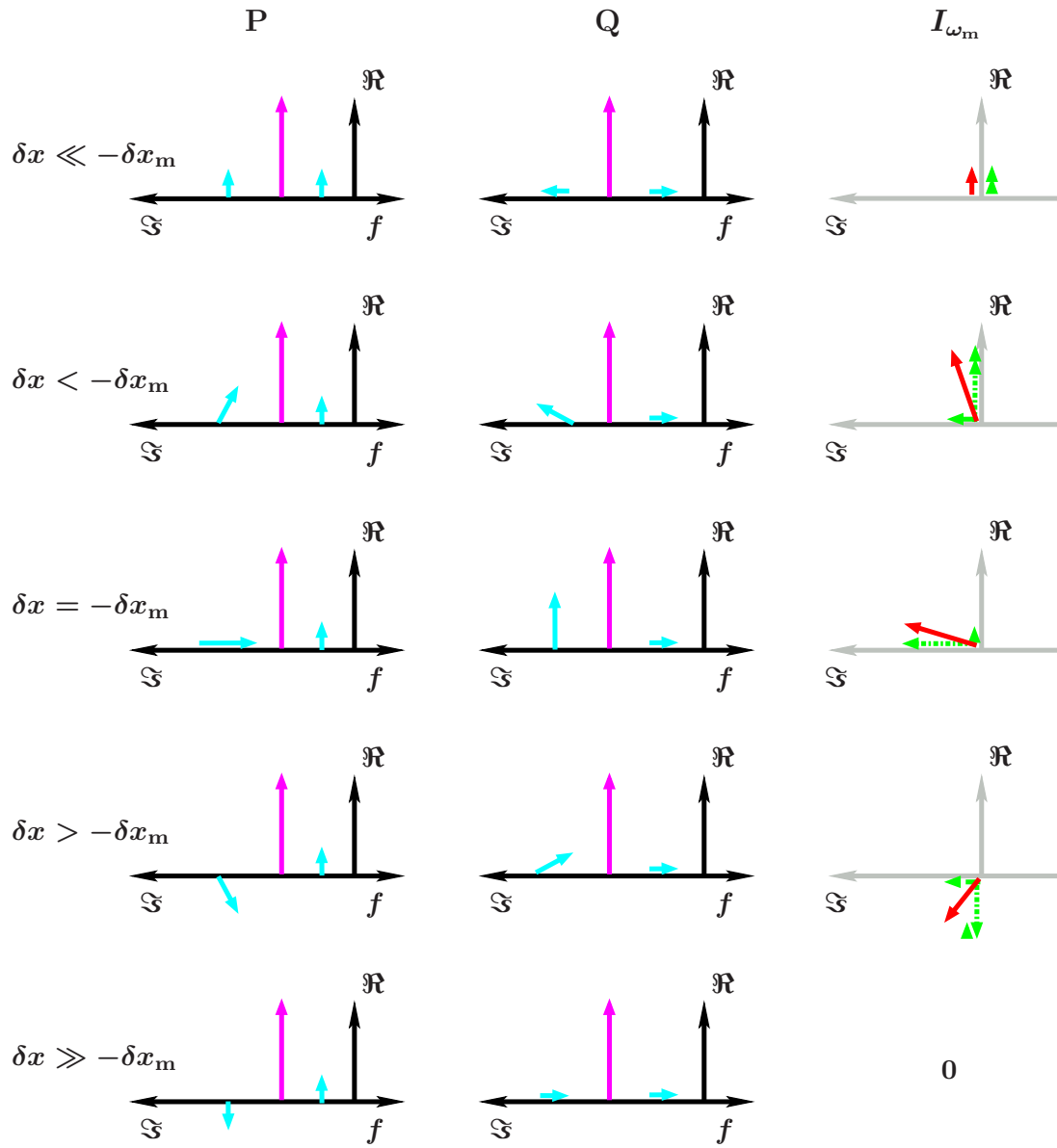


Figure 3.15.: Deduction of the signal-recycling error-signal vector for far negative MSR tunings. The figure is organised the same as the previous two. Here, the upper control sideband stays constant while the lower goes through a resonance when the MSR tuning increases. Again, the error-signal vector rotates downwards, but on the positive imaginary half of the complex plane.

The signal-recycling error-signal for far negative detunings is deduced in Figure 3.15, which is organised the same as Figure 3.14. The role of the sideband phasors are, this time, switched: whereas the upper sideband from the south of Figure 3.12 is attenuated and constantly rotated by $+90^\circ$ for all δx , the lower sideband goes through a resonance, rotating from $+90^\circ$ to -90° , as the signal-recycling cavity is elongated (compare with first row of Figure 3.10).

Accounting again first for the lower sideband only, the error signal phasor is exactly the same as for positive detuning, but mirrored by the real axis to the positive imaginary side of the complex plane. Thus, again a demodulation phase of $\Phi = 0^\circ$ (modulo 180°) is best, and for this Φ all other error-signal characteristics from above, like symmetry, zero crossing position, gain and capture ranges, are transferable.

In contrast to the positive detuning example, however, the upper sideband cancels the lower sideband for high **MSR** detuning, which is, again, the side closer to carrier resonance. With respect to the **MSR** position offset from the tuned state, the error-signals for the positive and negative tuning side are anti-symmetric and exhibit, for all demodulation phases, the same main observable properties:

- The zero crossings are symmetrically separated from the tuned **MSR** position. Thus, the sensitivity curves are (classically) indistinguishable.
- The gains have same size and sign. Thus, the feedback loops will work equally well for both tuning signs.
- All symmetry aspects, especially the capture ranges, are the same, but with $\delta x = 0$ Hz as “mirror” axis. Thus, observing the error signal symmetry experimentally, by tuning either the sideband frequency or the signal-recycling cavity, will give the same answer for both tuning sides.

All three features are visible in the overview plot of the signal-recycling error-signal, Figure 3.8, featuring a demodulation phase of 0° . In agreement to the phasor picture, the closer δf_m to 0 Hz, the larger the offset of the zero crossings from an ideal, linear diagonal, towards $\delta\chi = 0^\circ$.

With the understanding, gained by the phasor picture, the qualitative progression of relevant parameters of the signal-recycling error-signal, while tuning **MSR**, can be predicted. The tuning side is not relevant for this.

The best demodulation phases for very far detunings and the tuned detector, for example, are expected to be the same. While down-tuning, however, The power of the non-resonant sideband enhances and gains influence on the error signal phasor. As one consequence, the demodulation phase will monotonically rotate, by up to $\pm 90^\circ$, to maintain a symmetric error-signal and high gain²⁷. A second effect is an elongation of the error-signal vector length, which in general results in an increase of the optical gain.

The capture range is, in principle, limited by the bandwidth of the signal-recycling cavity. It is the same to both sides of the zero crossing, for far detunings and a demodulation

²⁷The experimental direction of rotation, however, could be opposite depending on the phase shifter.

phase yielding a symmetric error-signal. The lower the tuning, the smaller the capture range in carrier-resonance direction and the larger to the other side.

These features of the signal-recycling error-signal need to be considered during the development of a lock-acquisition and tuning procedure for the detector.

3.4. Michelson error-signal

To get an idea of how the Michelson error-signal vector will evolve when tuning the signal-recycling cavity, we can again consult the phasor picture to obtain qualitative answers.

Let us for simplicity, like in Section 2, assume a perfectly symmetric Michelson, except for the Schnupp asymmetry, and that the Michelson control sidebands are resonant inside the power-recycling cavity. Furthermore, the Michelson is locked to the dark fringe and remains at that operating point for any signal-recycling cavity tuning. Thus, only small deviations from the dark fringe need to be considered to determine the change of relative length and orientation of the error-signal vector.

Both simplifications mean, we can presume phasors like in the lower right quadrant of Figure 1.15 at the south port of the beamsplitter: with very small deviations from the dark fringe, some carrier light will appear in the south, and the control sidebands' phase and amplitude will negligibly change.

On these phasors, the resonance conditions as indicated in Figure 2.4 have to be applied. To determine the orientation of the error-signal vector, it is sufficient to trace the control sidebands' "snapshot" where the respective projections on the carrier annihilate. In Figure 1.15, this corresponds to the upper phasors in the lower right quadrant.

Figure 3.16 qualitatively displays the phasors of all light fields contributing to the Michelson error-signal, for several non-negative signal-recycling cavity tunings, increasing from top to bottom. The particular tuning is indicated on the very left. The left set of phasors represents the light fields at the south port of the beamsplitter with the signal-recycling resonance condition applied. In the set on the right, the control sidebands' phasors are evolved in time such that their projection terms regarding the carrier cancel. The phasors' rotation is indicated by the dashed black arrows.

In the case of a tuned detector, the lower and upper control sideband gets a positive and a negative phase shift, respectively, due to the signal-recycling cavity transfer function; their amplitudes are equal. To achieve an annihilation of the projection terms onto the carrier, both control sidebands have to evolve forward in time, to reach the position shown on the right of the first line. To progress in time is, however, equivalent to a negative demodulation phase (see footnote 24 on Page 30). The demodulation phase is equal to the phase shift of the lower sideband. With the given initial sideband pointings, it corresponds to the particular phase shift introduced by the signal-recycling cavity to the upper sideband.

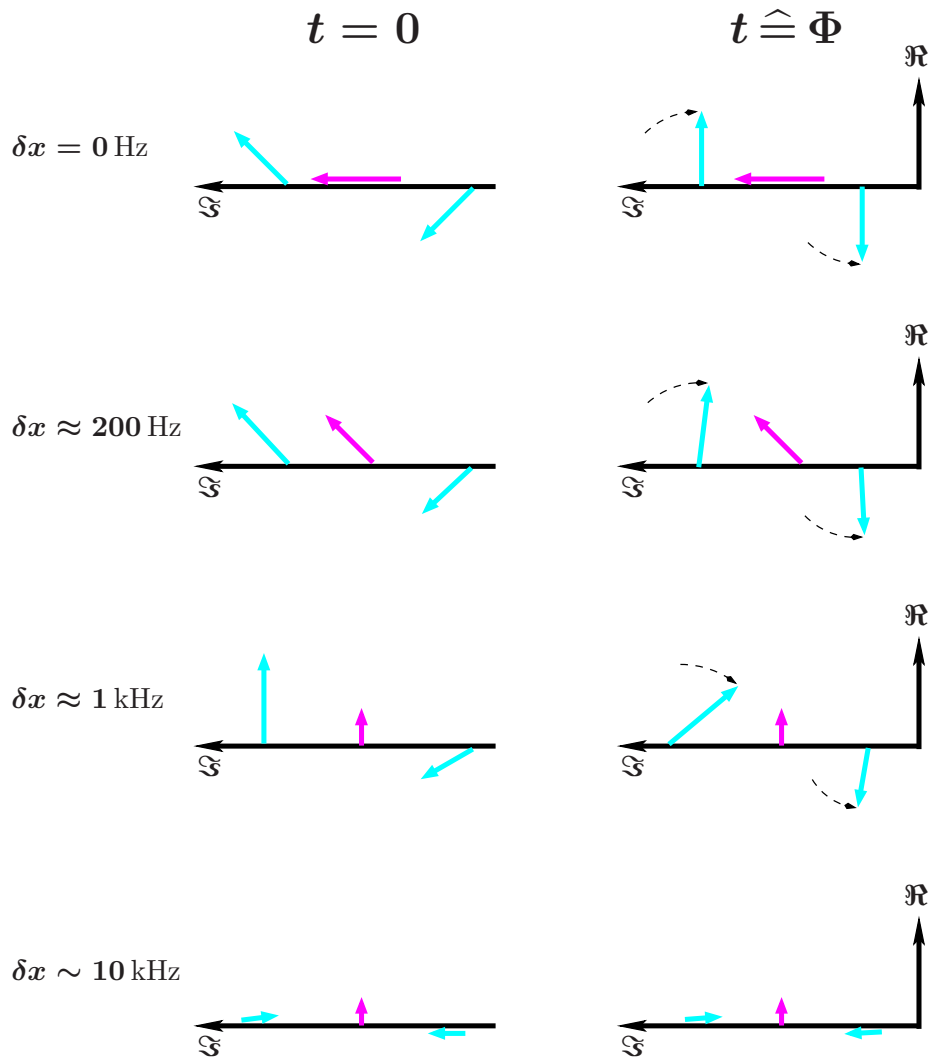


Figure 3.16.: Deduction of the Michelson error-signal vector characteristics for several non-negative **MSR** tunings. The figure applies the resonance conditions, contained in Figure 2.4, to the phasors of the upper picture situated in the lower right quadrant of Figure 1.15. Figure 3.16 is organised as follows: From top to bottom, four signal-recycling cavity tunings are accounted for, labelled on the very left. The left set of phasors qualitatively displays the phasors expected in the south due to the signal-recycling resonance conditions. In the right set, the control sideband phasors are evolved such that the projection terms cancel. The dashed black arrows indicate the rotation. Their lengths and orientations relate to the amount and sign of the associated demodulation phase, respectively.

If the signal-recycling cavity is detuned, three effects occur that compete in terms of demodulation phase evolution (please consult Figure 2.4).

- **Michelson sideband phases** With increasing signal-recycling cavity detuning, both the phases of the two control sidebands and the difference of the sidebands' phase shift decrease monotonically. For very low (< 200 Hz) and very large (> 3 kHz) **MSR** tunings, the gradient of this difference is negligible, but in between, the lower sideband's phase shift decreases much faster than for the upper. Around the resonance of the lower sideband, the gradient of the phase shift difference is maximal.

Assuming equal sideband amplitudes of anti-parallel phasors, for simplicity, the demodulation phase has to be half of that phase shift difference to make them cancel again²⁸. This means, the absolute demodulation phase should decrease with the same characteristics as the phase shift difference, very slightly for low and high detunings, and fastest around the lower sideband resonance.

- **Michelson sideband amplitudes** With increasing signal-recycling cavity detuning, the ratio of the lower and upper sideband amplitudes increases up to roughly the lower sideband resonance, then again decreases to 1. In a particular low-detuning region (here, roughly ≤ 500 Hz), the increase is almost linear.

Acting on the assumption that the sidebands already evolved to be anti-parallel (with the considerations from the item above), we see that they do not cancel any more with differing amplitudes. The sum of their components regarding the carrier only vanishes if the carrier in this constellation is perpendicular. Else, the absolute value of the component, regarding the carrier, of the lower sideband exceeds that of the upper. Depending on whether the carrier phasor pointing is closer to the upper or the lower sideband phasor, the sidebands need to evolve from this anti-parallel state backwards in time or with time, respectively, to yield vanishing projection terms. With a fixed carrier phasor pointing, the larger the amplitude ratio, the larger the required time evolution on top of that necessary for anti-parallelism.

- **Carrier phase** The phase of the carrier decreases with increasing detuning. Different from the lower sideband, however, the slope of the dispersion is maximal for a tuned detector and decreases monotonically for increasing detuning. Thus, the absolute phase shift of the carrier is, for low detunings, much larger than each of the two sidebands.

Due to this carrier phasor rotation, the pointing will for all detunings be closer to the lower control sideband phasor (see the phasor pictures in the second column of Figure 3.16). This, considering the item above, requires a progression of the sidebands in time, thus, an additional decrease of the demodulation phase. However, the higher the detuning, the fainter this effect will become as the two control sideband phasors' phase shifts sooner or later approach -90° (as well as for the carrier).

²⁸If parallel phasors are rotated by different amounts, during (positive or negative) time evolution both need to cover an equal rotation of half of their phase difference to again reach parallelism, even though they will not end up with the same absolute pointing. The same holds for anti-parallel sidebands.

Combining all three aspects, the demodulation phase yielding maximal (or minimal) optical gain for the Michelson will start with a negative value, then qualitatively first decrease, and then increase until it asymptotically converges to 0° . The decrease takes place as long as the carrier sideband-phasor pitch towards the lower sideband phasor, and the increase of amplitude ratio of the sideband phasors dominate the decrease of the absolute phase shift difference discussed in the first item.

The “crossover” detuning frequency for which the dominating effects change, delicately depends on the exact resonance conditions of all light fields. For the sake of clarity, Figure 3.16 only qualitatively follows these conditions. However, the example detunings very well illustrate the considerations made above.

If the signal-recycling cavity detuning is roughly around half the cavity bandwidth for the carrier (phasor diagrams in the second row of Figure 3.16), the carrier gets rotated by $\approx -45^\circ$. As the sideband phases only slightly decrease compared to the tuned case, by roughly the same amount, and already recognizably differ in amplitude, this necessitates a larger anti-clockwise rotation of the upper control sideband, compared with the tuned case, thus, a positive time evolution. As the demodulation phase value is just opposite to the direction of the upper sideband’s phasor rotation, it consequently decreases.

Once the carrier phase shift of $\approx -90^\circ$ is achieved, like at higher tunings, the appropriate demodulation phase depends on the combination of the control sideband phase shifts and their relative amplitudes. Around the lower sideband resonance (phasor diagrams in the third row of Figure 3.16), its phase shifts linearly with highest slope, whereas the amplitude ratio with the upper sideband is already at its turning point. Thus, the effect supporting an increase in demodulation phase steadily takes over.

The higher the detector detuning, the clearer the demodulation phase evolution. The phasor diagrams in the last row of Figure 3.16 illustrate that the demodulation phase increases asymptotically to 0° .

For low detunings, the length of the error-signal vector (and with it the optical gain) is expected to be dominated by the carrier amplitude. However, when the lower control sideband reaches signal-recycling resonance, the carrier amplitude is already significantly reduced. Thus, the optical gain change is at high detunings mainly influenced by the sidebands’ resonance conditions.

In addition to the fact that the phasor diagrams only qualitatively display the resonance conditions inside the signal-recycling cavity, there are two further aspects to keep in mind.

The direction of demodulation phase evolution depends on whether the upper or the lower sideband gets resonant when tuning the signal-recycling cavity positively. Here, we assumed GEO 600-like lengths and resonance of the control sidebands inside the power-recycling cavity. The resonance condition inside the signal-recycling cavity may differ for either different lengths or different control sideband frequencies.

The statement that the demodulation phase for the tuned detector is negative and equivalent to the phase shift introduced to the upper sideband by the signal-recycling cavity is only correct with respect to the initial sideband phasors’ orientation yielding maximum (or minimum) optical gain in the simple-Michelson case. In general, the de-

modulation phase offset around which the evolution, described above, takes place depends on the exact traversed optical pathlengths modulo the sideband wavelength.

3.5. Tuning script generation

When considering a tuning script, we presume a detector that is already locked. That means, all relevant degrees of freedom are stabilised by a control loop using a characteristic error-signal. In particular, the signal-recycling mirror (MSR) is captured at, and fixed to a certain tuning. In order to change this tuning, the idea is to shift the error-signal such that the zero crossing is off-set by a certain amount.

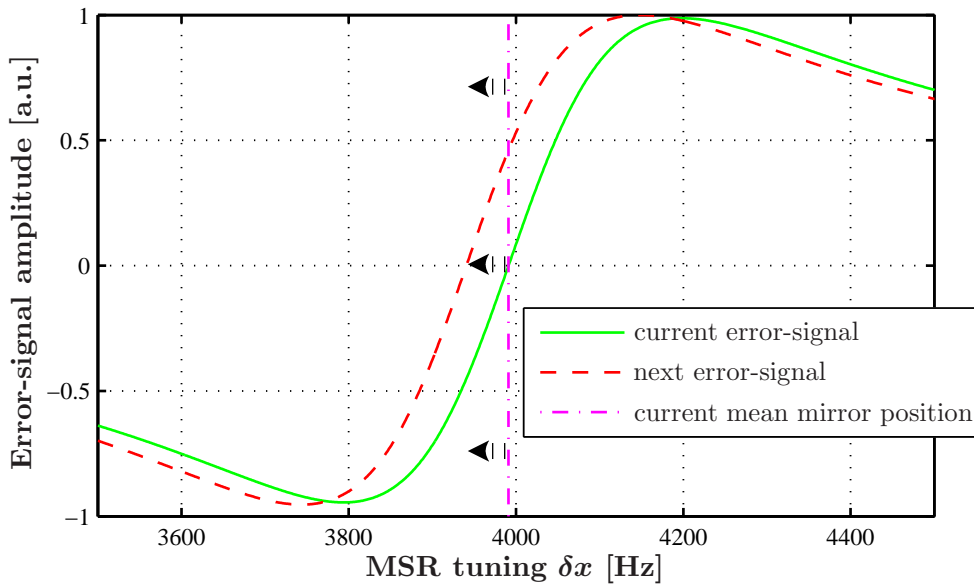


Figure 3.17.: Signal-recycling error-signal amplitudes for different tuning steps. The error-signals are generated with control sideband frequencies differing by 50 Hz. The demodulation phases are set to yield the most symmetrical shape around the zero crossing, and are in this case the same. The solid, green line describes the theoretical error-signal shape with which **MSR** is currently locked. Thus, the mirror is expected to be located on average at the respective zero crossing. This **MSR** position is in addition marked by the dashed-dotted, magenta vertical line. Switching abruptly to the other sideband frequency, the new error-signal, indicated by the dashed, red line, comes across the mirror shifted from the new operating point. As this **MSR** position is still within the monotonic region of the new error-signal, the feedback signal will drive the mirror towards the new zero crossing with a force proportional to the particular error-signal amplitude. This movement is indicated by the black arrows.

Figure 3.17 exhibits an example of two theoretical error-signal amplitudes, depending on the **MSR** tuning, for different tuning steps. The presumed current error-signal, de-

terminating the present mirror tuning, is represented by the solid, green line. It pins the **MSR** position to its zero crossing, which is indicated by the dashed-dotted, vertical magenta line. The dashed curve exhibits the error-signal amplitude yielded with a control sideband frequency offset of 50 Hz and the same demodulation phase. If the error signal abruptly switches to the dashed curve, **MSR** has a sudden offset from the new zero crossing, the newly set operating point. As the mirror is well within the monotonic region of the dashed graph, the control loop should be able to drive the mirror from the current to the desired position. Neglecting the frequency dependency of the electronic filters of the control loop, the applied force is proportional to the particular error-signal amplitude for each temporary **MSR** position. Thus, the overall energy transferred to the mirror on its way to towards its new equilibrium position is proportional to the integral of the error-signal between the current and the future mean mirror position. The associated movement is indicated by the black arrows.

A new zero crossing position can in principle be obtained by altering either the demodulation phase *or* the control sideband frequency generating the signal-recycling error-signal. The deduction of the error-signal with the projection picture makes, however, clear that a change of only one parameter will also deform the error-signal shape. This may, beyond a certain tuning interval, result in a signal that leads to an unstable control loop, either because of a too big alteration of the optical gain or a (one-sided) reduction of the capture range.

Thus, to enable an **MSR** tuning over a wide range and from any arbitrary initial position, for every signal-recycling sideband frequency (i) a demodulation phase should be set, to ensure a satisfying error-signal shape, and (ii) any gain change should be compensated, to maintain control loop stability. The optimal parameter values that are distributed to the phase shifter and the electronic gain, respectively, need to be determined by simulation.

In case of a successful **MSR** tuning, the resonance conditions of the Michelson control sidebands change as a consequence (a detailed discussion on this can be found in Section 2). This will also alter the properties of the respective error-signal. Thus, for every single signal-recycling cavity tuning, the demodulation phase and gain of the Michelson control loop need also to be determined²⁹.

In the following subsections, the criteria for an ideal error-signal will separately be introduced for the signal-recycling and the differential Michelson control loop. Subsequently, the simulation results for the parameters, characterising the optimised error-signals, are presented.

²⁹The power-recycling feedback is hardly influenced by the signal-recycling cavity tuning. Thus, the respective error-signal parameters can remain the same.

3.5.1. Signal-recycling control-loop parameters

Optimisation criteria

As explained above, a tuning process switches the signal-recycling error-signal amplitude from one shape to a different, off-set one. The signal-recycling mirror thus has to be moved towards and held at the new operating point. For this, one requirement for the subsequent error-signal is to comprise the current **MSR** position within its capture range, as plausible from Figure 3.17. The rms motion of **MSR** does not limit the maximum possible step size:

- As the detector is already locked, all mirrors are, except for the limited open loop gain, at rest. The free hanging **MSR** has a remaining rms motion of ~ 400 nm. Figure 3.18 shows the linear spectral density of the experimental feedback signal to **MSR**, calibrated to the mirror displacement. The motion is dominated by the peak around 0.25 mHz caused by feedback noise. This rms value is suppressed by the factor of the open loop gain of the control loop, $\sim 10^4$ and 10^6 for the acquisition and run mode, respectively (see Figure 3.6). For **MSR**, this means a residual rms motion at equilibrium of ~ 40 pm and 0.4 pm, corresponding to 10 Hz and 0.1 Hz, respectively. This is negligible compared with the signal-recycling cavity linewidth of 400 Hz that determines the extent of the monotonic error-signal region around the zero crossing.
- During the process of switching between error-signal parameters, for a short time in the order of maximally ~ 100 ms, the gain parameter might not match the corresponding modulation frequency. For the demodulation phase the response time is even longer, ~ 1 s (due to an integrator). However, if the tuning steps are small enough, the gain and demodulation phase of neighbouring modulation frequencies should not limit the performance. The probability for the mirror to extend its movement during the switching process is, thus, fairly low.

Whereas the capture range only limits the tuning step size, the control loop stability, depending on the optical gain, is an imperative requirement.

Unattached from that, the error-signal shape can change if one or more of the other degrees of freedom alter due to a limited gain of the respective control. If the signal-recycling gain or capture range are affected too much, a lock loss can occur either due to instability or because of an unfavourable position of the **MSR** within this altered error-signal. In a worst case scenario, even the zero crossing may vanish completely. To guarantee a fairly predictable error-signal, its dependency on other degrees of freedom needs to be investigated and minimised, if possible. First simulations (see 2.3.3 in [Grote03b]) for selected examples of signal-recycling demodulation phases identified the differential misalignment of the Michelson, the offset of the Michelson from a perfect dark fringe, and the offset of the power-recycling cavity from carrier resonance, to be of relevance for the signal-recycling error-signal shape. Thus, besides making the control loop as high-gain as possible, the goal is to find demodulation phases for which the influences are minimal

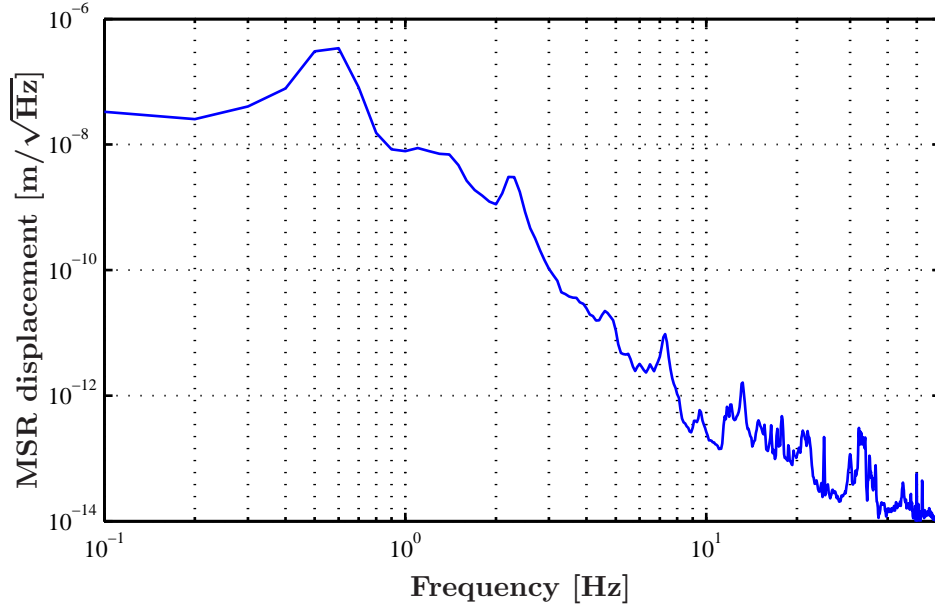


Figure 3.18.: Signal-recycling feedback calibrated to **MSR** displacement.

or at least uncritical. The intersection of these demodulation phases yields the allowed range applicable for a tuning script. In addition to the degrees of freedom mentioned above, the signal-recycling error-signal under the misalignment of **MSR** is observed.

Such an investigation is quite extensive to be carried out for each particular signal-recycling modulation frequency. In contrast, it is fairly easy to determine demodulation phases that specify particular error-signal properties. Thus, the error-signal susceptibility to other degrees of freedom is evaluated for selected frequencies only. The result is used to correlate the demodulation phases, yielding particular error-signal characteristics, to the error-signal susceptibility to other degrees of freedom³⁰.

Categories of error-signal properties are gain, capture range, energy transfer³¹ and symmetry. The relevance of these properties for a success of a tuning step decide on the way of optimisation:

- In the experiment, the overall feedback gain is set to yield a unity gain frequency at ~ 40 Hz. Thus, it may only vary by a factor of $[0.5, 2]$ to ensure a phase margin of the loop greater than 20° , and guarantee a stable control (compare with Figure 3.6). In principle, if the **optical gain** change between two tuning steps is known, the electrical counterpart can be set to the opposite direction to compensate for it. However, the larger the optical gain, the better the signal-to-noise ratio of the

³⁰This approach is legitimate, as a change of a particular property of, for example, a symmetric error-signal can be anticipated to be less essential for a good feedback performance than the same change applied to an already very asymmetric error-signal.

³¹The difference between gain and energy transfer becomes clear below.

error-signal³².

In the simulation, this criterion is met by simply identifying the error-signal with the highest slope at the zero crossing.

- A large **capture range** enables large tuning steps and thus a fast tuning³³. A fast tuning is desirable for several reasons: the detector is less stable during the tuning process than in the final state, as the auto alignment loop of **MSR** is only switched on at the targeted tuning. Secondly, large seismic events may interrupt the detector lock during data taking. Re-acquiring the intended sensitivity shape in a short time minimises the effect on the duty cycle of the detector.

The capture range is, in agreement with [Grote03b], defined as the monotonic region around the considered zero crossing. Thus, the local minima and maxima around the zero crossing are equivalent to the limits of the capture range. The region of the capture range with smaller tunings with respect to the zero crossing will henceforth be called *negative* or *lower (one-sided) capture range*, whereas the *upper* or *positive (one-sided) capture range* is situated on the positive tuning side.

The intended, continuous tuning in both directions equally adds weight to both capture-range sides. Thus, to prevent an optimisation of one side at the expense of the other, the smaller one-sided capture ranges of the error-signals need to be compared. The largest among them points, in this respect, to the optimal demodulation phase.

- The maximally possible **energy transfer** on one side of the zero crossing is proportional to the absolute integral of the error-signal amplitude between the zero crossing and the respective capture range limit, summing up the force applied on a mirror during a movement. Applying a new tuning step, the ideally resting mirror is dragged from its current position by providing it with the according kinetic energy. If the kinetic energy gained on the one side of the error-signal exceeds the one that is withdrawn on the other, the mirror may leave the capture range of the error-signal and be lost. Thus, the tuning step is limited to the range within which the energy transfer of the steeper side of the error-signal does not exceed the maximally possible transfer of the other side.

To yield maximum tuning steps, again, the smaller integrals of each error-signal are compared among each other to find the maximum, indicating the appropriate demodulation phase.

- As the tuning should work equally well to both directions, a certain **symmetry** of the error-signal shape will be required (see Figure 3.17 for illustration).

Perfect point-symmetry of a function $f(x)$ around x_0 is defined as $f(x_0 + a) - f(x_0) = -(f(x_0 - a) - f(x_0))$, $\forall a$. Thus, the deviation of each pair of amplitude, with same position offset from the zero crossing, needs to be evaluated. As only the symmetry within the capture ranges is of interest, the contributing pairs of ampli-

³²With the new, high-reflective **MPR**, the control sidebands at the **BSAR** are very weak. The corresponding, decreased *SNR* of the signal-recycling error-signal was discovered to limit the detector sensitivity.

³³The switching time between tuning steps has a lower limit of ~ 100 ms at GEO 600.

tudes have to sit closer around the zero crossing than the smaller one-sided capture range. The error-signal possessing the smallest mean deviation is the targeted one.

The exact knowledge of the **MSR** position yielded by the specific combination of sideband frequency and demodulation phase, is meaningless regarding the success of a tuning step. However, it gets important when choosing a particular frequency of peak sensitivity. Then, the modulation-frequency/demodulation-phase/gain parameter combination should be fine-tuned to obtain the intended **MSR** position. Consequently, the **MSR** position, corresponding to the particular parameters, is also recorded.

Simulation methods

This subsection describes how the signal-recycling error-signals were generated and evaluated with respect to the properties listed above, for every single signal-recycling control sideband frequency. The approach to the susceptibility to imperfect other degrees of freedom is explained afterwards.

For the investigation and optimisation of particular error-signal properties, all degrees of freedom (except for the signal-recycling tuning) are assumed to be perfect.

One consequence of Equation 1.20 in Section 1.2 is that the complete information on the error-signal amplitude is gathered by knowing both error-signal-vector components in an arbitrary ortho-normal basis. The fixed coordinate system only defines a constant demodulation phase offset. Thus, in order to save memory and calculation time, it is enough to generate two simulated error-signal data streams for one sideband frequency, demodulated with any pair of demodulation phases separated by 90° . This was done with FINESSE.

To ease the subsequent analysis of the error-signal, the **MSR** tuning interval and steps were uniquely set for all targeted detector tunings. Hence, as these tunings comprise a large range of roughly 5 kHz, the **MSR** tuning requires at least the interval of $[0 \text{ Hz}, 5 \text{ kHz}]$, including a margin not to miss any possible error-signal feature at the detector tuning edges.

To cover all targeted detector tunings, the modulation frequency is varied in a second axis. The FINESSE script for this specific simulation can be found in Appendix B.1.1.

For each **MSR** tuning, the signal value obtained with the lower demodulation phase can be regarded as the real part of I_{ω_m} , the other as the imaginary part. The error-signal amplitude for the particular mirror tuning for any arbitrary demodulation phase Φ can be acquired from I_{ω_m} by any of the equivalent operations given between Equation 1.18 and 1.20. The demodulation phase variation, and any of the following parameter optimisations were done with MATLAB. The respective MATLAB script is given in Appendix B.2.2.

The tuning steps for the control sideband frequency δf_m were set to 25 Hz, and to $1.44 \cdot 10^{-3} \text{ } \cong 1 \text{ Hz}$ for the **MSR** position $\delta\chi$ (see Appendix B.1.1). The increments for the demodulation phase Φ were 1° (see Appendix B.2.2). The step sizes are justified as follows:

- Guided by the capture ranges of $\approx \pm 200$ Hz, indicated in Figure 3.19 (see explanation of the figure at the end of this paragraph), and the negligible rms movement remaining (see subsection above), a modulation frequency tuning step of less than 25 Hz was not regarded to be necessary to guarantee a successful tuning process. As the peak sensitivity of the current GEO 600 detector gets worse by 10 % only ± 90 Hz away from the peak frequency, an increment for the adjustability of the **MSR** position of 25 Hz seems justifiable with respect to targeting a particular gravitational wave source.
- For the mirror position step size used in the FINESSE simulation, the crucial requirement is to be able to well determine the relevant error-signal properties like zero crossing, gain and capture range. The structure of the error-signal extends to the bandwidth of the signal-recycling cavity. Thus, the step size of 1 Hz being 1/400 of this bandwidth should resolve the error-signal accurately enough.
- To determine the necessary resolution of the demodulation phases, the corresponding deviations of the error-signal parameters gain and capture range need to be known. Coarse quantitative investigations made obvious that the amount of parameter change depends very much on the demodulation phase itself. The focus was set to demodulation phases yielding error-signals with decent symmetry. For most symmetric error-signals, the gain varies by far less than 1 %, and the capture ranges by not more than 11 Hz if the demodulation phase changes by 1° . The left and right pictures of Figure 3.19 display the error-signal for $\delta f_m = 4$ kHz and $\delta f_m = 300$ Hz, respectively. Each demodulation phase Φ is determined to yield highest error-signal symmetry close around the zero crossing. Also shown are the curves demodulated with a demodulation phase deviation of $\pm 1^\circ$. The signals are hardly distinguishable from each other by eye, even for small δf_m . The blue crosses mark the capture range limits. Please note that although the units of the error-signal amplitudes are arbitrary, the relative differences of the error-signals for varying f_m and Φ should agree with the experiment.

The MATLAB script successively evaluates the error-signals for each control sideband frequency. An overview over the single steps can be gathered from the content at the top of the script. The error-signals are evaluated and optimised corresponding to the considerations above, on Page 114 and the following. More explanations on the mathematical implementation can be found in the comments below the respective MATLAB script in Appendix B.2.2.

The optimal demodulation phases and corresponding parameters are used for further evaluation regarding the susceptibility to other degrees of freedom. An accommodation to the experiment is still necessary (see below).

The influence of other degrees of freedom on the signal-recycling error-signal shape is investigated separately for each degree. The FINESSE output file from above serves as reference for the comparison with the other detector setups, where particular degrees of freedom have an offset from the ideal states of Appendix B.1.1. Ten detector configurations with different modulation frequencies, equally spread in the interval of $\delta f_m \in [0 \text{ kHz}, 4 \text{ kHz}]$, are considered.

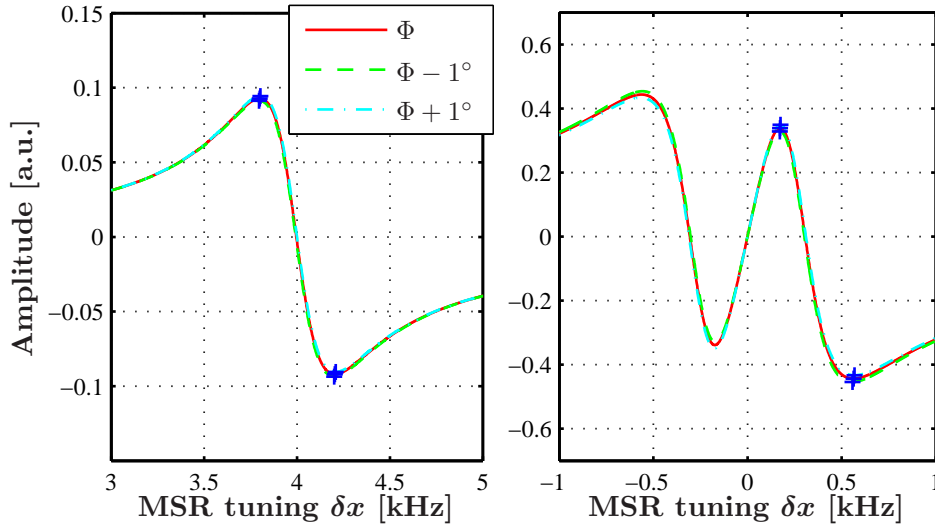


Figure 3.19.: Signal-recycling error-signal for a $\delta f_m = 4$ kHz (left) and $\delta f_m = 300$ Hz detector configuration (right). The demodulation phase Φ for each configuration yields the most symmetric curve around the zero crossing, within a region limited by the smaller capture range. Besides, each picture also displays the error-signal with a demodulation phase deviation of $\pm 1^\circ$. The blue crosses mark the respective capture range limits around the (positive) zero crossing. (Negative tunings exhibit exactly the same features and are, thus, neglected.)

The introduced offsets are larger than the expected rms offsets of the operating detector (at least slightly). The differential misalignment of the Michelson end mirrors **MCe** and **MCn**, defined according to [Grote03b] as a differential tilt or an anti-clockwise rotation of both mirrors at the same time, is set to 100 nrad, the same as the rotation of **MPR**. As the **MSR** misalignment is not controlled during tuning, the simulation uses $1 \mu\text{rad}$. The differential longitudinal rms motion of the Michelson end mirrors is assumed to be 100 pm each. As previous simulations already showed a difference in the error-signal shape depending on the sign of the differential offset, two separate simulations, accounting for different offset signs, are performed. The offset of the power-recycling cavity from carrier resonance is set to 10 pm. A detailed justification for the chosen values is given in the comments below the MATLAB script in Appendix B.2.1 that evaluates and compares the relevant error-signal properties.

Similarly to Appendix B.2.2, for each of the ten modulation frequencies the zero crossings, gains and capture ranges of each complex error-signal, projected onto different demodulation phases, are determined. If all parameters are calculated, the gain ratios to the reference, and the upper and lower capture range deviations from the reference are compared. For each kind of altered degree of freedom, the demodulation phases, yielding best agreement with the reference error-signal, are collected. The most extreme demodulation phases among them span the interval of demodulation phases yielding least susceptible

error-signals. More details on the evaluation can be found in the comments regarding Appendix B.2.1.

Simulation results

In the following, first some particular examples of the simulation results for the signal-recycling error-signal susceptibility to other degrees of freedom will be presented. The demodulation phases optimising for particular error-signal properties are afterwards directly related to these results.

Figure 3.20 presents the susceptibility of the error-signal gain and capture range depending on the demodulation phase, for a detuning of ~ 3 kHz. The upper and lower picture display the gain and capture range deviations, respectively, from the error-signal with perfectly controlled degrees of freedom. (The shown demodulation phase interval is determined to generate a zero crossing within ± 250 Hz around δx_m , for all examined degrees of freedom.)

For the gain ratio, the gains are normalised by the gain of the error-signal of a perfect detector, where the same demodulation phase is applied. Each curve represents the alteration of one particular degree of freedom. In the lower picture, the solid and dashed lines display the deviation of the lower and upper capture range limits, respectively. The reference capture range limits are subtracted from the other, corresponding limit positions such that positive values for the upper capture range, and negative values for the lower capture range represent an enlargement of the respective, one-sided capture ranges.

The capture range changes due to offsets of the various degrees of freedom are obviously uncritical. The offsets from perfect dark fringe, and power-recycling cavity misalignments are the only degrees of freedom that reduce the lower one-sided capture range, but only by a few Hertz. In all other cases, the one-sided capture ranges are rather enlarged. The minimal capture range changes occur around 150° .

With the exception of the power-recycling cavity longitudinal offset, the gain ratios are within the interval required for stability for all considered demodulation phases. The least varying gains³⁴ are achieved around 135° .

None of the demodulation phases yielding either a minimal gain or capture range deviation, lies in the critical gain ratio region of longitudinal power-recycling cavity offset. Thus, the demodulation phase interval between the maximum and minimum of these phases should yield an uncritical error-signal in terms of control stability.

For the other considered modulation frequencies targeting a particular detuning, the graphs look qualitatively the same with the exception that the demodulation phase with the least change of capture range may lie in a region which is forbidden by the gain change

³⁴Please note that **MSR** misalignment hardly influences the error-signal gain, and rather enhances the capture range. However, misaligning **MSR** on purpose in order to improve the error-signal for the tuning process seems no real option. Recently we see unexplained power fluctuations if **MSR** is not well enough aligned during downtuning.

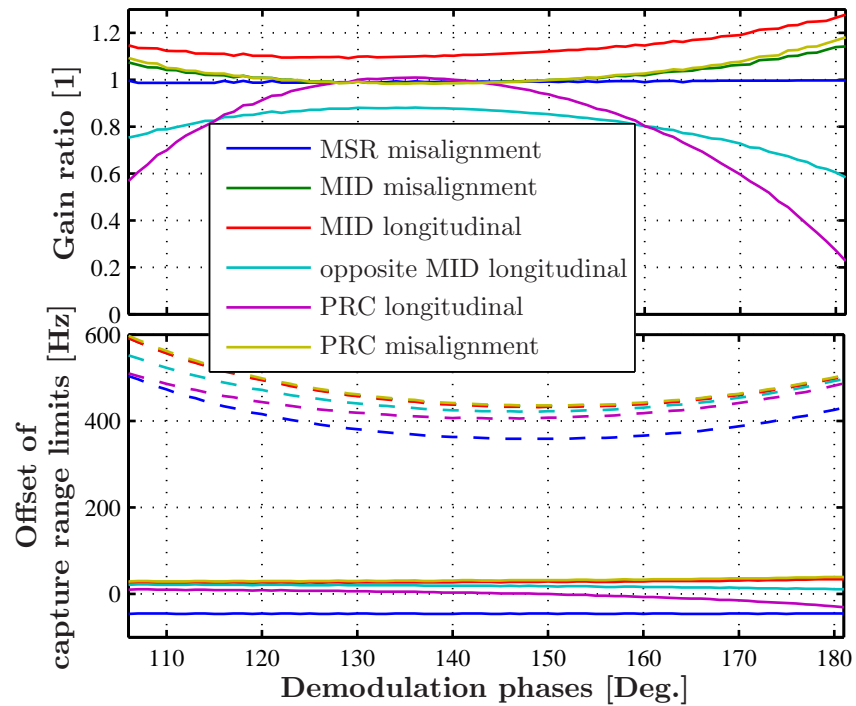


Figure 3.20.: Susceptibility of the signal-recycling error-signal, apparent with $\delta f_m \approx 4$ kHz, to the deviations of various degrees of freedom from their nominal operating points. The upper and lower pictures display the gain ratios and capture range deviations, respectively, regarding the reference error-signal utilising the same demodulation phase but perfect other degrees of freedom. In the lower picture, the solid and dashed lines display the deviation of the lower and upper capture range limits, respectively. Shown are only the results for the demodulation phases that create a zero crossing of the error-signal within an interval of ± 250 Hz surrounding δx_m .

due to the power-recycling cavity longitudinal offset. The only modulation frequency where the deviations exhibit significantly different features is the one used for a tuned detector. Figure 3.21 displays the respective simulation results. Here, the capture ranges

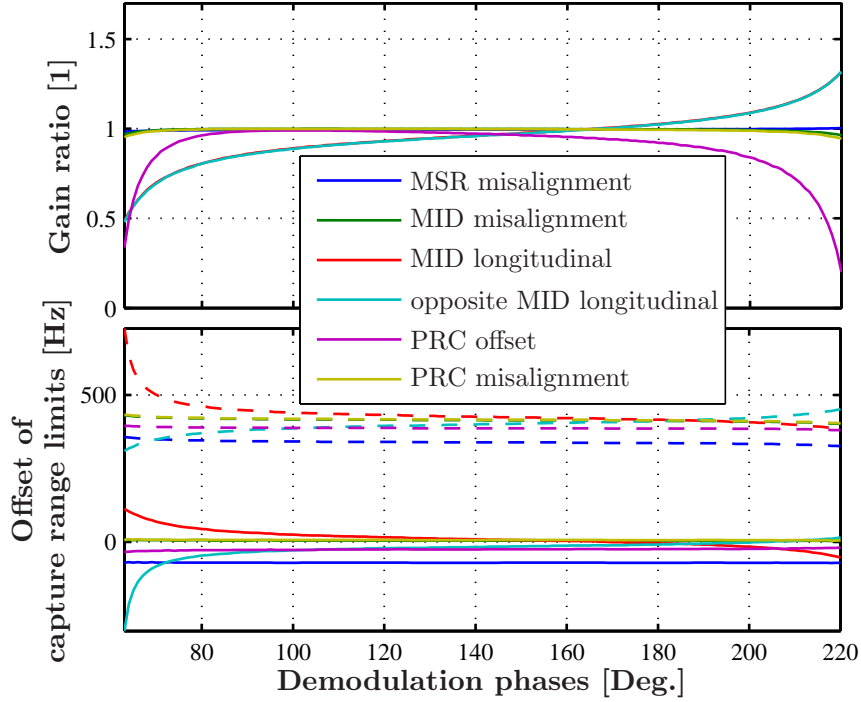


Figure 3.21.: Susceptibility of the signal-recycling error-signal, targeting a detector tuned to 0 Hz, to the deviations of various degrees of freedom from their nominal operating points. Alike Figure 3.20, the upper and lower picture show the gain ratio and capture range deviation referring to the error signal with perfect other degrees of freedom. Due to the symmetry of the resonance conditions of the contributing light fields, the interval of uncritical demodulation phases is quite large.

and gains are so insensitive, as the error-signal structure around the carrier resonance is observed, where the upper and lower control sideband equally beat with the carrier, and the phase and amplitude relations are almost ideally symmetric.

The demodulation phase intervals determined for each of the ten modulation frequencies will in the following help to decide which particular error-signal shapes stay most identical under a change of other degrees of freedom.

Before, however, let us glance at the kind of error-signals that are chosen by the property optimisation procedure. Figure 3.22 illustrates selected error-signal amplitudes for a modulation frequency of $\delta f_m = -400$ Hz. The property criteria that are satisfied best by the solid, dashed, and dashed-dotted lines are capture range, energy transfer, and symmetry, respectively. The blue crosses on the graphs mark the capture range limits. In order to put the capture ranges and zero crossings in perspective, the **MSR** tuning is

given as frequency. The shapes of the error-signals make already by eye plausible that they, indeed, are the best representations for the respective criterion. The capture range condition is the clearest of all.

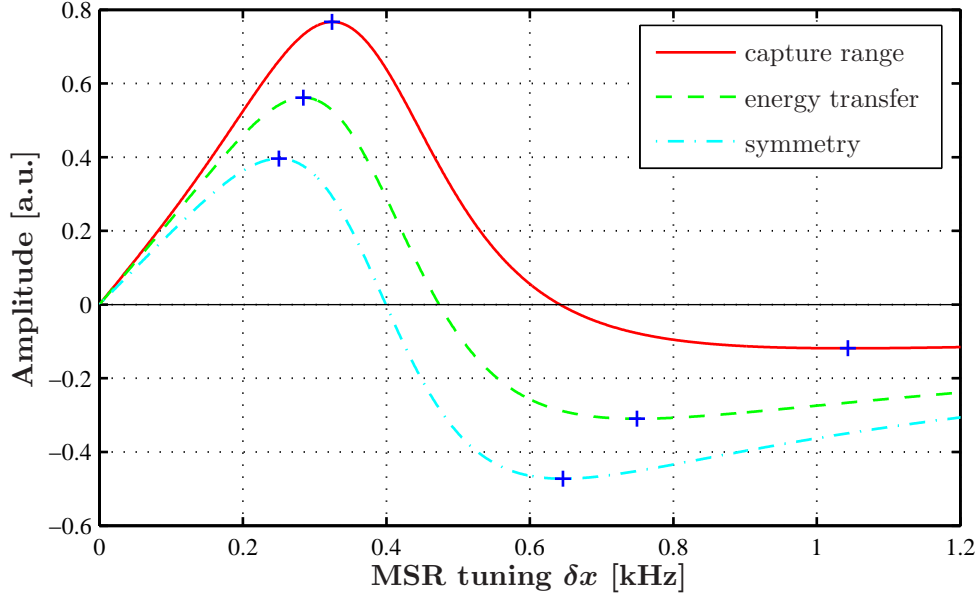


Figure 3.22.: Comparison of signal-recycling error-signal amplitudes optimised for the criteria of largest capture range, highest energy transfer and highest symmetry for $\delta f_m = -400$ Hz. The edges of the capture ranges are marked by the blue crosses. The MSR tuning is given as frequency facilitating to put the capture ranges and zero crossings in perspective. The shape of the graphs in connection with the capture ranges makes plausible how they meet the different property criteria.

Turning now to different modulation frequencies, the corresponding tuning script parameters and error-signal properties will be displayed with respect to the particular control sideband frequency, not the apparent detector tuning. The modulation frequency reference is set to $\delta f_{\text{ref}} = 72 \times FSR_{\text{SR}} = 9017397$ Hz. Due to the cross-coupling of the two recycling cavities, however, this reference deviates by +56 Hz from the frequency yielding exact sideband resonance in the tuned dual-recycled detector (see Section 3.7 for the effect of coupled cavities). Thus, the tuned modulation frequency, δf_{tuned} does not agree with $\delta f_m = 0$ Hz.

The tuning script parameters featuring different error-signal shapes, are shown in Figure 3.23. The upper graph exhibits the demodulation phases, the lower graph the optical gain. All gains are normalised by the highest value of all. The vertical black lines, limited by the crosses, mark the demodulation phase intervals for the particular modulation frequencies, where the error-signal is least susceptible to other degrees of freedom.

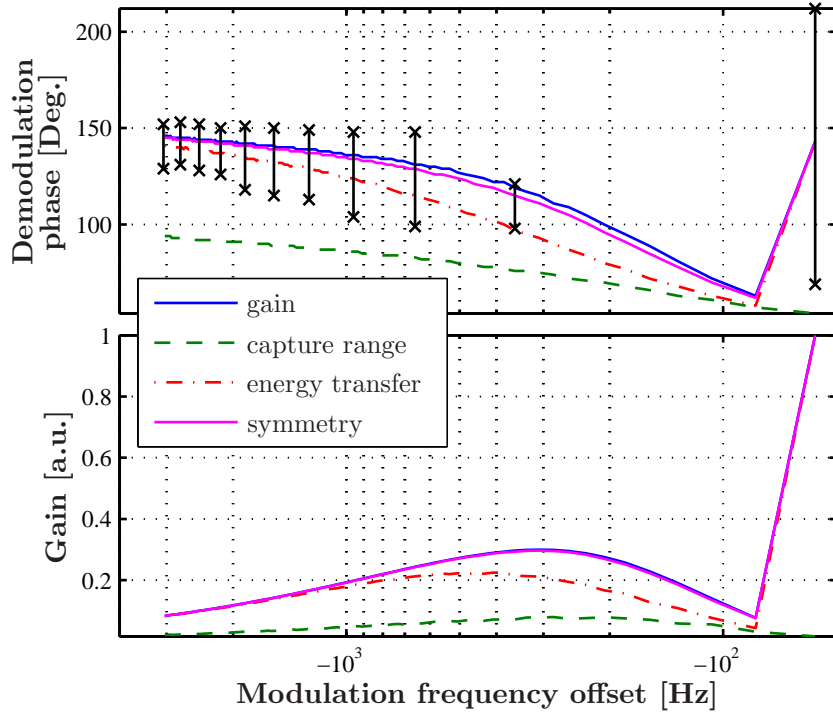


Figure 3.23.: Demodulation phases and gains of signal-recycling error-signals optimised for one particular property at a time (highest gain, largest capture range, highest energy transfer, and symmetry). The parameters are displayed for various control sideband frequencies. The modulation frequencies are given as an offset from $72 \times FSR_{SR}$. The vertical black lines in the upper graph indicate demodulation phase intervals preferable for a continuous tuning process, as the corresponding error-signals show minimal susceptibility to deviations of other degrees of freedom from their operating points.

As predicted by the phasor picture, the demodulation phases decrease with increasing modulation frequency, indicating an increasing influence of the lower sideband. The projection picture predicted that the demodulation phases, yielding highest gain, agree for very high absolute frequency offsets, and δf_{tuned} . In the FINESSE result, the tuned-case demodulation phase is slightly lower. The reason is the influence of the power-recycling cavity resonance whose impact gets stronger the higher the modulation frequency. Adding the phase dispersion of the power-recycling cavity to the middle and lowest row of Figure 3.10, illustrates that the presence of the power-recycling cavity lowers the upper sideband's phase and elevates the lower sideband's phase. To yield the same phasors' pointing as without power-recycling, the sidebands need to progress longer in time. Thus, the demodulation phase needs to be smaller.

The gain first increases with increasing sideband frequency due to the second sideband arising in amplitude the closer the signal-recycling cavity gets to a tuning in the region of the cavity bandwidth. There, the signal-recycling cavity significantly rotates the lower

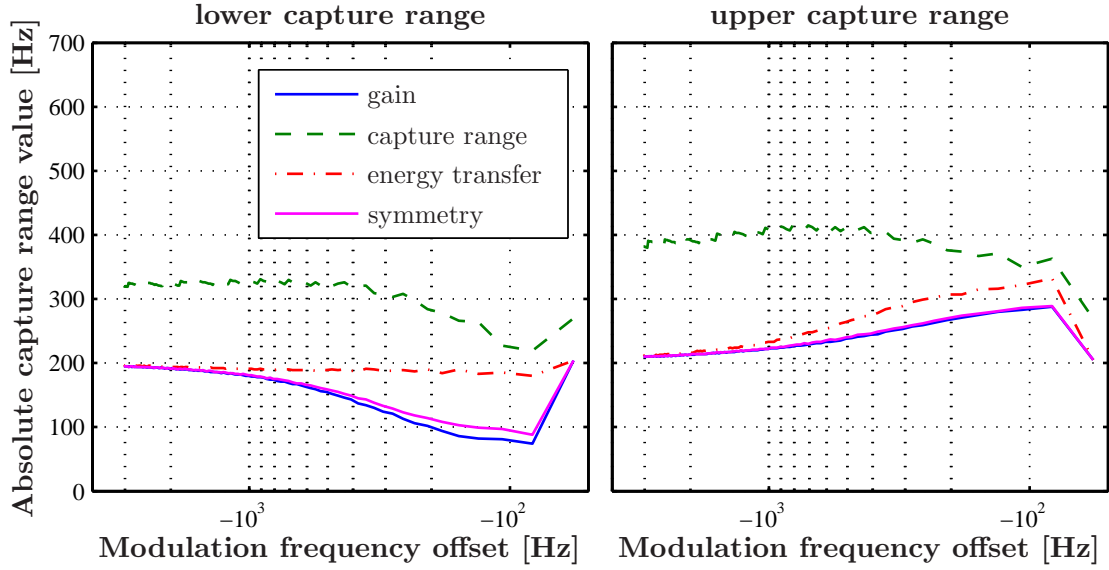


Figure 3.24.: Lower (left picture) and upper (right picture) capture ranges of the error-signals corresponding to the demodulation phases shown in Figure 3.23. The capture ranges vary between 80 Hz and 415 Hz.

sideband anti-clockwise. Figure 3.14 makes clear that this rotation direction reduces both error-signal vector components.

As the capture range is larger the larger the zero crossing offset from δx_m (see Figure 3.22), the respective demodulation phases depend on the limit set for the allowed deviation of the error-signal zero crossing from δx_m .

Including the consideration of error-signal susceptibility to other degrees of freedom, error-signals with highest symmetry are safest. The demodulation phases optimising gain, and energy transfer, however, also (just) lie inside the allowed demodulation phase range for the investigated modulation frequencies.

Beyond the parameters necessary for the tuning script, the error-signal properties like zero crossing positions and capture ranges are also of interest. Figure 3.24 exhibits the absolute values of the lower (left picture) and upper (right picture) one-sided capture ranges of the error-signals featuring the demodulation phases shown in Figure 3.23. Up to a modulation frequency offset of roughly -1 kHz, the capture ranges to both sides amount to ≈ 200 Hz, except for the error signal with largest capture range where the upper and lower capture ranges lie between 300 Hz and 400 Hz. For smaller detunings down to 20 Hz (i.e., $\delta f_m \approx -100$ Hz), the lower capture range decreases while the upper increases. Again, the graphs representing the capture range criterion are the exception. However, the dominating tendency of the graphs is understandable, as the symmetry of the error-signal vectors' distribution in Figure 3.14 and 3.15 gets distorted for lower

detunings due to the increasing influence of the lower control sideband. In case of a tuned detector configuration, all capture ranges are at least 200 Hz.

With the capture ranges shown in Figure 3.24, the tuning step size is absolutely limited to 80 Hz. To tune safely within the complete accessible region, a unique tuning step should, however, not exceed 50 Hz.

For very low detunings, already the additional zero crossing at the tuned point necessarily limits the lower capture range. Given the tuning steps for the modulation frequency of 25 Hz, and guided by the expected **MSR** position δx_m , associated with this frequency, it is at first sight rather astonishing that the lower capture range does not fall below 50 Hz. This gets plausible, though, with Figure 3.25. It displays the zero crossing position of the error-signals generated with the demodulation phases of Figure 3.23. For all of them, the position of the zero crossings, and thus of **MSR**, never falls below 150 Hz, except for the modulation frequency featuring a tuned detector.

Moreover, in Figure 3.25, besides the simulation results, a black, diagonal line indicating δx_m , the position associated with the modulation frequency offset δf_m , is also shown. To remind the reader, δf_m was defined as the modulation frequency offset from the 72nd multiple of FSR_{SR} . With the power-recycling cavity present, this reference frequency, however, does not (necessarily) resonate in the signal-recycling cavity tuned to carrier resonance.

Likewise due to power-recycling, the agreement of the **MSR** position with the simplified linear assumption decreases, even for the error-signals with largest optical gain, or symmetry, namely up to -25 Hz, or -12 Hz, respectively, for the frequency offset interval of $\sim [-3 \text{ kHz}, -600 \text{ Hz}]$ (not completely shown in Figure 3.25). The power-recycling cavity shifts all original signal-recycling cavity resonances depending on the modulation frequency's resonance condition inside the power-recycling cavity (an illustrating discussion on resonances of coupled cavities can be found in Section 3.7). The further the modulation frequency from power-recycling resonance, the fainter its influence and, consequently, the shift.

Above ~ -600 Hz, the impact of the lower signal-recycling sideband, pushing the zero crossing towards higher **MSR** tunings (see Section 3.3.2), starts dominating the power-recycling shift. At a frequency offset of ~ -370 Hz and ~ -220 Hz for highest symmetry and gain, respectively, both the power-recycling cavity and the lower sideband effects match.

The **MSR** positions of the error-signals with largest capture ranges deviate by 250 Hz from the black linear line. This is exactly the limit of the allowed zero crossing deviation from δx_m set inside the MATLAB script to reduce the demodulation-phase parameter space. Without any limit set, the respective zero crossings would sit at the outer most possible edge.

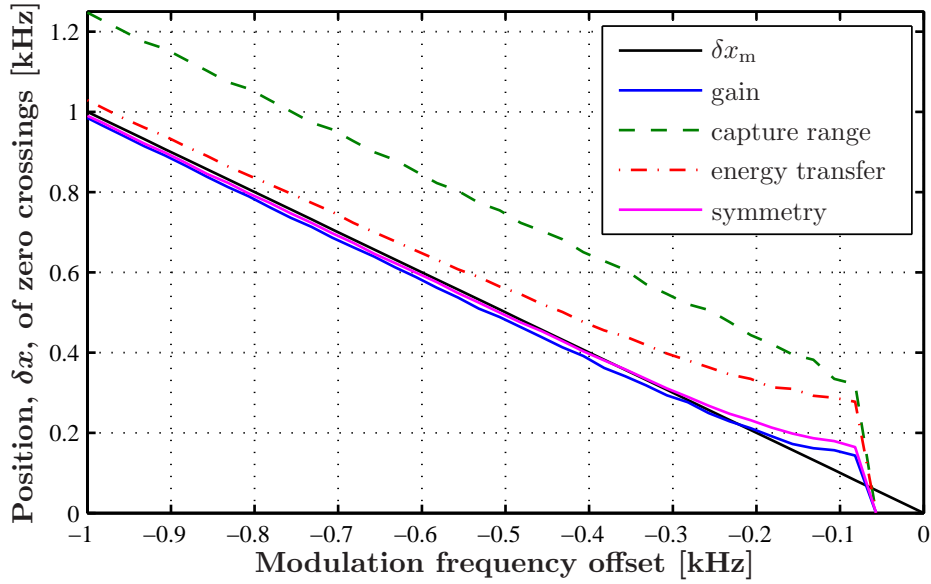


Figure 3.25.: Position of the zero crossings of the signal-recycling error-signals generated with the demodulation phases of Figure 3.23. The black line indicates the position associated with the modulation frequency resonance inside the purely signal-recycled Michelson. All positions are given in units of frequency.

3.5.2. Michelson control-loop parameters

Optimisation criteria

To determine sensible optimisation criteria for the Michelson error-signal, again the expected residual differential rms movement of the Michelson end mirrors needs to be compared with the error-signal structure.

The Michelson error-signal detected with a photodiode in transmission of **MSR** depends on the carrier and Michelson control sideband properties at this detection point. Unlike for a pure Michelson, to predict the error-signal shape of a dual-recycled detector requires the consideration of the influence of all cavities on the light fields.

Assuming for simplicity a perfectly symmetric, power-recycled Michelson interferometer only, a differential length change of the Michelson does not alter the power-recycling cavity length, but the reflectivity of the output mirror formed by the Michelson. Thus, the enhancement of the carrier and the control sidebands alters. In the south port, the increasing transmission of the carrier competes with its power decrease inside the power-recycling cavity, regardless of the direction of differential end mirror displacement. Folding both effects yields a symmetric amplitude and phase relationship regarding the operating point.

These competing effects occur similarly for the control sidebands. The difference is that the targeted operating point is, due to the Schnupp length, only a dark fringe condition for the carrier. However, depending on the sign of differential end mirror displacement, the Michelson in one direction fulfills a dark fringe condition for one of the two sidebands, for a particular amount of displacement. Folded with the enhancement inside the power-recycling cavity, the field properties exhibit a symmetry similar to the carrier, but with a symmetry axis off-set from the targeted operating point.

Needless to say, a precise, depictive prediction of the error-signal shape is difficult, if in addition Michelson asymmetries, higher order modes or higher order sidebands need to be accounted for.

In a power-recycled Michelson, i.e., without signal recycling, the error-signal structure depends only on the demodulation phase. The signal-recycling cavity, however, introduces further asymmetries which differ for particular cavity tunings.

Former simulations (see Figure 2.5 in [Grote03b]) indicate the narrowest error-signal structure at a tuned signal-recycling cavity³⁵. Thus, investigating the capture range of the Michelson error-signal for a tuned detector should yield a lower limit for all capture ranges to be expected while tuning the signal-recycling cavity. Figure 3.26 shows the error-signal for the Michelson for a signal-recycling cavity resonant with the carrier. The overall capture range amounts to 460 pm. The free-running differential rms movement of the Michelson end mirrors amounts, even including the micro-seismic peak at 0.15 Hz, to less than 10 μm (see Figure 1.14 in [Grote03b]). With an open loop gain of of the respective control loop of more than 120 dB, the residual rms will be less than 10 pm. Thus, the capture range should not limit the tuning performance.

Consequently, the only two error-signal properties that lend themselves as optimisation criteria are the gain maximisation, and a zero crossing position exactly at the origin. The position of the zero crossing, however, depends on the one hand on the assumed mode-mismatch inside the dual-recycled Michelson, as higher order modes have different Gouy phases and may give a non-zero error-signal contribution even if the detector is at a perfect dark fringe for the TEM₀₀ mode. On the other hand, the asymmetric losses in the Michelson arms lead to carrier power leaking to the south port, and to slightly rotated sideband phasors, in comparison with Figure 1.15. This can yield a non-zero projection term at the “darkest possible” fringe.

³⁵For a plausible explanation, let us for simplicity compare the effect of a far detuned, and a tuned signal-recycling cavity on the Michelson error-signal. The output mirror of the power-recycling cavity from above needs to be expanded by the signal-recycling cavity, altogether yielding the signal-recycled Michelson as compound mirror. A far detuned signal-recycling cavity increases the reflectivity of a simple Michelson for all differential end mirror displacements, whereas the tuned reduces the reflectivity of the signal-recycled Michelson for the carrier. The effect of the signal-recycling cavity on the carrier, however, makes no appearance until the Michelson leaves the dark fringe, and the impact is larger the larger the dark-fringe offset. Thus, with increasing differential Michelson end-mirror displacement, the enhancement of the power-recycling cavity drops much faster for the carrier with a tuned than with a far-detuned signal-recycled Michelson. As a consequence, the amplitude of the differential Michelson error-signal of a tuned detector is expected to fall off more rapidly than that of a far detuned detector. Thus, the error-signal structure is narrower.

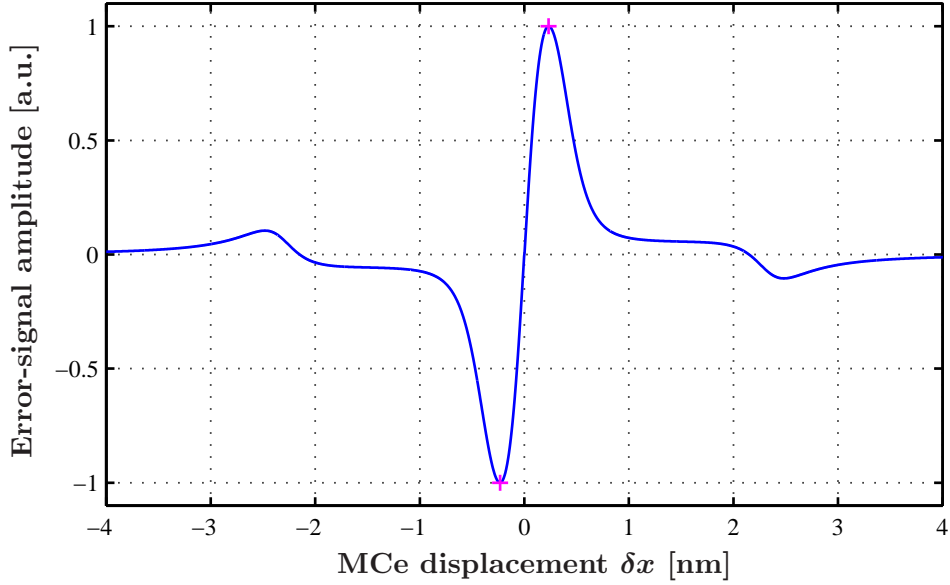


Figure 3.26.: Error-signal amplitude for the differential Michelson end mirrors' tuning for a tuned detector. For each **MCE** displacement δx , given in nanometers, **MCn** is detuned by the same amount but with opposite sign. The demodulation phase is set to yield maximum gain at the origin. The crosses at the global maximum and minimum indicate the capture range limits.

In order not to depend on asymmetry assumptions for the tuning parameters, the demodulation phases for the Michelson control loop are determined to yield a maximum gain at the zero crossing.

Simulation methods

Besides the demodulation phase yielding the maximum gain at the error-signal zero crossing around the origin, and the gain itself, the deviation of the zero crossing from the perfect dark fringe is important in the experiment, though not relevant for successful tuning. As the amount of deviation depends on the exact mode-mismatch and Michelson asymmetries incorporated in the model, it can potentially be used to validate these by comparison with the experimentally-seen off-sets.

The position of the zero crossing necessitates a simulation of the full Michelson error-signal with FINESSE, similarly for the case of signal recycling. However, as the capture ranges are not important, the maximal displacement of the end mirrors can be limited by the amount of expected deviation from dark fringe. Led by experimental observations that the Michelson error-signal offset from perfect dark fringe is dominated by the residual rms

movement, the mirrors' displacement limit is set to ± 10 pm, and the step size is 0.2 pm. The corresponding FINESSE command lines can be found at the end of Appendix B.1.1, with "MI-EP" as headline.

The MATLAB script in Appendix B.2.3 evaluates the FINESSE output file. The code is a very much simplified version of Appendix B.2.2, but utilising the same basic concept. (Thus, for explanations please consult the subsection "Simulation methods" in Section 3.5.1.) The evaluation results like demodulation phase, gain, position of the zero crossing, given as index and in degrees, are together with the respective **MSR** tuning written to a file for further processing.

Simulation results

As in the case of signal recycling, first the results of the script representing the most actual optical setup of GEO 600 will be presented, followed by those for the old and new scripts containing the low reflecting **MPR**.

Figure 3.27 displays the demodulation phases yielding highest gain (upper graph) and the respective, normalised error-signal slope at the zero crossing (lower graph), depending on the signal-recycling cavity tuning, given in units of kHz.

As expected, the optical gain increases the closer the signal-recycling cavity to carrier resonance (see Section 3.4), as the carrier gets additionally enhanced. However, the gain shape slightly deviates from an Airy-function in the tuning region between 0.5 kHz and 1.5 kHz. The slightly widened flank can be assigned to the control sideband resonance.

The demodulation phases increase towards lower detunings from -57° to -16° , above ~ 500 Hz, then again decrease to -27° , for a perfectly tuned detector.

The demodulation phase procession is, prima facie, counter-intuitive considering Figure 3.16 and the resonance conditions of the carrier and the Michelson control sidebands as shown in Figure 2.4. Starting from a tuned signal-recycling cavity, one would expect a decrease of the demodulation phase for low tunings, as long as the lower sideband goes through a signal-recycling resonance. However, as already explained in Section 3.4, the evolution is opposite if the sideband's role is flipped. Section 3.4 considered sidebands resonant inside the power-recycling cavity. In the current script of GEO 600, however, the modulation frequency is off-set from power-recycling resonance by +52 Hz. From the south port as view-point, the power-recycled Michelson is, even with the high reflective **MPR**, an under-coupled cavity for the control sidebands, as the Michelson transmission is roughly 280 ppm. The phase shift of light, reflected by this cavity and being +52 Hz away from resonance, is 5.3° . Such a phasor rotation shifts the resonance frequencies of the signal-recycling cavity by $\sim +1.8$ kHz. As $FSR_{SR} \approx FSR_{PR} - 10$ Hz, the upper control sideband is resonant for a signal-recycling cavity detuning of ~ 600 Hz instead of ~ -1.2 kHz (see Figure 2.4). The same holds for the lower sideband, with switched sign. Thus, for this choice of Michelson sideband frequency, indeed the upper sideband goes through a resonance for positive signal-recycling cavity detuning.

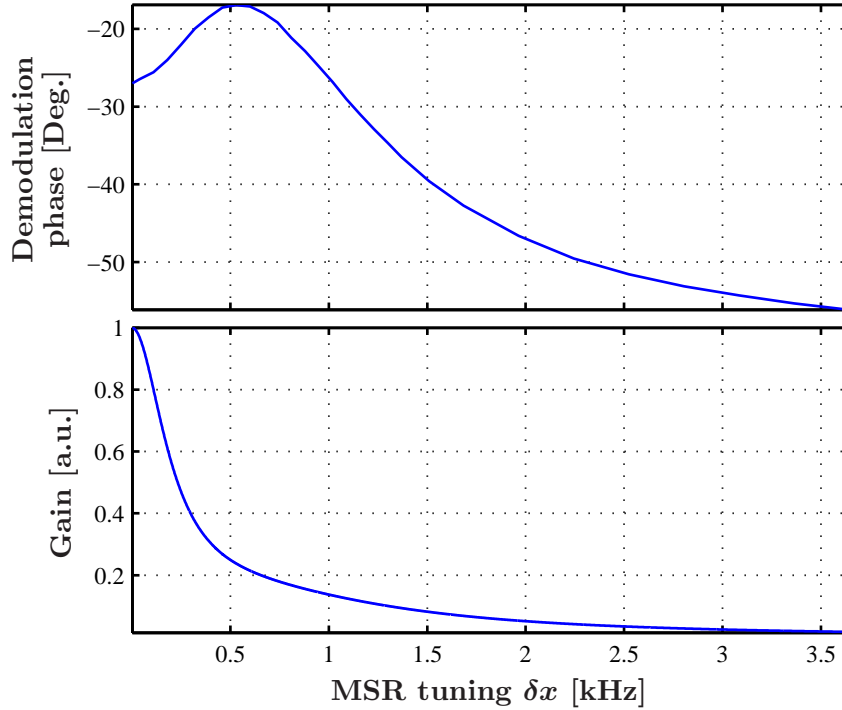


Figure 3.27.: Demodulation phases (upper graph) yielding highest Michelson error-signal gain, and the respective, normalised error-signal slope at the zero crossing (lower graph), for different signal-recycling cavity tunings. The position of **MSR**, $\delta x = FSR_{SR} \cdot \delta\chi/180^\circ$, is given in units of kHz.

The zero crossing positions of the respective Michelson error-signal are displayed in Figure 3.28. The four graphs were generated including different aspects in the preceding computation. As expected, for a beamsplitter with asymmetric reflectivity and transmission, but neither losses nor reflection at the rear surface, the Michelson end mirrors are locked to an ideal dark fringe (solid magenta line). Including asymmetric beamsplitter losses causes a large deviation from the intended operating point (dashed-dotted green line) of up to almost 8 pm. The maximum offset is achieved around 400 Hz detuning. Accounting in addition for higher order sidebands does not alter the result significantly (dashed red line). Higher order modes, however, obviously have an increasing effect on the zero crossing deviation, with increasing **MSR** tuning, of opposite sign (solid blue curve): together with the asymmetric losses at the beamsplitter, the offset vanishes at 2 kHz detuning. For higher detunings, the deviation increases again but with opposite sign.

The deviation from dark fringe does not exceed the experimentally observed rms differential lengths change of the Michelson armlengths. For low detunings around 400 Hz, however, it is comparable.

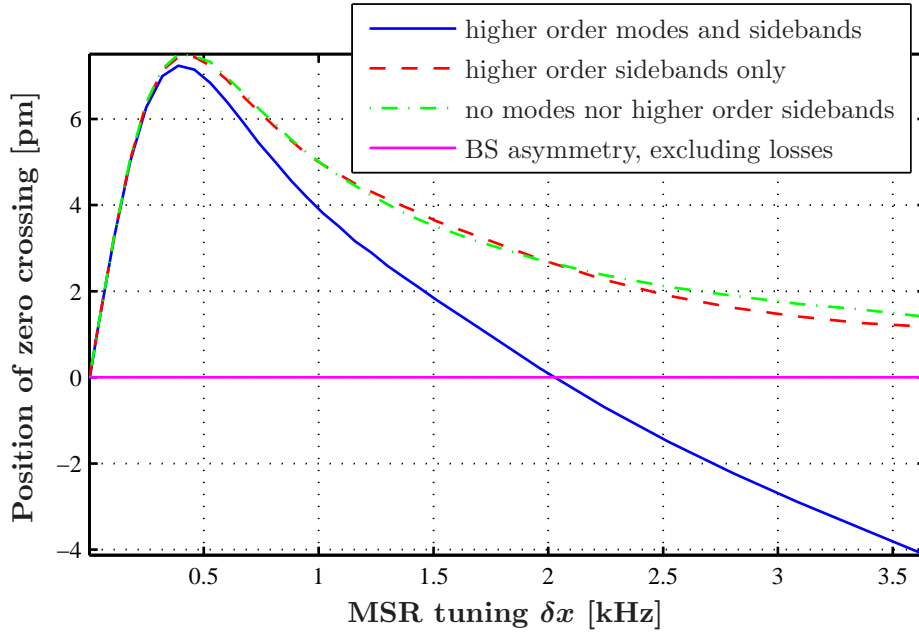


Figure 3.28.: Position of the zero crossings of the differential Michelson error-signals, generated with the demodulation phases from Figure 3.27, versus **MSR** tuning, given in kHz. The deviation from the intended operating point, the dark fringe, occurring at 0 pm, depends on the beamsplitter asymmetries and the field properties accounted for. The beamsplitter asymmetry included in the solid magenta line result refers to unequal transmission and reflectivity. Losses or reflections at the rear beamsplitter surface are ignored for this curve.

3.6. Experimental tuning

The phasor picture and the supporting simulation results enabled us to understand and predict what is happening inside the optical system of GEO 600 when tuning **MSR**. However, to apply the parameters obtained by simulation to the experiment, they have to be adapted to the experimental environment.

This section relates the theoretical results from above to the experiment. At the beginning measurements are presented that, with the knowledge gained about the resonance conditions of control sidebands, approve a positive detuning of the detector. The main topic is, however, the description of the calibration method of the simulated tuning parameters for the experiment. This will be followed by an estimation of the accuracies of optical lengths necessary to obtain a successful tuning script. This section ends with two suggestions to acquire a tuned detector.

3.6.1. Positive, or negative tuning side: this is the question...

The error-signal deductions with the phasor picture showed that the tuning parameters should not depend on the tuning side. However, this symmetry could be broken if higher-order modes become important. Moreover, the knowledge about the tuning side simplifies all discussions about resonance conditions of the occurring sidebands.

Further, the tuning direction is crucial for the existence of the optical spring effect [Buonanno02a, Buonanno02b]. It occurs only if the signal-recycling cavity is positively detuned. In this case, the signal sidebands, entering the Michelson from the south, differentially beat with the carrier inside the Michelson such that the differential displacement of the Michelson mirrors enhances at that frequency. The underlying cause is an oscillating amount of photon pressure on these mirrors. With negative detuning, the associated spring constant is negative.

To decide the tuning direction, the power of the signal-recycling control sidebands, contained in the light beam at the south port of the detector, needs to be known. For a detuned detector, only one of these sidebands should be resonant inside the signal-recycling cavity and appear behind the **MSR**. Figure 3.10 illustrates that, for example, the upper control sideband is resonant in a positively detuned signal-recycling cavity if the modulation frequency lies below $119 \times FSR_{SR}$, as it is the case at GEO 600, and vice versa.

To achieve a separation of the frequency components of the light, a Fabry-Perot interferometer was set up, and the light power was measured while scanning this cavity. Figure 3.29 shows two measurements done with the scanning Fabry-Perot cavity, and a detector setup of GEO 600 with a low-reflective **MPR** ($T_{MPR} = 1.35\%$), the so-called *old setup*³⁶. The detector tuning is 1 kHz. The upper and the lower graphs display the light powers occurring in reflection of **MPR** and in transmission of **MSR**, respectively, versus the Fabry-Perot cavity tuning, given as offset from carrier resonance in MHz.

As expected, the carrier dominates the power at the power-recycling mirror, but hardly appears at the south port. The carrier at **MPR** is, regarding the frequency axis, surrounded by the control sidebands. The frequency values of the particular local maxima indicate that we deal with the upper Michelson and both signal-recycling sidebands. The lower Michelson sideband is not apparent.

Contrary to the west port, the lower Michelson sideband exhibits the highest power of all sidebands at the south port. The lower signal-recycling sideband is missing. The power difference of the upper signal-recycling and Michelson sidebands is slightly smaller in the south than in the west.

With the considerations above, the upper signal-recycling sideband showing up at the south port unambiguously indicates that the current tuning direction of GEO 600 is positive.

³⁶The script describing the old setup is obtained by Appendix B.1.1, un-commenting the lines indicated by “old MPR”.

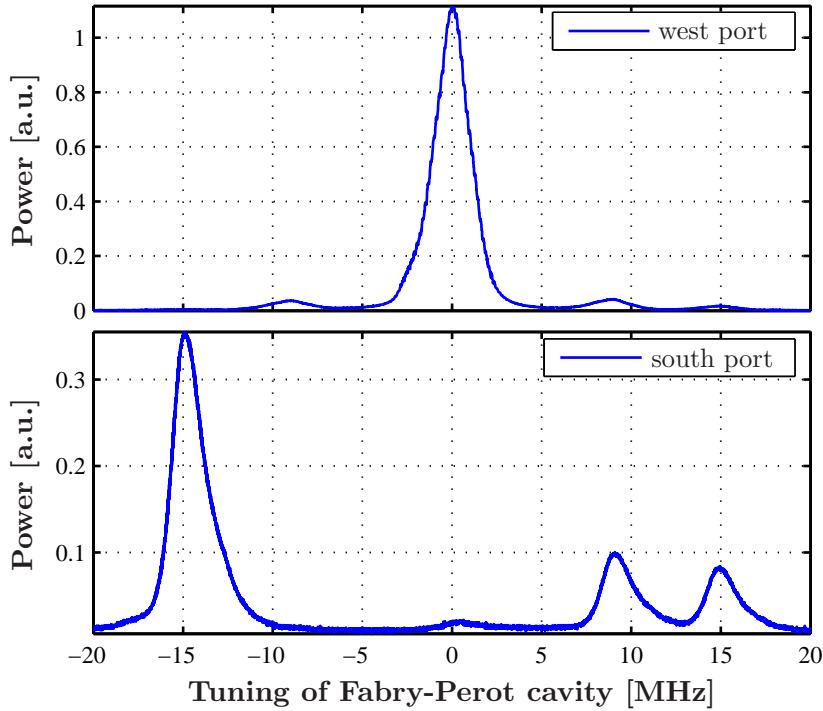


Figure 3.29.: Measurement of light power, passing a scanning Fabry-Perot cavity, in reflection of **MPR** (upper graph) and in transmission of **MSR** (lower graph). The measurement was performed with the old, low-reflective **MPR** ($T_{\text{MPR}} = 1.35\%$) implemented in GEO 600. The power is displayed depending on the Fabry-Perot cavity tuning which is given in MHz, as an offset from carrier resonance. For the measurements, the signal-recycling cavity was detuned to resonate with signal sidebands at 1 kHz. The absolute power values of the two measurements are arbitrary and not related to each other.

The measurements in addition prove the resonance of the lower Michelson sideband inside the signal-recycling cavity detuned to 1 kHz, as anticipated in Figure 2.4. In the old setup, the Michelson modulation frequency is, like the current, not exactly resonant inside the power-recycling cavity. But the deviation is only 26 Hz. The power-recycled Michelson is, from the signal-recycling cavity point of view, much more under-coupled in the old setup than with the high-reflective **MPR**. The phase shift occurring at reflection is more than an order of magnitude smaller than in the setup above, such that the shift of the signal-recycling cavity resonance is of the order of a few hundred Hertz only. This is negligible compared to the expected resonance offset of $\sim \pm 1$ kHz for a sideband frequency resonant inside the power-recycling cavity (compare again with Figure 2.4), such that the lower control sideband still traverses the resonance when elongating the signal-recycling cavity.

The upper signal-recycling sideband does not disappear in the west port as it is nearly anti-resonant inside the power-recycling cavity. This is also one reason for the reduced difference of the upper control sideband powers compared to the west port. The upper Michelson is indeed not resonant inside the signal-recycling cavity, but it is, on the one hand, already enhanced by power-recycling when it enters the signal-recycling cavity. On the other hand, the bandwidth of the signal-recycling cavity for the Michelson sidebands is ≈ 2 kHz (due to the high transmissive power-recycled Michelson; please note that the bandwidth is larger as the modulation frequency is closer to resonance than in the current setup) such that the signal-recycling cavity does not attenuate the Michelson sideband as much as the power-recycling cavity attenuates the signal-recycling sideband. The simulation predicts a ratio of the Michelson sideband powers of 0.17, the measurement supplies 0.20.

3.6.2. Calibration of simulated parameters

In the simulation, the optical gain has the dimension of Watts per degree, or per meter, or per frequency, depending on the choice of expressing the microscopic deviation from the operating point.

The absolute demodulation phase value depends on the underlying ortho-normal basis. One could argue that if the optical system was sufficiently well-established, the ortho-normal frame should naturally be one-to-one. However, the simulation is only capable of optical effects.

In the experiment, the overall gain has unit 1. With the optical gain given by the output of the mixer (after the photodiode), the electronic gain of the control loop is set to provide stability of the control.

The photodiode signal and the local oscillator each traverse a cable of arbitrary length before they get multiplied with each other at the mixer. Apart from that, the phase shifter, the experimental place to apply the demodulation phase, converts voltage into a phase delay, with arbitrary sign, and is situated in either of the two signal paths. However, the phase difference of the two signals, and the sign of the phase delay appearing at the mixer can in principle be measured, allowing to calibrate the phase shifter. (This was done at GEO 600. The absolute value of the phase delay, though, changes regularly due to commissioning work on the detector.)

The parameters of the Michelson and signal-recycling electronic circuits are supervised and set with the computer control system based on LabView. The *tune-VI*, a user program created for the tuning process, converts particular parameter input values into digital numbers that are fed via DA converters into the control electronics. The simulated parameters need to be adapted to the equivalent input values for the *tune-VI*.

In the following, the applied calibration of the control loop parameters for the signal-recycling and Michelson loop will be described. The starting point is the signal-recycling demodulation phase, as this determines the exact signal-recycling cavity tuning and optical gain of the respective error-signal. The signal-recycling cavity tuning, in turn, is the

crucial condition for the Michelson loop parameters, first the demodulation phase, and subsequently the gain. Naturally, this sets the order of parameter calibration.

Parameters for signal recycling

The demodulation phase increments of LabView correspond to degrees. Increasing values yield increasing delay in the signal path. Thus, the sign of the input value change agrees with the definition of the demodulation phase in Equations 1.18 to 1.20 that is also used for FINESSE.

The calibration of the signal-recycling demodulation phase was done in one coarse and one fine measurement. For the coarse calibration, the signal-recycling error-signal was observed while **MSR** was locked on the $2f$ signal. With the fixed **MSR**, the signal-recycling modulation frequency was swept. The equivalence of both the tuning of **MSR** and of the modulation frequency can be motivated with the phasor picture³⁷. The target was to determine the demodulation phase yielding the most symmetric error signal. The accuracy was limited due to variations of the $2f$ signal associated with fluctuations of mirror alignments, and due to the necessary setting of both the mean modulation frequency of the sweep, and the demodulation phase.

For the fine calibration, the signal-recycling error-signal was switched from the $2f$ signal to the sideband signal, applying the demodulation phase previously determined. Then, the demodulation phase was varied by $\pm 10^\circ$. For all three demodulation phases the transfer function, from differential Michelson end mirrors' deviation from dark fringe to the Michelson error-signal gained at PDO (see Figure 3.1), was measured. This transfer function is also referred to as *optical transfer function* of the detector. The shift of the peak frequency of the respective optical transfer functions' amplitude was identified with the relative **MSR** movement, caused by the shift of the signal-recycling error-signal operating point. Since the zero crossing position of the signal-recycling error-signal depends non-linearly on the demodulation phase, the demodulation phase in the middle can be determined by matching the measured peak-frequency shifts with the simulation³⁸.

Figure 3.30 shows the dependency of the signal-recycling error-signal zero crossing on the demodulation phase according to FINESSE, for a detector detuning of ~ 2 kHz. The **MSR** tuning offset refers to δx_m , the position associated with the modulation frequency. The demodulation phase axis already refers to the tune-VI input. Decreasing the demodulation phase in the experiment from 165° by 10° increased³⁹ the frequency of the

³⁷For the error-signal derivation with Figure 3.14, only the upper control sideband changed pointing and amplitude as passing the resonance of the signal-recycling cavity. The same is achieved with a change of modulation frequency: the carrier remains the same, and, with high detuning, the upper sideband passes the signal-recycling resonance, while the lower stays nearly untouched from it. Thus, the error-signal vectors for **MSR** tunings, and the corresponding modulation frequency tunings should approximately agree.

³⁸The gain exhibits a quadratical dependency on the demodulation phase, and may be used for a demodulation phase calibration, as well.

³⁹The direction of the peak shift, depending on the demodulation phase alteration, is one-to-one given the error-signal derivation in Figure 3.14. The phasor picture, together with this transfer-function

transfer-function peak by 86 Hz. Increasing the demodulation phase by the same amount lead to a peak-frequency decrease of 55 Hz. With these values, the simulated demodulation phase corresponding to 165° (red star in Figure 3.30) could be assigned with an accuracy⁴⁰ of $\pm 2^\circ$. The applied phase obviously deviates from that, generating the most symmetric error-signal (red diamond), by -41° .

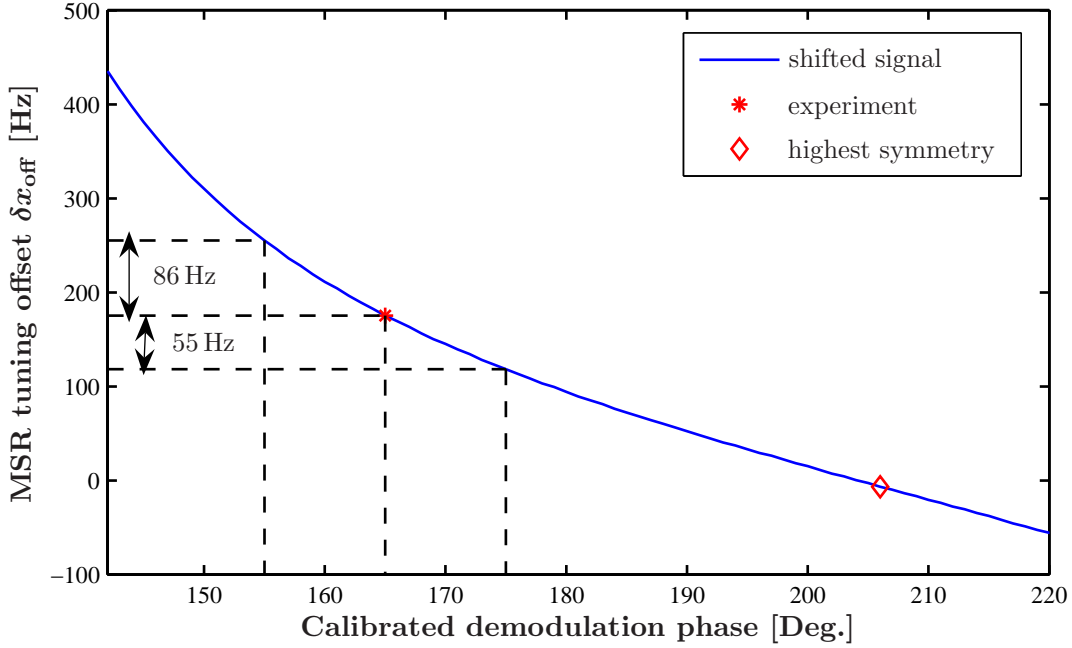


Figure 3.30.: Dependency of the signal-recycling error-signal zero crossing on the demodulation phase, for a detector tuning of ~ 2 kHz. The zero crossing deviation refers to δx_m , the demodulation phase axis is calibrated to the experimental input values of the tune-VI. The non-linear shape of the curve allows to match the simulated to the experimental demodulation phase (red star) by measuring the shift of the peak of the differential Michelson transfer function for different demodulation phases applied. The red diamond marks the demodulation phase yielding highest error-signal symmetry, and the associated **MSR** position.

The gain parameter input for the tune-VI is directly proportional to the optical gain of the signal-recycling error-signal. The experimental value was determined by setting the

measurement, helped to identify a sign bug in FINESSE respecting the location-dependent light phase evolution.

⁴⁰Appendix A exemplifies this calibration method to be of comparably low susceptibility to errors of optical parameters of the FINESSE input script if accomplished at high signal-recycling cavity tunings. Thus, the calibration accuracy is limited by the ability to determine the difference of the respective peak frequencies.

unity gain frequency of the control loop to 40 Hz, applying the demodulation phase for the highest error-signal symmetry for one particular modulation frequency.

Parameters for the differential Michelson

The demodulation phase input to the tune-VI, yielding maximal gain, was experimentally determined by maximising the open loop gain of the control loop. Then, with the gain input, the unity-gain frequency was set to roughly 90 Hz. (In contrast to the signal-recycling gain, though, the gain script-values for the Michelson control loop are anti-proportional to the optical gain of the error-signal.)

To relate the simulated parameters to the experiment, besides the particular tune-VI inputs also the current **MSR** tuning needs to be known. Considering the signal-recycling modulation frequency and demodulation phase, the mirror position was determined by the zero crossing of the error-signal in the simulation. The simulation results for this particular **MSR** position were then equated to the tune-VI input values.

Tuning script

Beyond the parameter calibration, for the tuning script generation there are some more aspects that require consideration. The corresponding MATLAB script, converting the simulated signal-recycling and Michelson error-signal parameters to input values for the tune-VI, can be found in Appendix B.2.4.

The GEO 600 control system using LabView has difficulties in addressing several digital busses at once. In particular, experimentally it turned out to be advantageous to change parameter values only as often as necessary. Thus, guided by experimental experience, all parameter values of the tuning script are rounded to differ by increments of 5.

One of the required parameters for the tuning script is the gain for Michelson auto alignment. So far, the FINESSE script for GEO 600 does not seem to be accurate enough to yield applicable results. Thus, the auto alignment gain needed to be adjusted by experiment. Consequently, generating the current tuning script, this parameter was set to a default value of 12 for all tunings and altered afterwards. The numerical value of 12 is experimentally motivated, yielding a stable loop performance at high detunings.

Figure 3.31 displays the resulting demodulation phases (upper graph) and gains (lower graph) applied for the signal-recycling (solid blue lines) and the Michelson (dashed magenta lines) control at GEO 600.

3.6.3. Necessary accuracy of the FINESSE script and of the calibration with respect to the tuning process

To successfully tune the detector, the parameters of the tuning script predominantly need to yield stable Michelson and signal-recycling control loops. Guided by the overall

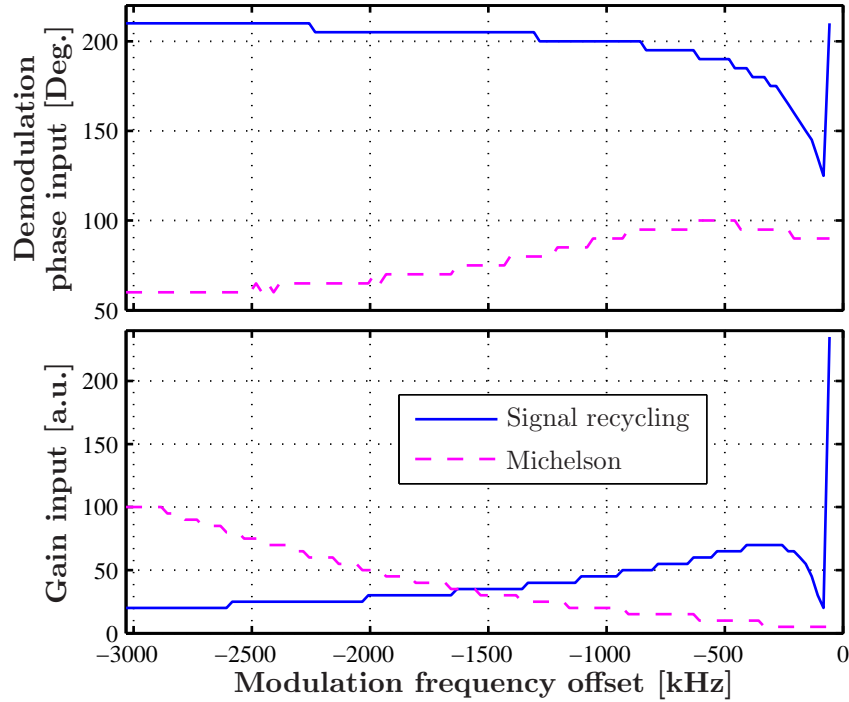


Figure 3.31.: Tuning script parameters of the signal-recycling (solid blue lines), and the Michelson control loop (dashed magenta lines), after calibration of the simulational results. The signal-recycling modulation frequency is related to the 72nd multiple of FSR_{SR} . The upper and lower graphs display the demodulation phases and gains, respectively. The increments are large in order to decrease the number of parameter changes by LabView.

open loop gains of the respective controls, the gain for the signal-recycling loop may vary by a factor 2 to both sides, whereas the gain margin for the Michelson is slightly asymmetric, $[0.275, 1.64]$, with the targeted unity gain frequency. Thus, the optical gains of the respective error-signals need to be determined (at least) to this accuracy. As the output parameters of FINESSE get calibrated for one particular f_m , the necessary accuracy relates to the relative gain evolution with signal-recycling modulation frequency.

The exact Schnupp and cavity lengths (and mirror properties) influence the resonance conditions of the control sidebands for particular detector configurations. Thus, to determine them is essential. The length of the power-recycling cavity could be specified experimentally with an accuracy of ~ 0.1 mm. This was achieved by minimising an intentionally introduced laser frequency noise peak in the spectrum of the differential Michelson output of the power-recycled Michelson. (More on this power-recycling cavity length measurement can be found in [Freise03a].) Thus, in the following accuracy investigations the power-recycling cavity length is fixed.

A method to specify the Schnupp and the signal-recycling cavity lengths in an operating, dual-recycled detector was developed during this work (see Section 4.2 and 4.3.1, respectively). With the earlier estimations being off by +17 mm and +9 mm, respectively, these length specifications were, besides the accuracy of the demodulation phase calibration, crucial for the successful prediction of the control loop parameters for tuning. This will become clear when investigating the accuracy requirement of the two lengths. The accuracy investigations below, considering each length separately, use the “right” value for the respective other length.

There are mainly two issues that principally require consideration when estimating gain errors for the signal-recycling and Michelson loops:

- The prediction of the optical gains will vary for different macroscopic lengths.

A difference in signal-recycling cavity length (not the tuning!), for example, shifts the gain shapes in the lower graph of Figure 3.31 sideways. For particularly low detunings a small change already ends up in large relative gain changes for the signal-recycling loop.

The Schnupp and power-recycling cavity lengths in particular determine the reflection of the power-recycled Michelson for the Michelson control sidebands. If the used Schnupp length differs from the real one, the signal-recycling linewidth for the Michelson sideband will be different, yielding a different optical gain for the Michelson loop. This is particularly relevant as the impact of the control sidebands on the optical gain varies for different regions of detuning. Thus, the gain relations between high and low frequencies alter.
- The prediction of demodulation phases alters for particular lengths.

Any deviation of the experimentally applied demodulation phase (from the targeted) varies the appearing optical gain. The signal-recycling demodulation phase in addition alters the exact tuning of the signal-recycling cavity which consequently shifts the Michelson loop parameters, depending on f_m , sideways.

For illustration, Figure 3.32 presents the effect of a wrongly shortened signal-recycling cavity in FINESSE, on the signal-recycling control loop parameters. As before, the upper and lower pictures show the demodulation phase and gain, respectively, of the resulting tuning script. The solid curves represent the parameter evolution for the correct script, the dashed curves for the wrong script. The shorter signal-recycling cavity presumably shifts the 72nd FSR_{SR} about +50 Hz. As the calibration of the demodulation phases and gains takes place for large detector tunings, a shift of such a small amount yields the same calibration offsets and factors, respectively (see Figure 3.31). In addition, we assume for simplicity that the reduction of the difference between the power-recycling and signal-recycling FSR hardly changes the demodulation phase and gain shape. Thus, the wrong FINESSE script yields the same gain and demodulation phase values for the tuning script, but occurring at higher modulation frequencies (the reference of 9.017397 MHz is common to all curves of Figure 3.32).

At -100 Hz the gains deviate by more than factor 2. The wrong script would in the experiment lead to a, by factor 2, too low electronic gain (to compensate for the wrongly

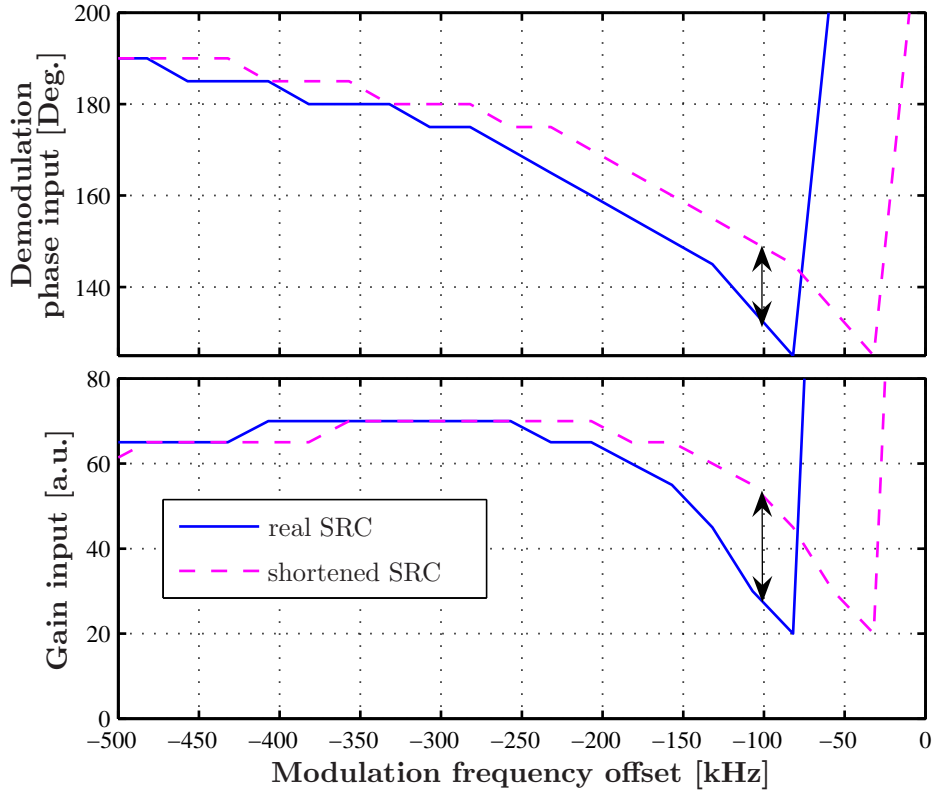


Figure 3.32.: Tuning script parameters for signal recycling, for a FINESSE input script with the signal-recycling cavity length agreeing to the experiment (solid blue lines), and being shorter by ~ 7 mm (dashed magenta lines). The two parameters of the shortened cavity are shifted with respect to the default by $\sim +50$ Hz.

assumed, relatively high optical gain). On top of all this, the demodulation phases were determined to yield most symmetric error-signal which are very close to those with highest gain (see Figure 3.23). Thus, the demodulation phase deviating by $\sim 20^\circ$ further reduces the optical gain of the error-signal.

Figure 3.33 displays the impact of the signal-recycling demodulation phase on the optical gain of the signal-recycling error-signal, for three different modulation frequencies⁴¹ The demodulation phase refers to the one yielding maximum gain, and the gains are normalised to yield a maximum of 1. The curves for the higher modulation frequencies abort for high phase offsets as the error-signal exhibits no zero crossing any more. (For positive demodulation phase offsets, the zero crossing moves towards lower **MSR** tunings until it reaches the structure around the carrier resonance (compare with the overview in Figure 3.8 or the figure below).)

⁴¹Please note that the detector tuning does not necessarily coincide with δf_m , but simultaneously changes with the demodulation phase (see also Figure 3.34 below). Thus, δf_m should not be mistaken as synonym for the detector tuning.

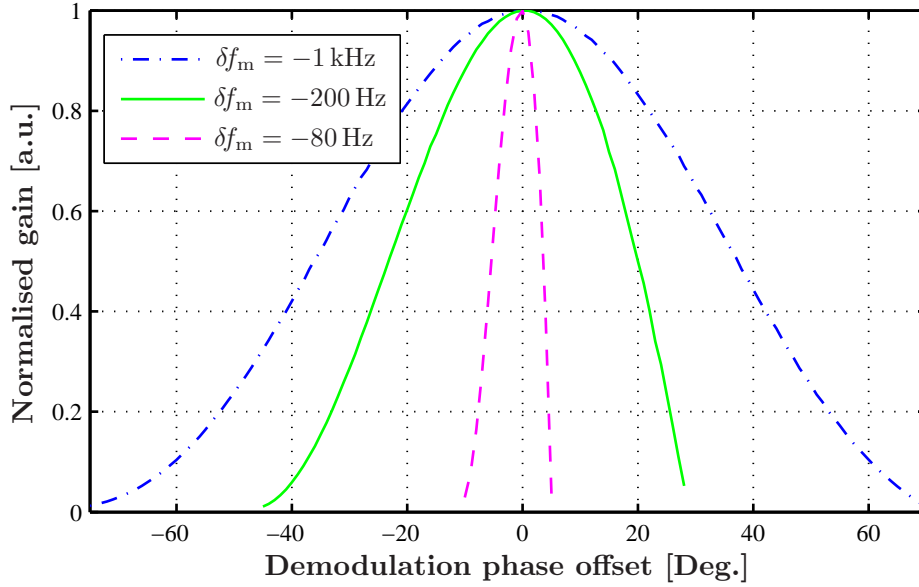


Figure 3.33.: Optical-gain dependency of the signal-recycling error-signal on the demodulation phase. The phase is displayed as offset from the demodulation phase yielding highest gain. The gains are normalised to allow a direct metering and judgement of the fall-off. Shown are the gains for three different modulation frequencies δf_m . The closer δf_m to the integer FSR_{SR} , the more sensitive is the optical gain on the demodulation phase.

The closer to the 72nd FSR_{SR} , the larger the demodulation phase influence on the optical gain. For $\delta f_m = -80$ Hz, the gain is attenuated to 0.5 already for a demodulation phase deviation of -6° or $+3^\circ$, whereas for the lower frequencies the tolerance is roughly $\pm 22^\circ$ and $\pm 35^\circ$. Given the example from Figure 3.32, the effect of the demodulation phase on the gain will presumably be limiting, when estimating the necessary accuracy of the signal-recycling cavity length targeting for stability for all modulation frequencies.

As mentioned above, the signal-recycling demodulation phase sets the exact **MSR** position, and thus additionally moves the Michelson parameters on the signal-recycling modulation frequency axis. Figure 3.34 shows the position of the signal-recycling error-signal zero crossings when off-setting the demodulation phases from those yielding highest gain, again for three different modulation frequencies. To comprise all zero crossing positions in one graph, they are displayed as offsets from the respective δx_m s.

Again, the larger δf_m , the larger the demodulation phase impact. With the range of demodulation phase shifts expected, however, the **MSR** position will hardly exceed an offset of ± 200 Hz from δx_m . Consulting the Michelson parameters given in Figure 3.27, a shift of ± 200 Hz sideways should not alter the Michelson gain by more than $[0.6, 1.64]$ for any particular frequency, unless the resulting Michelson demodulation phase offset itself

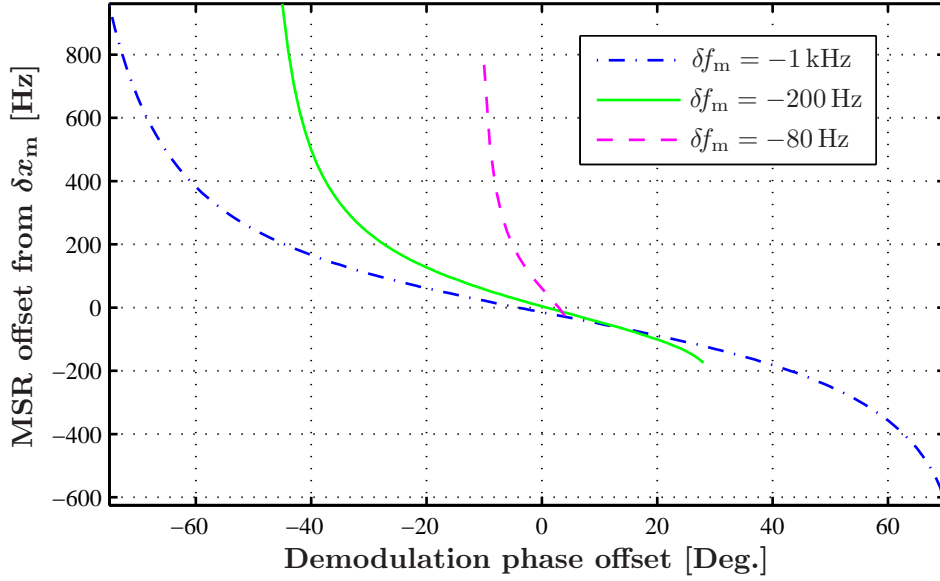


Figure 3.34.: MSR position dependency on the signal-recycling demodulation phase. The modulation frequencies and the demodulation phase interval are the same as in Figure 3.33. The mirror tuning is referred to the respective δx_m . The closer δf_m to the integer FSR_{SR} , the more sensitive is the MSR position on the demodulation phase. Particularly for $\delta f_m = -80$ Hz, the error-signal zero crossing vanishes for too large demodulation phase offsets to both sides.

attenuates the Michelson gain too much (which is not the case). Thus, the effect of the MSR position deviation may safely be neglected.

The same is true considering the Michelson demodulation phase dependency on the signal-recycling cavity length (for fixed MSR position): the signal-recycling cavity linewidth for the Michelson sidebands is ~ 1 kHz, while a signal-recycling cavity length deviation of ~ 10 Hz at $72 \times FSR_{SR}$ corresponds to ~ 17 Hz at $119 \times FSR_{SR}$. Thus, the signal-recycling resonance condition may safely be assumed to stay the same.

The decisive aspect to be accounted for regarding the signal-recycling cavity length is obviously the shift of the signal-recycling demodulation phase with modulation frequency, because of the demodulation phase impact on the gain. This yields an allowable signal-recycling cavity length deviation of -1 mm and $+2$ mm (shifting the curves of Figure 3.31 by $+7$ Hz and -14 Hz, respectively). However, it should be noted that the accuracy requirement gets very loose as soon as the modulation frequency, up to which the tuning should work, is decreased. Targeting for $\delta f_m = -200$ Hz, for example, already yields a tolerable length margin $\geq |\pm 10$ mm| if the other lengths and the tuning parameter calibration are correct.

The Schnupp length affects mainly the Michelson control: as the signal-recycling sidebands are, for the complete tuning process, comparably far away from power-recycling resonance (the respective linewidth for these sidebands is ~ 40 Hz), the power-recycled Michelson is simply a very high reflective input mirror to the signal-recycling cavity (the losses, including transmission amount to $L_{\text{prMI}} = 66$ ppm). If the Schnupp length increases, the main change would be the increased influence of the power-recycling resonance as its linewidth would increase. This, however, would only affect (very) low tunings.

The Michelson sidebands, though, are close to being resonant inside the power-recycling cavity, making the reflectivity of the prMI very low ($R_{\text{prMI}} = 84\%$ for the currently used modulation frequency, being off-resonant by 52 Hz). If the Schnupp length increases, R_{prMI} increases, and with it the sideband enhancement inside the signal-recycling cavity. At the same time, the signal-recycling bandwidth decreases. The opposite is true for a decrease of the Schnupp length.

The two margin sides of the Schnupp length will act slightly differently to the control loop parameters. As the R_{prMI} is already very low, a further reduction, for example, will of course reduce the sidebands' amplitude and thus the optical gain of the error-signal, but the impact on the relative gain change with tuning is expected to be lower than for an increase of R_{prMI} .

Consulting Figure 3.16 for the expectable change of demodulation phase, a further decrease of R_{prMI} should hardly alter the demodulation phase evolution with tuning: the influence of the sideband phase on the demodulation phase just further decreases, and the development at high tunings stays roughly the same. The impact of an increase of R_{prMI} is larger. For example, if the signal-recycling linewidth for the sideband decreases, and the sidebands' amplitude difference is larger at signal-recycling resonance, the phasors of Figure 3.16 will need to evolve longer at ~ 1 kHz to yield perfectly canceling beats with the carrier. Consequently, the phase difference between signal-recycling cavity resonance and large cavity tuning will be larger. For lower tunings, however, the "back-evolution" should still take place, as then the relation to the carrier is more relevant.

Figure 3.35 shows the demodulation phase and gain parameter evolutions for the Michelson control loop, for two different Schnupp lengths, labelled by their deviations $\Delta L_{\text{Schnupp}}$ from the default $L_{\text{Schnupp}} = 54$ mm (used in Appendix B.1.1). The calibration was done for $\delta f_m = -3$ kHz.

As expected, the signal-recycling linewidth is reduced for the larger Schnupp length (dashed magenta lines), and the demodulation phase peak sits at higher cavity tunings. The calibration point, however, reduces the appearing demodulation phase difference at large detector tunings (in the visible modulation frequency range) to 10° maximum. The maximal difference of 45° occurs around $\delta f_m = -500$ Hz.

Applying the parameters of the dashed lines to a detector that requires the parameters of the solid lines, the electronic gain of the Michelson control loop is in the interval of -1.9 kHz to -500 Hz by factor ≥ 1.64 larger than necessary. The only chance of balancing is the indeed reduced optical gain due to the false demodulation phase. The effect of the

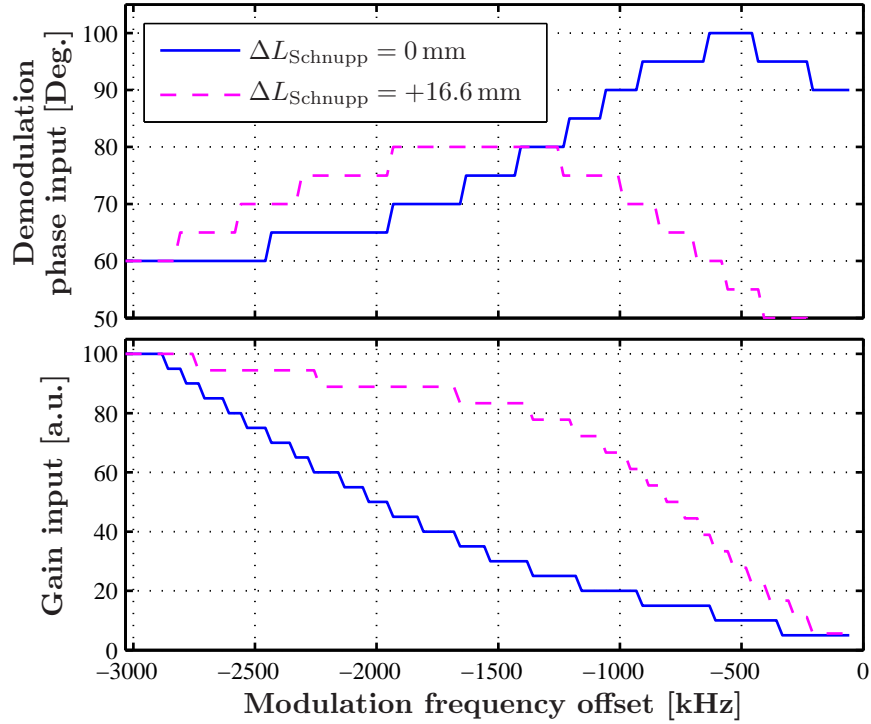


Figure 3.35.: Tuning script parameters for the Michelson control, for a FINESSE input script with the Schnupp length agreeing to the experiment (solid blue lines), and being longer by 16.6 mm (dashed magenta lines). The parameters are calibrated at $\delta f_m = -3 \text{ kHz}$.

demodulation phase on the optical gain is, however, much weaker than for the signal-recycling error-signal.

Figure 3.36 shows the optical gain reduction depending on the deviation of the demodulation phase from the value yielding highest gain. The curve is almost the same for all detector tunings. Clearly, only an offset of $\pm 60^\circ$ reduces the gain by factor 2. Thus, the wrong demodulation phase might balance the too high electronic gain at very low tunings, but at $\sim -1.8 \text{ kHz}$ the Michelson loop would already loose lock when tuning the detector down.

With the detuning frequency for which the parameter calibration is applied, the Michelson loop stability is obviously already affected at relatively high detector tunings. However, this instability is caused by the gain parameter. As, in addition, the demodulation phase impact on the open loop stability is, in general, fairly low, the demodulation phases are neglected when determining the allowable margin for the Schnupp length.

Investigations of the optical gains of the Michelson error-signal lead to the result, that the Schnupp length may vary by -20 mm or $+8 \text{ mm}$, with respect to the currently assumed

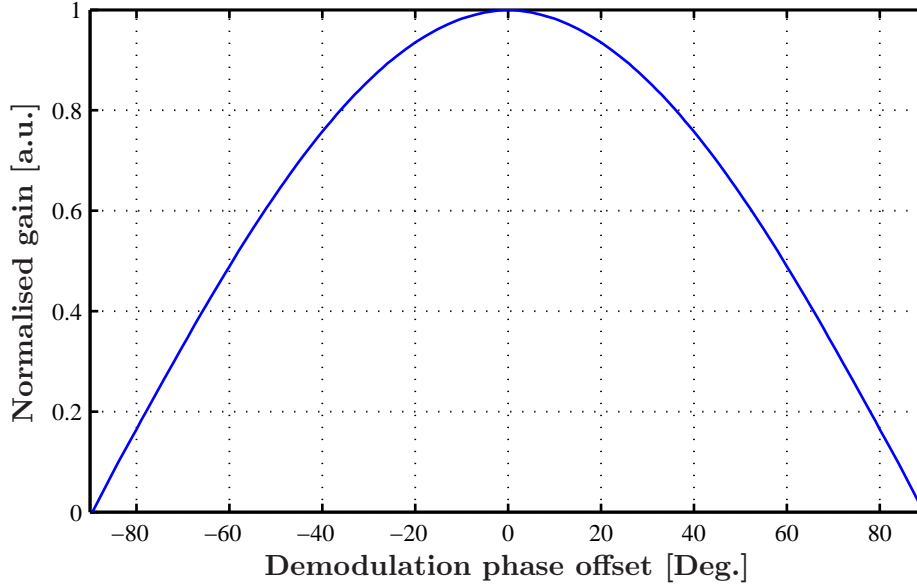


Figure 3.36.: Optical-gain dependency of the Michelson error-signal on the demodulation phase. The phase is displayed as offset from the demodulation phase yielding highest gain. The gains are normalised to allow a direct metering and judgement of the fall-off. They are obviously much less sensitive to demodulation phase offsets than in the signal-recycling case.

value⁴². Figure 3.37 displays the optical gains dependent on the detector tuning, for the reference, and the two Schnupp length deviations that just produce a tuning script yielding stable control if the calibration is done at -3 kHz. The one for $\Delta L_{\text{Schnupp}} = +8$ mm leads to instabilities at least at 600 Hz, the other at 500 Hz.

In summary, the signal-recycling length influences mainly the simulation results for the signal-recycling control parameters. The tolerances with respect to the current length are -1 mm and $+2$ mm if targeting for a continuous tuning in modulation frequency steps of 25 Hz. For high tunings, though, the allowed length margin is huge ($\geq |\pm 1$ cm). Thus, the old presumed signal-recycling cavity length ($\Delta L_{\text{SR}} = +9$ mm) alone would not have limited the tuning performance of the detector in the interval used up to date. The current length accuracy of ± 2 mm is enough to guarantee a stable loop over a tuning range of 10 kHz.

The Schnupp length mainly vitiates the Michelson control loop. The margin for $\Delta L_{\text{Schnupp}}$ is -20 mm or $+8$ mm. Thus, the old FINESSE script ($\Delta L_{\text{Schnupp}} \approx 18$ mm) required a new determination of the Schnupp length for the generation of a successful tuning script. The current Schnupp length is determined with an accuracy better than ± 3 mm, allowing for a stable tuning in the complete, targeted sensitivity bandwidth.

⁴²The margin differs depending on the reference length.

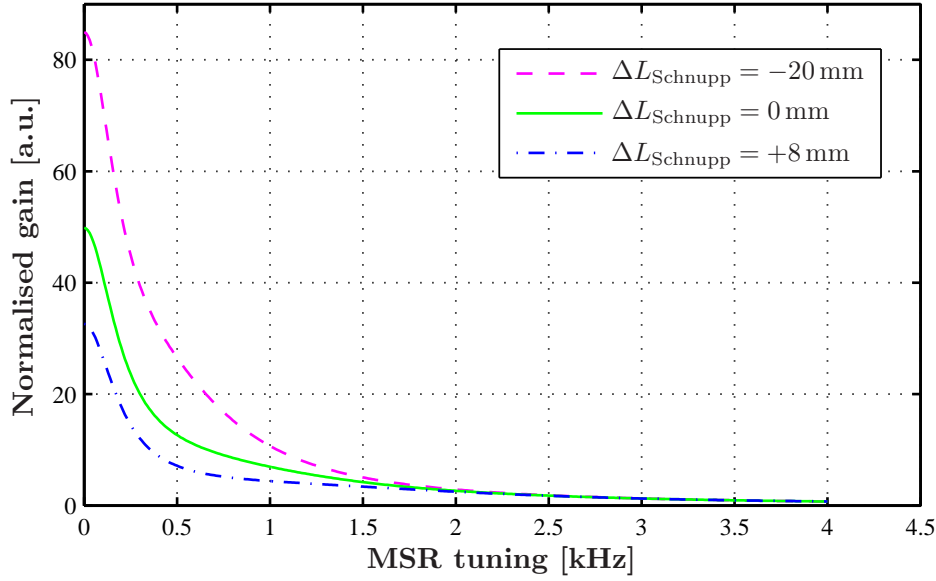


Figure 3.37.: Maximum optical gain of the Michelson error-signal versus **MSR** tuning. Shown are the trends for FINESSE input scripts with three different Schnupp lengths, with the default length (solid green line) agreeing with the experiment, and the others exhibiting gains that deviate from the default by just enough to yield control instabilities at particular tunings. In order to compare the gains with each other in view of the tuning-script, they are normalised to yield 1 at 3 kHz.

In the past, two further things turned out to be important: the calibration accuracy, and the direction of the phase evolution.

- Sequentially, two bugs were discovered in FINESSE that influence the definition of phase directions. The phasor picture called attention to a wrong definition of the demodulation phase direction. Later, experiments evaluating the shift direction of **MSR** with the signal-recycling demodulation phase discovered, with the help of the phasor picture, that the sign of the location-dependent light-phase evolution was wrong (i.e., the phase increased traversing a longer distance, in contradiction to Equation 1.1).
- During commissioning of the dual-recycled detector with the new, high-reflective power-recycling mirror, the parameters were calibrated for a modulation frequency of $\delta f_m = -3.4$ kHz. By chance, around this **MSR** tuning, the signal-recycling error-signal exhibits a structure independent of the choice of modulation frequency. (The origin of this false signal is still not clear.) Thus, the signal-recycling demodulation phase was accommodated to a wrong error-signal structure by symmetrising that shape with the modulation-frequency-sweep technique (see Section 3.6.2). Due to this false calibration, the signal-recycling loop was stable down to a detuning of

~ 1 kHz, despite the wrong demodulation phase evolution direction. The instability at lower tunings, however, necessitated the closer investigation.

To date, the signal-recycling demodulation phase can be calibrated with an accuracy of $\pm 2^\circ$, and the electronic gain with an accuracy of 1%. The Michelson gain and demodulation phase are known to 1% and $\pm 1^\circ$, respectively.

3.6.4. Towards a tuned detector

Currently, the lowest achieved detector tuning at GEO 600 is ~ 330 Hz. Targeting gravitational-wave sources in the band between 50 and 250 Hz, however, the tuned GEO 600 detector improves the shot-noise limited sensitivity in this band by a factor of up to 2.5.

The simulation results in Section 3.5.1 indicate that there is a tuning gap for **MSR** of ~ 150 Hz around the carrier-resonance position. However, with the upper and lower capture range of the signal-recycling error-signal being 200 Hz for carrier resonance, a tuning step of 150 Hz should, in principle, be possible.

In case the probability to lock **MSR** to the tuned state with such a huge tuning step turns out to be experimentally unfeasible, there are at least two further approaches possible:

- The **MSR** positions in Figure 3.25 do not fall below ~ 150 Hz, unless tuned, because of the respective demodulation phases being optimised to yield most symmetric error-signals. It is indeed possible to achieve lower **MSR** tunings, but with different demodulation phases, and only at the expense of optical gain and symmetry. (Please note that the demodulation phases yielding highest symmetry are, for all modulation frequencies, very close to those yielding highest gain). The way to go is to alter the demodulation phase, and accordingly the electrical gain (see below).
- Instead of a permanently working signal-recycling control, an artificial lock-acquisition situation can be created by releasing **MSR**, locked at ~ 150 Hz, until the free mirror swings through the carrier resonance. Then, a switch closes, and lock acquisition is attempted.

The advantage of the latter compared to the “simple” tuning step from above is that the mirror does not get accelerated by the error-signal when approaching the carrier resonance from the former position. Additionally, locked at ~ 150 Hz before, the mirror’s kinetic energy is presumably still low when crossing the carrier resonance. This gets particularly important considering the situation before the very first lock acquisition, where the experimental experience showed that the sideband error-signal capture range is too small to reliably lock the seismically excited **MSR**, with acceptable probability.

The feedback signal indicates the current **MSR** movement. Thus, the mirror can systematically be released when it is already approaching the carrier resonance. Nonetheless, the moment of release bears a considerable risk to loose the mirror’s control completely. Thus, the author prefers a controlled mirror transfer to lower tunings via an increase of

the demodulation phase and of the electronic gain, if necessary, using the last but one signal-recycling modulation frequency.

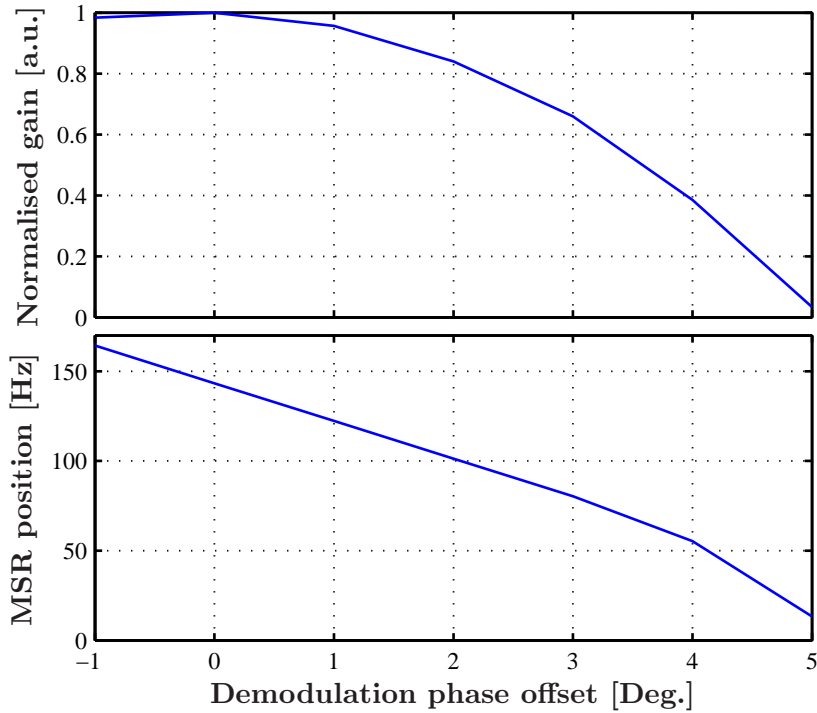


Figure 3.38.: Zoom of the gain and **MSR** position dependency on the signal-recycling demodulation phase for the curves belonging to $\delta f_m = -80$ Hz in Figures 3.33 and 3.34. A successive change of the demodulation phase using this modulation frequency transfers the **MSR** closer to carrier resonance. Starting point is the demodulation phase offset of -1° , yielding the most symmetric error-signal. A gain compensation is only necessary for demodulation phase offsets larger than 3° .

The upper and lower graphs of Figure 3.38 display a zoom of the dashed magenta curves of figures 3.33 and 3.34, respectively. Hence, the applied modulation frequency is $\delta f_m = -80$ Hz, and the demodulation phase is referred to the one yielding highest optical gain. The position of **MSR**, however, is shown as absolute value, not with respect to δx_m .

The demodulation phase of -1° is the one yielding a most symmetric error-signal, and marks the original state of the detector. With the signal-recycling gain margin of factor 2, increasing the signal-recycling demodulation phase successively to 2° , or even to 3° , should be possible without any gain modification. The respective **MSR** deviation from carrier resonance could then be reduced down to ~ 80 Hz. If even that turns out be insufficient, one more demodulation phase step is possible with the current control loop management of LabView that limits the lower end of the signal-recycling-gain parameter.

However, a demodulation phase higher than 4° should not be necessary as tuning steps of 50 Hz have already proved successful.

One last thing to be considered when switching to a tuned detector is the change of the Michelson open loop gain due to the signal-recycling cavity pole occurring at ~ 200 Hz. For the continuously controlled **MSR** steps, this change of effective transfer function can be accounted for by inserting a differentiator of 200 Hz corner frequency already at the currently lowest tuning of ~ 330 Hz. The associated increase of noise above unity-gain frequency can be avoided differentiating only in a small band, for example from 200 Hz to 400 Hz.

3.7. Tuning process alterations replacing **MSR** by an etalon

So far, signal-recycling mirrors with tuneable position but fixed reflectivity and transmission were considered. However, the frequency range occupied by gravitational waves varies for different types of sources: whereas a pulsar radiates at one very particular frequency, the signal originating from a supernova, for example, is expected to embrace a wide range of frequencies. In order to accommodate to targeted sources of gravitational waves, a variation of mirror reflectivity is desirable. This would allow for an optimal exploitation of the available light power by adjusting the detector bandwidth⁴³.

With conventional mirrors in the optical detector setup, for each intended detector bandwidth a separate signal-recycling mirror of adequate reflectivity needs to be installed. With the mirrors of advanced gravitational-wave detectors being suspended as complex cascaded pendulums in ultra-high vacuum tanks, every mirror exchange entails long detector down-times. To allow for a tunable signal-recycling cavity bandwidth in situ, the signal-recycling mirror can be exchanged by a compound mirror. The replacement of the signal-recycling mirror by a Michelson interferometer, and by a thermally tunable etalon was already successfully demonstrated ([Vine02, Kawabe], respectively).

The concept of the etalon, however, is regarded to be more suitable and easy to implement in GEO 600: the etalon's dimensions and material can be matched to the current **MSR**, allowing to retain the current suspension, and furthermore the longitudinal and alignment control. [Hild03] reports on two concepts for thermal actuation of the etalon tuning, a ring heater and a segmented heater. Currently, the homogeneity of the optical length of the etalon over a diameter of 18 mm (which is the beam size at **MSR**) is limited to 20 nm. Depending on the gradient of the Airy-function shaped transmission and reflection of the etalon, this sets a limit on the accuracy of these etalon properties. Reversed, the accuracy requirements for the reflectivity and transmission of the etalon will, with the achievable

⁴³According to the sensitivity theorem [Mizuno95], the achievable integral sensitivity for a wide frequency range is determined only by the energy of light stored inside the detector. As in the current gravitational-wave detectors the amount of energy is fixed by the laser power, the Michelson armlengths, and power-recycling factor of the optical setup, the bandwidth of the detector can only be increased at the expense of the peak sensitivity. Both have to be traded according to the requirements of the targeted gravitational-wave source.

| coating side | reflectivity | loss |
|--------------|--------------|--------|
| front | 0.994 | 50 ppm |
| back | 0.5 | 0 ppm |

Table 3.1.: Coating properties of the etalon applied in the presented FINESSE simulations. The front coating points towards the beamsplitter.

homogeneity of etalon thickness, set a limit on the maximal gradient of the Airy function, and thus determine the coating properties of the etalon (more about the choice of suitable etalon properties can be found in [Malec]).

3.7.1. Etalon characterisation

For the following investigations about the impact of an etalon on the tuning process of the signal-recycling cavity, however, a laterally perfectly homogeneous etalon is assumed. The etalon utilised in the FINESSE simulations is close to the etalon studied in [Hild03]. The properties assigned to the front and the back coatings are shown in table 3.1. The etalon losses are intentionally chosen to be small in order to focus on effects that are related to the tunability of the compound mirror reflectivity itself. The coatings are assumed to be affixed on a silicon substrate of refractive index of 1.45 and 7.5 cm thickness.

With the coatings of table 3.1 and the optical pathlength of ~ 109 mm, the etalon represents an under-coupled cavity with a free spectral range of 1.38 GHz, a finesse of 8.9 and a bandwidth of 155 MHz. The upper and lower graphs of Figure 3.39 display the normalised power and the phase shift, respectively, of light reflected by the etalon. The two graphs are given as functions of the light frequency offset from etalon resonance. The etalon reflectivity varies within [96.58 %, 99.89 %], shifting the light phase by maximally $\pm 0.5^\circ$.

The frequency dependence of the reflected field amplitude and phase has in principle two distinct consequences if installing the etalon as one cavity mirror⁴⁴: The etalon reflectivity provides fields of different frequencies (within one *FSR*) with different maximum enhancement factors inside the cavity. Thus, the respective cavity also exhibits different bandwidths. The phase dispersion of the etalon, however, in general shifts the resonance structure of the cavity for light fields of particular, different frequencies to different resonance frequency values, while the mirror positions are fixed.

Assuming, for example, a light field resonating inside the etalon, the back-reflected light from the front surface of the etalon will have no phase shift as if it was reflected by a high-reflective coating of a conventional mirror at that same position. A snapshot of a light field approaching (solid line) and being reflected (dashed line) from a resonant etalon

⁴⁴To prevent ambiguities in this section regarding the terms “cavity” and “etalon”, the term “cavity” will be exclusively be reserved for the optical system comprising either two conventional mirrors, or one conventional and one compound mirror. The term “etalon” will in the following be used for the Fabry-Perot cavity built by two reflecting surfaces of one substrate.

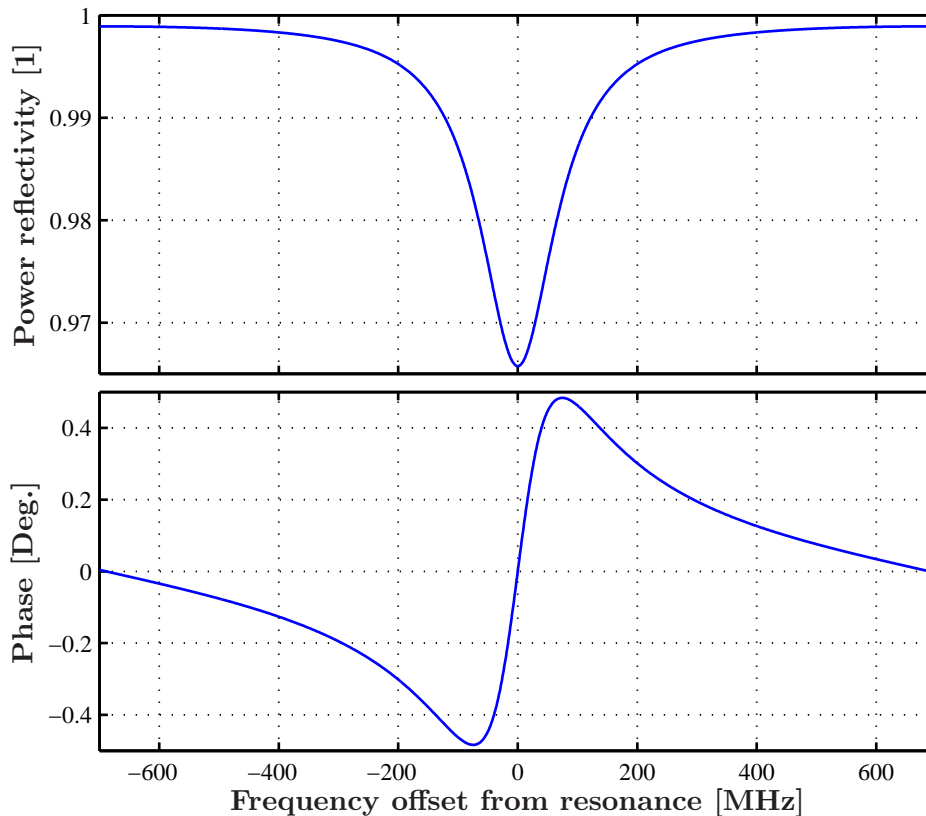


Figure 3.39.: Normalised power (upper graph) and light phase shift (lower graph) appearing in reflection of the etalon from table 3.1, for different light frequency offsets from etalon resonance.

is displayed in the left picture of Figure 3.40. The front surface of the etalon (thicker cyan line) can be regarded as the high-reflective front surface of a conventional mirror of reflectivity of 96.58 %. The position of this conventional mirror surface is indicated with the vertical dashed black line and overlaps with the front surface of the etalon. The tuning of a cavity containing this etalon is then equivalent to the microscopic optical path length between the high-reflective surfaces of the (compound) mirrors.

Assuming light with a frequency shifted by 75 MHz from etalon resonance, its phase will, at reflection, be provided with a phase shift of roughly 0.5° . An equivalent situation is shown in the right column of Figure 3.40. For the sake of clarity, the phase shift⁴⁵ is very much exaggerated to 90° . In that case, the etalon effects the reflected light in the same way as a conventional mirror of 98.2% reflectivity, with a position of the front surface

⁴⁵Due to the phase convention, the light phase decreases for increasing x , i.e., for the “positions of measurement” following the direction of light propagation. Thus, if the light obtains a positive phase shift $\delta\varphi^{\text{et}}$ at the etalon surface, its time-constant phase corresponds to the light phase appearing backwards with respect to the propagation direction.

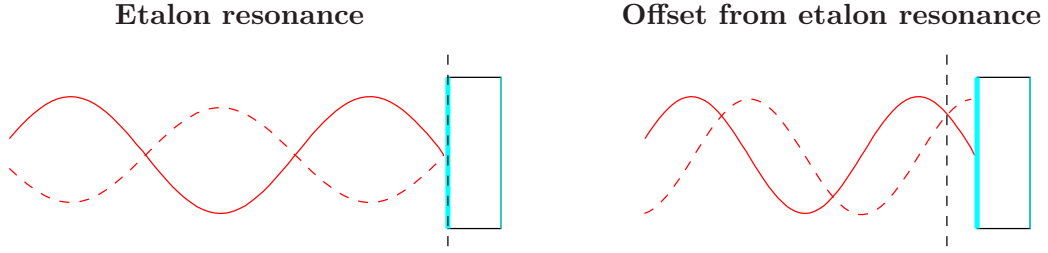


Figure 3.40.: Reflection from an etalon with fixed tuning for light fields with different frequencies. The left picture displays a light frequency resonant inside the etalon, the other an off-resonant, higher frequency. The reflected light field (dashed sine) gets no and 90° phase shift at the high-reflective surface of the etalon, compared to the impinging light (solid sine), respectively. This corresponds to a position of a conventional mirror (vertical dashed black line) agreeing with the front surface of the etalon and away from it by one eighth of the respective wavelength, respectively.

shifted to the left (or towards the light source) by an eighth of the wavelength from the front surface of the etalon. The corresponding position of the conventional mirror coating is indicated by the dashed black line. In the following, the conventional-mirror representation of the etalon will be called *imaginary mirror*.

Using this particular etalon/light-frequency configuration within a cavity, the *effective tuning* of the cavity is determined by the optical pathlength between the imaginary and the opposing, facing mirror. Thus, in order to obtain resonance, the etalon front surface needs to have a further (optical) distance from the other high-reflective mirror surface than an integer multiple of the respective wavelength, namely by

$$\delta x^{\text{et}} = \frac{\pi}{180^\circ} \cdot \frac{\delta \varphi^{\text{et}}}{2k}. \quad (3.4)$$

Here, δx^{et} denotes the position of the etalon front surface with respect to the high-reflective (other cavity-) mirror surface, modulo the wavelength of the light, $\delta \varphi^{\text{et}}$ is the particular phase shift of the light leaving the etalon front surface, given in degrees, and $k = \omega/c = 2\pi/\lambda$ is the wavenumber of the light field.

In order to distinguish the position of the etalon front coating with respect to the other mirror, and the rear etalon coating, they will be called *etalon position* and *etalon tuning*, respectively. Dealing with an etalon as a compound mirror, the position of its corresponding imaginary mirror is relevant (besides its optical properties, of course). In combination with one further mirror, for example, this *imaginary-mirror position* leads to the effective tuning of the cavity. The position of the imaginary mirror depends on both the etalon tuning, with respect to a light field of particular frequency, and the etalon position. Figure 3.41 illustrates all positions with a configuration corresponding to the left picture of Figure 3.40.

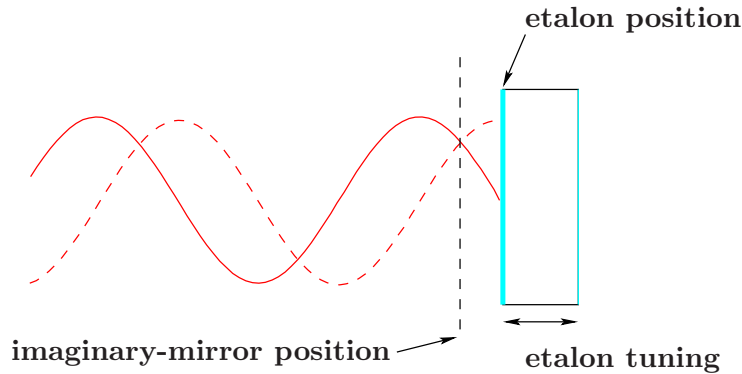


Figure 3.41.: Definition of the three tunings associated with an etalon being one compound mirror. The distance between the two etalon surfaces is the etalon tuning. If this is fixed, there is one remaining degree of freedom which is the position of the etalon. Here, it is defined as the position of the front or high-reflective etalon surface. A conventional mirror surface representation of the etalon (called imaginary mirror) has a position that depends on the phase shift the etalon introduces to a reflected light field. This position is called imaginary-mirror position.

Applying this etalon for the signal-recycling cavity of GEO 600, the consequences for the involved sidebands differ. The signal sidebands, for example, cover a frequency range of ± 10 kHz which is negligible compared to the etalon bandwidth of 155 MHz. Thus, for particular etalon tunings, the etalon position will appear shifted with respect to the position of the imaginary mirror. The effective cavity tuning, and the imaginary-mirror reflection is, though, with good approximation the same as for the carrier, for all signal sidebands.

This is different for the control sidebands with their modulation frequencies of roughly 9 MHz and 15 MHz. In general, their phase shift differs significantly not only from the carrier but also from each other. However, the consequences of the etalon for the signal-recycling and Michelson error-signal will be different, not only because of the distinct modulation frequency values but also because the Michelson sidebands are close to power-recycling cavity resonance for all signal-recycling cavity tunings, whereas the signal-recycling sidebands need to be resonant inside the signal-recycling cavity for each tuning.

3.7.2. Sideband resonance alterations in the signal-recycling cavity

The target is to predict parameters for the signal-recycling and Michelson control loops when tuning the signal-recycling cavity. Thus, as for the respective error-signals the resonance conditions of the carrier and the sidebands inside the signal-recycling cavity are crucial, we need to investigate these as, for example, done in Figure 3.11.

To apply, as much as possible, the knowledge gathered via the investigation of a dual-

recycled Michelson with a conventional **MSR**, the examination of the control sideband resonances for different signal-recycling cavity tunings will be made with particular, fixed etalon tunings. In order to reduce the parameter space for the etalon tuning, determined tunings representing extreme situations will be investigated. This way, one can get an estimate of how critical the etalon impact may become at all. In the following, the effect of a light phase shift, at etalon reflection, on the resonance features of the control sidebands will be discussed in more detail. As the signal-recycling sidebands are of particular importance for the ability to tune, special attention will be drawn to the consequences of these sideband properties' alterations for the tuning process. This will lead to particular, exceptional phase shift conditions (depending on the particular etalon tunings) that can be critical and are thus worth a closer investigation.

As the targeted signal-recycling cavity tuning is maximally 10 kHz, the maximal modulation frequency range necessary for the examination is presumably again in the order of ± 10 kHz. Thus, the etalon reflectivity and associated phase shift may well be assumed to be constant for each particular sideband. A further simplification can be made for the wavenumbers k of all control sidebands: as 15 MHz is only 5×10^{-8} of the carrier frequency, k is the same for all light fields.

If we for a start assume a positive phase shift in reflection of the etalon of the same size for all involved light fields, the imaginary mirror position will shorten the signal-recycling cavity with respect to the etalon position (see Figure 3.40, with a power-recycled Michelson added at the left). Thus, any light field resonance will appear at an etalon position offset of δx^{et} , according to Equation 3.4, from the tuning of a conventional **MSR**. Imagine the etalon position as the x-axis parameter of Figure 3.11, the two diagonal lines should move to the right. Overlaying them, their point of common maximal sideband enhancement (intersection point) will remain at the same modulation frequency ($\delta f_m = 0$ Hz), but occur at a position $\delta \chi$ larger than 0° . If the carrier would still be resonant at 0° , a continuous tuning of the signal-recycling cavity in the positive tuning region would be impossible. One reason is that at the intersection point the lock could in principle switch from one to the other sideband, moving the etalon back to the same region of positions. Another reason is the result of Figure 3.25 showing that **MSR** cannot be tuned lower than 80 Hz. Around the intersection point, the influence of the two sidebands on the error-signal becomes comparable, prohibiting a continuous tuning of the (compound) mirror. For a conventional mirror, the point of intersection always occurs with a tuned signal-recycling cavity. Considering a configuration with an etalon having similar reflectivity as the **MSR** used for Figure 3.25, the carrier resonance could well disagree with the point of intersection. This would make it impossible to achieve a perfectly tuned detector.

However, in this thought experiment we assumed the same phase shift for all involved light fields, thus, also for the carrier. With respect of the resonance for the carrier, the locations of the sideband maxima in the plane of modulation frequency and signal-recycling cavity tuning are the same as in Figure 3.11. From the point of resonance positions or resonance frequencies (thus, neglecting the effect of different power reflectivities of the etalon for the sidebands), this constellation is indistinguishable from a conventional mirror.

This situation of equal phase shifts for all involved fields is roughly achieved for an etalon tuning around the maximum possible phase shift, appearing at 75 MHz in Figure 3.39 and involving a power reflection around 98.2%. A simulation of the signal-recycling and Michelson sideband resonances inside the signal-recycling cavity for the corresponding etalon tuning is shown in the lower left and right pictures of Figure 3.42, respectively. They are similar to Figure 3.11, where the sideband amplitudes of the upper and lower signal-recycling sidebands are displayed in the plane of modulation frequency and **MSR** tuning. For Figure 3.42, however, the etalon position yielding the maximal sideband amplitude was determined for each modulation frequency, and the results for the upper and lower sideband are comprised in one graph (solid blue lines). For comparison, the same results for a conventional **MSR** are displayed as well (dashed magenta lines). To enable the comparison, the horizontal direction of the parameter plane represents the position of the high-reflective coating of either the etalon or the conventional mirror. The axis is given in kHz, relating the microscopic position via the carrier wavelength to FSR_{SR} (according to Equation 3.2 and 3.1). The etalon position for which the carrier is resonant is marked by the green vertical line, labelled “tuned”. (For the conventional mirror, the carrier is by FINESSE definition resonant at 0 Hz.)

Please note that for signal recycling and Michelson different tuning ranges are displayed: the right picture shows tunings in a region of 4 kHz around the Michelson sideband frequency currently used at GEO 600 (i.e., close to power-recycling resonance), whereas for the signal-recycling sidebands a smaller region of 400 Hz around the frequency resonant in the “conventional” signal-recycling cavity, tuned to carrier resonance, is shown. This illustrates the resonances according to their relevance for the particular control loop. Zooming out of the region in the left graph, the picture looks very similar to the right one.

Figure 3.42 approves the considerations from above: the locations of the sideband resonances, in the plane of modulation frequency and etalon position, are, together with the carrier resonance, shifted to the right. This maintains the relationships between sideband frequencies and effective signal-recycling cavity tuning for the carrier. Thus, assuming the same etalon reflectivity for all fields, the control-loop parameters should be the same as for a conventional mirror.

The next step is to consider different phase offsets for the light fields. Then, the diagonals in Figure 3.11 are shifted by different amounts, and the point of intersection will appear at $\delta x_{\times}^{\text{et}} = (\delta x_{+}^{\text{et}} + \delta x_{-}^{\text{et}})/2$, where δx_{+}^{et} and δx_{-}^{et} are shifts of the diagonals⁴⁶ belonging to the upper and lower control sidebands, respectively, along the horizontal axis. At the same time, the modulation frequency of the intersection point will be shifted by

$$\delta f_{\text{m}}^{\text{et}} = \frac{FSR_{SR}}{\lambda/2} \cdot \frac{\delta x_{+}^{\text{et}} - \delta x_{-}^{\text{et}}}{2} = \frac{FSR_{SR}}{180^{\circ}} \cdot \frac{\delta \varphi_{+}^{\text{et}} - \delta \varphi_{-}^{\text{et}}}{4}. \quad (3.5)$$

⁴⁶Please note that with the definition given in Equation 3.4, $\delta x_{\times}^{\text{et}}$, δx_{+}^{et} , and δx_{-}^{et} have dimensions of meters. To convert these values to frequencies, the conversion factor $FSR_{SR}/(\lambda/2)$ is necessary.

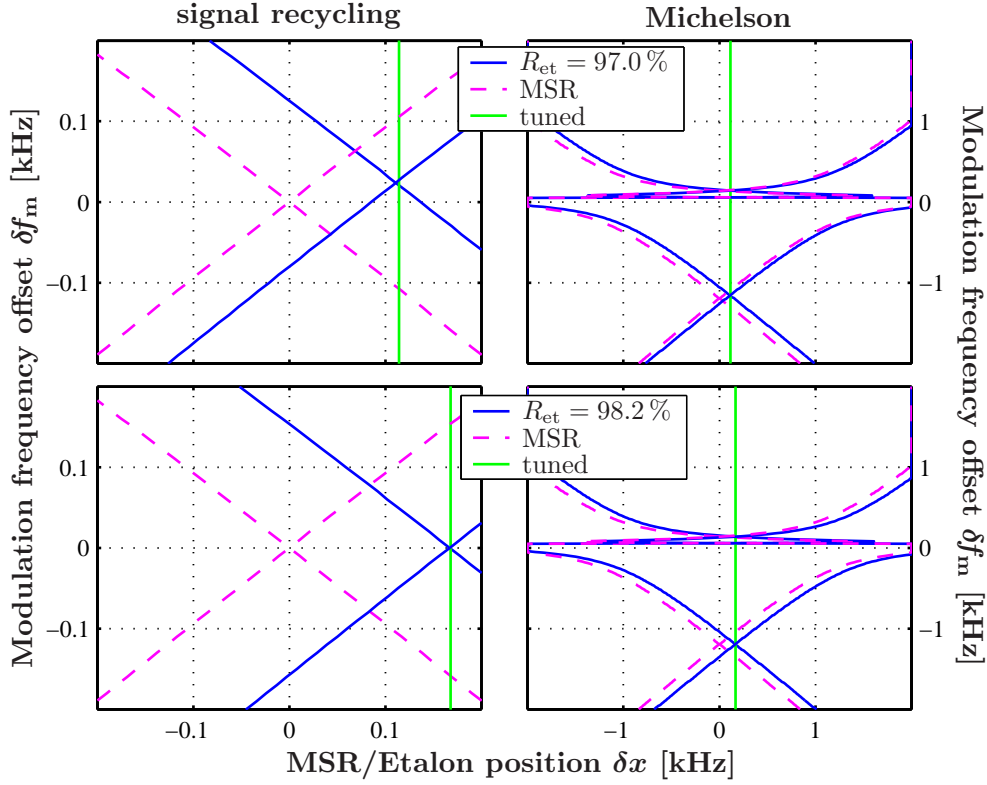


Figure 3.42.: Positions of the signal-recycling (right) and the Michelson control sideband resonances (left) inside the signal-recycling cavity, applying an etalon as compound output mirror of the cavity instead of the conventional **MSR**. The upper and lower pictures show the cases of etalon reflectivities of 97.0% and 98.2%, respectively, for the carrier. For comparison, the resonances appearing for a conventional **MSR** of same reflectivity are displayed as well (dashed magenta lines). To enable the comparison, the horizontal direction of the parameter plane represents the position of the high-reflective coating of either the etalon or the conventional mirror (in kHz). The signal-recycling and Michelson modulation frequencies are displayed with respect to $72 \times FSR_{\text{SR}} = 9.017397$ MHz and $119 \times FSR_{\text{PR}} = 14.904875$ MHz, respectively. (Please note the frequency range differences.) The etalon position for which the carrier is resonant is marked by the solid green vertical line, labelled “tuned”.

In case the slope of the phase dispersion is linear, the carrier's phase shift will be exactly the mean of $\delta\varphi_+^{\text{et}}$ and $\delta\varphi_-^{\text{et}}$ which are the phase shifts of the upper and lower sideband, respectively, at etalon reflection. Thus, the carrier resonance inside the signal-recycling cavity will appear at the same etalon position $\delta x_0^{\text{et}} = \delta x_{\times}^{\text{et}}$ where the intersection point of the diagonals occurs. In that case, the signal-recycling modulation frequencies to obtain particular signal-recycling cavity tunings are all shifted by δf_m^{et} compared to before. Besides, the resonance relationships are almost the same as with a conventional mirror, with one exception: the power-recycling resonance occurs at a different frequency distance for particular signal-recycling cavity tunings which can, in principle, influence both the sidebands' amplitude and phase. Please note that the etalon reflectivity is, in general, different for the two sidebands. Thus, the heights of the sidebands' amplitude maxima differ.

Perfect linearity of the phase dispersion is, however, rather the exception⁴⁷. With the present etalon, though, the carrier resonance will deviate from the intersection point by maximally ± 3.5 Hz and ± 10 Hz for the signal-recycling and Michelson control sidebands, respectively. These asymmetries are negligible.

For illustration, the upper left and right pictures of Figure 3.42 display the locations of the sideband amplitude maxima in the plane of etalon position and modulation frequency for signal-recycling and Michelson sidebands, respectively, for an etalon tuning corresponding to 30 MHz in Figure 3.39. (At this tuning, the difference of the light phase shifts is close to maximum.) The associated etalon reflectivity is around 97%. Whereas the intersection points are recognisably shifted to positive modulation frequencies, the carrier resonance offset from this intersection point is small.

3.7.3. Tuning parameter alterations

With respect to the sideband resonance positions discussed in the section above, the signal-recycling and Michelson control loops are in principle able to operate with an etalon, as specified in table 3.1, instead of a conventional mirror. The expected absolute shift of the signal-recycling modulation frequencies to obtain particular signal-recycling cavity tunings is for all etalon tunings below 20 Hz.

As the signal-recycling cavity bandwidth (for the carrier and the signal-recycling sidebands) varies with different etalon tunings within $\sim [20 \text{ Hz}, 700 \text{ Hz}]$, the impact of the etalon reflectivity on the tuning parameters can be expected to be more significant than

⁴⁷Generally, depending on the asymmetry of the phase shift differences between the carrier and the two sidebands, the carrier resonance occurs at an etalon position of

$$\delta x_0^{\text{et}} = \frac{\delta x_+^{\text{et}} + \delta x_-^{\text{et}}}{2} - \frac{\pi}{180^\circ} \cdot \frac{(\delta\varphi_+^{\text{et}} - \delta\varphi_0^{\text{et}}) - (\delta\varphi_0^{\text{et}} - \delta\varphi_-^{\text{et}})}{4k},$$

with $\delta\varphi_0^{\text{et}}$ being the phase shift of the carrier at etalon reflection.

Thus, the carrier resonance is potentially different from the intersection point of the sidebands' resonances. The possible consequences were already explained on Page 154.

the phase dispersion. How the bandwidth in principle influences the tuning parameters can be deduced by the discussion in sections 3.3.2 and 3.4.

Let us, for a start, assume the same reflectivity for all involved light fields. The wider the signal-recycling bandwidth the larger is the non-resonant sideband already for high detector tunings, and the larger is its impact on the signal-recycling error-signal vector pointing (see Figure 3.14). In that case, the length of the vector is, at large, reduced. According to the bandwidth, the non-resonant sideband broadens the error-signal gain shape.

For the Michelson error-signal, rather the signal-recycling bandwidth for the carrier is important. The control sideband properties get dominant only at larger signal-recycling cavity tunings. The absolute demodulation phase values, however, should in principle be smaller for all detunings, the wider the signal-recycling cavity bandwidth: a large bandwidth globally reduces the phase shift difference of the control sidebands. The effect, though, becomes negligible for high detunings, where both control sideband phasors are rotated by -90° . Both the demodulation phase and gain evolutions should broaden according to the signal-recycling bandwidth.

In order to highlight the peculiarities of the etalon in comparison to a conventional mirror, rather the effect of having (slightly) different reflectivities, for the light fields contributing to one error-signal, are of interest. The situation of $R_{\text{et}} \approx 98.2\%$, where the sideband resonance positions relative to the carrier resonance agree to those with a conventional **MSR** with $R_{\text{MSR}} = 98.2\%$ (see Figure 3.42), is very well suited for a control-loop-parameter comparison between the two optical configurations: it allows to focus on the effect of the different etalon reflectivities for the light fields involved in the error-signal generation (whereas the reflectivities of a conventional **MSR** are always the same for all fields). The example of $R_{\text{et}} \approx 97\%$, however, is interesting to investigate as the reflectivity gradient is close to maximum, and it includes also a shift of the modulation frequency resonances for particular signal-recycling cavity tunings.

Signal-recycling parameters

The values of signal-recycling demodulation phase and gain for these two etalon reflectivities for the carrier are displayed in the upper and lower pictures of Figure 3.43, respectively. The results for the etalon reflectivities of 97% and 98.2% are represented by blue and red lines, respectively. Positive and negative etalon tunings (yielding same reflectivities) are distinguished by dashed and dashed-dotted line styles, respectively. This distinction is, however, only necessary for the $R_{\text{et},\pm} = 98.2\%$ case (that ideally brings out the effect of different reflectivities for the control sidebands, s.a.). For comparison, the respective parameters for a detector, with a conventional mirror of 97% (solid cyan line) and 98.2% reflectivity (solid magenta line), are shown.

Please note that the horizontal axis represents the signal-recycling modulation frequency as an offset from the frequency yielding a tuned detector being equivalent to the

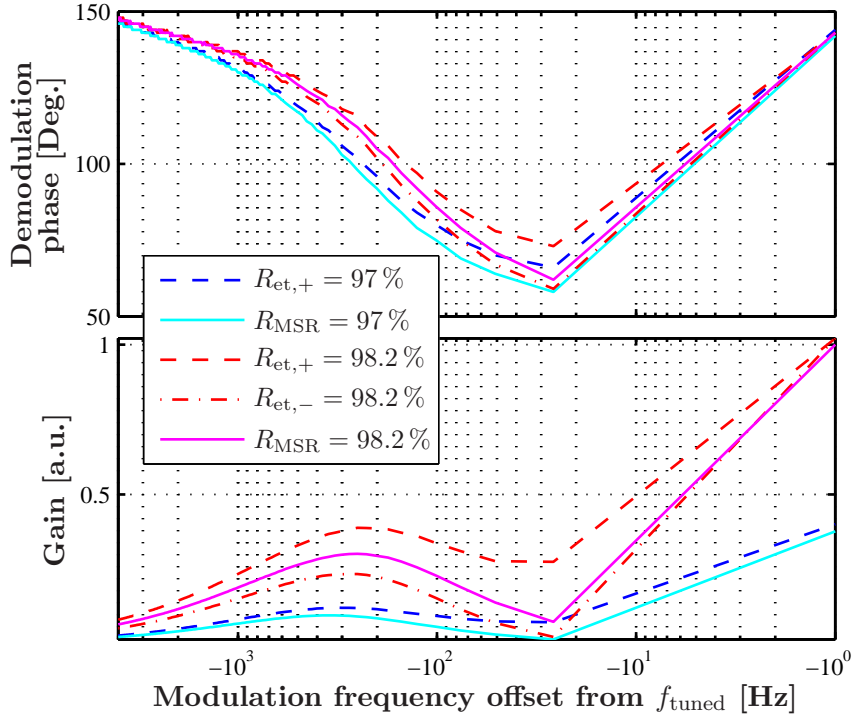


Figure 3.43.: Demodulation phases (upper) and gains (lower) of the most symmetric signal-recycling error-signals. Compared are detector configurations with a conventional mirror (solid lines) and an etalon with correspondingly same carrier reflectivity. Positive (dashed) and negative (dashed-dotted) etalon tuning sides are distinguished. For all curves, the horizontal axis displays the signal-recycling modulation frequency as an offset from the one being resonant inside a tuned detector. If the reference was constant, the curves representing a (compound) mirror reflectivity of 97% would be shifted towards higher values by ~ 20 Hz.

frequency value of the intersection point in Figure 3.42. Thus, if the reference frequency was constant, the etalon result for $R_{\text{et},+} = 97\%$ would be shifted by $+20$ Hz.

The demodulation phase range for the positively detuned etalon configurations is (for both reflectivities) less than for the detector configurations with the conventional mirror. At the same time, the range is larger for a negatively detuned etalon. This gets very plain with the phasor picture in Figure 3.14: without the non-resonant control sideband, the demodulation phase would remain constant. The non-resonant, lower signal-recycling sideband rotates the error-signal vector the more, the lower the signal-recycling cavity detuning, and the larger the lower sideband's amplitude. With the etalon positively detuned, its reflectivity for the lower sideband is less compared to the upper. Thus, the lower sideband's influence is weaker and the demodulation phase evolves more smoothed. The opposite is the case for a negatively detuned etalon, where the signal-recycling cavity enhancement of the lower control sideband is larger than that of the upper.

For the same reason, the optical gain of the error-signal is largest with a positively detuned etalon: the error-signal vector-length is mainly determined by the carrier and upper sideband amplitude. Thus, it reflects the different signal-recycling cavity enhancements of the upper sideband.

Consequently, the optical gain differences are slightly larger for $R_{\text{MSR}/\text{et},+} = 97\%$, as the reflectivity gradient is there close to maximum. The respective demodulation phases, however, are slightly closer, because for the amount of error-signal vector rotation the ratio between the signal-recycling cavity enhancements of the two sidebands is relevant.

However, relating the demodulation phases in the $R_{\text{MSR}/\text{et},+} = 97\%$ case to each other with respect to the absolute modulation frequency values, the differences will further increase as the line representing the etalon results gets shifted by +20 Hz.

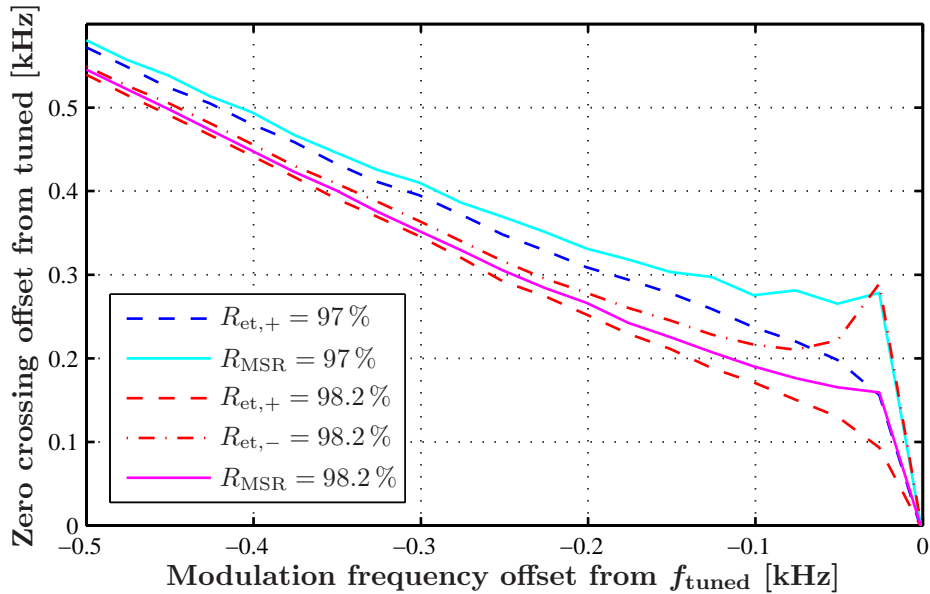


Figure 3.44.: Offsets of the signal-recycling error-signal zero crossings from carrier resonance, for the detector configurations, the modulation frequencies, and demodulation phases from Figure 3.43.

The effective signal-recycling cavity tunings, applying the demodulation phases from Figure 3.43, are shown in Figure 3.44, again depending on the signal-recycling modulation frequency as an offset from the frequency yielding a tuned detector. The colour and line-style coding is the same as in Figure 3.43. Obviously, for both reflectivity cases, with the conventional mirror the signal-recycling cavity is less continuously tunable around the carrier resonance than with the respective, positively detuned etalon. This is also explainable with the different etalon reflectivities for the sidebands, together with the phasor picture of Figure 3.14. As already stated above, the larger the non-resonant sideband amplitude, the larger the rotation of the error-signal vector, and the larger the

vector length for higher signal-recycling cavity detunings. If optimising for highest gain or symmetry, the (almost) largest error-signal vector is perpendicular to the demodulation phase vector. Thus, the resulting zero crossing of the error-signal will appear at tunings $\delta x > \delta x_m$, with δx_m being the **MSR** tuning for which one of the control sidebands resonates inside the signal-recycling cavity. In the positive etalon tuning cases, the non-resonant, lower sideband amplitude is weaker than with the conventional mirror, and even more weak compared to a negatively detuned etalon. Consequently, the impact of the lower sideband on the error-signal is less, and the signal-recycling cavity tuning will be closer to the upper control sideband resonance for all modulation frequencies⁴⁸. Close to the carrier resonance, the lower sideband influence is largest. Thus, the attenuation effect gets more significant, and the effective signal-recycling cavity tuning is more linear.

Summarising the effect of the etalon on the signal-recycling cavity tuning, in general, a positively detuned etalon improves all signal-recycling error-signal characteristics, compared to a negative detuning: the demodulation phase evolves smoother which is preferable with the current LabView performance⁴⁹, the optical gain is larger supporting higher signal-to-noise ratios, and the signal-recycling cavity tuning can be adjusted more continuously around carrier resonance, facilitating the transition to a tuned detector.

Michelson parameters

The resulting tuning parameters of the Michelson error-signal, the demodulation phase and optical gain, are comprised in the upper and lower picture of Figure 3.45, respectively. The colour and line-style codings are the same as in Figure 3.43. To enable a sensible comparison between the etalon position and the **MSR** tuning, the horizontal axis displays the position and tuning with respect to the position and tuning corresponding to carrier resonance, respectively. This is equivalent to the effective signal-recycling cavity tuning.

As expected, for lower reflectivities the curve shapes of the gain and the demodulation phases are broader, as the signal-recycling cavity bandwidth is larger. Furthermore, with **MSR**, the demodulation phases for the broader bandwidth are lower than for the smaller bandwidth, and they meet for high detunings.

Applying an etalon, the optical gain is, in general, smaller than applying a conventional mirror, but one loses less than 4% of optical gain with an etalon that is positively detuned. In the negatively detuned case, however, the optical gain is, within the displayed frequency region, by up to 40% smaller with respect to the detector with the conventional **MSR**, and it gets even lower for higher detunings.

The demodulation phases with a positively detuned etalon evolve the same as with the plain **MSR**, but are negatively shifted. The shift is larger for the $R_{\text{MSR/et,+}} = 97\%$ case.

⁴⁸This is also the reason why the signal-recycling cavity detuning is larger for the lower signal-recycling (compound) mirror reflectivity, for all modulation frequencies: with the larger signal-recycling bandwidth, the influence of the lower sideband is enhanced.

⁴⁹LabView has difficulties to alter two parameters at once. Thus, it is preferable to change parameter values as rarely as possible.

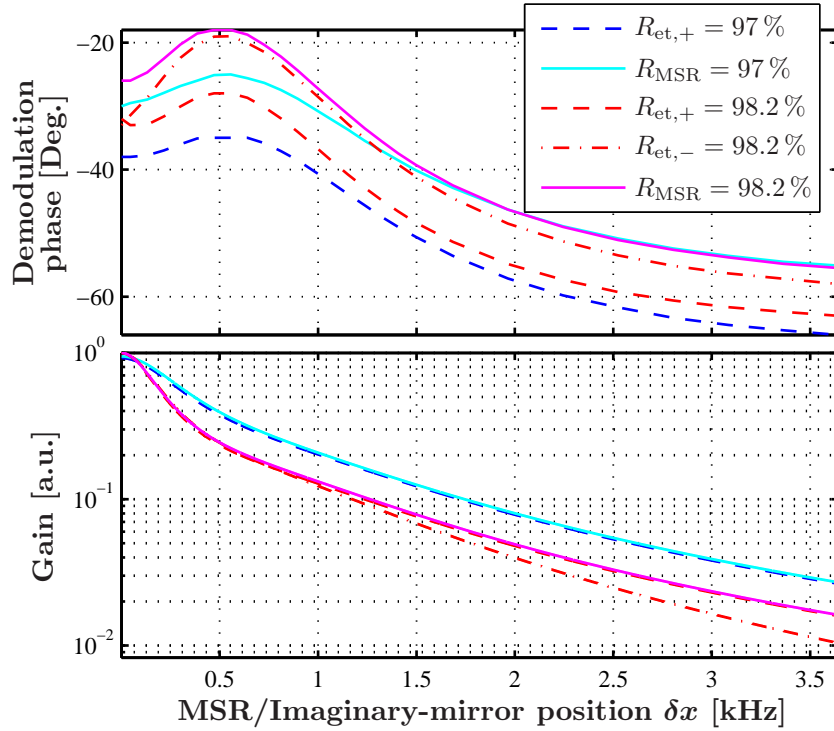


Figure 3.45.: Demodulation phases (upper) and gains (lower) of the Michelson error-signals with highest gain. Compared are the same detector configurations as in Figure 3.43. The horizontal axis displays the (imaginary) mirror position as an offset from the one yielding carrier resonance, ensuring the comparability of the curves.

For the negatively detuned etalon, the demodulation phase is closer to the **MSR** results and does not follow the same shape.

The shift of the demodulation phases is related to the phase shift associated with the etalon in transmission. (For the signal-recycling sidebands this is not relevant, as the detection takes place at the **BSAR**.) This phase shift amounts to $\sim \pm 11^\circ$ and $\sim \pm 8^\circ$ for $R_{\text{et}} \approx 97\%$ and $R_{\text{et}} \approx 98.2\%$, respectively, with respect to the carrier phase shift.

As already mentioned in Section 3.4, the shape of the demodulation phase evolution depends delicately on the exact amplitude ratios and phase shift differences of the control sidebands. Thus, the dependencies are too difficult to comprehend intuitively and to discuss with the phasor picture.

However, the results suggest that with a positive etalon detuning the control loop parameters qualitatively are the same as those using a conventional mirror. It should, though, be kept in mind that the Michelson modulation frequency, applied at GEO 600 and in these simulations, is slightly off-resonant regarding the power-recycling cavity. Only due to this, the upper control sideband resonates inside the positively detuned signal-recycling cavity during the tuning process. With the sidebands being resonant inside the power-recycling

cavity, or off-resonant to the other direction, the lower sideband is the one resonating inside the signal-recycling cavity (see Figure 2.4). In that case, the optical gain for high signal-recycling cavity tunings is expected to be smaller with a positively detuned etalon.

3.8. Conclusion

This chapter describes the current control of the dual-recycled GEO 600 detector, and in particular the tuning process, i.e., the controlled microscopic movement of the signal-recycling mirror. Furthermore, it gives an outlook not only on how to yield a tuned detector, but also on the possible impact of an etalon (replacing the signal-recycling mirror at the output port) onto the error-signals of the signal-recycling, and the differential Michelson control.

Starting with an overview of the lock strategy applied at GEO 600 (see Figure 3.1), the techniques used for error-signal generation, and the open loop gains of the relevant control loops are introduced. These comprise the laser frequency, the signal-recycling, and the differential Michelson control (see sections 3.2.1 to 3.2.3). The laser-frequency loop is almost independent of the signal-recycling cavity tuning.

In the rest of this chapter, the tuning process of the signal-recycling cavity is investigated for the fully operated detector. To guarantee control loop stability during the tuning process, the open loop gains of the Michelson and signal-recycling loops demand the optical gains of the respective error-signals to remain within a margin of 0.275 to 1.64 and 0.5 to 2, respectively. These margins are valid for original unity-gain frequencies of ~ 80 Hz and ~ 40 Hz, respectively (see Figure 3.4 and 3.6, respectively).

Beyond, the success of shifting the position of **MSR** by a certain microscopic distance depends on the properties of the signal-recycling error-signal. In particular, the error-signal shape around the zero crossing is important. The error-signal symmetry reduces the susceptibility of the error-signal to fluctuations in other degrees of freedom (see Figures 3.20, 3.21, and 3.23). The capture range, being the monotonic region around the zero crossing, limits the maximally achievable step size in the tuning process (see Figure 3.17). The signal-recycling error-signal shape, and in particular the zero crossing position, depends on the combination of the modulation frequency and the demodulation phase (see Figure 3.8 and 3.22).

For the Michelson error-signal, the only property to supervise is the optical gain which depends not only on the **MSR** position but also on the Michelson demodulation phase. In addition to adjusting the electronic gain, the demodulation phase yielding maximum gain is retraced during the tuning process (see Figure 2.4 and 3.16).

In the experiment, the demodulation phases and electrical gains of the Michelson and signal-recycling control loops are set by an automated computer control system (see Section 3.2.4). The distributed parameters are looked-up in a tuning script (see Section 3.5.1, 3.5.2, and 3.6.2) that was created with FINESSE simulations ([FINESSE]). Today, the detector may be tuned down to ~ 330 Hz.

Tuning further down to carrier resonance is, in principle, possible, though not yet implemented. Two suggestions to yield a tuned detector without the loss of lock are presented (see Section 3.6.4): one features a short switch-off of the signal-recycling control, to let the free mirror swing through carrier resonance, and there to again acquire lock. The other retains the tuning procedure, successively changing the signal-recycling error-signal parameters to move the signal-recycling mirror in a controlled way (see Figure 3.38). The tuned detector in any case requires an additional differentiator stage for the Michelson control loop to compensate for the appearing signal-recycling cavity pole with ~ 200 Hz corner-frequency.

In general, to successfully implement a parameter script for the tuning process in the experiment two aspects turned out to be important. One is the accuracy of the FINESSE input file describing the optical system of the detector, the other is the matching of the resulting control loop parameters to the experiment. For both, the stability of the control loops, determined by their respective open loop gain functions, is the limiting factor.

The optical gains and the determined demodulation phases alter for different signal-recycling and Schnupp lengths (see Figures 3.32 and 3.35, respectively). Whereas a difference of the Schnupp length of +4 mm already leads to instabilities around 1.5 kHz (see Figure 3.37), a signal-recycling cavity length deviation of more than -1 mm or $+2$ mm only disrupts at very low detunings (see Figure 3.33, in combination with Figure 3.32).

For the calibration accuracy of the control loop parameters, the impact of the signal-recycling demodulation phase on the optical gain is crucial (see Figure 3.33). In the past, this demodulation phase estimation prevented from successful tuning, partly because a FINESSE bug flipped the demodulation phase sign. With the current way of parameter calibration (see Section 3.6.2), however, not only the FINESSE bug was discovered, but also an accuracy of the signal-recycling demodulation phase of $\pm 2^\circ$ could be achieved. The Michelson demodulation phase yielding highest gain can be measured to $\pm 1^\circ$. The calibration accuracy for both gains is 1%.

The investigations of the tuning process were guided by the phasor picture, and in particular by the projection picture, illustrating qualitatively the expected signal-recycling error-signal (see Section 3.3.2, and particularly Figures 3.13 to 3.15). The understanding gained with the phasor picture allowed the prediction of the parameter evolutions necessary for both the signal-recycling and the Michelson control (see Section 3.3 and 3.4, respectively), and gave confidence in the FINESSE results (after detecting two FINESSE bugs). Understanding the fundamental mechanisms, also the relation between the exact signal-recycling mirror tuning and the control loop parameters could be explained (see Figure 3.25). Identifying the signal-recycling error-signal features on the two possible tuning sides to be identical (see Figures 3.8, 3.10, 3.14, and 3.15), the tuning side was determined with sideband resonances inside the detector (see Figure 3.29). In addition, it made clear that, in principle, the detector tuning on both tuning sides is possible.

However, the main profit of the phasor picture during the tuning investigations was that it enabled to identify relevant regions in the huge parameter space influencing the error-signals. It helped, for example, to find one demodulation phase enabling an overview of

the signal-recycling error-signal over a large interval of modulation frequency and signal-recycling cavity tuning. Compared with preceding simulations (see Figures 3.16 and 3.17 in [Freise03a]) this result is very instructive. (The plot is displayed in Figure 3.8, the corresponding phasor pictures are shown in Figure 3.13 to 3.15). The phasor picture was also very effective in yielding the necessary accuracy of the FINESSE input script, leading to the question of changes of control sideband resonance conditions.

For the impact of an etalon, as compound signal-recycling mirror at the output port, on the tuning parameters the insights yielded by the phasor picture enabled a fast and elegant, targeted investigation. Generally crucial etalon features are worked out. For example, the linear relation between the signal-recycling cavity tuning and the applied modulation frequency is not off-set, with respect to a conventional mirror, by the phase shift of the signal-recycling control sidebands yielded in etalon reflection, but depending on the difference of the particular phase shifts (see Equation 3.5, and Figure 3.39 and 3.42).

With the examined etalon (see table 3.1), in principle, a continuous tuning within the complete detection bandwidth of ~ 10 kHz is possible. For the accessible etalon reflectivity margin, the shift of the 72nd multiple of FSR_{SR} , associated with the phase shift appearing at etalon reflection, is limited to ~ 20 Hz. The different etalon reflectivities for the involved light fields are crucial for the gain and demodulation phase evolutions of the control parameters. In the comparison of positive and negative etalon tunings, of same carrier reflectivity, a positive etalon tuning significantly improves all relevant features of the two error-signals (see Figures 3.43 to 3.45): the optical gains are larger, the demodulation phases alter less, and the signal-recycling cavity tuning is closer to a linear relation to the signal-recycling modulation frequency. The only premise is that for each control loop the respective upper control sideband is resonant inside the signal-recycling cavity. In comparison with a conventional mirror, the optical gain of the Michelson error-signal is slightly less, by $\sim 4\%$. This is, though, together with the small shift of the signal-recycling resonance frequency of 35 Hz (in comparison to the signal-recycling cavity linewidth for the Michelson control sidebands of ~ 1 kHz), negligible for the detector sensitivity.

Chapter 4.

Detector characterisation utilising simulations

4.1. Introduction

For the successful development and commissioning of a gravitational-wave detector, simulations of transfer functions, resonances and error-signals are indispensable. The accuracy to which particular parameters need to be known depends on the detector type, and on the feature under investigation.

To determine control-loop parameters for a successful tuning of the GEO 600 detector without the loss of lock, for example, the tolerable length deviation of the simulation from the experiment can amount to up to several centimeters. This, however, presupposes the calibration method described in Section 3.6.2 for the Michelson and signal-recycling demodulation phases and gains, and restricts the targeted detector tunings to lie in the kHz region.

The prediction of the tuning of GEO 600, and at the same time of the shot-noise limited detector sensitivity requires more precise optical parameter specifications: a deviation of the power-recycling and signal-recycling cavity lengths of ± 1 mm shifts the resonances of the 72nd and 119th multiple of the two *FSRs* by roughly ± 8 Hz and ± 12 Hz, respectively. A shift of the resonance condition for the signal-recycling control sidebands linearly affects the position of the peak sensitivity. A change of the Michelson control sidebands alters the shape of the shot-noise limited sensitivity curve (see Figure 2.13). Due to the coupling of the two cavities, the precise signal-recycling resonance condition of the two sorts of control sidebands depend on both cavities¹ at the same time. As differential Michelson arm-length deviations determine the coupling level of the two cavities, the macroscopic difference in the length of the Michelson arms as well influences both the peak position and shape of the sensitivity curve.

¹This holds also for the signal-recycling control sidebands, even though the power-recycling influence is weak due to the respective anti-resonance: investigations of the signal-recycling error-signal showed that the optimum demodulation phase gets slightly shifted for lower signal-recycling cavity tunings by several degrees (see the explanations concerning Figure 3.23) due to the power-recycling cavity impact. According to Figure 3.34, depending on the tuning and on the region of demodulation phase a deviation from the targeted demodulation phase by $\sim 10^\circ$ may change the detector tuning by ~ 100 Hz.

To understand and reproduce the coupling of noise to the detector output signal or the error-signal for misalignments, for example, an even more detailed knowledge about the optical system is necessary. Beyond the overall cavity and differential Michelson armlengths, the beamsplitter and far end mirror positions and specifications change the exact phases of all light fields and modes at the photodiode.

Cavity lengths can be determined during operation of the corresponding control by looking for the resonance of another control sideband inside that cavity. If resonant, frequency noise peaks get attenuated in the spectrum of the respective error-signal (generated in either the reflection or transmission of the cavity). In the current configuration of GEO 600, the length of the (compound) power-recycling cavity is determined with this method by evaluating the Michelson error-signal under **MSR** misalignment (see [Freise03a], page 71, and [Grote03b], pages 20 – 21). The precision of this measurement is better than $\pm 1 \text{ Hz} \hat{=} \pm 0.1 \text{ mm}$. Thus, the power-recycling cavity length was assumed to be known for all simulations.

For other degrees of freedom or script parameters, new measurements were necessary. The amplitude of the differential Michelson error-signal, demodulated at twice the modulation frequency ($2f$ signal), for example, depends strongly on the control sidebands' enhancement inside the power-recycling cavity. The signal-recycled Michelson (srMI) is the compound output mirror of this cavity. Thus, sweeping the modulation frequency, the shape of the $2f$ -signal amplitude depends on particular properties of both the Michelson and the signal-recycling cavity, like lengths and losses.

The transfer function shape of differential end mirrors' movements to the output signal of the dual-recycled Michelson (optical transfer function), contains further information on several degrees of freedom of GEO 600: the reflectivity of **MSR** can, for example, directly be extracted from the bandwidth. The shape also depends on the signal-recycling cavity tuning and length, and on the Schnupp length. The optical transfer function is not only used for parameter adjustments, but also to confirm the determined degrees of freedom at different detector tunings.

The term *detector characterisation* does not only apply to the determination of degrees of freedom by fitting measurements. Section 4.4 examines the laser amplitude noise coupling to the differential Michelson output, joining both FINESSE simulations, and the phasor or projection picture. The appearance of notch-like patterns in the measured noise transfer-function is qualitatively explained. The illustration of the coupling mechanisms reveals modulation-index variations as an alternative noise source with similar characteristics in the strain signal.

4.2. $2f$ signal

The $2f$ signal is generated by demodulating the photodiode signal of PDO with twice the Michelson modulation frequency (see the dashed-dotted lines in Figure 3.1). Considering Equation 1.17, the $2f$ signal is a measure of the two Michelson control sidebands' amplitudes appearing at the output. In the configuration of GEO 600 these sidebands have

a constant frequency chosen to be roughly resonant inside the power-recycling cavity. Hence, we expect an Airy-like dependency of the 2f signal under modulation frequency variations, mainly determined by the detuning from power-recycling resonance², and the properties of the input and output mirrors.

The output mirror comprises the Michelson and the signal-recycling mirror, together called the signal-recycled Michelson (srMI). With $R_{\text{MSR}} = 98.14\%$ and $R_{\text{MI}} \approx 99.85\%$, the srMI is undercoupled from the power-recycling cavity point of view. Whereas R_{MSR} is an intrinsic property of **MSR** (although to be determined), R_{MI} changes with Schnupp length, interferometer losses and misalignment, and is different for different light frequencies. Furthermore, due to the asymmetric losses in the two Michelson arms the phase shift at reflection of the (isolated) Michelson gets sensitive to the amount of Schnupp length. Thus, the Schnupp length's impact on the light phase shift at reflection of the srMI is twofold: through the phase shift by the Michelson, and the phase shift originating from the undercoupled signal-recycling cavity, having different input mirrors.

The dependency of the 2f signal on the Michelson modulation frequency should be suitable for the determination of the combination of Schnupp and signal-recycling cavity lengths, and interferometer losses. Figure 4.1 shows a measurement of the 2f signal with the detector being detuned to ~ 1 kHz. The Michelson modulation frequency was varied around the mid frequency of $f_{\text{mid}} = 14.904927$ MHz by ± 80 Hz in steps of 10 Hz, forward and back.

Figure 4.2 comprises the 2f signal dependency on the modulation frequency in the experiment (solid blue line with error bars³), and the output from the original FINESSE script (dashed magenta line) describing GEO 600 (i.e., the optical system comprised in Appendix B.1.2). In the following, this script will be called *default script* and the corresponding parameters *default parameters*. The default detector tuning is set to $1.419^\circ \hat{=} 990$ Hz, according to the zero crossing of the signal-recycling error-signal, applying the experimentally used signal-recycling modulation frequency and demodulation phase. Obviously, the simulation result is shifted by approximately 30 Hz, and the shape is narrower compared to the experiment. There is also a slight asymmetry that does not agree with the measurement.

Before optimising the FINESSE input file to yield a simulated 2f signal that matches the experimental data, the impact of some promising parameters on the 2f signal were investigated separately. The examined parameters were signal-recycling cavity length and tuning, Schnupp length, misalignment, common Michelson losses, and **MSR** properties. The influence of the signal-recycling cavity tuning, of **MSR**, and of misalignment turned out to be negligible. The three parameters left to be accounted for are the Schnupp and

²For illustration, Figure 2.16 on page 67 shows the amplitude dependency on the modulation frequency in combination with the **MSR** tuning.

³The points of the curve were gained from the measurement shown in Figure 4.1. The error bars were determined by the standard deviation from the mean value. However, as the measurement times for each modulation frequency were indeed short, it is assumed that the largest of all error bars in principle holds for all measurements (except for f_{mid}), even if the standard deviation is, by chance, small for some measured frequency periods. In particular the boundaries legitimate this approach.

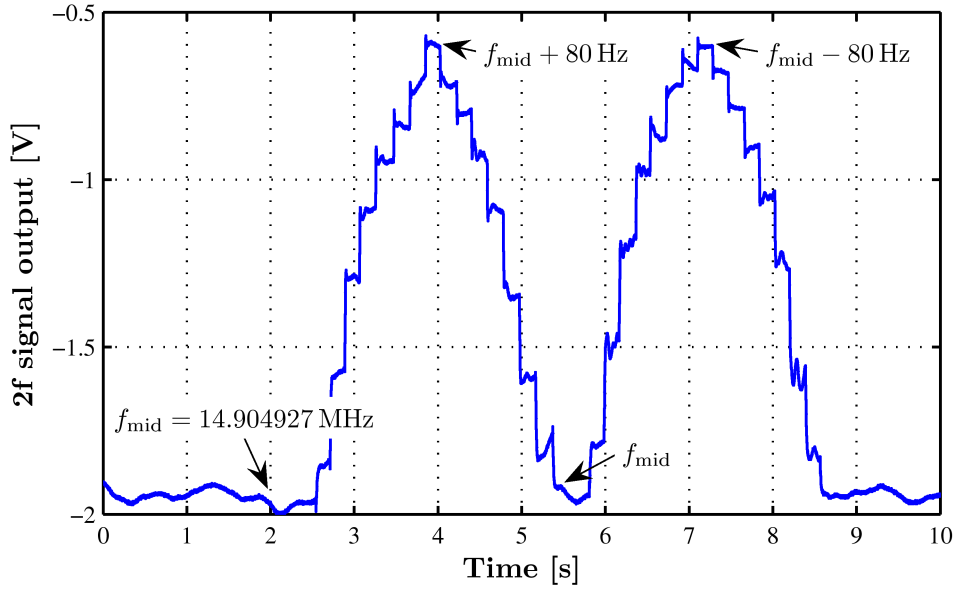


Figure 4.1.: Measurement of the $2f$ signal while varying the Michelson modulation frequency around the mid frequency of $f_{\text{mid}} = 14.904927$ MHz by ± 80 Hz in steps of 10 Hz, forward and back. The duration of the shifted frequency values was limited by the Michelson auto alignment performance.

signal-recycling cavity lengths (L_{Schnupp} and L_{SR} , respectively), and the common losses in the Michelson. Whereas the common Michelson losses only vary the width of $2f$ signal curve, the Schnupp and signal-recycling cavity alter all curve properties at the same time. However, the signal-recycling cavity length predominantly changes the symmetry, the Schnupp length in the first instance shifts the curve with respect to the frequency axis (see Appendix C for the respective graphs and further explanations).

To fit the simulational curve to the measurement, the $2f$ signal was computed in this 3-dimensional parameter space. The curves for each parameter triple were compared to the measurement with the least-square method (LSQ), seeking the minimum of

$$lsq = \sum_{i=1}^{17} (y_{\text{meas}}(f_i) - y_{\text{sim}}(f_i))^2. \quad (4.1)$$

f_i are the particular Michelson modulation frequencies applied in the measurement, $y_{\text{meas}}(f_i)$ are the experimental $2f$ signal values for the respective f_i , and $y_{\text{sim}}(f_i)$ are the corresponding simulational signal values ($i = 1, \dots, 17$).

From left to right, the three subplots of Figure 4.3 show the LSQ for an offset, $\Delta L_{\text{Schnupp}}$, from the default L_{Schnupp} of -16 mm, -18 mm, and -20 mm, in the plane of common Michelson losses and ΔL_{SR} . The lsq values vary most with $\Delta L_{\text{Schnupp}}$. Whereas the minima in all three subplots indicate the common losses to amount to roughly 700 ppm, the supposed optimum ΔL_{SR} shifts by more than 2 cm.

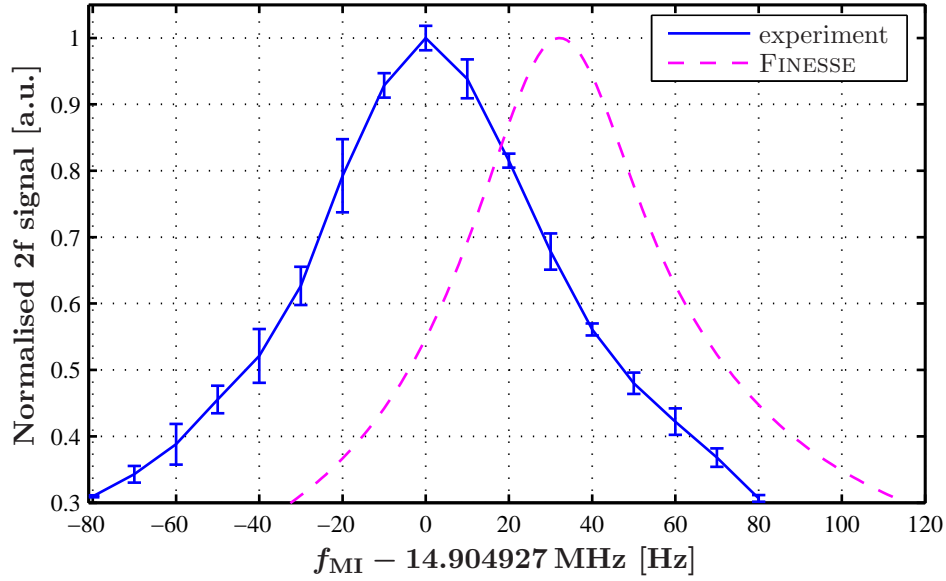


Figure 4.2.: Experimental 2f signal of the detector detuned to ~ 1 kHz, depending on the Michelson control sideband frequency, in comparison with simulation. The simulation was done with the FINESSE default input script of Appendix B.1.2. The modulation frequency is given as offset from the one yielding maximum signal value in the experiment.

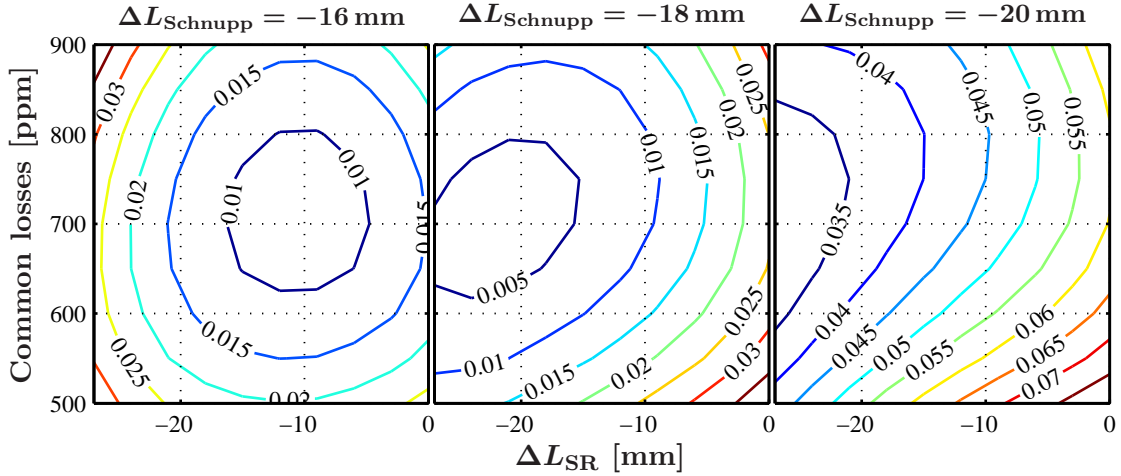


Figure 4.3.: lsq for a $\Delta L_{\text{Schnupp}}$ of -16 mm (left), -18 mm (middle), and -20 mm (right), in the plane of common Michelson losses and ΔL_{SR} . Please note the different lsq values of the contour lines comparing the subplots.

Considering the errors of the measurement, the associated accuracy of the signal-recycling cavity length is too poor, even for a reliable prediction of tuning parameters (see Section 3.6.3). As a consequence, the signal-recycling cavity length is determined differently (see the following section). The result for the signal-recycling cavity retrospectively fine-tunes the Schnupp length and common losses, with respect to the LSQ results.

4.3. Optical transfer function

One of the most important signals of GEO 600 to be modelled is the gravitational-wave-signal transfer function of the detector: the so-called *optical transfer function*. It is equivalent to the transfer of differential Michelson armlength variations to the output signal at the south port.

Besides its significance for the shot-noise limited detector sensitivity the measured transfer function yields suitable information on detector characteristics. The measurement of the $2f$ signal, for example, is not sensible if targeting the reflectivity of the signal-recycling mirror. Neither is it accurate enough for the signal-recycling cavity length. With the optical transfer function, R_{MSR} can be adjusted such that the simulation fits the detector bandwidth, whereas the signal-recycling cavity length influences the frequency position of the peak amplitude transfer.

4.3.1. Determining the signal-recycling cavity length

The signal-recycling cavity's impact on the optical transfer function shape acts through the **MSR** tuning which is determined by the zero crossing of the signal-recycling error-signal (see Section 3.3). For large detunings on the tuning side opposite to the 72nd FSR_{PR} , this zero crossing roughly coincides with the **MSR** tuning, for which one of the signal-recycling control sideband resonates (see Figure 3.10 and 3.25). A variation of the signal-recycling cavity length alters $f_{\text{m,tuned}} = 72 \times FSR_{\text{SR}}$, and consequently the resonance condition of any signal-recycling control sideband.

However, the error-signal zero crossings depend also on the demodulation phase (see Figure 3.22). Assuming the demodulation phase is known, the signal-recycling cavity length offset from the experiment would directly show up as an offset of the peaks of the optical transfer functions: +1 mm length offset shifts the 72nd FSR_{SR} by ~ -7.5 Hz. However, in order to minimise the error, the accuracy of the demodulation phase has to be considered.

In section 3.6.2 the non-linear zero crossing dependency on the demodulation phase was used to calibrate the phase. This calibration was done for a detuning of ~ 2 kHz (see Figure 3.30 and the corresponding explanations), with an accuracy of $\pm 2^\circ$.

This demodulation phase uncertainty can, with Figure 3.30, be directly translated into the maximum achievable accuracy for the signal-recycling cavity length when comparing the measured optical transfer functions with simulation. Given the slope of the curve,

applying the highest demodulation phase should yield the least uncertainty for the **MSR** tuning in the simulation. There, $\pm 2^\circ$ yields a tuning deviation of ± 10 Hz (compared to ± 20 Hz for the lowest demodulation phase of 155°).

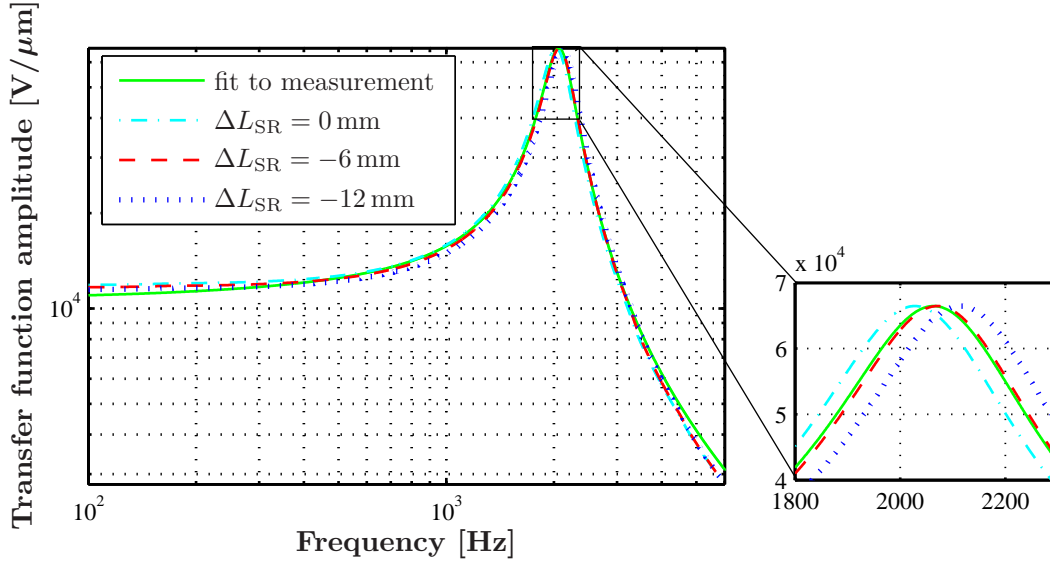


Figure 4.4.: Comparison between a fit of the measured optical transfer-function amplitude, and three simulations that use different signal-recycling cavity lengths. In order not to be sensitive to the Michelson demodulation phase, two perpendicular quadratures are quadratically added. To ease the comparison of the peak frequencies, the simulated transfer functions are normalised to fit with the maximum of the measured transfer function.

Figure 4.4 displays the fit of the measured optical transfer function applying 175° as demodulation phase (solid green line), together with three simulated curves, with the same demodulation phase, and different signal-recycling cavity lengths. To be independent of the experimentally used (uncalibrated) Michelson demodulation phase, the transfer functions' amplitudes are maximised for each frequency by quadratically adding the two measured perpendicular quadratures (which is equivalent to optimising the Michelson demodulation phase for each frequency). The simulations are normalised to yield the same maximal amplitude value as the experiment. The peak of the transfer function with the default length (dashed dotted cyan line) is -36 Hz away from the measurement, the one with -12 mm offset (dotted blue line) is 50 Hz too high. Although the middle of them is still off by $+7$ Hz, it is the length that satisfies both the transfer function, and the $2f$ signal measurements best within the given accuracy limits.

Going back to Figure 4.3, the LSQ for a signal-recycling cavity length offset of ~ -6 mm rather suggests a Schnupp length of -16 mm. For validation, Figure 4.5 compares the $2f$ signal for the FINESSE input file, with the final parameters, with the measure-

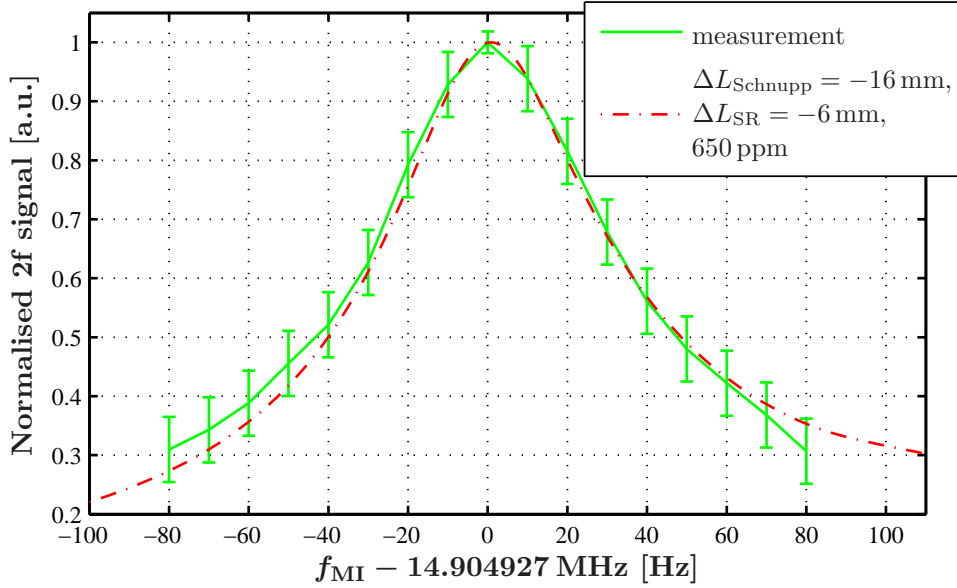


Figure 4.5.: Comparison of the measured and simulated 2f signal. The simulation applies the common Michelson losses, Schnupp length and signal-recycling cavity length, commonly determined by the optical transfer function and the results of the LSQ of the 2f signal. The parameters obviously satisfy the 2f signal measurement within the respective errors.

ment. The common losses, fitting the 2f signal best with the given length parameters ($\Delta L_{\text{Schnupp}} = -16$ mm, and $\Delta L_{\text{SR}} = -6$ mm), are 650 ppm.

4.3.2. Anticipating the optical transfer function of GEO 600

Ideally, inserting a particular signal-recycling modulation frequency and demodulation phase of the experiment into the simulation yields the right **MSR** tuning if it generates an optical transfer function whose peak amplitude position agrees with the measurement. Beyond R_{MSR} setting the signal-recycling cavity linewidth, the shape of the transfer function is further determined by the resonance condition of the Michelson control sidebands inside the dual-recycled detector (see chapter 2), and the Michelson demodulation phase.

The optical transfer function measurements at ~ 2 kHz allow (fine-)adjustments of the Schnupp and signal-recycling cavity length, the common Michelson losses, and the **MSR** reflectivity. Moreover, the signal-recycling and Michelson demodulation phases could be calibrated.

The new input script, together with the calibration, can be best tested by predicting the optical transfer function for different, experimentally used combinations of signal-recycling modulation frequency and demodulation phase. The optical transfer functions, shown in Figure 4.6, feature a signal-recycling cavity tuning of ~ 1 kHz. In the simulation,

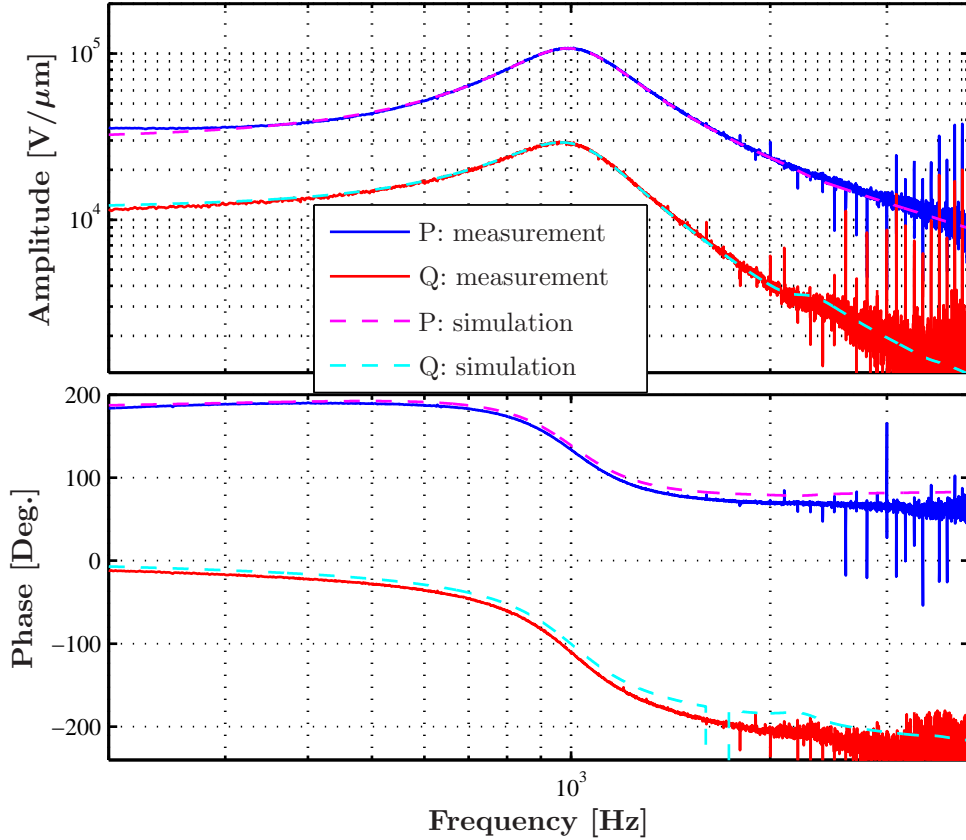


Figure 4.6.: Comparison of measured and simulated optical transfer functions of GEO 600. The detector is detuned to ~ 1 kHz. For the simulation, **MSR** is tuned to the signal-recycling error-signal zero crossing, applying the experimental tuning script parameters and the signal-recycling and Michelson demodulation phase calibrations determined at a different detuning.

the **MSR** is tuned to the zero crossing of the signal-recycling error-signal that is generated with the tuning script parameters used for the present measurement. The blue and red solid lines in the upper and lower graphs of Figure 4.6 respectively display the measured optical transfer functions in amplitude and phase, in two perpendicular quadratures P and Q. The dashed magenta and cyan lines are the respective FINESSE predictions, normalised to the experimental peak amplitude value. For this simulation no further parameter adjustment nor calibration was done.

The agreement of the presented amplitude curves is for both quadratures better than 5% within the interval of $\sim [250 \text{ Hz}, 2150 \text{ Hz}]$. A similarly excellent agreement is achieved predicting the optical transfer function for detector tunings of ~ 2 kHz and ~ 330 Hz. The disagreement in Figure 4.6 between simulation and experiment at lower signal frequencies is most likely caused by errors in the model of the Michelson control loop filters that were

accounted for: the DC values of the optical transfer functions are very sensitive to the assumed open loop gain. The accuracy at high frequencies is mainly limited by the bump occurring around 2.3 kHz. Amasingly enough, though, it is – at least roughly – predicted by the simulation. It originates from the beat of the carrier, appearing at the dark port due to asymmetric losses in the Michelson arms, with the signal sidebands generated around the Michelson control sidebands (see also Section 4.4).

4.4. Laser amplitude noise

Nowadays, the construction of all interferometric, large-scale gravitational-wave detectors of the current, first generation network, is completed. The effort is now to improve, on the one hand, the robustness of operation, i.e., of the acquisition and duration of locks or of the tuning process, and, on the other hand, to reduce technical noise sources that prevent the detectors from reaching their design sensitivities. To identify and eliminate technical noise sources is often referred to with the term *noise hunting*.

A technique to facilitate noise hunting is the so-called *noise projection*. This method is very much used at GEO 600. It allows estimations of coupling levels of noise sources into the differential output signal containing the gravitational-wave signal, $h(t)$ [Smith06]. The basic procedure of noise projection is:

- Find a recordable signal, $N(t)$, that is a good measure for a particular noise source, $n(t)$.
- Build the transfer function from $N(t)$ to $h(t)$, $\text{TF}_{N \rightarrow h}$. For this, the noise appearing in $N(t)$ has to be dominated⁴ by $n(t)$.
- Measure the amplitude spectral density (ASD) of the signal $N(t)$, and multiply it with $\text{TF}_{N \rightarrow h}$. This yields the coupling level of $N(t)$ showing up in $h(t)$.

The noise projection method is a very useful tool to systematically determine noise sources limiting the current sensitivity and track their propagation through the detector (investigating various output signals). Especially where intuition fails, noise projection is invaluable.

If the projection indicates the considered noise to be dominating, either the source itself can be improved, or the coupling reduced. For a coupling reduction, however, the mechanism has to be established. Some coupling mechanisms are, though, difficult to access. Simulations may help to enlighten the subject.

The following section shows the adoption of simulations in combination with the phasor picture to explain the coupling of laser amplitude noise (LAN) to $h(t)$.

⁴This may require the introduction of some extra noise at the particular source.

4.4.1. Experimental laser-amplitude-noise coupling into $h(t)$

One of the reasons to operate the Michelson interferometer of the dual-recycled detector with a perfect dark south port, is to decouple $h(t)$ from laser-power noise. In case of differential losses in the interferometer arms, mode-mismatch or small offsets from a perfect dark fringe, however, a particular amount of carrier appears in the south port, making it susceptible to variations of the laser amplitude.

Figure 4.7 shows the gain and phase of the transfer function of the LAN that was injected into the interferometer, to the gravitational-wave channel output. The DC output of PDPR (see Figure 3.1) was used as a measure of the LAN⁵. The detector tuning was ~ 1 kHz for this measurement which was made in May 2005. During this time, the low-reflective **MPR** was installed.

The gains exhibit 3 to 4 dips. The respective phase shapes differ in characteristics, pointing to different relations between competing processes. At 700 Hz, the phase evolution of $\text{TF}_{\text{PDPR}_{\text{DC}} \rightarrow \text{P}}$, together with the smoothness of the dip, could originate from a “simple” crossover⁶ between two competing contributions. The two transfer function gain and phase shapes around 2 kHz, in contrast, clearly point to a crossover between contributions having an incidental phase difference of 180° , in both P and Q. Such a gain collapse will henceforth be referred to as *notch*. Just above 3 kHz, a notch-like structure occurs in the experimental Q quadrature only. The respective phase drops steeply in contrast to the notches at 2 kHz.

4.4.2. Coupling mechanism

It is impossible to explain the complexity of the two measured transfer functions by the noise sidebands around the carrier only (see Section 2.3). We need to look for light fields that exhibit a significantly different phase evolution from the carrier sidebands.

One possibility are the amplitude modulation sidebands, appearing around the control sidebands as a consequence of laser amplitude variations. Figure 4.8 displays the beam configuration of the light entering the dual-recycled detector, with LAN. Only the first-generation (at $f_{\text{AN}\pm}$), and Michelson phase-modulation sidebands (at $f_{\text{M}\pm}$) around the carrier (at 0), and the second-generation amplitude-noise sidebands around the Michelson control sidebands (at $f_{\text{M}\pm, \text{AN}\pm}$) are considered. In the following, all sidebands appearing due to amplitude noise will be denoted as *AN sidebands*. As the resonance condition for the control sidebands is so different from the carrier, the respective AN sidebands will evolve differently in amplitude and phase.

⁵Please note that $\text{TF}_{\text{PDPR}_{\text{DC}} \rightarrow \text{P}}$ denotes the transfer of LAN, in general, to the P quadrature of $h(t)$. PDPR_{DC} in the index is (only) used for the correct reference to the measurement shown in Figure 4.7. Same holds for the transfer of LAN to the Q quadrature.

⁶The term “simple” distinguishes this case of crossovers between competing contributions, without any particular phase relation at the crossover frequency, from others, having a phase difference of 180° .

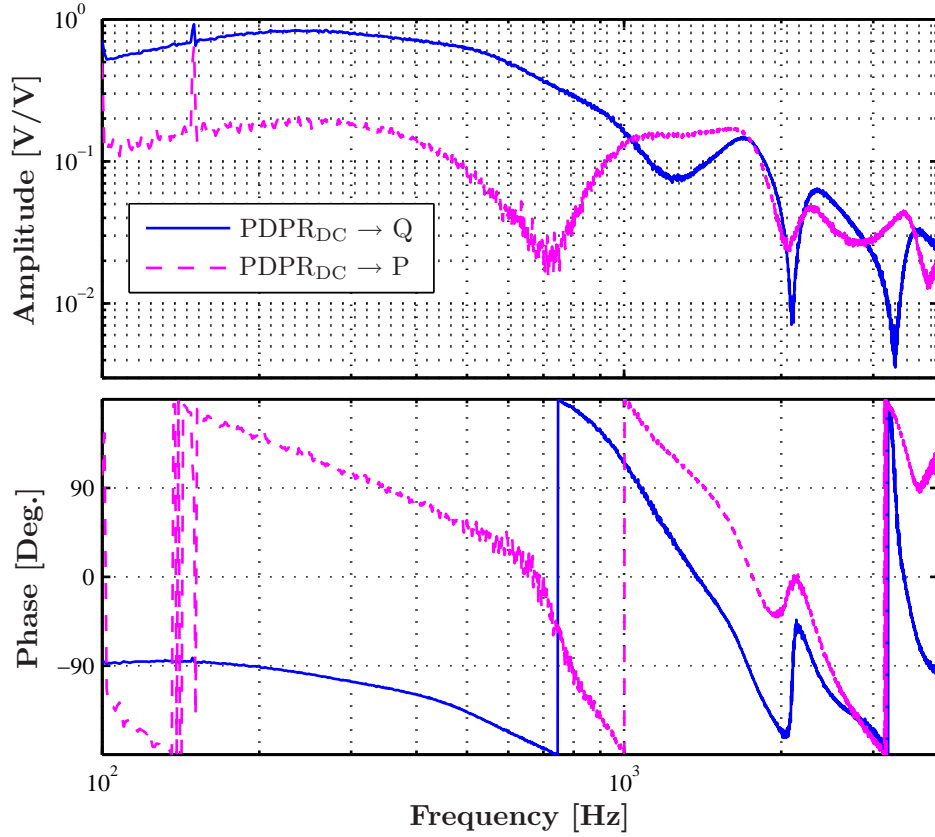


Figure 4.7.: Transfer function of laser amplitude noise to the HP output in P and Q, for a detector detuned by ~ 1 kHz. The LAN was measured with the DC output of PDPR (see Figure 3.1). The transfer function gain is contained in the upper figure, the phase in the lower. The combination of gains and phases indicate a notch at ~ 2 kHz, and a crossover of competing contributions at 700 Hz in $\text{TF}_{\text{PDPR}_{\text{DC}} \rightarrow \text{P}}$.

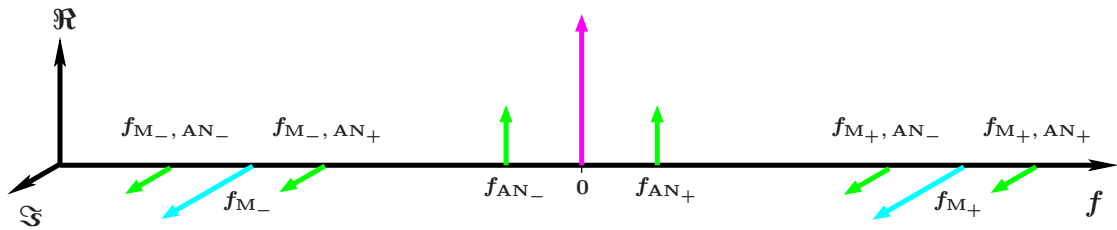


Figure 4.8.: Change of light beam composition due to laser amplitude noise. The noise creates two amplitude-modulation sidebands around each primarily existing light field, i.e., around the carrier (0), and the upper (M_+) and lower (M_-) control sidebands. The lower and upper amplitude-noise sidebands are marked by the indices AN_- and AN_+ , respectively.

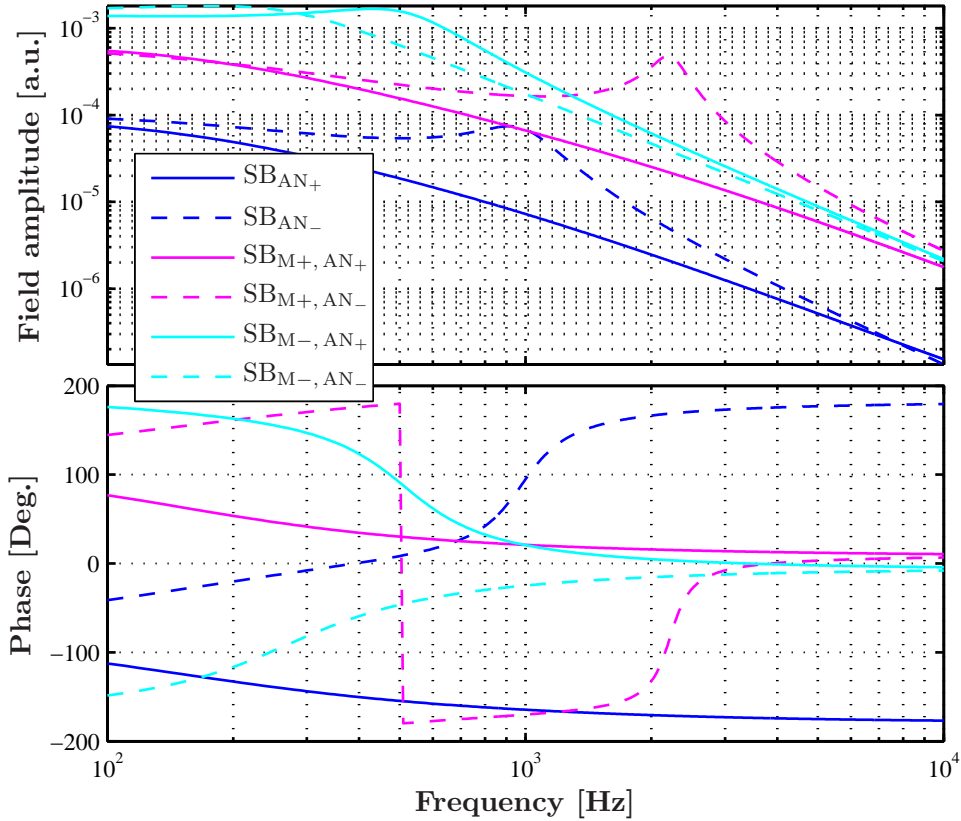


Figure 4.9.: Amplitude (upper graph) and phase (lower graph) of the AN sidebands appearing behind **MSR**, for a Michelson with an offset from dark fringe of 5 pm, and differential losses in the arms of 300 ppm. The upper and lower sidebands (SB) are distinguished by solid and dashed lines, respectively. The SB indices agree with those used for the respective frequencies in Figure 4.8.

The upper and lower pictures of Figure 4.9 illustrate the AN sidebands' amplitudes and phases, respectively, appearing behind **MSR**. As expected for a positive detector tuning of ~ 1 kHz (see Figure 2.4), SB_{AN-} is resonant inside the signal-recycling cavity being ~ 1 kHz off from the carrier, and the resonances for the AN sidebands around the Michelson sidebands differ extremely from each other. Both $SB_{M-, AN+}$ and $SB_{M-, AN-}$ have resonance peaks close to each other⁷. The lower AN sideband around SB_{M+} gets resonant inside the signal-recycling cavity for a frequency offset of ~ -2 kHz from f_{M+} .

With the overall three sideband resonances, a transfer-function shape as shown in Figure 4.7 is, in principle, imaginable. To yield the notches around 2 kHz, however, both

⁷Please remember the Michelson sidebands not being exactly resonant inside the power-recycling cavity. Besides, the resonance condition inside each cavity influence the resonance frequency of each other.

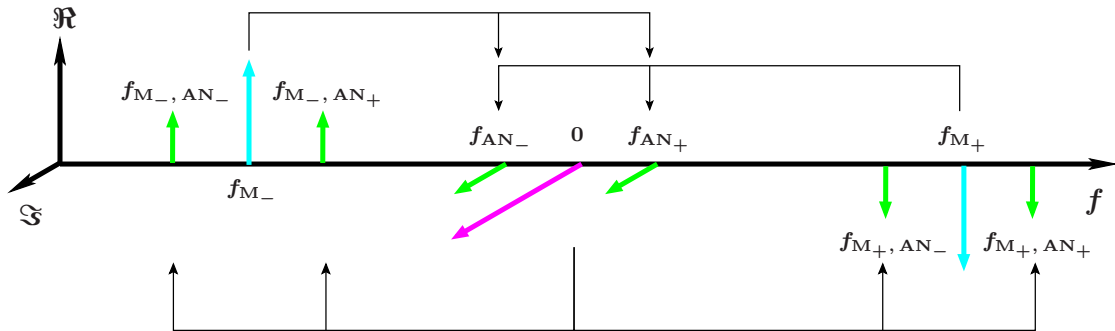


Figure 4.10.: Sidebands of Figure 4.8, appearing at the south port of a plain Michelson interferometer, having a small offset from the dark fringe. Please compare with the upper phasor picture of the lower right quadrant of Figure 1.15. The phasors projected onto each other for the respective error-signal are connected with the thin black arrows on the top and the bottom: the DC carrier beats with all four AN sidebands around the control sidebands, and each control sideband beats with the two AN sidebands around the carrier.

the phase difference and the amplitudes of the resulting error-signal contributions need to match.

In a Michelson interferometer there exist, in principle, two possible coupling mechanisms for LAN. One coupling mechanism acts through the offset from dark fringe, the other comprises asymmetries regarding the amplitudes of the interfering light fields coming from the two Michelson arms⁸. That the beats differ in phase and amplitude becomes plausible with the respective phasor pictures. Figure 4.10 shows the phasors of Figure 4.8, appearing in transmission of a simple Michelson interferometer, slightly off-set from perfect dark fringe. The chosen phasor pointings refer to the upper phasor picture of the lower quadrant of Figure 1.15. The relevant beats are connected via the thin black arrows on the top and the bottom of Figure 4.10. The beats of the DC carrier add up to the beats of the control sidebands with the same quadrature.

With the same phasors impinging on a plain Michelson operated at a perfect dark fringe, but with asymmetric losses in the two arms, the phasors look very different at the south port. The situation of larger losses in one arm is displayed in Figure 4.11. As all phasors from the north are longer, the carrier is real and negative, whereas the lower and upper control sidebands are rotated clockwise and anti-clockwise, respectively (i.e., they both get a negative imaginary component). The respective AN sidebands behave the same. Due to the symmetry of the sidebands' rotation, the phasors still represent a perfect phase modulation considering the Michelson (de-)modulation frequency.

⁸Possible sources for the latter are asymmetric losses or mode mismatch (the thermal lens, for example, only influences the light in the east arm).

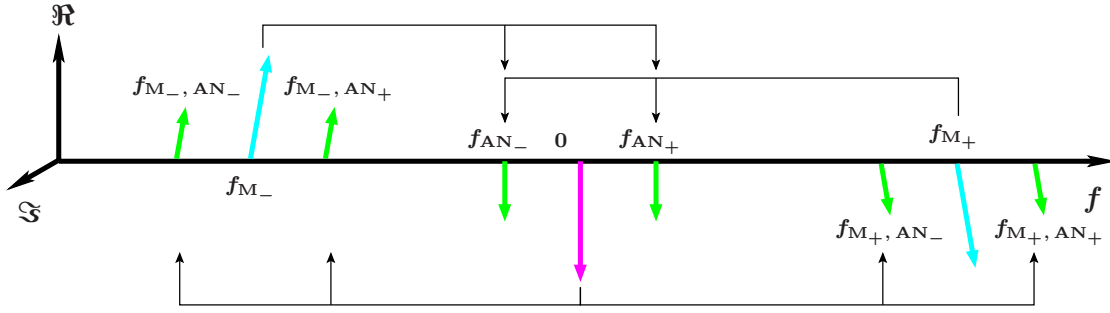


Figure 4.11.: Sidebands of Figure 4.8, appearing at the south port of a plain Michelson interferometer, operated at perfect dark fringe, but having asymmetric losses in the two arms. The phasor rotations of the outer sidebands are the consequence of larger losses in the east arm, applied to the phasors of the upper phasor picture of the lower right quadrant of Figure 1.15. The thin black arrows again connect the phasors that are projected onto each other for the respective error-signal.

4.4.3. FINESSE results for the amplitude-noise transfer function

As the appearance of a notch not only depends very delicately on the phase and amplitude relations of the competing carrier and control-sideband contributions, but also on the considered demodulation phase of the error-signal, it is quite challenging to find the right amount of dark fringe offset and asymmetric loss by observing the complete transfer function. It is rather favorable to be able to compare the phase and gains of the different transfer-function contributions. This allows for a targeted adjustment of the phase and gain of the complete transfer function by altering the losses and dark fringe offset. With parameters yielding promising properties, the transfer function can be investigated under diverse demodulation phases.

To get an idea of the carrier and control sideband beat contributions to the transfer function for each mechanism separately, Figure 4.12 shows the gains and phases of the carrier and control sideband beats, referring to the control sidebands as a cosine (P) and sine (Q) phase modulation (before entering the dual-recycled detector). The beats were calculated with MATLAB, using the light fields' amplitudes and phases of the TEM₀₀ modes at **MSR**, provided by FINESSE. Figure 4.12 is organised as follows: the left and right columns display the amplitudes and phases, respectively, whereas the three rows represent different detector situations. The middle assumes a perfect dark fringe and equal losses in both Michelson arms, though accounting for mode-mismatch. The upper row includes an increased loss in the east Michelson arm of 300 ppm, the lower a differential end mirrors' offset from dark fringe of $\pm 5 \mu\text{m}$. The graphs are labeled correspondingly. In each graph, P and Q are distinguished by solid and dashed lines, respectively. The legends are valid for all six graphs. The (dark) blue lines indicate the four beats of the carrier (see lower arrows in Figure 4.10 and 4.11), and the magenta lines the sum of all control sideband beats (see upper arrows in Figure 4.10 and 4.11). In the middle row, the sideband beats are, in fact, smaller by 10 orders of magnitude. For the

sake of visibility, however, the respective amplitudes are scaled up, and they are displayed in cyan to make the difference to the magenta curves obvious. In general, the amplitudes have arbitrary units, but the relative values agree to enable a comparison between the three different cases.

The upper two situations are noticeably similar, particularly the amplitude and phase shapes of P_{car} and Q_{car} . With a perfect dark fringe tuning and same loss in the two Michelson arms, there is still the asymmetry due to mode-mismatch of the interfering beams that can cause a small amount of carrier to appear at the south port. As the thermal lens applies to the east arm only, more power is transferred from TEM_{00} to higher order modes, yielding the same carrier orientation in the south as the exaggerated east arm losses in the first row (compare with Figure 4.11).

The amplitude peaks and dips appearing in P_{car} and Q_{car} become plausible with Figure 4.9, particularly considering the carrier beats with $\text{SB}_{\text{M}_-, \text{AN}_+}$ and $\text{SB}_{\text{M}_+, \text{AN}_-}$.

The AN sidebands around the carrier evolve differently in the two cases, and consequently, so do the control-sideband beats. In a perfectly symmetric, dark Michelson interferometer, the power-recycled Michelson is a perfect mirror, especially for the AN sidebands being non-resonant. Thus, the amplitude is enhanced only by the signal-recycling cavity and falls off towards 100 Hz. So do the respective beats. If the losses in the east are further increased, the Michelson couples the power-recycling and signal-recycling cavity, and the power-recycling cavity resonance becomes visible.

To construct a notch in the sum of these transfer functions, we need a phase difference of 180° between carrier and control sideband beats. In P, two frequencies come into question, close above 1 kHz and again close above 2 kHz, whereas in Q the phase dispersion of Q_{car} supports a notch only slightly above 2 kHz. The amplitudes are, however, too different to really yield notches.

The amplitude and phase characteristics look very different in the lowest row. However, the peaks of P/Q_{car} clearly exceed both P_{M} and Q_{M} , like with asymmetric losses. The only phase difference of 180° appears in the Q contributions around 6 kHz.

With the considerations made above, a notch at 2 kHz seems impossible with the current virtual detector configuration: both mechanisms yield a much stronger P/Q_{car} transfer function compared to the P/Q_{M} transfer function. Still, the notch just above 3 kHz is worth further examination. A coarse investigation into the parameter plane of differential dark fringe-offset/asymmetric losses yields notches for higher losses in the east arm by roughly 300 ppm, and for differential offsets of the end mirrors between ± 5 pm and ± 8 pm. Best results are obtained with ± 5 pm. According to the simulational results about the Michelson error-signal zero crossing offset from perfect dark fringe for various detector tunings, shown in Figure 3.25 in Section 3.5.2, this is the expected dark fringe offset for a detector detuning of 1 kHz.

Figure 4.13 displays the simulated transfer functions of the LAN to h , for a detector configuration of 1 kHz detuning, ± 5 pm dark fringe offset, and 300 ppm larger losses in the east Michelson arm. The shown demodulation phases vary in steps of 15° between 90° and 180° . $\Phi_{\text{Q}} = 90^\circ$ is the demodulation phase corresponding to the control sidebands of

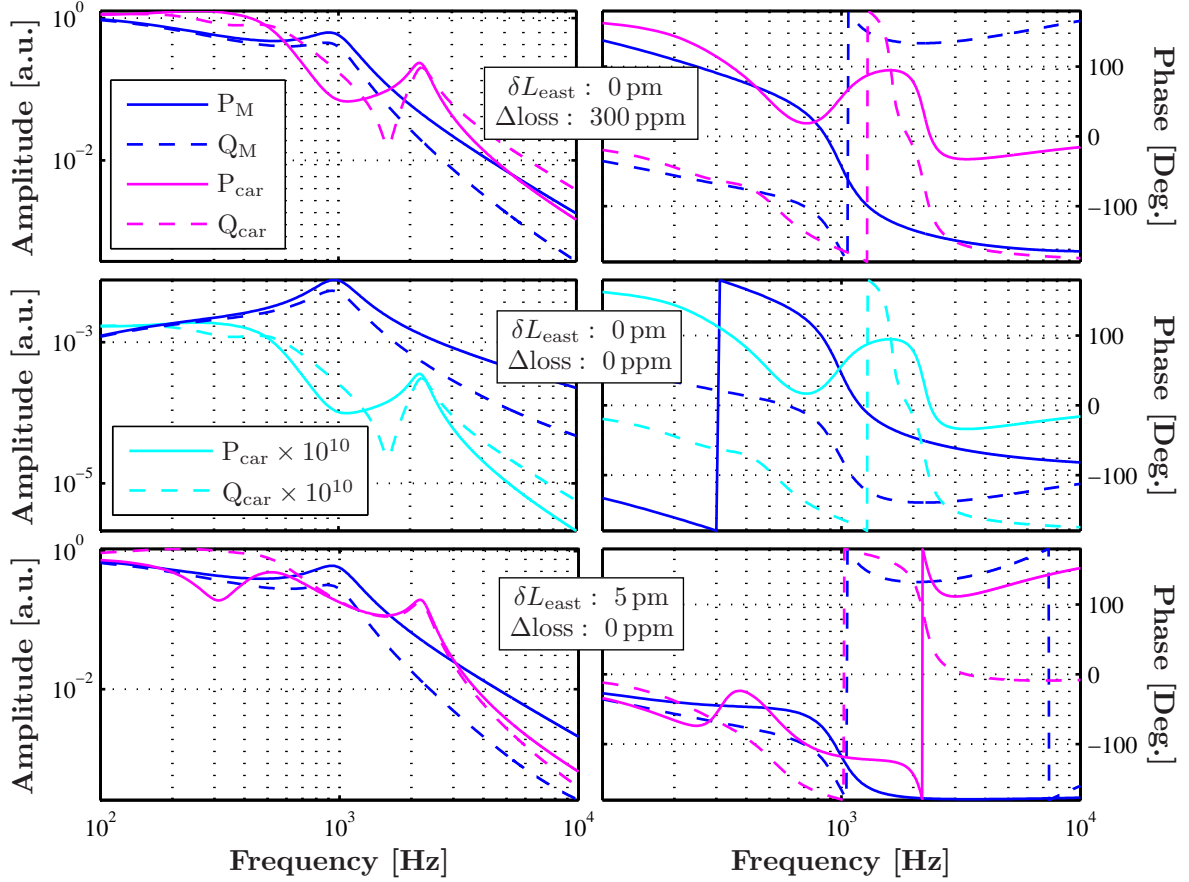


Figure 4.12.: Amplitudes (right column) and phases (left column) of the carrier and control sideband beats. The beats refer to an initial cosine (P) and sine (Q) Schnupp modulation of the carrier. From top to bottom, the simulation assumes a perfect dark fringe with 300 ppm more loss in the east than in the north Michelson arm, a perfect dark fringe and equal losses, and a differential end mirrors' offset from dark fringe of ± 5 pm with equal losses. (All cases account for mode-mismatch.) The legends apply for all six subplots: whereas the (dark) blue lines represent the beats of the carrier, the control-sideband-beat curves are magenta. Those in the middle row are distinguished by the cyan colour, because they are scaled up by 10 orders of magnitude. Beside of this scaling, the amplitudes of the three cases can be related to each other.

the simulation being in the Q quadrature. The graphs outside the shown demodulation phase interval do not exhibit any notch-like structure (except for those, again, between 270° and 360° , of course).

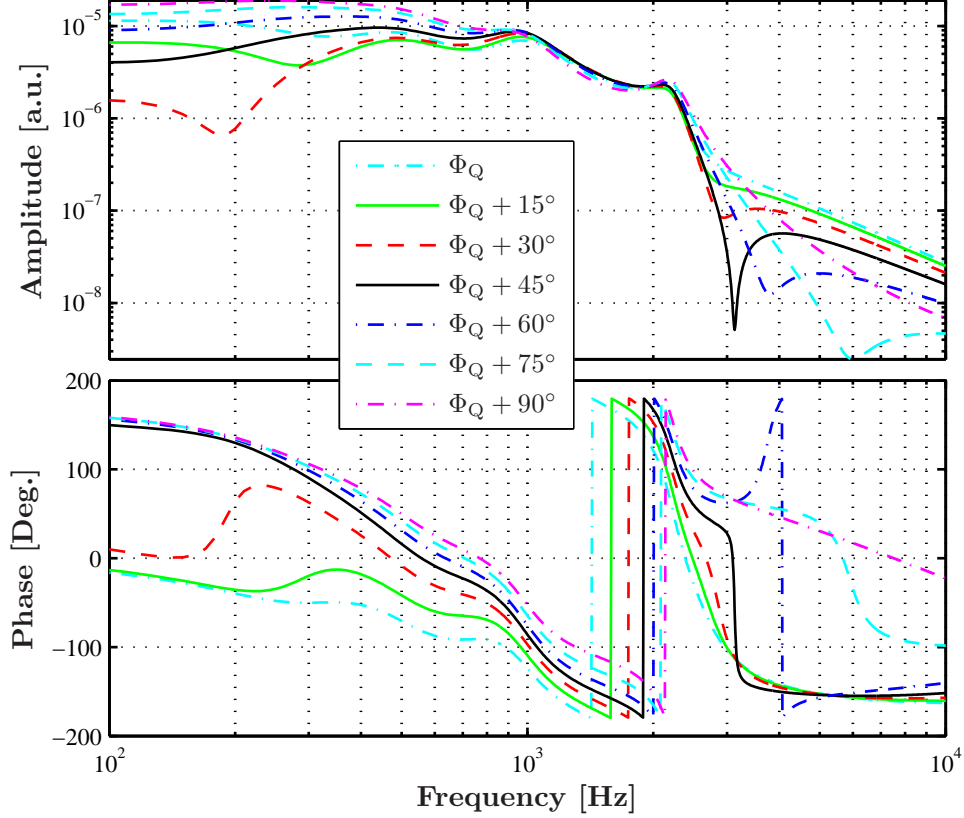


Figure 4.13.: FINESSE simulation of the transfer function of LAN to h . The detector is tuned to 1 kHz, has 300 ppm larger losses in the east than in the north Michelson arm, and a differential end mirrors' offset from dark fringe of 5 pm. Shown are the amplitudes (upper graph) and phases (lower graph) for 7 demodulation phases, in an interval of 90° , framing the curve with $\Phi_Q + 45^\circ$, exhibiting the clearest notch. Φ_Q is the demodulation phase corresponding to the control sidebands being in the Q quadrature.

Comparing the simulated curves with the measurement in Figure 4.7, the amplitude and even the phase evolution for $\Phi_Q + 45^\circ$ agrees qualitatively around the sharp notch above 3 kHz with $\text{TF}_{\text{PDPR}_{\text{DC}} \rightarrow \text{Q}}$. However, the simulation seems to principally miss one effect at 2 kHz that might also influence the amplitudes and phases around. Besides, the dip at 700 Hz is for all demodulation phases much smaller than that of $\text{TF}_{\text{PDPR}_{\text{DC}} \rightarrow \text{P}}$ in Figure 4.7. Instead, for $\Phi_Q + 15^\circ$ and $\Phi_Q + 30^\circ$, some notch-like structures show up around 300 Hz and 200 Hz, respectively.

Similar structures are obtained in the experiment using different demodulation phases. Figure 4.14 shows some transfer functions of the same measurement exhibited in Fig-

ure 4.7, with different demodulation phases applied and only for frequencies below 1 kHz. The demodulation phase offsets from the one used at GEO 600 for Q, are noted as arguments of $\text{TF}_{\text{PDPR}_{\text{DC}} \rightarrow \text{Q}}$. For 10° and 15° , the phase shapes occurring at the amplitude dips are comparable to Φ_{Q} and $\Phi_{\text{Q}} + 15^\circ$ in Figure 4.13. The deepest dip and largest phase dispersion are yielded for 5° , corresponding best to the properties of the curve belonging to $\Phi_{\text{Q}} + 30^\circ$ in Figure 4.13.

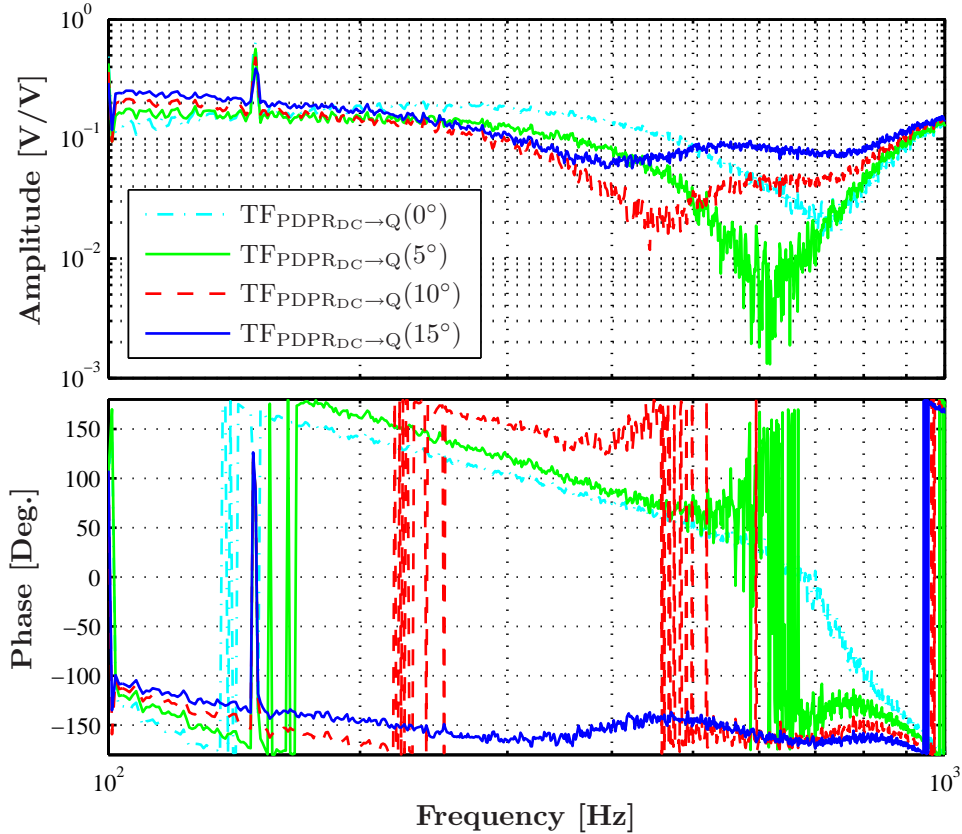


Figure 4.14.: Same measurement as shown in Figure 4.7, but with different demodulation phases. $\text{TF}_{\text{PDPR}_{\text{DC}} \rightarrow \text{Q}}(0^\circ)$ labels the same curves as $\text{PDPR}_{\text{DC}} \rightarrow \text{Q}$ in Figure 4.7. The phase in the argument of $\text{TF}_{\text{PDPR}_{\text{DC}} \rightarrow \text{Q}}$ indicates the applied demodulation phase with respect to the one used in the experiment for Q.

Despite the quantitative disagreements of the simulations to the measurement, the qualitative agreement shows the AN sidebands generated by the laser amplitude noise to be the main cause for the transfer functions obtained. Thus, considering which other noise source could exhibit similar noise-projection features, those come into question that lead to similar impinging light fields. Comparing Figure 1.5 with Figure 4.8, the sidebands appearing due to modulation index variations clearly suggest these as an alternative to LAN. (This suggestion was confirmed during GEO 600 commissioning.)

A better quantitative agreement between simulation and experiment could be aimed for by further investigations of the LAN transfer function by varying particular parameters that were not optimised yet.

- For the simulations so far, some global optical lengths were required. Determining the Schnupp, or the power-recycling and signal-recycling cavity length, for example, never required the exact position of the beamsplitter or of the far end mirrors. With the positions of notches being so delicately dependent on phase differences, the absolute Michelson armlengths gain importance.
- The nature of the losses appearing in the detector is unknown. Measurements of the interferometer mirrors' properties do not explain the losses getting obvious by the power-recycling performance. One of the considered options is a beam cut-off within the vacuum tubes. Up to now, the common losses were mainly inferred in the Michelson end mirrors, the asymmetric losses in the **BSAR**. If the beam cut-off happens between **MPR** and **BS**, and would correspondingly be accounted for in the simulation, the signal-recycling cavity could exhibit slightly different features for the control sidebands⁹, and for the AN sidebands of these.
- Although the notches measured in the two quadratures cannot be generated with the optical features accounted so far, the SB_{M_+, AN_-} resonating around 2 kHz make an association very likely. Thus, either some further optical effect occurs, or some non-optical feature interacts. As the measurement was done in-loop, using the Michelson error-signal in P as a differential feed-back for the end mirrors, an electronic disturbance of the measurement, for example, cannot be excluded. However, the open loop gain at 2 kHz is already very low (see Figure 3.4).

A different idea is a possible coupling of the LAN with the modulation index noise: the AN sidebands around the carrier have opposite directions in Figure 1.5 and Figure 4.8. If the coupling was in-phase, P_M and Q_M would further decrease with respect to P_{car} and Q_{car} (see Figure 4.12), for all frequencies. Assuming anti-phasing, though, the peaks appearing in P_M and Q_M could just be attenuated enough to yield a notch.

4.5. Conclusion

This section is devoted to the application of simulations to gain a better understanding of the GEO 600 experiment. Partly, this includes the adjustment or calibration of particular parameters of the simulation input file describing the optical system, in order to fit special, sensitive measurements. The main goal is, however, the prediction of other, measurable features without any further accommodation.

⁹As the signal-recycling cavity linewidth for the gravitational-wave signal-sidebands is adjustable by the bandwidth of the optical transfer function measured at GEO 600, the signal-recycling features should not change for the AN sidebands around the carrier.

The frequency dependency of the differential Michelson error-signal, demodulated at twice the modulation frequency ($2f$ signal), is used to determine common Michelson losses, the Schnupp length difference between the Michelson arms, and, very coarsely, the signal-recycling cavity length. The $2f$ signal turns out to be comparably insensitive to misalignments, and even less sensitive on the **MSR** tuning or reflectivity.

To facilitate the search for the common losses, and signal-recycling cavity and Schnupp lengths in a three-dimensional parameter space, the particular simulations are compared with the measurement via the least-square method. Due to the errors of the measurement, various parameter combinations are possible.

The range of possible solutions is narrowed by fitting the optical transfer function, i.e., the transfer from the Michelson end mirrors' movement to the differential output behind **MSR**, for a detector detuned by ~ 2 kHz. This allows determination of the **MSR** reflectivity, and the signal-recycling cavity length. Moreover, the transfer function enables the calibration not only of the simulational signal-recycling demodulation phase, but also of the demodulation phase of the Michelson error-signal.

With the signal-recycling cavity length gained from the transfer-function measurement, with an accuracy of ± 1 mm, the least-square fit results allow determination of the Schnupp length with at least the same accuracy, and the common losses with an error limited to ± 50 ppm. The **MSR** reflectivity could be determined by the optical transfer-function bandwidth to up to ~ 100 ppm accuracy.

Applying the experimentally used control-loop parameters to the improved FINESSE input script (using the signal-recycling demodulation phase calibration), any experimental signal-recycling cavity tuning can be predicted with a precision better than ~ 10 Hz (see Section 4.3.1). This is shown by comparing the measured optical transfer functions for several signal-recycling modulation frequencies and demodulation phases. With the Michelson demodulation phase calibrated for the detector being tuned to 2 kHz, the simulated transfer functions for other detunings agree simultaneously with each experimental quadrature with an accuracy better than 15% in the complete detector bandwidth of 5 kHz.

The presented transfer-function example shows that the accuracy is limited mainly due to the frequency region below 200 Hz, and due to “bumps” occurring in Q at particular, higher frequencies that depend on the exact detector tuning. The low-frequency deviation originates from inaccuracies accounting the Michelson control loop for this closed-loop transfer-function measurement. The measured bump occurs also in the simulation, but it is slightly higher in the simulation. The reason for the bump are beats of the DC carrier, appearing at the output port due to asymmetric losses in the Michelson arms, with AN sidebands generated around the control sidebands. In the frequency interval of [250 Hz, 2150 Hz] the accuracy of the transfer function prediction is better than 5%.

Another example of FINESSE simulations being able to explain and gain insights into experimental features is presented by investigating laser amplitude couplings into the differential Michelson error-signal. Based on the phasor picture, the diverse resonance characteristics of the noise sidebands appearing around both the carrier and the control sidebands could qualitatively be correlated with the shape of the noise transfer to the

output. Discovering the diverse AN sidebands as being responsible for the particular coupling, variations of the Michelson modulation index could be identified exhibiting similar coupling characteristics. The experimental sensitivity improvements, after successively reducing both the laser and the modulation index noise, confirm the considerations.

Quantitatively, the notch appearing in the experimental noise transfer function above 3 kHz is obtainable with the simulation. The agreement in the frequency region below 1 kHz can presumably be improved with a better adjustment of some remaining optical parameters, like for example the absolute Michelson arm-lengths. The notch around 2 kHz that appears in the experiment in both quadratures, however, does not seem to be achievable in the simulation with the assumptions made so far, although the AN sideband resonances very much offer themselves to be the reason for the notch. A correlation of the laser amplitude noise to another effect is necessary, generating the same sidebands but with different phases. One option is the modulation index noise, flipping the sign of either the AN sidebands around the carrier or around the control sidebands. This could be subject to further investigations. In addition, further measurements with different detector tunings and varying modulation index and laser amplitude noise levels could yield additional information on the correlations of the two, or even hint to a completely different effect causing the 2 kHz-notch, as for example electronic radio-frequency pick-up.

Appendix A.

Signal-recycling demodulation phase calibration

The signal-recycling demodulation phase calibration described in Section 3.6.2 exploits the non-linear relation of the signal-recycling error-signal zero crossing position and the demodulation phase. The susceptibility of the curve shape of Figure 3.30 to particular degrees of freedom of the detector, though, were not discussed. With the help of the phasor picture it gets plain that the curve shape depends mainly on two aspects: the amplitude of the lower control sideband, and the linewidth of the signal-recycling cavity for the signal-recycling sidebands.

Figure A.1 shows the signal-recycling error-signal vectors for three situations. The upper and middle pictures assume different signal-recycling cavity linewidths, and a very large, positive detuning such that only one control sideband contributes to the error-signal. The detector in the lowest picture exhibits the same signal-recycling cavity linewidth as the middle, but a smaller detuning such that both control sidebands need to be accounted for the error-signal.

Each of the red or magenta arrows represents the error-signal vector for one particular **MSR** position. The green dashed lines are two examples of demodulation phases, with an angle (or shift) of 20° between them. Relating this error-signal representation to the more commonly used error-signal amplitude curve, like for example in Figure 3.9, each **MSR** position on the horizontal axis of Figure 3.9 corresponds to one vector. The respective error-signal amplitude is given by this vector's component regarding the dashed green line representing the particular demodulation phase. (This is equivalent to projecting the vector onto this dashed line.) Thus, the error-signal vector perpendicular to the demodulation phase line marks the respective error-signal zero crossing.

The evaluated **MSR** positions in plots like Figure 3.9 are usually constantly spaced. In agreement, the error-signal vectors in Figure A.1 represent equally spaced **MSR** positions whose increments are the same for all three subfigures. Three of the error-signal vectors are magenta, and non-solid. The dashed-dotted vector agrees to the **MSR** position where the upper control sideband is resonant inside the signal-recycling cavity. For the other two magenta vectors, **MSR** is located at the edges of the respective Airy-function linewidth. The dashed and dotted vectors represent a positive and negative **MSR** detuning with

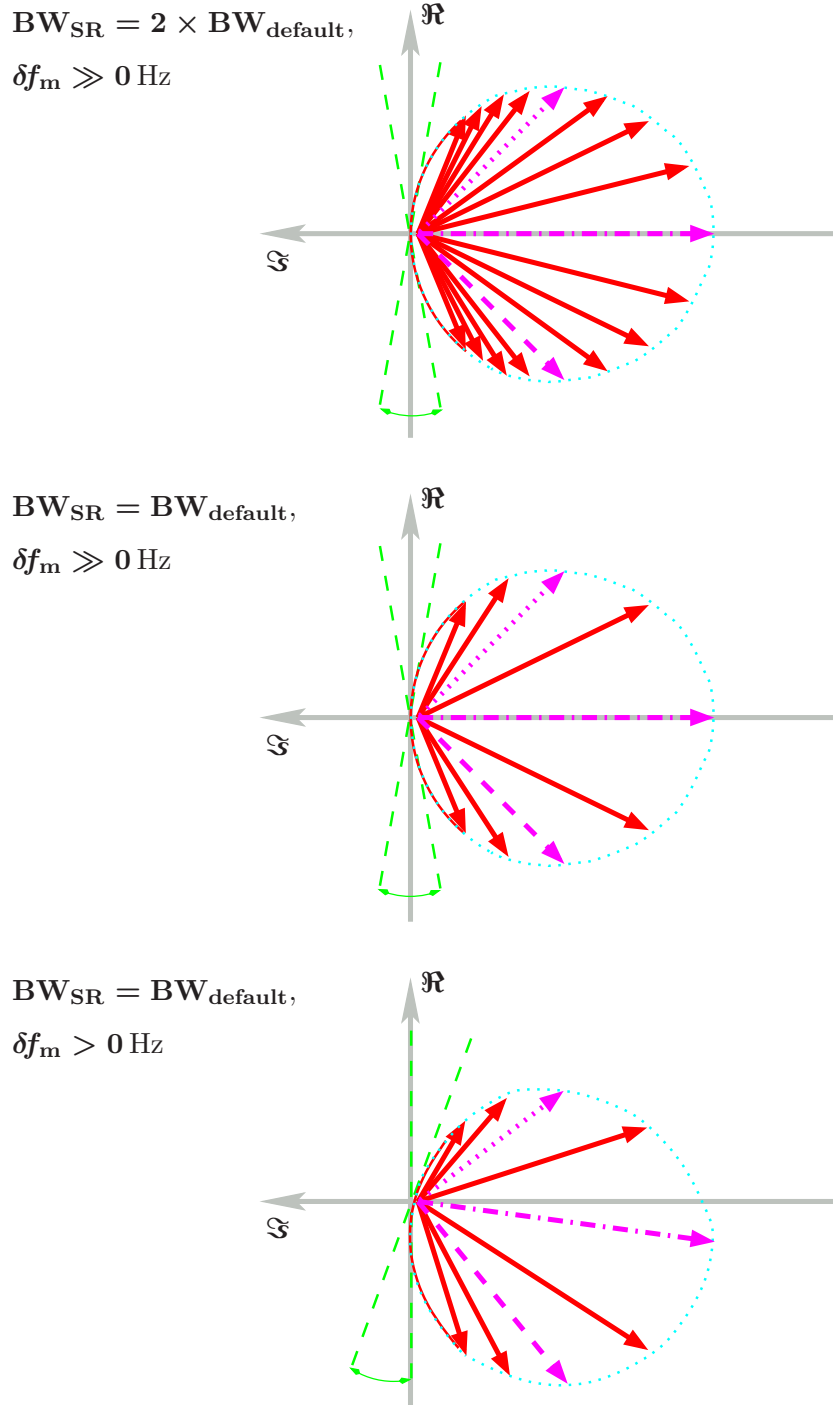


Figure A.1.: Signal-recycling error-signal vectors for three different detector configurations. The three configurations differ either in signal-recycling cavity linewidth for the control sideband, or in the cavity tuning. The situation is accordingly labeled. The dashed-dotted magenta vector represents the error-signal for the sideband resonating inside the signal-recycling cavity, the dotted and dashed vectors mark the Airy-function linewidth edges in negative and positive tuning direction, respectively. The dashed green lines are particular demodulation phases.

respect to the sideband resonance. A comparison with some examples of error-signal vector deductions, presented in Figure 3.14, may help for illustration.

In agreement with the phase dispersion associated with a resonance, the error-signal vector spacing gets narrower, the farther the **MSR** position from sideband resonance, i.e., the closer to the real axis. (These very narrow-spaced vectors are omitted for clarity. Instead, the corresponding vector end points are indicated by the red curve.) Comparing different cavity linewidths, the vector spacing gets narrower, the larger the linewidth. Accounting for the contribution of the lower control sideband, all real components of the error-signal vectors from the middle picture get negatively shifted (compare with Figure 3.14).

For all three cases a demodulation phase increase shifts the zero crossing position negatively, as the **MSR** tuning associated with the error-signal vectors increases clockwise. The amount of shift is determined by the number of vectors passed perpendicularly when rotating the line of demodulation phase. The zero crossing shifts are obviously non-linear to demodulation phase changes. In the upper two subfigures, the dashed-dotted vector sets a symmetry axis for the demodulation phases regarding this non-linear behaviour. This is similar for the lowest case. However, for positive demodulation phase shifts, the zero crossing shift is comparably steeper than for negative demodulation phase shifts¹.

The larger the linewidth of the signal-recycling cavity, the more vectors are perpendicularly passed when rotating the demodulation phase line by one particular amount. Thus, the zero crossing shifts, in general, more for larger cavity linewidths.

The demodulation phase calibration inaccuracy, associated with wrong assumptions on both the signal-recycling cavity linewidth, and the exact detector tuning, can be minimised using high detector tunings.

- For high signal-recycling cavity detunings from carrier resonance, the control sidebands can be assumed to be anti-resonant inside the power-recycled Michelson. With $R_{\text{prMI}} \approx 99.993\%$ compared to $R_{\text{MSR}} = 98.05\%$, the linewidth will hardly alter with different Schnupp lengths. R_{MSR} is determined via the bandwidth of the sensitivity curve of GEO 600 to an accuracy of ~ 100 ppm. Simulations show that a deviation of ± 4000 ppm is necessary to alter the result of the demodulation phase calibration by $\pm 1^\circ$.
- With Figure 3.23 (or 3.43) the impact of the lower control sideband on the demodulation phase calibration can well be estimated. Around a detuning of 2 kHz an uncertainty of the tuning of > 250 Hz is necessary to alter the demodulation phase by 1° . The corresponding signal-recycling cavity length difference exceeds even the large interval of ~ 30 mm investigated for the 2f signal (see Figure 4.3).

¹Please note that for very low tunings, the error-signal vector spacing in the fourth quadrant gets so narrow, and the vector's orientation is so close to the imaginary axis that the zero crossing vanishes completely, even for small demodulation phase shifts. This, and the other mentioned features get visible in Figure 3.34.

Appendix B.

Simulation scripts

B.1. FINESSE scripts

The commands in the FINESSE input script below work with FINESSE versions older than 0.99.

B.1.1. Most adequate FINESSE script for the current optical setup

```
#
#     GEO file for the time from May 05
#
#     M. Malec, 2005-05-31
#

l i1 1.7 0 nMU3in

mod eom3 $fPR 0.126433 2 pm 0 nMU3in nMU3_1 # PR control
mod eom4 $fSR 0.199417 2 pm 0 nMU3_1 nMU3_2 # Schnupp1 (SR control)
mod eom5 $fMI 0.1225 2 pm 0 nMU3_2 nMU3_3 # Schnupp2 (MI control)

lens lpr 1.8 nMU3_3 nMU3_4
# some rather arbitrary thermal lense for the isolators and the EOMs:
lens therm 5.2 nMU3_4 nMU3_5
isol d2 120 nMU3_5 nMU3out # Faraday Isolator

# corrected length with respect to OptoCad (Roland Schilling)
s smcpr3 4.391 nMU3out nBDIPR1
bs* BDIPR 50 30 0 45 nBDIPR1 nBDIPR2 dump dump

s smcpr4 0.11 nBDIPR2 nMPRo
```

Appendix B. Simulation scripts

```

##-----
## main interferometer ##
##
## Mirror specifications for the _final_ optics are used.
#
## first (curved) surface of MPR
m    mPRo 0 1 0 nMPRo nMPri
attr mPRo Rc -1.85842517051051 # Rc as used in OptoCad (layout_1.41.ocd)
s    smpr 0.075 1.44963 nMPri nPRo
# second (inner) surface of MPR
m    MPR 0.99905 0.0009 0. nPRo nPRI          # T= 900 ppm PR
#m   MPR 0.9865 0.0135 0. nPRo nPRI          # old MPR
s    swest 1.1463 nPRI nBSwest                # new length with T_PR=900 ppm
#s   swest 1.1452 nPRI nBSwest                # old MPR

## BS
##
##
##
##
##          nBSnorth      ,'-
##          |             +   '
##          |             ,   :
##          |             +1  +
##          |             ,:._ i2 ,
##          |             + \ '-. +          nBSeast
##          |             , i3\ , '-----
##          |             +   \ +
##          |             , i4.'
##          |             '-. .
##          |             '- , |nBSsouth
##          |             -   |
##          |             |
##          |             |

bs   BS 0.4859975 0.5139975 0.0 42.834 nBSwest nBSnorth nBSi1 nBSi3
s    sBS1a 0.041 1.44963 nBSi1 nBSi1b
# here thermal lense of beam splitter (Roland: f about 1000m for 10kW at BS)
lens bst 8.5k nBSi1b nBSi1c
#lens bst 20k nBSi1b nBSi1c          # for old MPR
s    sBS1 0.051 1.44963 nBSi1c nBSi2
s    sBS2 0.091 1.44963 nBSi3 nBSi4
bs   BS2 150u 0.99982 0 -27.9694 nBSi2 dump nBSeast nBSAR
bs   BS3 150u 0.99982 0 -27.9694 nBSi4 dump nBSsouth dump

## north arm

```

```
s snorth1 598.5682 nBSnorth nMFN1
bs* MFN 150 10 0.0 0.0 nMFN1 nMFN2 dump dump
attr MFN Rc 666
```

```
s snorth2 597.0241 nMFN2 nMCN1
m* MCN 640 10 -0.0 nMCN1 dump
attr MCN Rc 636
```

```
## east arm
```

```
s seast1 598.4497 nBSeast nMFE1
bs* MFE 150 10 0.0 0.0 nMFE1 nMFE2 dump dump
attr MFE Rcx 665          # 71 W heater power
attr MFE Rcy 662          # 71 W heater power
```

```
s seast2 597.0630 nMFE2 nMCE1
m* MCE 640 10 0.0 nMCE1 dump
attr MCE Rc 622
```

```
## south arm
```

```
s ssouth 1.109 nBSsouth nMSRi
```

```
m MSR 0.9814 0.01855 0 nMSRi nMSRo      # tuned
```

```
##-----
```

```
## commands
```

```
maxtem 2
time
phase 3
# PR cavity (north arm)
cav prc1 MPR nPRi MCN nMCN1
# PR cavity (east arm)
cav prc2 MPR nPRi MCE nMCE1
# SR cavity (north arm)
cav src1 MSR nMSRi MCN nMCN1
# SR cavity (east arm)
cav src2 MSR nMSRi MCE nMCE1
```

```
##-----
```

```
pause
```

```
var fSR 9017375
var fMI 14.904927M # used for lock acquisition and tuning
var fPR 37.16M
var phip 110
var phiq 200

/*
# determine resonant control sideband frequency for the tuned detector
ad SRSB $fSR nMSRo
ad SRSB- -$fSR nMSRo
xaxis eom4 f lin 9017000 9017500 100
xparam SRSB f 1 0
xparam SRSB- f -1 0
*/

/*
# determine best demodulation phase for the tuned detector
fsig sig1 MSR phi 1 0
pd2 SREP $fSR 0 1 max nBSAR
xaxis SREP phase1 lin 0 180 180
*/

#/*
# SR-EP
pd1 SREP1 $fSR $phip nBSAR
pd1 SREP2 $fSR $phiq nBSAR
x2axis MSR phi lin -2.874 10.061 9000
xaxis eom4 f lin 9013375 9017375 160
xparam SREP1 f 1 0
xparam SREP2 f 1 0

gnuterm no
#*/

/*
# MI-EP
pd1 MIEP1 $fMI 0 nMSRo
pd1 MIEP2 $fMI 90 nMSRo
xaxis MSR phi lin 0 5.7489 4000
x2axis MCE phi lin -3.4m 3.4m 100
x2param MCN phi -1 0

gnuterm no
*/
```


B.1.2. FINESSE script used before May 2005

```

#
#   GEO file containing the optical setup assumptions made up to
#   May 2005
#
#   M. Malec, 2005-04-12
#

l i1 1.75 0 nMU3in

mod eom3 $fPR 0.323002 2 pm 0 nMU3in nMU3_1 # PR control
mod eom4 $fSR 0.50391 2 pm 0 nMU3_1 nMU3_2 # Schnupp1 (SR control)
mod eom5 $fMI 0.27758 2 pm 0 nMU3_2 nMU3_3 # Schnupp2 (MI control)

lens lpr 1.8 nMU3_3 nMU3_4
# some rather arbitrary thermal lense for the isolators and the EOMs:
lens therm 5.2 nMU3_4 nMU3_5
isol d2 120 nMU3_5 nMU3out # Faraday Isolator

# corrected length with respect to OptoCad (Roland Schilling)
s smcpr3 4.391 nMU3out nBDIPR1
bs* BDIPR 50 30 0 45 nBDIPR1 nBDIPR2 dump dump

s smcpr4 0.11 nBDIPR2 nMPRo

##-----
## main interferometer ##
##
## Mirror specifications for the _final_ optics are used.
#
## first (curved) surface of MPR
m mPRo 0 1 0 nMPRo nMPRi
attr mPRo Rc -1.85842517051051 # Rc as used in OptoCad (layout_1.41.ocd)
s smpr 0.075 1.44963 nMPRi nPRo
# second (inner) surface of MPR
m MPR 0.9865 0.0135 0. nPRo nPRi # T= 1.35%
s swest 1.145 nPRi nBSwest

## BS

```

Appendix B. Simulation scripts

```

##
##
##          nBSnorth      ,'-
##          |      +      '
##          |      ,      ':'
##          |      +i1      +
##          |      ,:._ i2 ,
##          |      + \ '-. +      nBSeast
##          |      , i3\      , -----
##          |      +      \ +
##          |      , i4.'
##          |      '._ ..
##          |      '._ , |nBSsouth
##          |      - |
##          |      |
##          |      |

bs   BS 0.4859975 0.5139975 0.0 42.834 nBSwest nBSnorth nBSi1 nBSi3
s    sBS1a 0.041 1.44963 nBSi1 nBSi1b
# here thermal lense of beam splitter (Roland: f about 1000m for 10kW at BS)
lens bst 20k nBSi1b nBSi1c
s    sBS1 0.051 1.44963 nBSi1c nBSi2
s    sBS2 0.091 1.44963 nBSi3 nBSi4
bs   BS2 50u 0.99992 0 -27.9694 nBSi2 dump nBSeast nBSAR
bs   BS3 50u 0.99992 0 -27.9694 nBSi4 dump nBSsouth dump

## north arm
s snorth1 598.5682 nBSnorth nMFN1
bs* MFN 50 10 0.0 0.0 nMFN1 nMFN2 dump dump
attr MFN Rc 666

s snorth2 597.0158 nMFN2 nMCN1
m* MCN 50 10 -0.0 nMCN1 dump
attr MCN Rc 636

## east arm
s seast1 598.4497 nBSeast nMFE1
bs* MFE 50 10 0.0 0.0 nMFE1 nMFE2 dump dump
attr MFE Rcx 665      # 71 W heater power
attr MFE Rcy 662      # 71 W heater power

s seast2 597.0713 nMFE2 nMCE1
m* MCE 50 10 0.0 nMCE1 dump

```

```

attr MCE Rc 622

## south arm
s ssouth 1.115 nBSsouth nMSRi

m MSR 0.979 0.02095 0 nMSRi nMSRo      # tuned

##-----
## commands
maxtem 2
time
phase 3
# PR cavity (north arm)
cav prc1 MPR nPRi MCN nMCN1
# PR cavity (east arm)
cav prc2 MPR nPRi MCE nMCE1
# SR cavity (north arm)
cav src1 MSR nMSRi MCN nMCN1
# SR cavity (east arm)
cav src2 MSR nMSRi MCE nMCE1

##-----

pause

var fSR 9017334
var fMI 14.904915M
var fPR 37.16M

var phip 88      # maximal SR-EP-gain
var phiq 178    # minimal SR-EP-gain

/*
# determine best demodulation phase for the tuned detector
fsig sig1 MSR 1 0
pd2 SREP $fSR 0 1 max nBSAR
xaxis SREP phase1 lin 0 180 180
*/

#/*
# SR-EP
pd1 SREP1 $fSR $hip nBSAR
pd1 SREP2 $fSR $hiq nBSAR
x2axis MSR phi lin -2.874 10.061 9000

```

```
xaxis eom4 f lin 9012334 9017334 500
xparam SREP1 f 1 0
xparam SREP2 f 1 0
gnuterm no
#*/

/*
# MI-EP
pd1 MIEP1 $fMI 0 nMSRo
pd1 MIEP2 $fMI 90 nMSRo
xaxis MSR phi lin 0 7.186 5000
x2axis MCE phi lin -3.4m 3.4m 100
x2param MCN phi -1 0

gnuterm no
*/
```

B.2. MATLAB scripts

B.2.1. MATLAB script for the estimation of signal-recycling error signal susceptibility to various degrees of freedom

Contents

- Separated error signal evaluation for each frequency
- Complex error signal
- Vector of demodulation phases
- Relevant zero crossing
- Gain
- Capture ranges
- Evaluation of the results

```
% Determine the range of demodulation phases for which the signal recycling
% error signal deviates minimally or uncritically.
```

```
clear all
```

```
% perfect detector
x=load('downtng_SR.out');
[M,N]=size(x);
```

```
steps=9001;      % MSR tuning step number
tun=M/steps;    % number of SB frequencies

% SB frequency
f=reshape(x(:,1),steps,tun);
f=f(1,:);

% MSR position in degrees
pos=reshape(x(:,2),steps,tun);
pos=pos(:,1);

% real and imaginary part of the error signal phasor
pd_p1=reshape(x(:,3),steps,tun);
pd_p2=reshape(x(:,4),steps,tun);

% MSR misaligned by 1 urad
x=load('misal_MSR.out');
[M,N]=size(x);
steps=9001;      % MSR tuning step number
tun=M/steps;    % number of SB frequencies

% SB frequency
f2=reshape(x(:,1),steps,tun);
f2=f2(1,:);

% real and imaginary part of the error signal phasor
pd_msr1=reshape(x(:,3),steps,tun);
pd_msr2=reshape(x(:,4),steps,tun);

% MCE and MCN each misaligned by 100 nrad
x=load('misal_MID.out');
[M,N]=size(x);
steps=9001;      % MSR tuning step number
tun=M/steps;    % number of SB frequencies

% real and imaginary part of the error signal phasor
pd_mcx1=reshape(x(:,3),steps,tun);
pd_mcx2=reshape(x(:,4),steps,tun);

% MCE and MCN off-set by 0.1 nm
x=load('MIDoff.out');
[M,N]=size(x);
```

```
steps=9001;      % MSR tuning step number
tun=M/steps;    % number of SB frequencies

% real and imaginary part of the error signal phasor
pd_off1=reshape(x(:,3),steps,tun);
pd_off2=reshape(x(:,4),steps,tun);

% MCE and MCN off-set to the other direction
x=load('MIDoff2.out');
[M,N]=size(x);
steps=9001;    % MSR tuning step number
tun=M/steps;  % number of SB frequencies

% real and imaginary part of the error signal phasor
pd_off21=reshape(x(:,3),steps,tun);
pd_off22=reshape(x(:,4),steps,tun);

% PRC off-set by 10 pm
x=load('PRCoff.out');
[M,N]=size(x);
steps=9001;    % MSR tuning step number
tun=M/steps;  % number of SB frequencies

% real and imaginary part of the error signal phasor
pd_prc1=reshape(x(:,3),steps,tun);
pd_prc2=reshape(x(:,4),steps,tun);

% PRC misaligned by 100 nrad
x=load('misal_PRC.out');
[M,N]=size(x);
steps=9001;    % MSR tuning step number
tun=M/steps;  % number of SB frequencies

% real and imaginary part of the error signal phasor
pd_prcoff1=reshape(x(:,3),steps,tun);
pd_prcoff2=reshape(x(:,4),steps,tun);

% find the frequency lines in the large file corresponding to the ones
% evaluated in the other files
for k=1:length(f2)
    u(k)=find(f==f2(k));
end
```

Separated error signal evaluation for each frequency

```
for p=1:tun
    h=u(p);
```

Complex error signal

```
detuned(:,1)=complex(pd_p1(:,h),pd_p2(:,h));
detuned(:,2)=complex(pd_msr1(:,p),pd_msr2(:,p));
detuned(:,3)=complex(pd_mcx1(:,p),pd_mcx2(:,p));
detuned(:,4)=complex(pd_off1(:,p),pd_off2(:,p));
detuned(:,5)=complex(pd_off21(:,p),pd_off22(:,p));
detuned(:,6)=complex(pd_prc1(:,p),pd_prc2(:,p));
detuned(:,7)=complex(pd_prcoff1(:,p),pd_prcoff2(:,p));
```

Vector of demodulation phases

Complex vector of demodulation phase that gives zero crossing close to SB resonance (is thus perpendicular to maximal error signal phasor)

```
s=find(abs(detuned(2001:end,1))==max(abs(detuned(2001:end,1))))+2000;
demph_c = detuned(s) * exp(-i * pi /2)./abs(detuned(s));
% in degrees
demph_d=round(angle(demph_c)/pi*180);
% maximally necessary demodulation phases
demph=demph_d-90:1:demph_d+89;
```

Relevant zero crossing

index of MSR position associated with the SB frequency

```
tuning_i=find(abs(pos+(f(h)-9017375)/125241*180)==...
    min(abs(pos+(f(h)-9017375)/125241*180)));
```

% with demph demodulated error signals

```
s_ph=[];
n=0;
for k=1:length(demph)
    ep = [cos(demph(k)/180*pi)*real(detuned)+...
        sin(demph(k)/180*pi)*imag(detuned)];
```

% determine the indices of all occurring zero crossings of each demodulated

```

% error signal, with the function "Ocr"
    % s_ph shall contain zero crossing indices of all error signals for only
    % one frequency
        clear s_ph
j=0;
for q=1:7
    s_ph(q).i=Ocr(ep(:,q));

    % eliminate demph that have no zero crossing
    if length(s_ph(q).i)==0
        j=1;
        break
    end
end

end

if j==1
    fprintf( 'warning demph: no %f \n',demph(k))
    continue
end
% define a region of +/- 250 Hz (= 0.36 deg.) within which the zero crossing
% can be regarded to be related to a SB resonance
lim=find(pos>=(pos(tuning_i)-0.36) & pos<=(pos(tuning_i)+0.36));
% upper and lower index of region limitations
ulim=lim(end);
llim=lim(1);

% determine for each demph, leading to an error signal with at least one zero
% crossing, whether the zero crossing or which of the zero crossings
% is related to the SB resonance
% extract the index of the further considered Ocr
index=[]; %
for q=1:7
    % for all detector tunings except carrier resonance
    if f(h)~=f(end)

        % choose the zero crossings related to SB resonance only
        s=find([s_ph((q)).i]>2005);
        % closest zero crossing(s) to targeted tuning
        s2=find(abs([s_ph((q)).i(s)]-tuning_i)==min(abs([s_ph(q).i(s)]-tuning_i)));
        s=s(s2);

        % for carrier resonance
    else

```

```

s=find(abs([s_ph(q).i]-tuning_i)==min(abs([s_ph(q).i]-tuning_i)));

end

% eliminate demph that have no zero crossing
if length(s)==0
    j=1;
    break
end

% decrease the number of zero crossings further down if the zero
% crossing is too far away from the point related to SB resonance
for m=1:length(s)
    if s_ph(q).i(s(m))<=l1lim | s_ph(q).i(s(m))>=ulim
        j=1;
        break
    end
end

if j==1
    break
end

index=[index;s_ph(q).i(s)];
end

% eliminate demph that have no zero crossing
if j==1
    fprintf( 'warning demph: no %f \n',demph(k))
    continue
end

% demphase that is evaluated
n=n+1;
demph2(p).val(n)=[demph(k)];

Gain

% gain at relevant zero crossing
g=[];
for q=1:7
    g =[g;(ep(index(q)+1,q)-ep(index(q)-1,q))/2];
end

g_r(p).val(n,:)=g;

```

Capture ranges

```
% capture ranges defined as monotonic region around zero crossing
cr_i=[];
cr_abs=[];

for q=1:7
    s=minimax(ep(:,q));
    s1=find(s<index(q));
    s2=find(s>index(q));
        % index of capture range
        cr_i=[cr_i [s(s1(end)) s(s2(1))]];
        % absolute value of capture range
        cr_abs=[cr_abs abs([s(s1(end)) s(s2(1))]-index(q))];
end
cr(p).i(n,:)=cr_i;
cr(p).abs(n,:)=cr_abs;
end
end

cputime
```

Evaluation of the results

```
demph1=[];
for p=1:tun
    clear gain cr_n cr_p
    s=[];
    s1=[];
    demph=[];
    for k=2:7
        gain(:,k)=g_r(p).val(:,k)./g_r(p).val(:,1);
        s=[s;find(abs(abs(gain(:,k))-1)==min(abs(abs(gain(:,k))-1)))];
        s1=[s1;find(gain(:,k)<1/2 | gain(:,k)>2)];
        n=1:2:14;
        cr_n(:,k)=cr(p).i(:,n(k))-cr(p).i(:,1);
        n=2:2:14;
        cr_p(:,k)=cr(p).i(:,n(k))-cr(p).i(:,1);
        s=[s;find(abs(cr_p(:,k))==min(abs(cr_p(:,k))))];
    end
    s=sort(s);
    s2=find(diff(s)>=1);
    s=s([1;s2+1]);
    chunk=chunks(s1);
```

```

for k=1:length(s)
j=0;
for q=1:length(chunk)
if s(k)>=min(chunk(q).ch) & s(k)<=max(chunk(q).ch)
j=1;
end
end
if j==0
demph=[demph;demph2(p).val(s(k))];
end
end
demph1=[demph1;min(demph) max(demph)];

end

% for the tuned frequency determine the range of demodulation phases
% by the complement of the "forbidden":
ma=[];
mi=[];
for q=1:length(chunk)
ma=[ma;max(chunk(q).ch)];
mi=[mi;min(chunk(q).ch)];
end
demph1(tun,:)= [demph2(p).val(max(ma)+5) demph2(p).val(min(mi)-5)+180];

result=[f2' demph1];
save demphase_range.txt result -ASCII

```

Comments

The influence of other degrees of freedom on the signal-recycling error-signal shape is investigated separately for each degree. The FINESSE output file from above serves as reference for the comparison with the other detector setups, where particular degrees of freedom have an offset from the ideal states of Appendix B.1.1. Ten detector configurations with different modulation frequencies, equally spread in the interval of $\delta f_m \in [0 \text{ kHz}, 4 \text{ kHz}]$, are considered. The **MSR** tuning steps agree in size and number with the reference file to facilitate the automated evaluation.

Most of the introduced offsets exaggerate the expected rms offsets of the operating detector:

The differential misalignment of the Michelson end mirrors **MCE** and **MCn**, defined according to [Grote03b] as an anti-clockwise rotation or tilt of both mirrors at the same time, was measured to be roughly $1 \mu\text{rad}/\sqrt{\text{Hz}}$ in the frequency region between 10 mHz and 0.6 Hz (see figure 3.32 in [Grote03b]). With an open loop gain of the fast auto alignment of the Michelson of roughly 30 dB within this frequency regime, a residual rms

alignment of $30 \text{ nrad}/\sqrt{\text{Hz}}$ can be expected. In the simulation, the offset is set to 100 nrad. Between 50 mHz and 1 Hz, the rms **MPR** misalignment of the free mirror was also measured to have a maximal value in the overall spectrum of $1 \mu\text{rad}/\sqrt{\text{Hz}}$ (see figure 3.22 in [Grote03b]). The open loop gain of the power-recycling auto alignment is $\geq 40 \text{ dB}$ below 1 Hz. This reduces the misalignment to $\sim 10 \text{ nrad}/\sqrt{\text{Hz}}$. For a worst-case estimation, the rotation of **MPR** was set to 100 nrad.

The **MSR** misalignment is not at all controlled. Given the measurements of the end mirror and **MPR** misalignment, the free rms rotation and tilt of **MSR** at low frequencies can be presumed to amount as-well to $1 \mu\text{rad}/\sqrt{\text{Hz}}$. This was applied in the respective simulation.

The differential longitudinal rms motion of the Michelson end mirrors was measured to be less than $\sim 10 \mu\text{m}/\sqrt{\text{Hz}}$ around the micro-seismic peak at 0.15 Hz (see figure 1.14 of [Grote03b]). The control loop has, at this frequency, an open loop gain of $\sim 120 \text{ dB}$, reducing the rms motion to less than $10 \text{ pm}/\sqrt{\text{Hz}}$. The simulation assumes an end mirror offset of 100 pm each. As previous simulations already showed a difference in the error-signal shape depending on the sign of the differential offset, two separate simulations, accounting for different offset signs, are accomplished.

The offset of the power-recycling cavity from carrier resonance is determined mainly by the noise of the second mode-cleaner compared with the power-recycling cavity. Figure 1.5 in [Grote03b] shows an equivalent residual rms frequency noise of the laser light of $\sim 1 \text{ MHz}/\sqrt{\text{Hz}}$ at roughly 2 Hz. At this frequency, the open loop gain of the power-recycling control loop is 140 dB, slashing the noise down to $0.1 \text{ Hz}/\sqrt{\text{Hz}}$. In the simulation, the power-recycling cavity needs to be detuned equivalently, which is by $\delta L = \delta f \cdot \lambda/2/FSR_{\text{PR}} \approx 0.4 \text{ pm}$. For a worst-case estimation, the detuning is set to 10 pm.

The evaluation and comparison of the relevant error-signal properties gain and capture range, leading to an interval of allowed demodulation phases, are executed by a MATLAB script, given in Appendix B.2.1.

Similarly to Appendix B.2.2, for each of the ten modulation frequencies the zero crossings, gains and capture ranges of each complex error-signal, projected onto different demodulation phases, are determined. As soon as one of the signals has no zero crossing within $\pm 250 \text{ Hz}$, around the **MSR** position associated with δf_m , the respective demodulation phase is ignored in the further investigation on that modulation frequency. This criterion also ensures that the **MSR** position deviations do not alter the optical gain for differential Michelson control by more than maximum 20 %.

If all parameters are calculated, the gain ratios to the reference (which is the perfect setup in terms of other degrees of freedom) and upper and lower capture range limit deviations from the reference are compared among all remaining demodulation phases. For each kind of altered degree of freedom, the demodulation phases, yielding best agreement with the reference error-signal, are collected. However, before the minimum and maximum is determined to yield the interval of suitable demodulation phases, each is cross-checked with the requirement that for this particular demodulation phase none of the error-signal gains deviates more from the reference than by a factor within $[0.5, 2]$. This is neces-

sary for the automatic evaluation, since for some demodulation phases the capture ranges minimally change, but the respective gain all the more.

B.2.2. MATLAB script for signal-recycling error signal property optimisation

Contents

- Complex error signal
- Vector of demodulation phases
- Relevant zero crossing
- Gain
- Capture ranges defined as monotonic region around zero crossing
- Highest gain
- Largest capture range
- Largest energy transfer
- Highest symmetry

```
% Determine the error signal parameters for the signal recycling control
% loop.
% The output for each optimisation criterion will be written in a
% respective file in the order
%
% f  Phi  Ocr_index  Ocr_pos  gain  cr_l_index  cr_u_index  Phi_index
%
% with the following definitions
% f      : SB frequency
% Phi    : demodulation phase
% Ocr_index : index of zero crossing
% Ocr_pos : position of zero crossing [deg.]
% gain   : gain at zero crossing [1/Hz]
% cr_l_index : lower capture range index
% cr_u_index : upper capture range index
% Phi_index : index specifying the right demodulation phase
%

clear all
x=load('downtng_SR.out');
[M,N]=size(x);
steps=9001;      % MSR tuning step number
tun=M/steps;    % number of SB frequencies

% SB frequency
f=reshape(x(:,1),steps,tun);
```

```
f=f(1,:);

% MSR position in degrees
pos=reshape(x(:,2),steps,tun);
pos=pos(:,1);

% real and imaginary part of the error signal phasor
pd1=reshape(x(:,3),steps,tun);
pd2=reshape(x(:,4),steps,tun);

% evaluate each tuning frequency separately
for h=1:tun

    % s_ph shall contain zero crossing indices of all error signals for only
    % one frequency
    if h>1
        clear s_ph
    end
end
```

Complex error signal

```
detuned=complex(pd1(:,h),pd2(:,h));
```

Vector of demodulation phases

Complex vector of demodulation phase that gives zero crossing close to SB resonance (is thus perpendicular to maximal error signal phasor)

```
s=find(abs(detuned(2001:end))==max(abs(detuned(2001:end))))+2000;
demph_c = detuned(s) * exp(-i * pi /2)./abs(detuned(s));
% in degrees
demph_d=round(angle(demph_c)/pi*180);
% maximally necessary demodulation phases
demph=demph_d-90:1:demph_d+89;

% with demph demodulated error signals
ep=[];
for k=1:length(demph)
    ep = [ep cos(demph(k)/180*pi)*real(detuned)+...
          sin(demph(k)/180*pi)*imag(detuned)];
end
```

Relevant zero crossing

index of MSR position associated with the SB frequency

```
tuning_i=find(abs(pos+(f(h)-9017375)/125241*180)==...
    min(abs(pos+(f(h)-9017375)/125241*180)));

% determine the indices of all occurring zero crossings of each demodulated
% error signal, with the function "Ocr"
n=[];
for k=1:length(demph)
    s_ph(k).i=Ocr(ep(:,k));

    % mark demph that have at least one zero crossing
    if length(s_ph(k).i) ~=0
        n=[n;k];
    end
end

end

% define a region of +/- 250 Hz (= 0.36 deg.) within which the zero crossing
% can be regarded to be related to a SB resonance
lim=find(pos>=(pos(tuning_i)-0.36) & pos<=(pos(tuning_i)+0.36));
% upper and lower index of region limitations
ulim=lim(end);
llim=lim(1);

% determine for each demph, leading to an error signal with at least one zero
% crossing, whether the zero crossing or which of the zero crossings
% is related to the SB resonance
n2=[];
for k=1:length(n)
    n1=[];
    t1=[];

    % for all detector tunings except carrier resonance
    if f(h)~=f(end)

        % choose the zero crossings related to SB resonance only
        s=find([s_ph(n(k)).i]>2005);
        % closest zero crossing(s) to targeted tuning
        s2=find(abs([s_ph(n(k)).i(s)]-tuning_i)==min(abs([s_ph(n(k)).i(s)]-tuning_i)));
        s=s(s2);
    end
end
```

```

    % for carrier resonance
    else

    s=find(abs([s_ph(n(k)).i]-tuning_i)==min(abs([s_ph(n(k)).i]-tuning_i)));

    end

    % decrease the number of zero crossings further down if the zero
    % crossing is too far away from the point related to SB resonance
    for m=1:length(s)
        if s_ph(n(k)).i(s(m))>=llim & s_ph(n(k)).i(s(m))<=ulim
            n1=[n1;n(k)];      % demph index
            t1=[t1;s(m)];      % label of zero crossing for particular demph
        end
    end
    n2=[n2;n1 t1];
end

% extract the index of the further considered zero crossing
index=[]; %
[d,n]=size(n2);
for k=1:d
    index=[index;s_ph(n2(k,1)).i(n2(k,2))];
end

n2=n2(:,1);

for k=1:d
    ep(:,k)=ep(:,n2(k))-ep(index(k),n2(k));
end
ep=ep(:,1:k);

```

Gain

```

% gain at relevant zero crossing
g=[];
for k=1:d
    g =[g;(ep(index(k)+1,k)-ep(index(k)-1,k))/2];
end

```

Capture ranges defined as monotonic region around zero crossing

```

cr_i=[];

```

```

cr_abs=[];

% determine the local minima and maxima by the function "minimax" and
% choose those around the considered zero crossing
for k=1:d
    s=minimax(ep(:,k));
    s1=find(s<index(k));
    s2=find(s>index(k));
    % index of capture range edges
    cr_i=[cr_i [s(s1(end));s(s2(1))]];
    % absolute value of capture ranges
    cr_abs=[cr_abs abs([s(s1(end));s(s2(1))]-index(k))];
end

% Optimisation criteria

Highest gain

s=find(abs(g)==max(abs(g)));

if length(s)>1
    m=[s' f(h)];
    res_gain_alt(h,:)= [f(h) demph(n2(s(2))) index(s(2)) pos(index(s(2))) g(s(2)) ...
        cr_i(1,s(2)) cr_i(2,s(2)) s(2)];
    fprintf( 'warning_gain: %f %f %f\n',m)
end

res_gain(h,:)= [f(h) demph(n2(s(1))) index(s(1)) pos(index(s(1))) g(s(1)) ...
    cr_i(1,s(1)) cr_i(2,s(1)) s(1)];

Largest capture range

s1=[1];
s=find(min([cr_abs])==max(min([cr_abs])));

if length(s)>1
    % take the error signal with the zero crossing closest to the SB
    % frequency related one
    s1=find(abs(index(s)-tuning_i)==min(abs(index(s)-tuning_i)));
end

s=s(s1);
if length(s)>1

```

```

    m=[s f(h)];
    fprintf( 'warning_cr: %f %f %f\n',m)
    res_cr_alt(h,:)= [f(h) demph(n2(s(2))) index(s(2)) pos(index(s(2))) g(s(2)) ...
    cr_i(1,s(2)) cr_i(2,s(2)) s(2)];
end

res_cr(h,:)= [f(h) demph(n2(s(1))) index(s(1)) pos(index(s(1))) g(s(1)) ...
    cr_i(1,s(1)) cr_i(2,s(1)) s(1)];

```

Largest energy transfer

```

s1=[1];
en=[];

% determine integral to both sides of the zero crossing, limited by the
% respective capture ranges
for k=1:d
    en=[en [sum(abs(ep(cr_i(1,k):index(k)-1,k)));...
    sum(abs(ep(index(k)+1:cr_i(2,k),k)))]];
end

s=find(min(en)==max(min(en)));

if length(s)>1
    % take the error signal with the zero crossing closest to the SB
    % frequency related one
    s1=find(abs(index(s)-tuning_i)==min(abs(index(s)-tuning_i)));
end

s=s(s1);
if length(s)>1
    m=[s f(h)];
    res_en_alt(h,:)= [f(h) demph(n2(s(2))) index(s(2)) pos(index(s(2))) g(s(2)) ...
    cr_i(1,s(2)) cr_i(2,s(2)) s(2)];
    fprintf( 'warning_en: %f %f %f\n',m)
end

res_en(h,:)= [f(h) demph(n2(s(1))) index(s(1)) pos(index(s(1))) g(s(1)) ...
    cr_i(1,s(1)) cr_i(2,s(1)) s(1)];

```

Highest symmetry

```

symi=[];

```

```

for k=1:d
    % find smallest cr side:
    s=find(cr_abs(:,k)==min(cr_abs(:,k)));
    % determine integral to both sides of the zero crossing, limited by the
    % smaller capture range
    s1=abs(ep(index(k)-cr_abs(s,k):index(k)-1,k));
    s2=flip(abs(ep(index(k)+1:index(k)+cr_abs(s,k),k)));
    % determine the difference of both integrals in %
    symi=[symi mean(abs((s1-s2)*2./(s1+s2)))]];
end

if length(symi)>1

if f(h)~=f(end)
s1=[1];

% determine local minima of symi with function "minimax"
% that indicates minima by
[s, val, ch]=minimax(symi');
s2=find(ch==-1);
s=s(s2);

if length(s)==0
    s=find(symi==min(symi));
end

if length(s)>1
    % take the error signal with the zero crossing closest to the SB
    % frequency related one
    s1=find(abs(index(s)-tuning_i)==min(abs(index(s)-tuning_i)));
end
s=s(s1);

else

s=find(symi==min(symi));

end

else
    s=1;
end

if length(s)>1
    m=[s f(h)];

```

```

res_sym_alt(h,:)= [f(h) demph(n2(s(2))) index(s(2)) pos(index(s(2))) g(s(2)) ...
    cr_i(1,s(2)) cr_i(2,s(2)) s(2)];
    fprintf( 'warning_sym: %f %f %f\n',m)
end

res_sym(h,:)= [f(h) demph(n2(s(1))) index(s(1)) pos(index(s(1))) g(s(1)) ...
    cr_i(1,s(1)) cr_i(2,s(1)) s(1)];

end
cputime

save SREP_newMPR_cr.txt res_cr -ASCII
save SREP_newMPR_en.txt res_en -ASCII
save SREP_newMPR_sym.txt res_sym -ASCII
save SREP_newMPR_gain.txt res_gain -ASCII

```

Comments

The MATLAB script successively evaluates the error-signals for each control sideband frequency. An overview over the single steps can be gathered from the content at the top of the script.

First, the error-signals for a range of demodulation phases of $[0^\circ, 179^\circ]$ are determined. Then, the zero crossings are calculated. As the existence of only one zero crossing is rather the exception for this large tuning interval, all zero crossings not belonging to the sideband resonance have to be eliminated. They are discriminated in first instance by considering only the zero crossing closest to the **MSR** tuning $\delta\chi_m$, associated with δf_m (see Equation 3.2). If even this closest zero crossing exceeds a range of $\pm 0.36^\circ \cong \pm 250$ Hz around $\delta\chi_m$, the respective error-signal or demodulation phase is ignored in the further evaluation steps.

As the **MSR** tuning steps are equally separated by $1.44 \times 10^{-3} \text{ }^\circ \cong 1$ Hz, for the optical gain of the error-signal it is enough to calculate the difference of the signal amplitude around the further considered zero crossing. The gain is then given in [amplitude/Hz]. The capture range is, in agreement with [Grote03b], defined as the monotonic region around the considered zero crossing. Thus, the local minima and maxima around the zero crossing are equivalent to the limits of the capture range. The region of the capture range with smaller tunings with respect to the zero crossing will henceforth be called *negative* or *lower (one-sided) capture range*, whereas the *upper* or *positive (one-sided) capture range* is situated on the positive tuning side.

The error-signals are evaluated regarding the properties listed on page 114 ff. Once the optimal error-signal is discovered, its most interesting features are stored in matrices, one for each optimisation criterion. These features are the sideband frequency, the appropriate demodulation phase, the zero crossing as index and **MSR** position $\delta\chi$, the optical gain, the index of upper and lower capture range, and the index associated with

the demodulation phase. In case there exist by chance several error-signals that yield the best numerical value, representing the targeted optimisation criterion, the one with a zero crossing closest to $\delta\chi_m$ is given priority over the other solutions. In case even this condition is not one-to-one, a second matrix is created, gathering the alternative solution. In the following, the mathematical implementation of the criteria is commented in more detail.

The criterion of highest **optical gain** is met by simply identifying the error-signal with the highest slope at the zero crossing.

The crucial point for an optimisation by the **capture range** is that both tuning sides, with respect to the zero crossing, need to be considered, at the same time. As estimated above, the rms mirror motion is not expected to be a limit in first instance. It is rather the intended, continuous tuning to both directions that equally adds weight to both capture ranges. Thus, to prevent an optimisation of one side at the expense of the other, for every demodulation phase the smaller one-sided capture range is stored in a vector, and the largest among them points to the desired demodulation phase.

For the largest **energy transfer**, the integrals of each error-signal from the zero crossing to the respective capture range limits are calculated¹. Again, the smaller values for each demodulation phase are compared among each other to find the maximum, indicating the appropriate demodulation phase.

Perfect point-symmetry of a function $f(x)$ around x_0 is defined as $f(x_0 + a) - f(x_0) = -(f(x_0 - a) - f(x_0))$, $\forall a$. Thus, for an error-signal optimisation in **symmetry**, the deviation of each pair of amplitude, with same position offset from the zero crossing, is evaluated separately². To yield a deviation independent from the absolute amplitude value, each deviation is normalised by the respective total amplitude.

As only the symmetry within the capture ranges is of interest, the contributing pairs of amplitudes have to sit closer around the zero crossing than the smaller one-sided capture range. The sum of all deviations has to be normalised by the number of accounted pairs, not to adulterate the result by the size of the capture range. Thus, the error-signal possessing the smallest mean deviation is the targeted one.

Gathering the optimal demodulation phases and corresponding parameters in the particular matrices, after the last sideband frequency, all matrix contents are saved in separate files for further evaluation and adjustment to the requirements of the experimental script.

B.2.3. MATLAB script for differential Michelson error signal evaluation

Contents

- Complex error signal

¹To avoid biasing of the comparison of both sides around the zero crossing, the error-signal amplitude is set to be exactly 0 at the zero crossing index (see the loop before the header “Gain”).

²As the error-signal amplitude is set to be exactly 0 at the zero crossing index, the evaluation is free of any arbitrary offset.

- Vector of demodulation phases
- With demph demodulated error signals
- Relevant zero crossing
- Gain
- Determine demph yielding maximum gain

```
% Determine the error signal parameters for the differential Michelson control loop.
% The output is written in a file in the order
%
% f  Phi  Ocr_index Ocr_pos gain
%
% with the following definitions
% f          : MSR tuning
% Phi        : demodulation phase
% Ocr_index  : index of zero crossing
% Ocr_pos    : position of zero crossing [deg.]
% gain       : gain at zero crossing [1/pm]
%
```

```
clear all
x=load('downtng_MI.out');
[M,N]=size(x);
steps=101;
tun=M/steps;

% MSR tuning
f=reshape(x(:,1),steps,tun);
f=f(1,:);

% MCE (=-MCN) position
pos=reshape(x(:,2),steps,tun);
pos=pos(:,1);

% real and imaginary part of the error signal
pd1=reshape(x(:,3),steps,tun);
pd2=reshape(x(:,4),steps,tun);

% index of MCE tuning corresponding to dark fringe
tuning_i=find(abs(pos)==min(abs(pos)));

% evaluate each MSR tuning separately

for h=1:tun
```

Complex error signal

```
detuned=complex(pd1(:,h),pd2(:,h));
```

Vector of demodulation phases

```
demph=(-90:1:90);
```

With demph demodulated error signals

```
ep=[];  
for k=1:length(demph)  
    ep = [ep cos(demph(k)/180*pi)*real(detuned)+...  
         sin(demph(k)/180*pi)*imag(detuned)];  
end
```

Relevant zero crossing

```
% determine the indices of all occurring zero crossings of each demodulated  
% error signal, with the function "0cr"
```

```
n=[]; % indices of demph  
index=[];  
for k=1:length(demph)  
    O=0cr(ep(:,k));  
    s=1;  
    % choose the zero crossing closest to 0 deg. if there are several  
    if length(O)>1  
        s=find(abs(O-tuning_i)==min(abs(O-tuning_i)));  
    end  
    % mark demph that yield a zero crossing  
    if length(O)~=0  
        n=[n;k];  
        index=[index;O(s)];  
    end  
end  
end
```

Gain

```
% gain [1/pm] at relevant zero crossing  
g=[];  
for k=1:length(n)
```

```
% distinguish between zero crossing right at the edge of the simulated
% displacement interval and those inside
if index(k)~=1 & index(k)~=101
    g =[g;(ep(index(k)+1,n(k))-ep(index(k)-1,n(k)))/4];
elseif index(k)=1
    g =[g;(ep(index(k)+1,n(k))-ep(index(k),n(k)))/2];
else
    g =[g;(ep(index(k),n(k))-ep(index(k)-1,n(k)))/2];
end
end
```

Determine demph yielding maximum gain

```
s=find(abs(g)==max(abs(g)));

if length(s)>1
    m=[s f(h)];
    fprintf('warning: %f %f %f\n',m)
    res_g_alt=[f(h) demph(n(s(2))) index(s(2)) pos(index(s(2))) g(s(2))];
end

res_g(h,:)= [f(h) demph(n(s(1))) index(s(1)) pos(index(s(1))) g(s(1))];
end
cputime

save MIEP_newMPR_max2_2SB.txt res_g -ASCII
```

B.2.4. MATLAB script for the tuning script generation

Contents

- Experimental tune-VI input-values belonging to the most symmetric signal-recycling error-signal
- Calibration of signal-recycling parameters
- Consider Michelson error-signal evaluation: refer parameters to the modulation frequency instead of the MSR tuning
- Calibration of Michelson parameters
- Generate tuning script

```
% Calibrate the simulated parameters for the signal-recycling and Michelson
% loop to match the experiment, and generate a tuning script
%
% The signal-recycling parameters in the input file
```

```

% are in the order
%
% f  Phi  Ocr_index Ocr_pos gain cr_l_index cr_u_index Phi_index
%
% with the following definitions
% f      : SB frequency
% Phi    : demodulation phase
% Ocr_index : index of zero crossing
% Ocr_pos : position of zero crossing [deg.]
% gain   : gain at zero crossing [1/Hz]
% cr_l_index : lower capture range index
% cr_u_index : upper capture range index
% Phi_index : index specifying the right demodulation phase
%
% The script, as displayed here, applies to the GEO setup with the new MPR.
% Lines explicitly differing for the GEO setup with the old MPR
% are commented and indicated by a corresponding header.
%

clear all
% input file
% (contains 161 different modulation frequencies for a range of 4 kHz)
v = load('SREP_newMPR_sym.txt');

% % old MPR
% % input file
% % (contains 501 different modulation frequencies for a range of 5 kHz)
% v = load('SREP_oldMPR_sym.txt');
% v = v(2:5:501,:);
%
% % experimental tuning script
% x = load('tune_S3eGavinsamp.dat');

% modulation frequencies
f = v(:,1);

% prevent phase jumps of 360 degrees with the function "cont"
v(:,2) = cont(v(:,2));

% change the demodulation phases for the last three SB frequencies to yield
% a consistent gain, regarding sign, in the experiment
v(end-2:end,2) = v(end-2:end,2)-180;

% change the respective gain sign for the last three SB frequencies
v(end-2:end,5) = -v(end-2:end,5);

```

```
% % old MPR
% % change the demodulation phases for the last SB frequency to yield
% % a consistent gain, regarding sign, in the experiment
% v(end,2) = v(end,2)-180;
%
% % change the respective gain sign for the last SB frequency
% v(end,5) = -v(end,5);
```

Experimental tune-VI input-values belonging to the most symmetric signal-recycling error-signal

```
% signal-recycling modulation frequency
f_exp = 9014365;

% signal-recycling demodulation phase
exsym = 150 ;

% signal-recycling gain
g_exp = 20;

% Michelson demodulation phase
dem_exp_MI = 120;

% Michelson gain
g_exp_MI = 100;

% % oldMPR
%
% % signal-recycling modulation frequency
% f_exp = 9014197;
%
% % determine line in the experimental data corresponding to f_exp
% se = find(x(:,1) == f_exp);
%
% % signal-recycling demodulation phase for most symmetric error-signal
% % (experimentally not used)
% exsym = 117 ;
%
% % signal-recycling gain in the experiment
% g_exp = x(se,3);
%
% % Michelson demodulation phase in the experiment
% dem_exp_MI = x(se,5);
```

```
%  
% % Michelson gain in the experiment  
% g_exp_MI = x(se,6);
```

Calibration of signal-recycling parameters

```
% determine the line of the simulated data agreeing with the experimentally  
% investigated modulation frequency  
sf = find(abs(f_exp-f) == min(abs(f_exp-f)));
```

```
% simulational demodulation phase difference regarding the one that is  
% going to be calibrated  
d_off = v(:,2)-v(sf,2);
```

```
% new demodulation phases, accounting for evolution with opposite sign,  
% in increments of 5  
demph_sym = 5*round((exsym-d_off)/5);
```

```
% gain ratio of the experimental tune-VI input and the simulational gain  
% value for that modulation frequency  
g = g_exp/v(sf,5);
```

```
% % old MPR  
%  
% % gain ratio of the experimental tune-VI input and the simulational gain  
% % value for that modulation frequency with the experimental demodulation  
% % phase applied  
% g = g_exp/4.723356e-07;
```

```
% new gains, in increments of 5  
g_sym = 5*round(v(:,5)*g/5);
```

Consider Michelson error-signal evaluation: refer parameters to the modulation frequency instead of the MSR tuning

```
%  
% The input file contains  
%  
% MSR Phi Ocr_index Ocr_pos gain  
%  
% with the following definitions  
% MSR : MSR tuning in [deg.]  
% Phi : demodulation phase
```

```
% 0cr_index      : index of zero crossing
% 0cr_pos       : position of zero crossing [deg.]
% gain         : gain at zero crossing [1/pm]
%
% input file
MI = load('MIEP_newMPR_max2_2SB.txt');
% % old MPR
% % input file
% MI = load('MIEP_oldMPR_max2_2SB.txt');
% MSR positions at the particular modulation frequencies, determined by the
% signal-recycling error-signal zero crossing
pos_sym = v(:,4);
% find for each modulation frequency the corresponding Michelson script
% line; this is determined by the respective MSR position
sp = [];
for k = 1:length(f)
    sym = abs(pos_sym(k)-MI(:,1));
    sp = [sp;find(sym == min(sym))];
end
```

Calibration of Michelson parameters

```
% determine the line of the simulated data agreeing with the experimentally
% investigated modulation frequency
s = sp(sf);
% % old MPR
% % with the experimental demodulation phase applied to the signal-recycling
% % error-signal in the simulation, the resulting MSR position is at 4.591 deg.;
% % determine the line of the simulated data closest to 4.591 deg.
% sym = abs(4.591-MI(:,1));
% s = find(sym == min(sym));
% simulational demodulation phase difference regarding the one that is
% going to be calibrated
dMI_off = MI(sp,2)-MI(s,2);
% new demodulation phases, accounting for evolution with opposite sign,
% in increments of 5
dem_MI = 5*round((dem_exp_MI-dMI_off)/5);
```

```
% gain ratio of the experimental tune-VI input and
% the inverse simulational gain value for that modulation frequency
g_mi = g_exp_MI*MI(s,5);

% new gains, in increments of 5
compens = 5*round(g_mi./MI(sp,5)/5);

% prevent Michelson-gain input-values greater than 100
s1 = find(compens>100);
compens(s1) = 100;
```

Generate tuning script

```
% dummy Michelson auto-alignment parameters, guided by some successful
% parameter value
comp = [12*ones(length(f),1)];

% % old MPR
% % experimental Michelson auto-alignment parameters, filling the last rows
% % with the last experimental value to obtain a vector of same size as the
% % rest of the parameters
% comp = [x(:,4);10*ones(length(f)-length(x(:,1)),1)];

% summarise parameters
SYM = [f demph_sym g_sym comp dem_MI compens];

% write tuning script
fid = fopen('tune_sym_SRMI.dat','w');
    fprintf(fid,'%0f %0f %0f %0f %0f %0f\n',SYM);
    fclose(fid);

% % old MPR
% % write tuning script
% fid = fopen('tune_sym_SRMI2.dat','w');
%     fprintf(fid,'%0f %0f %0f %0f %0f %0f\n',SYM);
%     fclose(fid);
```


Appendix C.

Impact of various parameters on the 2f signal

In Section 4.2 the simulated 2f signal was matched to the experimental data by the least-square method. The choice of parameter space based on preceding investigations on the separate impact of the obvious parameters, like signal-recycling cavity length and tuning, Schnupp length, misalignment, and common Michelson losses and **MSR** properties. The corresponding results are presented here.

C.1. Signal-recycling cavity length and tuning

Figure C.1 shows the 2f signal for various signal-recycling cavity lengths and tunings. The respective parameters are referred to as deviations from the default values. The subplots belong to different signal-recycling cavity lengths marked at the top, the lines to different signal-recycling cavity tunings, allocated in the legend. The 2f signal is normalised to yield the same maximal value of 1, as the unit is anyway arbitrary in comparison with the experiment.

Apparently, compared to the signal-recycling cavity length the signal-recycling cavity tuning only minimally shifts the 2f signal sideways (~ 5 Hz for the complete tuning difference of 100 Hz) nor changes the signal symmetry. In particular for the peak position it is worth considering that a signal-recycling cavity length shift of 5 mm decreases FSR_{SR} by roughly -0.5 Hz. For the Michelson sidebands, being close to $119 \times FSR_{SR}$, this adds up to ~ -60 Hz. The associated shift of the signal-recycling cavity resonance is, hence, comparable to that, associated with the **MSR** tuning. The unequal impact can be understood consulting Figure 2.4: tuning **MSR** shifts all resonance structures to the same direction, whereas a change of FSR_{SR} alters the separation between the resonances.

As a consequence, when intending to assimilate the experimental and simulational 2f signal, the signal-recycling cavity tuning requires only a rough setting. When optimising the signal-recycling cavity length alone, approaching an agreement in symmetry changes the peak position to the wrong side. At the same time, the signal width is slightly altered.

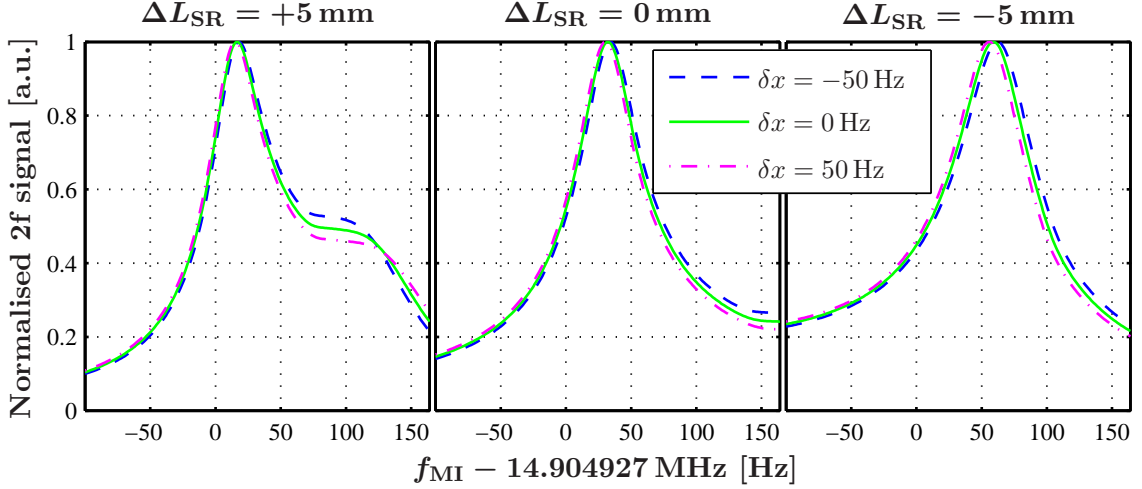


Figure C.1.: 2f signal for various signal-recycling cavity lengths and tunings. The signal-recycling cavity length deviations, ΔL_{SR} , from the default value are indicated at the top of each subplot, the **MSR** position offsets, δx , (in Hz) from the default value are assigned in the legend.

C.2. Schnupp length

The Schnupp length, L_{Schnupp} , influences the Michelson sideband enhancement in two properties. By changing the Michelson reflectivity for the sidebands, on the one hand the power reflectivity of the srMI alters, varying the appearing power-recycling linewidth for the sidebands. On the other hand the resonance gets shifted in frequency, according to the phase shift in reflection of the srMI. This phase shift, however, depends not only on the resonance condition inside the signal-recycling cavity, influenced by the Schnupp length through the Michelson reflection, but also on the phase shift appearing at the isolated Michelson, due to the Schnupp length.

This change of phase shift at the Michelson naturally also influences the pure power-recycling resonance (i.e., with **MSR** being misaligned). Figure C.2 shows the normalised upper (left graph) and lower (right graph) Michelson control sideband amplitudes at the output port of the default power-recycled Michelson of GEO 600, for $f_{\text{MI}} = 119 \times FSR_{\text{PR}} = 14.904875$ MHz. The amplitude is displayed in the plane of Schnupp length and power-recycling tuning deviation from the respective default values. In order to easier relate the power-recycling tuning to the shift of resonance frequency, it is given in Hertz.

The position of peak frequency f_{p} of the upper sideband obeys in this parameter plane the approximation

$$f_{\text{p}} \approx -1.8 \left[\frac{\text{Hz}}{\text{cm}} \right] \cdot \Delta L_{\text{Schnupp}}. \quad (\text{C.1})$$

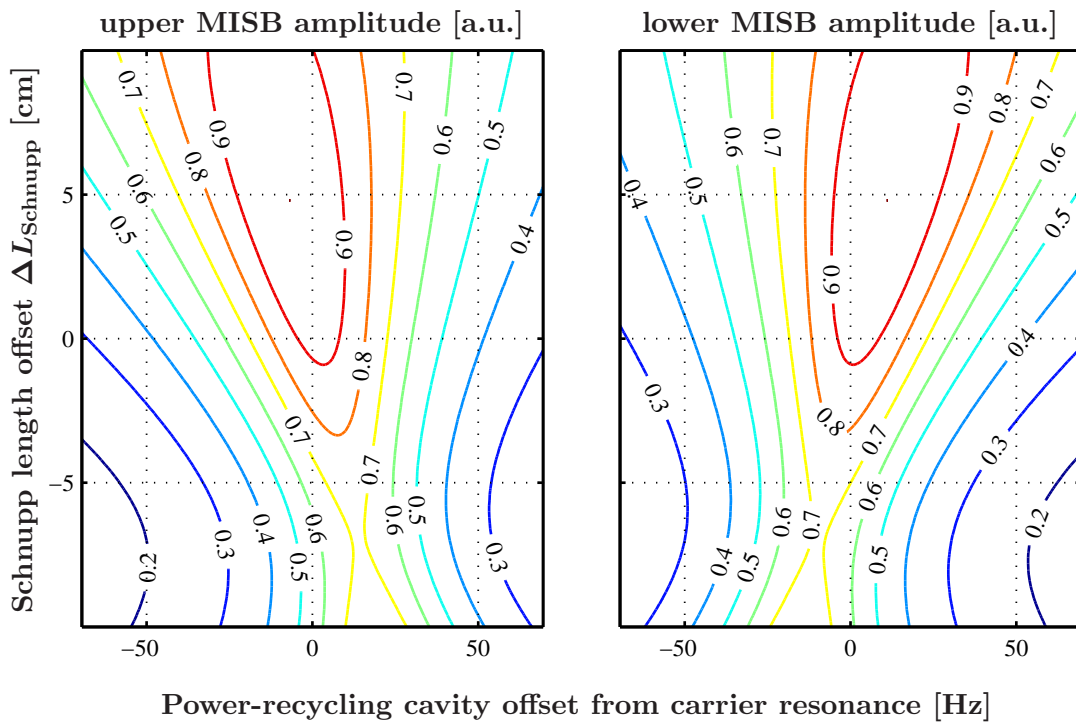


Figure C.2.: Normalised upper (left graph) and lower (right graph) Michelson control sideband amplitudes at the output port of the default power-recycled Michelson of GEO 600. The amplitudes are displayed in the plane of Schnupp length and power-recycling tuning deviation from the respective default values. The power-recycling tuning is given in Hertz. The modulation frequency is chosen to be 14.904875 MHz which corresponds to the frequency experimentally determined to be resonant inside the pure power-recycled Michelson, being resonant for the carrier.

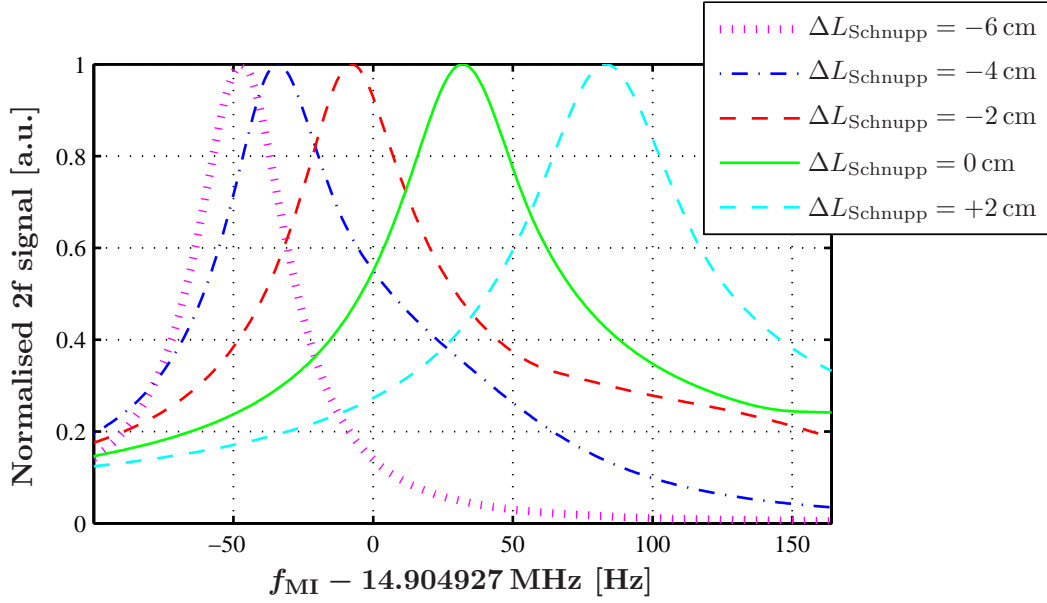


Figure C.3.: 2f signal for various Schnupp length offsets $\Delta L_{\text{Schnupp}}$ from the default value (solid green line). The power-recycling cavity length is adjusted to yield a resonance frequency of 14.904875 MHz in the only power-recycled Michelson.

Considering Figure 2.16, a small shift of the power-recycling resonance can for particular detunings already noticeably change both the peak and the symmetry of the 2f signal. Thus, in the following for each Schnupp length the power-recycling cavity length is accordingly adjusted.

Figure C.3 displays the 2f signal for various Schnupp length offsets¹ $\Delta L_{\text{Schnupp}}$ from the default value. The Schnupp length obviously influences all signal characteristics, i.e., the width, the symmetry and the peak frequency. In particular the dependency of the peak frequency on the Schnupp length is larger than on the signal-recycling cavity length, whereas the symmetry change is less extreme here.

C.3. Common losses and MSR reflectivity

Losses of the Michelson mirrors or of **MSR** alter the reflectivity of the srMI. For the Michelson mirrors two losses can be considered, common and differential. Due to the

¹The results for Schnupp length offsets larger than 1 cm and smaller than -3 cm are not displayed: the peaks of the larger ones are already either at the edge or completely outside the shown frequency interval (and thus not relevant considering the experimental curve). The signals for smaller offsets almost perfectly agree with those for the offsets ≥ -3 cm. As the default Schnupp length is ~ 7 cm, an offset of smaller than -3.5 cm repeats the Michelson properties for the control sidebands, just with exchanged arms.

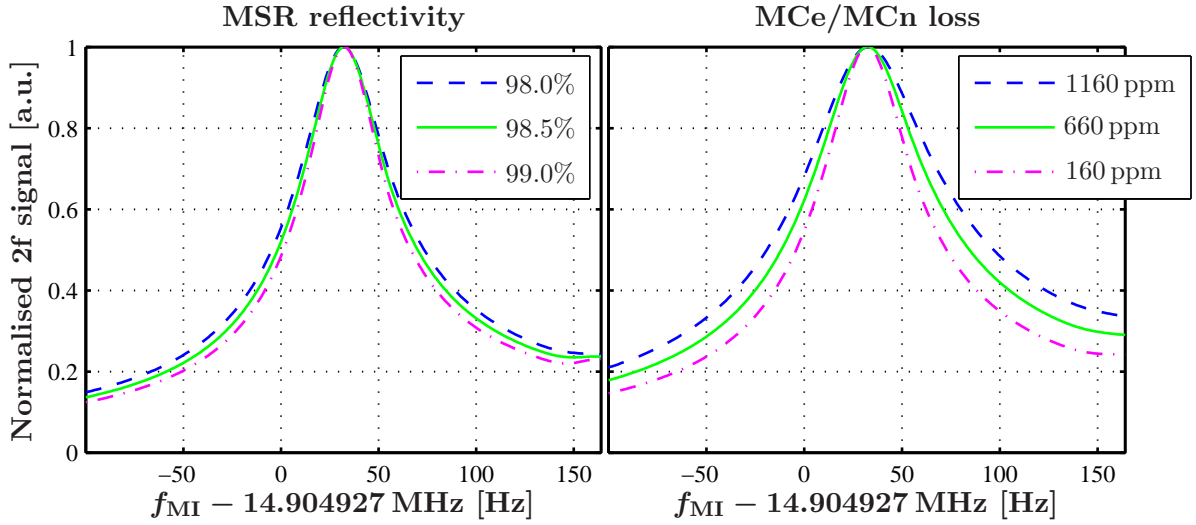


Figure C.4.: 2f signal for various **MSR** (left graph), and **MCe/MCn** reflectivities (right graph). The common reflectivities of each of the end mirrors are given as losses, including the respective transmission. Please note the different reflectivity ranges of **MSR** and the end mirrors.

BSAR, the losses inside the two Michelson arms are already asymmetric. Asymmetric losses appear as Michelson loss by half of their size. Their contribution to the phase shift of the reflected or transmitted Michelson sidebands is negligible compared with the phase shift due to the default Schnupp length. Thus, they can be treated as common losses, and only these l_{comm} are considered in this subsection.

The left and right graph of Figure C.4 display the 2f signal for various **MSR**, and **MCe/MCn** reflectivities, respectively. The end mirror's reflectivities are given as losses which include the mirrors' transmissions as-well. The given losses apply to each of the end mirrors.

As expected, different mirror reflectivities mainly alter the width of the 2f signal. However, the impact of the end mirrors is much larger than of **MSR**: although the losses of **MSR** vary by 5000 ppm, compared to 500 ppm loss difference inside the Michelson, the 2f signals hardly differ, whereas on the right hand side the widths noticeably change by ~ 20 Hz.

To understand this, one has again to consider the undercoupled srMI as the output mirror of the power-recycling cavity. With the default Michelson and **MSR** reflectivities being so different ($R_{\text{MSR}} = 98.14\%$ and $R_{\text{MI}} \approx 99.85\%$), the overall srMI reflectivity is much more sensitive to slight variations of the Michelson mirrors.

Thus, if the width of the experimental 2f signal is the only remaining property to be fitted, the common Michelson losses need to be adjusted. The **MSR** reflection can then

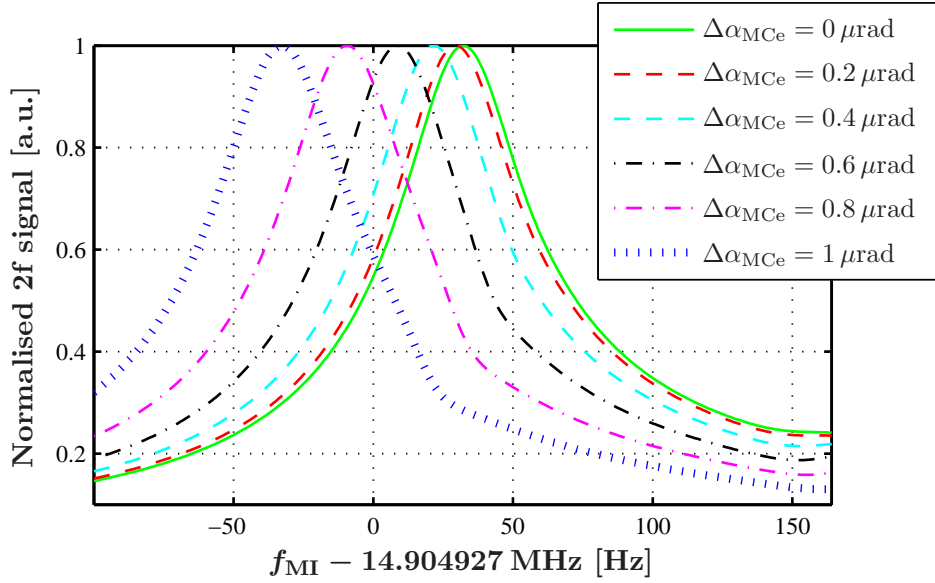


Figure C.5.: 2f signal for various differential Michelson end mirrors' misalignments in the optical plane of the detector. The curves are labeled with the corresponding east end mirror's amount of misalignment, $\Delta\alpha_{\text{MCe}}$, implying the same misalignment for the north end mirror, but with opposite sign. For symmetry reasons, only positive $\Delta\alpha_{\text{MCe}}$ are displayed.

be used as a free parameter to customise the bandwidth of the optical transfer function of the differential Michelson for signal sidebands.

C.4. Misalignment

Michelson mirror misalignments change the Hermite-Gauss mode composition of the light inside the dual-recycled detector. Hence, similarly to the Schnupp length, they alter the Michelson losses, and correspondingly the phase shift in reflection of the srMI.

Common and differential misalignments, in both parallel and perpendicular directions regarding the optical plane, exhibit very similar features in the 2f signal. As an example, Figure C.5 displays the impact of differential end mirrors' misalignment in the interferometer plane on the 2f signal.

The particular curves are labeled by $\Delta\alpha_{\text{MCe}}$, the angle of misalignment of the east arm's end mirror, implying the same amount of misalignment, but with opposite sign, for **MCn**. The misalignments indeed have an impact on all three signal properties of peak frequency position, width and symmetry. However, Figures 3.31 and 3.32 in [Grote03b], showing the open loop gain and phase of the Michelson fast auto alignment and the amplitude spectral density of the differential-wavefront signals for **MCE** and **MCn** rotation, respectively,

indicate an expectable residual misalignment of $< 0.2\mu\text{rad}$. A misalignment of such low level only slightly alters the $2f$ signal, as visible in Figure C.5. Thus, misalignments were neglected for the fits of the $2f$ signal.

Bibliography

- [Acernese05] F. Acernese et al. 2005 *Status of Virgo* Class. Quantum Grav. **22** 869–880. 1
- [Ageev04] A. Ageev et al. 2004 *Class. Quantum Grav.* **21** 3887–3892. 36
- [Ando05] M. Ando et al. 2005 *Current status of the TAMA300 gravitational-wave detector* Class. Quantum Grav. **22** 881–889. 1
- [Barr03] B.W. Barr 2003 *Experimental Investigations into Advanced Configurations and Optical Techniques for Laser Interferometric Gravitational Wave Detectors* Ph.D. Thesis, University of Glasgow, 88–94 and 96–98. 26
- [Bongs95] K. Bongs 1995 *Automatische Gain-Kontrolle für Fabry-Perot-Resonatoren mit variablen Verlusten* Diploma Thesis, Universität Hannover. (The thesis is currently available at <http://www.amps.uni-hannover.de/diplomarbeiten/dipl.bongs.ps.zip>.) 21
- [Brozek99] O. Brozek 1999 *Frequenzstabilisierung eines Nd:YAG-Hochleistungs-Laser-Systems für den Gravitationswellendetektor GEO 600* Ph.D. Thesis, Universität Hannover. 80
- [Brozek00a] O. Brozek et al. 2000 *The GEO 600 laser source: a 12 W frequency-stabilised injection-locked Nd:YAG laser system* in: S. Kawamura, N. Mio (eds.) *Gravitational Wave Detection II* University Academy Press, Tokyo 295–300. 80
- [Brozek00b] O. Brozek, I. Zawischa, M. Peterseim, B. Willke, K. Danzmann 2000 *The GEO 600 laser system* in: J. Trân Than Vân, J. Dumarchez et al. (eds.) *Gravitational waves and experimental gravity* World Publ., Hanoi 183–188. 80
- [Buonanno02a] A. Buonanno and Y. Chen 2002 *Signal recycled laser-interferometer gravitational-wave detectors as optical springs* Phys. Rev. D **65** 042001. 132
- [Buonanno02b] A. Buonanno and Y. Chen 2002 *Laser-interferometer gravitational-wave optical-spring detectors* Class. Quantum Grav. **19** 1569–1574. 132
- [Drever83] R.W.P. Drever, J.L. Hall, F.V. Kowalski, J. Hough, G.M. Ford, A.J. Munley, H. Ward 1983 *Laser Phase and Frequency Stabilization Using an Optical Resonator* Appl. Phys. **B 31** 97–105. 21
- [FINESSE] A. Freise 2002 *FINESSE: Frequency domain interferometer simulation software* Internal note. (The program is currently available at <http://www.rzg.mpg.de/~adf>.) 78, 163

- [Freise00] A. Freise et al. 2000 *Demonstration of detuned dual recycling at the Garching 30 m laser interferometer* Phys. Lett. **A 277** 135–142. 92
- [Freise03a] A. Freise 2003 *The Next Generation of Interferometry: Multi-Frequency Optical Modelling, Control Concepts and Implementation* Ph.D. Thesis, University of Hannover. 2, 35, 80, 138, 165, 168
- [Freise03b] A. Freise 2003, personal communication. 80
- [GEO] K. Danzmann and the GEO 600 team 1995 *GEO 600 — a 600 m laser interferometric gravitational wave antenna* in: E. Loccia, G. Pizzella, F. Rouga (eds.) *Gravitational wave experiments* World Scientific, Singapore 100–111. 1
- [Goßler02] S. Goßler et al. 2002 *The modecleaner system and suspension aspects of GEO 600* Class. Quantum Grav. **19** 1835–1842. 80
- [Goßler03] S. Goßler et al. 2003 *Mode-cleaning and injection optics of the gravitational-wave detector GEO600* Rev. Scientific Instr. **74** 3787–3796. 80
- [Goßler04] S. Goßler 2004 *The suspension systems of the interferometric gravitational-wave detector GEO 600* Ph.D. Thesis, University of Hannover. (The thesis is currently available at http://www.amps.uni-hannover.de/dissertationen/grossler_diss.pdf.) 82
- [Grote03a] H. Grote et al. 2003 *Dual Recycling for GEO 600* Class. Quantum Grav. **21** 473–480. 77, 92
- [Grote03b] H. Grote 2003 *Making it Work: Second Generation Interferometry in GEO 600!* Ph.D. Thesis, University of Hannover. (The thesis is currently available at http://www.amps.uni-hannover.de/dissertationen/grote_diss.pdf.) 24, 77, 81, 83, 88, 92, 95, 113, 115, 118, 127, 168, 207, 208, 216, 232
- [Grote04] H. Grote et al. 2004 *Automatic beam alignment for the modecleaner cavities of GEO 600* Appl. Opt. **43** 1938–1945. 80
- [Harms03] J. Harms, Y. Chen, S. Chelkowski, A. Franzen, H. Vahlbruch, K. Danzmann, R. Schnabel 2003 *Squeezed-input, optical-spring, signal-recycled gravitational-wave detectors* Phys. Rev. D **68** 042001. 35
- [Heinzel95] G. Heinzel 1996 *Resonant Sideband Extraction — Neuartige Interferometrie für Gravitationswellendetektoren* Diploma Thesis, Universität Hannover. (The thesis is currently available at <http://www.amps.uni-hannover.de/diplomarbeiten/dipl.heinzel.ps.zip>.) 19
- [Heinzel99] G. Heinzel 1999 *Advanced optical techniques for laser-interferometric gravitational-wave detectors* Ph.D. Thesis, University of Hannover. (The thesis is currently available at http://www.mpg.de/~ros/geo600_docu/text/theses/Gerhard_Heinzel.pdf.) 33, 77

-
- [Hewitson04a] M. Hewitson 2004 *On aspects of characterising and calibrating the interferometric gravitational-wave detector, GEO 600* Ph.D. Thesis, University of Glasgow. 1
- [Hewitson04b] M. Hewitson, G. Heinzel, J.R. Smith, K.A. Strain, H. Ward 2004 *Principles of calibrating the dual-recycled GEO 600* Rev. Scientific Instr. **75** 4702–4709. 44
- [Hewitson05] M. Hewitson (for the LIGO Scientific Collaboration) 2005 *Preparing GEO 600 for gravitational wave astronomy — a status report* Class. Quantum Grav. **22** 891–900. 1
- [Hild03] S. Hild 2003 *Thermisch durchstimmbares Signal-Recycling für den Gravitationswellendetektor GEO 600* Diploma Thesis, Universität Hannover. 1, 149, 150
- [Kawabe] K. Kawabe, W. Winkler, S. Hild 2006 *Demonstration of thermal tuning of a dual-recycled interferometer for gravitational-wave signal detection*, to be submitted. 149
- [Kötter04] K. Kötter 2004 *Data Acquisition and Data Analysis for the Gravitational-Wave Detector GEO 600* Ph.D. Thesis, University of Hannover. 1
- [LIGO] A. Abramovici et al. 1992 *LIGO: The Laser Interferometer Gravitational-Wave Observatory* Science **256** 325–333. 1
- [Malec] M. Malec, R. Schilling *Requirements for the homogeneity of an etalon replacing the signal-recycling mirror at GEO 600* Internal paper, in preparation. 150
- [Mizuno95] J. Mizuno 1995 *Comparison of optical configurations for laser-interferometric gravitational wave detectors* Ph.D. Thesis, University of Hannover. 1, 35, 39, 149
- [Mizuno97] J. Mizuno, A. Rüdiger, R. Schilling, W. Winkler, K. Danzmann 1997 *Frequency response of Michelson- and Sagnac-based interferometers* Optics Commun. **138** 383–393. 35
- [Penn] S.D. Penn et al. 2005 *Frequency and Surface Dependence of the Mechanical Loss in Fused Silica* arXiv:gr-qc/0507097. 36
- [Rüdiger98] A. Rüdiger 1998 *Phase relationships at a symmetric beamsplitter* Internal note. 17, 18
- [Sigg05] D. Sigg 2005, talk at the *6th Edoardo Amaldi Conference* Okinawa. (The talk is currently available at http://amaldi6.nao.ac.jp/04.scd/Tue1100_G050300-00.pdf.) 1
- [Schnupp88] L. Schnupp 1988, talk at the *European Collaboration Meeting on Interferometric Detection of Gravitational Waves* Sorrento. 33
- [Smith04a] J.R. Smith et al. 2004 *Mechanical quality factor measurements of monolithically-suspended fused silica test masses of the GEO600 gravitational wave detector* Class. Quantum Grav. **21** 1091–1098. 82

- [Smith06] J.R. Smith, et al. 2006 *Linear projection of technical noise for interferometric gravitational-wave detectors* Class. Quantum Grav. **23** 527–537. 176
- [TAMA] K. Tsubono 1995, in: E. Coccia, G. Pizzella, and F. Ronga (eds.) *Gravitational Wave Experiments* World Scientific, Singapore 112–114. 1
- [Vine02] G. de Vine, D.A. Shaddock, D.E. McClelland 2002 *Variable reflectivity signal mirrors and signal response measurements* Class. Quantum Grav. **19** 1561–1568. 149
- [VIRGO] C. Bradaschia et al. 1990 *The VIRGO Project: A wide band antenna for gravitational wave detection* Nuclear Instruments and Methods in Physics Research A **289** 518–525. 1
- [Willke00] B. Willke, S. Brozek, V. Quetschke, S. Gossler, K. Danzmann 2000 *Frequency stabilisation of a monolithic Nd:YAG ring laser by controlling the power of the laser-diode pump source* Opt. Lett. **25** (14) 1019–1021. 80
- [Zawischa02] I. Zawischa et al. 2002 *The GEO 600 laser system* Class. Quantum Grav. **19** 1775–1781. 80

Acknowledgements

Many people supported my work during the last years, in different ways.

First of all I would like to thank Prof. Dr Karsten Danzmann for offering me the opportunity to participate in the GEO 600 project. It is a pleasure to work in the very stimulating and open atmosphere provided by the Albert-Einstein-Institute.

Without Benno Willke's support and input, this work would not have been accomplished in its present form. I am especially grateful for his willingness to comprehend and discuss the topics of my work, enabling me to structure my thoughts.

I would also like to thank the commissioning team at the detector site in Ruthe. They not only do a great scientific job, providing the gravitational-wave community with a very reliable and sensitive detector, but also managed to sacrifice some time for various measurements presented in this work. My special thanks go to Hartmut Grote and Harald Lück who both very patiently discussed my countless questions (not only) about the details of the GEO 600 detector control.

My work would have been much harder without the simulation tool FINESSE. Many thanks to Andreas Freise, not only for making his program available to the public, but also for the support at the start of my work, and the combating discussions. Besides, it is my pleasure to thank Gerhard Heinzl who provided his experience and knowledge about control loops and error-signals. He is a rare and amazing example of productivity, diversified abilities, friendliness and modesty.

Martin Hewitson was always very helpful, especially in calibration and MATLAB issues. (Besides, I very much enjoyed our duets at the karaoke bar in Japan. . .) Moreover, I would like to thank Joshua Smith for the discussions on noise projections, and Stefan Hild and André Thüring, for the cooperation regarding the compound signal-recycling mirror. I very much appreciate the discussions with my colleagues from Garching, Roland Schilling and Albrecht Rüdiger. Konrad Mors and Gerrit Kühn were of invaluable and great help in terms of computer issues.

Substitutionally for the remaining members of the Albert-Einstein-Institute, I would like to thank Johanna Bogenstahl, Carlo Nicola Colacino, Antonio García Marín, Stefan Gößler, Walter Grass, Felipe Guzmán Cervantes, Klaus Haupt, Ik Siong Heng, Michèle Heurs, Volker Leonhardt, Luca Spani Molella, Konrad Mors, Ajith Parameswaran, Michaela Pickenpack, Luciano Ribichini, Andreas Weidner, and Uta Weiland for making the institute an enjoyable place to work at.

The institute's choir *die QuintenphysikerInnen* has been an invaluable source of joy and motivation during the past years. Many thanks to Prof. Dr Karsten Danzmann who supported the choir from the foundation on. Substitutionally for all singers it is my pleasure to thank Robin Eckert, Cristina Figl, Christel Franko, Prof. Dr Achim Groß, Klaus Haupt, Jobst Heitzig, Markus Kottke, Harald Lück, Cornelia Vogelsang, and Andreas Weidner who assisted the musical work with their particular dedication (and allowed me to casually work on my thesis. . .).

I would like to thank Prof. James Hough and Prof. Ken Strain for their support during my stays in Glasgow. Bryan Barr not only introduced me to his experiment, but also to scottish humor (which was quite brave to try, with such an ignorant german person

like me...). I also enjoyed the discussions I had with Malik Rakhmanov and Geppo Cagnoli. Substitutionally for all others, I would like to thank Caroline Cantley, Morag Casey, David Crooks, Eoin Elliffe, Alastair Grant, Alastair Heptonstall, Russel Jones, Valerie Nadeau, Gail Penny, Neil Robertson, and Ken Skeldon (and Janet and Kate) for the enrichment of my social life in Glasgow.

The European Graduate College on *Interference and Quantum Applications* is very much indebted to Prof. Dr Tiemann. His commitment and personality crucially influenced Graduate College's nature. For further animating it, I particularly would like to thank Olivier Allard, Cristina Figl, André Grimpe, Kirsten Jaspers, Nils Rehbein, and Uta Weiland.

For proofreading this thesis I would like to thank Hartmut Grote, Francesca Ferrari, Martin Hewitson, Albrecht Rüdiger, Fritzi Trautwein, and Benno Willke.

Finally, I thank my parents, my brother's family, and Silke Busse for the great support and patience during the past years.

Curriculum vitae

Michaela Malec
Tulpenstr. 6
30167 Hannover

Born 18th of October 1972 in Hannover, Germany

- 01 2006 Albert-Einstein-Institut Hannover, Max-Planck-Institut für Gravitationsphysik und Institut für Gravitationsphysik der Universität Hannover
- 2002 three and two months long visits at the Institute for Gravitational Research, University of Glasgow, Great Britain
- 01 2001 – 12 2003 scholarship holder at the European Graduate College “Interference and Quantum Applications”
- 10 2000 – 02 2006 Ph.D. student at the University of Hannover
- 02 – 08 1997 Eötvös Loránd University, Budapest, Hungary
- 02 – 08 1997 “TEMPUS” scholarship holder, University of Hannover
- 10 1994 – 06 2000 Physics Diploma, University of Hannover
- 10 1992 – 09 1994 Secondary school lectureship for German and Mathematics, University of Hannover
- 05 1992 Abitur, St. Ursula-Schule, secondary school, Hannover
- 1985 – 1992 St. Ursula-Schule, secondary school, Hannover
- 1983 – 1985 Orientierungsstufe Nackenberg, Hannover
- 1979 – 1983 Hinrich-Wilhelm-Kopf-Schule, basic primary school, Hannover

Publications

H. Grote, B. Allen, P. Aufmuth, C. Aulbert, S. Babak, R. Balasubramanian, B.W. Barr, S. Berukoff, A. Bunkowski, G. Cagnoli, C.A. Cantley, M.M. Casey, S. Chelkowski, D. Churches, T. Cokelaer, C.N. Colacino, D.R.M. Crooks, C. Cutler, K. Danzmann, R. Davies, R.J. Dupuis, E. Elliffe, C. Fallnich, A. Franzen, A. Freise, S. Goßler, A. Grant, S. Grunewald, J. Harms, G. Heinzl, I.S.Heng, A. Hepstonstall, M. Heurs, M. Hewitson, S. Hild, J. Hough, Y. Itoh, R. Jones, S.H. Huttner, K. Kawabe, C. Killow, K. Kötter, B. Krishnan, V. Leonhardt, H. Lück, B. Machenschalk, M. Malec, R.A. Mercer, C. Messenger, S. Mohanty, K. Mossavi, S. Mukherjee, P. Murray, S. Nagano, G.P. Newton, M.A. Papa, M. Perreux-Lloyd, M. Pitkin, M.V. Plissi, V. Quetschke, V. Re, S. Reid, L. Ribichini, D.I. Robertson, N.A. Robertson, J.D. Romano, S. Rowan, A. Rüdiger, B.S. Sathyaprakash, R. Schilling, R. Schnabel, B.F. Schutz, F. Seifert, A.M. Sintes, J.R. Smith, P.H. Sneddon, K.A. Strain, I. Taylor, R. Taylor, A. Thüring, C. Ungarelli, H. Vahlbruch, A. Vecchio, J. Veitch, H. Ward, U. Weiland, H. Welling, P. Williams, B. Willke, W. Winkler, G. Woan, I. Zawischa 2005
The status of GEO 600 Class. *Quantum Grav.* **22** 193–198.

H. Grote, A. Freise, M. Malec, G. Heinzl, B. Willke, H. Lück, K.A. Strain, J. Hough, K. Danzmann 2004
Dual Recycling for GEO 600 Class. *Quantum Grav.* **21** 473–480.

M. Malec, H. Grote, A. Freise, G. Heinzl, K.A. Strain, J. Hough, K. Danzmann 2004
Towards dual recycling with the aid of time and frequency domain simulations
Class. Quantum Grav. **21** 991–998.

S. Gossler, M.M. Casey, A. Freise, A. Grant, H. Grote, G. Heinzl, M. Heurs, M.E. Husman, K. Kötter, V. Leonhardt, H. Lück, M. Malec, K. Mossavi, S. Nagano, P.W. McNamara, M.V. Plissi, V. Quetschke, D.I. Robertson, N.A. Robertson, A. Rüdiger, R. Schilling, K.D. Skeldon, K.A. Strain, C.I. Torrie, H. Ward, U. Weiland, B. Willke, W. Winkler, J. Hough, K. Danzmann 2003
Mode-cleaning and injection optics of the gravitational-wave detector GEO 600
Rev. Scientific Instr. **74** 3787–3796.

A.M. Sintes, P. Aufmuth, C. Aulbert, S. Babak, R. Balasubramanian, B.W. Barr, S. Berukoff, S. Borger, G. Cagnoli, C.A. Cantley, M.M. Casey, S. Chelkowski, D. Churches, C.N. Colacino, D.R.M. Crooks, C. Cutler, K. Danzmann, R. Davies, R. Dupuis, E. Elliffe, C. Fallnich, A. Freise, S. Goßler, A. Grant, H. Grote, S. Grunewald, J. Harms, G. Heinzl, I.S. Heng, A. Hepstonstall, M. Heurs, M. Hewitson, J. Hough, R. Ingley, Y. Itoh, O. Jennrich, R. Jones, S. Hutter, K. Kawabe, C. Killow, K. Kötter, B. Krishnan, V. Leonhardt, H. Lück,

B. Machenschalk, M. Malec, C. Messenger, K. Mossavi, S. Mohanty, S. Mukherjee, S. Nagano, G.P. Newton, M.A. Papa, M. Perreux-Lloyd, M. Pitkin, M.V. Plissi, V. Quetschke, S. Reid, L. Ribichini, D.I. Robertson, N.A. Robertson, S. Rowan, A. Rüdiger, B.S. Sathyaprakash, R. Schilling, R. Schnabel, B.F. Schutz, F. Seifert, J. Smith, P. Sneddon, K.A. Strain, I. Taylor, C.I. Torrie, A. Vecchio, H. Ward, U. Weiland, H. Welling, P. Williams, B. Willke, W. Winkler, G. Woan, I. Zawischa 2003
Detector characterization in GEO 600 Class. Quantum Grav. **20** 731–740.

M. Hewitson, P. Aufmuth, C. Aulbert, S. Babak, R. Balasubramanian, B.W. Barr, S. Berukoff, G. Cagnoli, C.A. Cantley, M.M. Casey, S. Chelkowski, D. Churches, C.N. Colacino, D.R.M. Crooks, C. Cutler, K. Danzmann, R. Davis, R.J. Dupuis, E. Elliffe, C. Fallnich, A. Freise, S. Goßler, A. Grant, H. Grote, G. Heinzl, S. Heng, A. Hepstonstall, M. Heurs, J. Hough, Y. Itoh, O. Jennrich, R. Jones, S. Hutter, K. Kawabe, C. Killow, K. Kötter, B. Krishnan, V. Leonhardt, H. Lück, B. Machenschalk, M. Malec, K. Mossavi, S. Mohanty, S. Mukherjee, S. Nagano, G.P. Newton, B.J. Owen, M.A. Papa, M. Perreux-Lloyd, M. Pitkin, M.V. Plissi, V. Quetschke, S. Reid, L. Ribichini, D.I. Robertson, N.A. Robertson, S. Rowan, A. Rüdiger, B.S. Sathyaprakash, R. Schilling, R. Schnabel, B.F. Schutz, F. Seifert, A.M. Sintes, J. Smith, P. Sneddon, K.A. Strain, I. Taylor, C.I. Torrie, A. Vecchio, H. Ward, U. Weiland, H. Welling, P. Williams, B. Willke, W. Winkler, G. Woan, I. Zawischa 2003
A report on the status of the GEO 600 gravitational wave detector Class. Quantum Grav. **20** 581–592.

G. Woan, P. Aufmuth, C. Aulbert, S. Babak, R. Balasubramanian, B.W. Barr, S. Berukoff, S. Bose, G. Cagnoli, M. Casey, D. Churches, C.N. Colacino, D.R.M. Crooks, C. Cutler, K. Danzmann, R. Davis, R.J. Dupuis, E. Elliffe, C. Fallnich, A. Freise, S. Goßler, A. Grant, H. Grote, G. Heinzl, A. Hepstonstall, M. Heurs, M. Hewitson, J. Hough, O. Jennrich, K. Kawabe, K. Kötter, V. Leonhardt, H. Lück, M. Malec, P. McNamara, K. Mossavi, S. Mohanty, S. Mukherjee, S. Nagano, G.P. Newton, B.J. Owen, M.A. Papa, M.V. Plissi, V. Quetschke, D.I. Robertson, N.A. Robertson, S. Rowan, A. Rüdiger, B.S. Sathyaprakash, R. Schilling, B.F. Schutz, R. Senior, A.M. Sintes, K.D. Skeldon, P. Sneddon, F. Stief, K.A. Strain, I. Taylor, C.I. Torrie, A. Vecchio, H. Ward, U. Weiland, H. Welling, P. Williams, W. Winkler, B. Willke, I. Zawischa 2003
The GEO 600 Gravitational Wave Detector — Pulsar Prospects in: M. Bailes, D. Nice, S. Thorsett (eds.) *Radio Pulsars*. ASP Conference Series **CS-302** 351–355.

K. Kötter, C. Aulbert, S. Babak, R. Balasubramanian, S. Berukoff, S. Bose, D. Churches, C.N. Colacino, C. Cutler, K. Danzmann, R. Davies, R. Dupuis, A. Freise, H. Grote, G. Heinzl, M. Hewitson, J. Hough, H. Lück, M. Malec, S.D. Mohanty, S. Mukherjee, S. Nagano, M.A. Papa, D. Robertson, B.S. Sathyaprakash, B.F. Schutz, A.M. Sintes, K.A. Strain, I.J. Taylor, A. Vecchio, H. Ward, U. Weiland, B. Willke,

G. Woan 2002

Data acquisition and detector characterization of GEO 600 Class. Quantum Grav. **19** 1399–1407.

B. Willke, P. Aufmuth, C. Aulbert, S. Babak, R. Balasubramanian, B.W. Barr, S. Berukoff, S. Bose, G. Cagnoli, M.M. Casey, D. Churches, D. Clubley, C.N. Colacino, D.R.M. Crooks, C. Cutler, K. Danzmann, R. Davies, R. Dupuis, E. Elliffe, C. Fallnich, A. Freise, S. Goßler, A. Grant, H. Grote, G. Heinzl, A. Heptonstall, M. Heurs, M. Hewitson, J. Hough, O. Jennrich, K. Kawabe, K. Kötter, V. Leonhardt, H. Lück, M. Malec, P.W. McNamara, S.A. McIntosh, K. Mossavi, S. Mohanty, S. Mukherjee, S. Nagano, G.P. Newton, B.J. Owen, D. Palmer, M.A. Papa, M.V. Plissi, V. Quetschke, D.I. Robertson, N.A. Robertson, S. Rowan, A. Rüdiger, B.S. Sathyaprakash, R. Schilling, B.F. Schutz, R. Senior, A.M. Sintes, K.D. Skeldon, P. Sneddon, F. Stief, K.A. Strain, I. Taylor, C.I. Torrie, A. Vecchio, H. Ward, U. Weiland, H. Welling, P. Willams, W. Winkler, G. Woan and I. Zawischa 2002

The GEO 600 gravitational wave detector Class. Quantum Grav. **19** 1377–1387.

Overview of carrier, and **SR** and **MI** control SB frequency relations,
and of their resonance conditions inside the dual-recycled Michelson interferometer

